Global Environmental Impact of Supersonic Cruise Aircraft in the Stratosphere

Raymond L. Speth, Sebastian D. Eastham, Thibaud M. Fritz, Inés Sanz-Morère, Akshat Agarwal, Prakash Prashanth, Florian Allroggen, Steven R. H. Barrett
Laboratory for Aviation and the Environment
Department of Aeronautics and Astronautics
Massachusetts Institute of Technology

Abstract

We analyze the climate and ozone impacts of commercial supersonic aircraft using state-of-the-science modeling capabilities ranging from plume to global scale. A scenario-based approach captures variability and uncertainty in the impacts with market adoption, aircraft design choices and regulatory scenarios, focusing on different overland flight restrictions. We find that the notional aircraft considered could attract a market of up to 2.5% of year-2035 seat-kilometers. Overland flight restrictions reduce this market by 80–100%. In comparison to subsonic aircraft, contrails are found to be $\sim$ 10 times less likely to form behind supersonic jets. A Mach 1.6 jet cruising at 17 km altitude causes 0.85 mDU of depletion per billion seat-km, with 54% of this impact attributable to sulfur emissions and 35% to NO_x emissions. As a result, we find a net non-CO_2, non-contrail radiative forcing of $-0.020\,\mathrm{mW\,m^{-2}}$ per billion seat-km. Long-term adjoint simulations show that net ozone-neutral cruise can be achieved by flying near 14 km, subject to fuel sulfur content and NO_x emissions index.

Acknowledgments

The authors would like to thank the the following individuals (listed alphabetically) who contributed to this research project, including graduate students, research staff, co-investigators, and other collaborators. The contents of this report do not necessarily reflect the views of all contributors. Those individuals without a listed institutional affiliation were at MIT at the time of their contributions.

Luis E. Alvarez
Fabio Caiazzo
Irene C. Dedoussi
Daven Henze, University of Colorado, Boulder
Luke Kulik
Robert Malina
Ronald G. Prinn
Jayant S. Sabnis
Susan Solomon
Laurens Voet
Ian A. Waitz
Qiqi Wang
Lawrence Wong

Global Environmental Impact of Supersonic Cruise Aircraft in the Stratosphere

---

Table of Contents

EXECUTIVE SUMMARY

Environmental impacts associated with the operation of supersonic aircraft in the stratosphere have been an object of scientific interest since the 1970s when the first commercial supersonic airliners, the Tupolev Tu-144 and the Concorde, entered into service. Because supersonic aircraft emit NO_x at high altitudes, stratospheric ozone depletion has been a primary subject of investigation (Cunnold et al., 1977; Tie et al., 1994; Kawa et al., 1999). Studies have also quantified the climate impacts associated with supersonic aircraft (Pitari and Mancini, 2001; Baughcum et al., 2003; Grewe et al., 2007; Lee et al., 2010), which, among others, result from ozone depletion, water vapor emissions and CO_2 emissions.

Interest in supersonic passenger aircraft has been recently renewed, and several companies are actively developing new supersonic aircraft (e.g. Boom, Aerion, and Spike). With more than a decade having passed since the last assessment of the environmental impacts of supersonic aircraft, we apply and advance state-of-the-science models for this purpose. Specifically, we improve established global atmospheric models to accurately represent effects unique to high-altitude flight, and develop new models to estimate the market potential for commercial supersonic aircraft and to evaluate aircraft plume-scale chemistry and microphysics. Using a scenario-based approach, we study the sensitivity of impacts to aircraft design choices, regulatory scenarios, and market forces, thereby informing policy and future aircraft design choices from an environmental perspective.

Future scenarios

We develop emissions inventories for commercial supersonic air services for the year 2035 using a scenario-based approach. The scenarios allow us to consider variability and uncertainty in outcomes with regard to aircraft specification, regulatory scenarios, and market adoption of commercial supersonic services. For the aircraft specification scenarios, we identify a set of notional aircraft spanning the range of aircraft currently being developed with ranges between 3,500 nmi and 6,000 nmi, passenger capacities between 20 and 100 seats, and cruise speeds between Mach 1.4 and Mach 2.2. While we do not aim to develop detailed aircraft concepts, we constrain the characteristics of our notional aircraft based on data from aircraft concepts discussed in the literature. For regulatory scenarios, we model unrestricted flight scenarios as well as overflight restrictions both over all land areas and over land areas meeting specific population density thresholds. The regulatory scenarios also encompass scenarios with Mach cutoff flight over restricted areas. Market adoption scenarios are computed based on the potential willingness-to-pay of passengers for supersonic services. This approach allows us to quantify the market feedbacks to changes in regulatory restrictions and aircraft capabilities.

In the scenarios with unrestricted flight paths, we find fleets of 130–870 commercial supersonic aircraft operating between 100,000 and 750,000 round-trip flights annually,

thereby serving up to 2.5% of the expected global commercial seat-kilometers. This would result in a net increase of fuel burn from commercial passenger aviation by up to 7% and of NO_x emissions by up to 10%, which considers reductions in fuel burn and emissions due to replaced subsonic flights. The market is largely focused on high-income countries, with, for example, 36% of the global projected supersonic operations serving the North American market (see Figure E1 for our baseline notional aircraft, the SST45-1.6-60 with a range of 4,500 nmi, cruise speed of Mach 1.6, and 60 seats. This is due to the expected high costs of supersonic flights, which result in a cost premium of 185 to 281 USD per hour of time saving for the baseline aircraft. The market potentials are sensitive to aircraft design, with global seat-km varying by a factor of up to 30 across the notional aircraft under consideration (see Figure E1 for a subset of results). Economies of scale in aircraft seat capacity are the strongest driver of this variability, followed by speed and range.

Our results indicate that 78% to 100% of the potential market for unrestricted supersonic flights would not be served if supersonic flight was prohibited over all land areas. This decrease in market size results from increases in fuel burn and higher costs combined with lower time savings. In turn, reducing the stringency

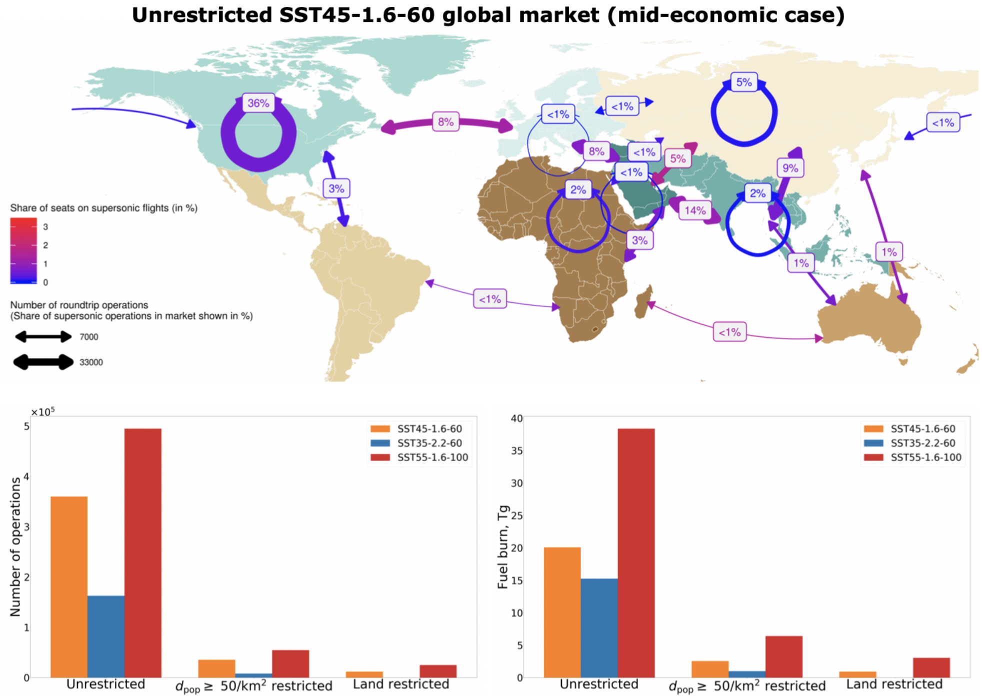

Figure E1: Market potentials for commercial supersonic air services with different notional aircraft and routing restrictions. Top panel shows a map of the global market without overflight restrictions for our baseline notional aircraft SST45-1.6-60 (Range: 4,500 nmi, Cruise speed: Mach 1.6, 60 seats). The bottom left panel shows annual round-trip operations for three notional aircraft (baseline aircraft SST45-1.6-60; SST35-2.2-60 with a range of 3,500 nmi, cruise speed at Mach 2.2 and 60 seats; SST55-1.6-100 with a range of 5,500 nmi, cruise speed at Mach 1.6, and 100 seats) under different overflight restriction scenarios. The bottom right panel shows the corresponding global annual fuel burn. All results are presented for the mid economic scenario for 2035.

of overflight restrictions (e.g. restricting flight over areas with population density higher than 50 inhabitants per sq. km only) can make supersonic routes viable in significant markets (e.g. North America). Using Mach cut-off technology, which could enable cruise speeds of Mach 1.05 for flight over restricted areas, can constitute a competitive advantage for supersonic aircraft over subsonic aircraft.

Plume-scale effects

Global, 3-D atmospheric chemistry transport models are typically not able to resolve non-linear chemical impacts due to the concentrations of reactive species in aircraft plumes, which are orders of magnitude higher than the background atmosphere. Under-resolving these plume-scale effects leads to inaccurate estimation of the plumes' chemical effects on the environment.

We develop the Aircraft Plume Chemistry, Emissions, and Microphysics Model (APCEMM) to assess the chemical processing that occurs in aircraft plumes in the first 24–48 hours after emission, including both gas phase chemistry as well as heterogeneous chemistry occurring on aerosols which form in the plume (Fritz et al., 2020). We find that the instant dilution approach leads to a positive bias in ozone production and NO_x to NO_y conversion rates that is largest during the summer when ozone production is enhanced across the Northern Hemisphere. Using adjoint-derived sensitivities (described in detail in a subsequent section), we find that accounting for plume-scale effects decreases the estimated ozone impact of subsonic aviation and of supersonic aviation at Mach numbers below ~ 1.8, as shown in Figure E2. However, at higher Mach numbers, the instant dilution approach underestimates the extent of ozone destruction.

APCEMM can also be used to model the formation and evolution of contrails, and to evaluate their chemical impacts and optical properties. We find that contrail-induced impacts on ozone production are within $\sim 10\%$ of the pure gas-phase response, with the greatest effects at high altitudes.

Contrails

Condensation trails ("contrails"), the ice clouds which form in the exhaust plume of aircraft engines, are known to contribute to aviation-attributable radiative forcing (RF). They have previously been estimated to cause up to half of the net RF impacts associated with the fleet of subsonic aircraft. However, the effect of supersonic flights which operate at higher altitude has not been widely studied. Furthermore, the majority of contrail coverage and impact studies have relied on model data with limited accuracy and reliability in the upper troposphere and lower stratosphere, where supersonic aircraft fly.

Using a five-year archive of radiosonde measurements, we find that contrail formation and persistence for supersonic aircraft is likely to differ significantly from the formation and persistence of contrails formed by subsonic aircraft. The determining factors for this difference are (1) the flight altitude of the aircraft design which is related to cruise Mach number, and (2) the latitude of flights. Increasing cruise altitude from typical subsonic altitudes (9–12 km) to 17 km, where our baseline

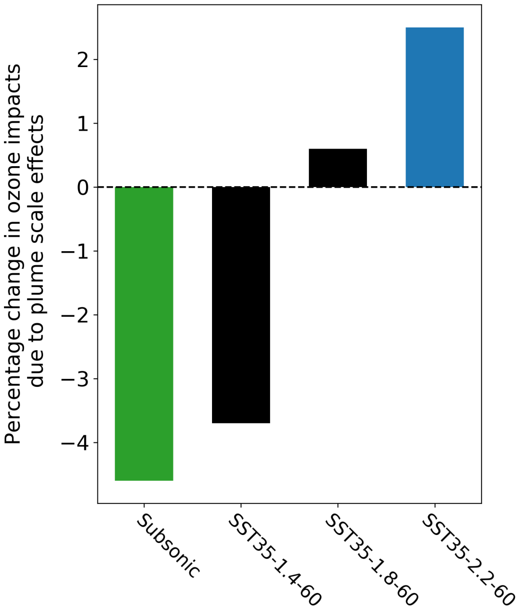

Figure E2: Change in long-term ozone impacts resulting from plume-scale chemistry, and the effect of increasing cruise altitude. The three notional designs shown cruise at Mach 1.4, 1.8, and 2.2 respectively. A negative value indicates a reduction in the magnitude of the calculated change in column ozone; all supersonic designs are found to yield net ozone destruction, while the subsonic fleet yields net ozone production.

notional aircraft SST45-1.6-60 would operate in cruise, decreases the likelihood of persistent contrail formation by a factor of three when averaged over all locations globally (Figure E3). Within northern mid-latitudes, where we expect 50–60% of all supersonic aviation fuel burn to occur, flying at an altitude of 17 km results in a greater than 75% reduction in the likelihood of persistent contrail formation. In contrast, the same increase in altitude results in a doubling in persistent contrail formation likelihood in the tropics. Flying at even higher altitudes, for example at 19 km for SST35-2.2-60, a Mach 2.2 aircraft, results in the likelihood of persistent, tropical contrail formation falling to a similar level as for subsonic aircraft, while the likelihood of mid-latitude contrails remains at around one quarter of that for subsonic aviation.

The combined effect is that supersonic flights are expected to result in fewer persistent contrails, per km traveled, than subsonic flights. Although contrails forming at higher altitude may have longer lifetimes, displacement of subsonic travel by supersonic travel is expected to result in a net decrease in contrail impacts.

Long-term atmospheric response

To evaluate the environmental impacts of supersonic aviation, we implement improvements in the global chemistry-transport model (CTM) GEOS-Chem, including an updated stratospheric aerosol scheme, and enhancements to enable the evaluation of impacts of aviation emissions on stratospheric water vapor concentrations and

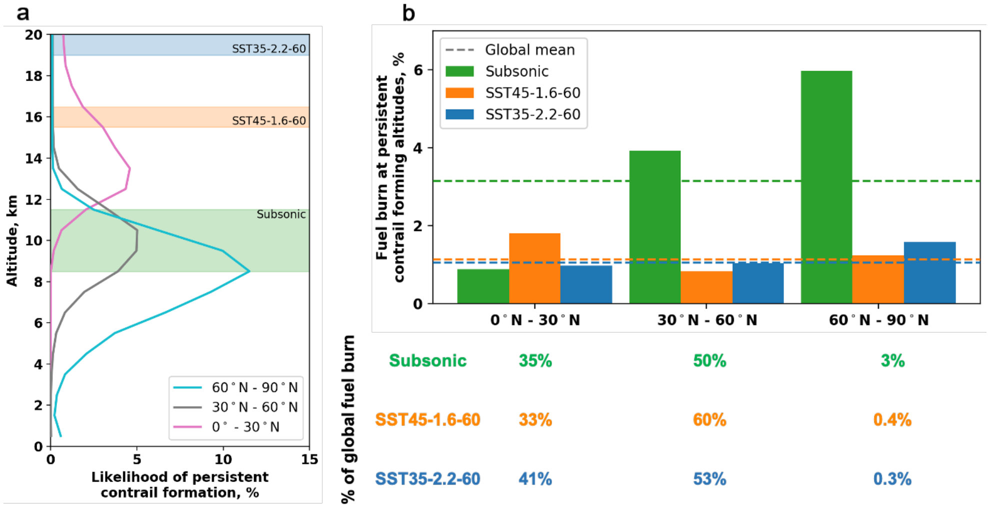

Subsonic	35%	50%	3%
SST45-1.6-60	33%	60%	0.4%
SST35-2.2-60	41%	53%	0.3%

Figure E3: Effects of cruise altitude on potential for contrail formation. Panel a: likelihood of persistent contrail formation for three latitude bands as a function of altitude. Shaded regions show the approximate cruise altitudes of each aircraft. Panel b: Likelihood of persistent contrail formation for two notional supersonic aircraft (orange: SST45-1.6-60, a Mach 1.6 notional aircraft; and blue: SST35-2.2-60, a Mach 2.2 notional aircraft) compared to subsonic aircraft (green) for three latitude bands, based on the vertical distribution of fuel burn for that aircraft. Dashed lines show the global mean, not accounting for variations in traffic density by latitude and longitude.

long-term methane destruction from aviation-attributable ozone.

Considering non-CO_2, non-contrail effects, we estimate that the SST45-1.6-60 notional aircraft, a Mach 1.6 aircraft with 60 seats and a range of 4,500 nmi, will produce a net radiative forcing of $-20 \times 10^{-3}\,\mathrm{mW\,m^{-2}}$ per billion seat-km flown, as compared to a positive forcing of $1.3 \times 10^{-3}\,\mathrm{mW\,m^{-2}}$ for subsonic aircraft. These net impacts include positive radiative forcing due to water vapor and ozone, and negative radiative forcing resulting from sulfur aerosols, whereas the impacts of contrails and CO_2 emissions are not evaluated. At the fleet level for the simulated SST45-1.6-60 fleet (0.86% of global seat-km in 2035), this results in a net radiative forcing attributable to commercial supersonic flights of $-3.2\,\mathrm{mW\,m^{-2}}$.

While water vapor emissions contribute 29% of the positive radiative forcing component, the radiative forcing due to ozone depletion is over two times as large. For the SST45-1.6-60 notional aircraft our results indicate an ozone depletion of 0.85 mDU per billion seat-km flown, with 54% of this depletion being attributable to sulfur emissions and 35% to NO_x emissions. This impact is a factor of 14 greater than the ozone increase resulting from subsonic aviation per billion seat-km (see Figure E4), mainly due to the higher cruise altitude (17 km cruise altitude for SST45-1.6-60). Because net ozone production in the troposphere almost equals ozone depletion in the stratosphere, changes in mean column ozone are near-zero. However, net zero column change will still result in non-zero radiative forcing and non-zero environmental impact. Long-term methane feedbacks reduce the net ozone production resulting from subsonic aviation, such that the net increase in ozone would be increased by 41% if methane feedbacks were not accounted for. For supersonic aviation, excluding methane feedbacks would instead reduce net ozone depletion by 11%. Equivalently, methane feedbacks decrease the net ozone depletion due to subsonic aviation by 29%, but increase depletion due to SST45-1.6-60 by 10%.

In line with previous studies, we find the ozone impacts to be highly sensitive to changes in flight altitude. The SST35-2.2-60 notional aircraft, which operates at Mach 2.2 and a cruise altitude of 19 km, is found to cause an order of magnitude increase in ozone depletion per billion seat-km flown as compared to SST45-1.6-60, and two orders of magnitude more ozone change than subsonic aviation. If long-term methane feedbacks are neglected, as has been the case in some prior work, the radiative forcing from SST35-2.2-60 is $0.10\,\mathrm{mW\,m^{-2}}$. This is an order of magnitude greater than the negative forcing from the lower-altitude SST45-1.6-60. However, inclusion of methane feedbacks results in an additional negative term which reduces the forcing from SST35-2.2-60 to $0.026\,\mathrm{mW\,m^{-2}}$. Although these effects are magnified by the greater fuel burn per seat-km of supersonic aviation, ozone and (non-CO_2, non-contrail) radiative forcing impacts per unit of fuel burn are still one to two orders of magnitude greater for supersonic than subsonic aviation.

Sensitivity to aircraft design and emissions

The impacts of supersonic aviation can be moderated or exacerbated by changes in aircraft design parameters or performance assumptions, including cruise altitude, routing, and emissions indices. This is because our models find the effect of aviation emissions on column ozone to vary strongly as a function of altitude and fuel sulfur content. Using the GEOS-Chem UCX adjoint, developed as part of this project, we find that ozone destruction due to sulfur emissions is greater than the change due to NO_x emissions at 12–16 km altitude (Figure E5).

Cruising at 13–15 km results in annual average, net zero change in column ozone, when typical subsonic emissions indices and current-day fuel sulfur content values

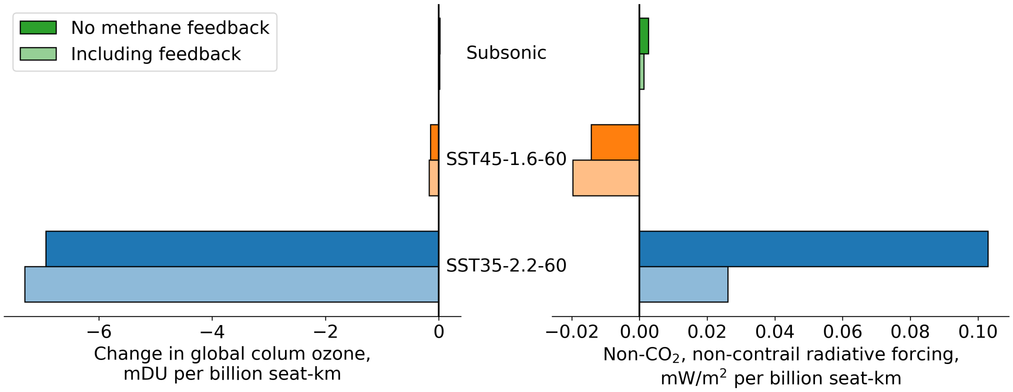

Figure E4: Ozone and radiative forcing impacts of subsonic and supersonic aviation. Impacts of the year-2035 subsonic aircraft fleet (top, green), a notional Mach 1.6 supersonic aircraft (middle, orange), and a notional Mach 2.2 supersonic aircraft (bottom, blue) are reported per billion seat-km traveled. Left: changes in global mean column ozone. Right: changes in stratospherically-adjusted, global mean radiative forcing. Darker (upper) bars show impacts evaluated when excluding long-term atmospheric feedbacks mediated by methane. Lighter (lower) bars show impacts when including these long-term feedbacks.

are used. This is due to a balance between increasing tropospheric ozone in response to NO$_x$ emissions and depletion of lower stratospheric ozone due to increasingly long-lived sulfur aerosols. Water vapor is a minor contributor at all altitudes. Although NO$_x$-related depletion effects exceed those of sulfur for emissions above 23 km, the NO$_x$-related depletion exceeds all other factors for any cruise altitudes above 19 km.

Applying these sensitivities to our set of notional aircraft, we find that net ozone depletion increases monotonically with increasing Mach number (i.e. cruise altitude). NO$_x$ emissions from aircraft with cruise altitudes in the 13–15 km range will be approximately net neutral in terms of column ozone depletion, but any sulfur in the fuel will result in additional depletion which may exceed the NO$_x$ impacts. Applying overland flight restrictions slightly increases impacts, mostly due to the reduced fuel efficiency because the aircraft are forced to reroute and fly at lower-than-optimal altitudes. Chemistry on the surface of contrails behind supersonic aircraft will result in greater ozone depletion than for lower-altitude subsonic aircraft for each hour that the contrail persists.

Conclusions

The impact of supersonic aircraft on the environment is complex, and depends on factors including the altitude at which these aircraft would fly, the emissions characteristics of the engines used on these aircraft, the properties of the fuel, and the size of the fleet. We find the market for commercial supersonic air services to be small and highly sensitive to aircraft characteristics and flight restrictions. Across the

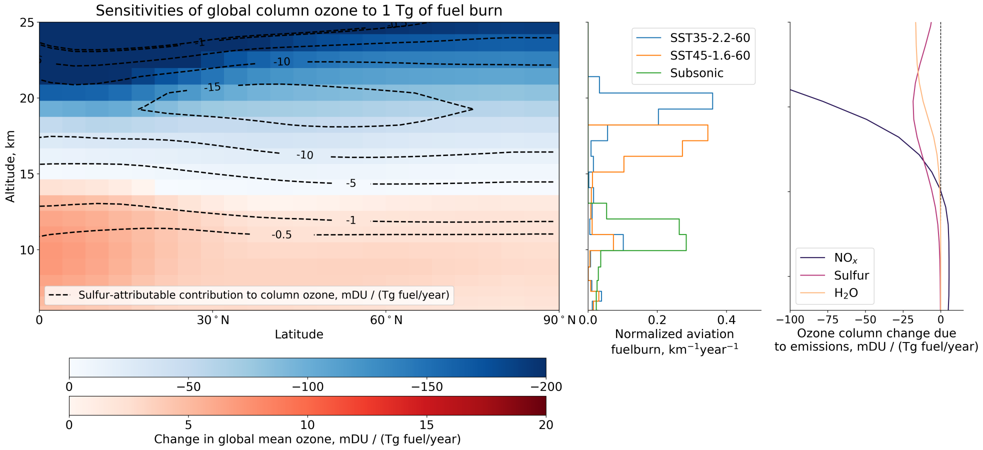

Figure E5: Sensitivity of global column ozone to aircraft emissions at different altitudes and latitudes. Left: colors show the net change in global, annual mean column ozone due to an additional unit of fuel burn for any latitude and altitude in the Northern hemisphere, up to 25 km altitude. Red indicates that fuel burn at that location will cause an increase in annual, global mean column ozone, while blue indicates that fuel burn at that location will cause a decrease. Dashed lines show the contribution of emitted sulfur to this change. Center: vertical distribution of fuel burn due to subsonic aircraft and two notional supersonic aircraft designs, normalized by total fuel burn per year. Right: sensitivity of global, annual mean column ozone to an additional unit of fuel burn, broken down by component. Left and right panels assume a NO$_x$ emissions index of 15 g per kg of fuel (NO$_2$ mass basis) and 600 ppm fuel sulfur.

range of altitudes where supersonic aircraft might fly, environmental metrics such as the change in total ozone column and net (non-CO_2, non-contrail) radiative forcing change not only in magnitude but in sign in response to aircraft emissions. This variability means that the environmental impacts of specific supersonic aircraft, which have significantly different flight altitudes, emissions characteristics, fuel properties, or route networks as compared to the notional aircraft discussed here, cannot be directly inferred from the results that we present. However, our adjoint-based approach does provide the capability to rapidly assess the impacts of aircraft with different characteristics. Furthermore, the adjoint model can be used to identify regions where the sensitivities of environmental metrics to emissions are lower, thereby enabling the design of supersonic aircraft with minimal environmental impacts. We hope that our findings provide valuable insight into the potential effects of design and regulatory choices from an environmental perspective and contribute to the understanding of the economic feasibility of the market for commercial supersonic aviation.

Terminology

Acronyms, abbreviations, and initialisms used in this report.

AEIC	Aircraft Emissions Inventory Code
AOD	Aerosol optical depth
APCEMM	Aircraft Plume Chemistry, Emission & Microphysics Model
BAU	Business as usual
BC	Black carbon (soot)
BTS	US Bureau of Transportation Statistics
CFC	Chlorofluorocarbon
CISS	Cold ice supersaturated region
CO	Carbon monoxide
CTM	Chemistry-transport model
DJF	December, January, February
DU	Dobson unit
EDB	ICAO's emissions databank
EI	Emissions index
EIS	Entry into service
FOX	Formation OXidation method
FSC	Fuel sulfur content
GEOS-5	Goddard Earth Observing System, Version 5
GPW	Gridded Population of the World
HC	Hydrocarbons
HCFC	Hydrochlorofluorocarbons
ICAO	International Civil Aviation Organization
IGRA	Integrated Global Radiosonde Archive
IQR	Interquantile Range
ISS	Ice Supersaturated region
JJA	June, July, August
KPP	Kinetics Pre-Processor
LHV	Lower Heating Value
MA	March, April, May
MEGAN	Model of Emissions of Gases and Aerosols from Nature
MERRA	Modern Era Retrospective for Research and Analysis
MLS	Microwave Limb Sounder
MTOW	Maximum take-off weight
NAT	Nitric acid trihydrate
NH	Northern Hemisphere
NPSS	Numerical Propulsion System Simulation
OC	Organic carbon
O/D	Origin-destination pair
OEW	Operating empty weight
OM	Organic matter
OMI	Ozone Monitoring Instrument
PCC	Persistent Contrail Criteria

POLINAT	Pollution from Air Traffic Emissions in the North Atlantic Flight Corridor (observation campaign)
RCP	Representative Concentration Pathway
RF	Radiative forcing
RPK	Revenue passenger kilometers
RRTMG	Rapid Radiative Transfer Model for Global simulations
SAC	Schmidt-Appleman Criterion
SH	Southern Hemisphere
SN - $\mathrm{C_{BC}}$	Smoke-number based estimate of black carbon concentration
SON	September, October, November
SST	Supersonic transport
SST[R]-[M]-[N]	Notional aircraft with a maximum range of $R \times 100$ nautical miles, cruise speed of Mach M, and seat count N
STCA	NASA's Supersonic Technology Concept Aeroplane
SUCCESS	Subsonic aircraft: Contrail and Cloud Effects Special Study
SUT	Subsonic transport
TAS	True air speed
TSFC	Thrust-specific fuel consumption
UCX	Unified Chemistry eXtension
USD	United States dollars
UTC	Universal Time Coordinated
VMR	Volumetric mixing ratio
VOC	Volatile organic compound
VOT	Value of time

Symbols used in this report.

c_p	Heat capacity of air
C_p	Ice crystal capacitance
c	Cost of flight
$\frac{dh}{dt}$	Rate of climb
d_pop	Population density threshold
D	Diffusivity
D_k	Diffusion coefficient of species k in air
D_h	Horizontal diffusion coefficient
D_v	Vertical diffusion coefficient
$D_\mathrm{v,eff}$	Effective water vapor diffusion coefficient in air
E	Emission
ECF_X	Emission Conversion Factor of species X
EIBC	Black carbon engine emission index
F_n	Thrust requirement
F_PCC	Fuel burn weighted PCC
g	Gravitational acceleration
G	Gradient of T and p_wv mixing line in exhaust plume Aggregate consumption (at fixed price level)
h_cruise	Cruise altitude

$H_\mathrm{p}^\mathrm{act}$	Function accounting for activation of an ice particle
HO_x	Hydrogen oxides
J	Adjoint cost function
k_B	Boltzmann constant
$K_{i,j}$	Coagulation kernel for collisions between size bins i and j
L	Leisure time
$\frac{L}{D}$	Lift-to-Drag ratio
$M_\text{high-speed}$	Cruise Mach number over unrestricted areas
M_k	Molecular mass of species k
$M_\text{low-speed}$	Cruise Mach number over restricted areas
m_p	Mass of an ice particle
N_seats	Passenger capacity
$N_{k,p}$	Number of molecules of type k on particle of type p
n_k	Number density of particles in bin k
NO_x	Reactive nitrogen oxide family (NO, NO_2, ...)
NO_y	Extended nitrogen oxide family (NO_x, HNO_3, ...)
OPE	Ozone production efficiency
p	Pressure
	Price
p_t	Total (stagnation) pressure
p_k	Partial pressure of species k
p_k^sat	Saturation pressure of species k
P_PCC	Proportion of space-time satisfying the PCC
r_p	Particle radius
$\mathrm{RH_i}$	Relative humidity with respect to ice
$\mathrm{RH_w}$	Relative humidity with respect to water
$\mathrm{RH_{w,C}}$	Critical $\mathrm{RH_w}$ to satisfy the SAC
s	Species
SO_x	Sulfur oxides
t	Time (including travel time)
T	Temperature
T_d	Dew point temperature
T_LM	Max threshold plume temperature at $RH_w = 100\%$
T_t	Total (stagnation) temperature
U	Individual utility
V	Flight speed
	Indirect utility function
w	Wage rate
W	Instantaneous aircraft weight
	Working time
wv (subscript)	Water vapor
wi (subscript)	Water ice
z	Altitude
β	Uptake fraction
η_o	Overall engine efficiency

λ	Longitude
ϕ	Latitude
θ	Fractional coverage of the particle liquid coating
τ	Optical depth
	Total available time
τ_{pre}	Predominant optical depth

1 Introduction

Environmental impacts associated with the operation of supersonic aircraft in the stratosphere have been an object of scientific interest since the 1970s (Grobecker et al., 1974) when the first commercial supersonic airliners, the Tupolev Tu-144 and the Concorde, entered into service. With the recently renewed interest in supersonic passenger aircraft and several companies actively developing new supersonic aircraft (Boom, 2020; Aerion, 2020), an environmental assessment of such aircraft using state-of-the-science modeling capabilities can inform policy and design decisions which would affect a new generation of supersonic aircraft. This report describes the development of the modeling tools required to perform such an assessment, and the use of those models in a scenario-based approach to assess the climate and atmospheric impacts of future commercial supersonic fleets under a range of scenarios incorporating different aircraft designs, economic trajectories, and policy options.

1.1 Background and previous work

Previous research on the atmospheric impacts of supersonic aircraft has focused mainly on their contribution to stratospheric ozone depletion (Cunnold et al., 1977; Tie et al., 1994; Kawa et al., 1999). In the stratosphere, emissions of nitrogen oxides (NO_x) can catalytically destroy ozone. Water formed during fuel combustion provides a source of oxides of hydrogen (HO_x) which also destroys ozone. Additionally, Kawa et al. (1999) found that sulfate aerosols formed from fuel sulfur were a significant cause of ozone destruction. For these impacts, the higher flight altitudes of supersonic aircraft are associated with increased atmospheric residence times for aircraft emissions, which increases the chemical sensitivities.

The climate impacts from supersonic aircraft have been evaluated in terms of radiative forcing (RF) (Pitari and Mancini, 2001; Baughcum et al., 2003; Grewe et al., 2007; Lee et al., 2010). The largest contributors to climate impacts identified by Grewe et al. (2007) were warming from emitted water vapor and cooling from sulfate aerosol. Smaller contributions to RF were estimated from stratospheric ozone destruction (cooling), black carbon (warming), methane destruction (cooling), and reductions in contrails (cooling).

Many prior studies have focused on examining the impacts of large (200–300 passenger), very fast (Mach 2.0 and above), and high-flying commercial supersonic aircraft with rather long ranges (5,000 nmi or more). For instance, Kawa et al. (1999) examined a 300 passenger, Mach 2.4 aircraft design with cruise altitudes between 18 and 20 km and a range of 5,000 nmi. In contrast, the supersonic aircraft currently under development are smaller, and span a range of speeds and corresponding altitudes, including the 10–15 passenger Aerion AS2 (Aerion, 2020) flying at Mach 1.4 and altitudes of 14–17 km as well as the 55-passenger Boom Overture (Boom, 2020) flying at Mach 2.2 and altitudes of 16–18 km. Furthermore, the range of proposed aircraft is shorter than what has been studied (up to 9,000 nautical miles)

Previous studies of market potential of commercial supersonic aircraft have relied on either an assumed fixed aircraft design and fleet size (Prather et al., 1992; Kawa et al., 1999; Dutta et al., 2005; Kharina et al., 2018; Jain et al., 2020); and/or estimations of market potentials by assuming fixed shares of passengers who are willing to substitute subsonic air services with supersonic air services (Grewe et al., 2007; Wen et al., 2020). These approaches have been combined with additional criteria, including minimum time savings (Wen et al., 2020; Jain et al., 2020) or minimum fleet sizes (Prather et al., 1992).

Studies of supersonic aircraft have taken a variety of approaches for calculating emissions from supersonic aircraft. Some previous studies estimate NO_x emissions indices as a function of combustor technology (Prather et al., 1992), while other studies (Kawa et al., 1999; Dutta et al., 2005) assume constant EIs. Studies considering other emissions like CO and HC, assume EIs for these species to be constant (Kawa et al., 1999). In addition, previous studies have made differing assumptions about the future sulfur content of jet fuel. While Dutta et al. (2005) did not study the impacts of fuel sulfur (on the assumption that fuel in the future would be desulfurized), Kawa et al. (1999) found that high-altitude sulfur emissions may significantly increase total ozone depletion.

1.2 Approach

We are contributing to the literature on the environmental impacts of supersonic aircraft by presenting a suite of tools, which enables us to study the atmospheric impacts of supersonic aircraft. The tools include both new and improved state-of-the-science atmospheric models as well as a scenario-based approach for studying the sensitivity of the impacts to aircraft design, regulatory scenarios, and market forces. This section provides an outline of our approach. It is organized according to the structure of this report. The full description of each modeling component is contained within the corresponding section of the report.

Scenarios for commercial supersonic aviation We first present our scenario approach, which allows us to develop emissions inventories for future commercial supersonic air services, while considering variability and uncertainty in outcomes with regard to aircraft specifications, regulatory scenarios, and market adoption.

In a first step, this requires us to establish the performance characteristics for a set of notional aircraft considered in our study. To account for the range of potential characteristics of supersonic vehicles we include notional aircraft spanning the design space in terms of passenger count, range, and Mach number. The set of notional aircraft considered in this study are informed by recent developments and proposals including efforts by Boom and Aerion (Boom, 2020; Aerion, 2020), aircraft design studies by NASA (Morgenstern et al., 2015; Berton et al., 2020), and an updated Concorde design (Roxburgh, 2004). We use scaling relationships to approximate aircraft performance parameters for intermediate designs since this study does not aim to propose detailed aircraft designs.

Secondly, the impact of supersonic cruise aircraft depends on the routes and schedules of supersonic air services. We add to the existing literature by simultaneously (i) estimating market potentials from market characteristics (e.g. income distribution of passengers) and aircraft characteristics (e.g. speed, costs); and (ii) considering different policy scenarios with overflight restrictions for supersonic aircraft. Our approach allows us to analyze the market response to different supersonic overflight restrictions (e.g.: over land and over land with certain population density thresholds) and aircraft specifications. As part of this effort, we develop an aircraft routing model which estimates market-optimal routes for supersonic aircraft considering two different cruise regimes (supersonic cruise and a "low-speed regime" for restricted areas) and potential detours to avoid restricted regions.

Thirdly, since emissions characteristics are a function not only of engine characteristics but also of flight conditions (altitude and Mach number), we use engine cycle models and a consistent representation of combustor technology to estimate variations in NO_x, CO and HC emissions indices for each notional aircraft. Emissions characteristics of each notional aircraft are combined with the routes and schedules for those aircraft in the Aviation Emissions Inventory Code (AEIC) (Simone et al., 2013) to produce a global emissions inventory, which is then used for evaluating environmental impacts.

Plume-scale impacts The chemical effects of emissions from aircraft are typically simulated in global atmospheric models using an "instant dilution" approach, in which the aircraft emissions are released into homogeneously-mixed grid cells that are orders of magnitude larger than the aircraft plume (Brasseur et al., 1998; Meijer et al., 2000; Eyring et al., 2007). This approach does not explicitly model local chemical effects associated with the high concentrations of reactive species and aerosols in the aircraft plume, which has been shown to interact with estimates of the plume's impact (Petry et al., 1998; Kraabøl et al., 2000; Cariolle et al., 2009; Huszar et al., 2013). To enable sub-grid representation of aircraft plumes in global atmospheric models, we have developed the Aircraft Plume Chemistry, Emissions, and Microphysics Model (APCEMM) (Fritz et al., 2020) and applied it under a variety of conditions. The results improve our understanding of the influence of changes in environmental conditions, aircraft characteristics, and fuel properties on in-plume chemistry and aerosols. The plume-scale processing which occurs in the first 24–48 hours after emission can then be considered as a transformation of the emissions which are introduced into the global chemistry model. The application of this transformation is considered as part of the sensitivity analysis in this report.

Contrails To assess the potential for supersonic aircraft to produce contrails, we use observations on the atmospheric profile from radiosondes which are part of the Integrated Global Radiosonde Archive (IGRA) (Durre and Yin, 2008; Durre et al., 2006). We select profiles measured using the RS92 sensor in order to have a consistent dataset based on a single sensor that is well-characterized and common in the IGRA dataset (Dirksen et al., 2014; Wang et al., 2013; Miloshevich et al., 2009). We focus on the potential for persistent contrail formation by altitude and identify trends by latitude band, season and time. We develop the persistent contrail criterion (PCC), which defines conditions in which persistent contrails can form based on the local meteorology and engine and fuel characteristics. We then estimate the fuel burn-weighted PCC, which defines the proportion of the fuel burn profile in a PCC region. This metric provides insights into how the operating characteristics of supersonic aircraft (primarily, cruise altitude) affect the potential for persistent contrail formation, and how this varies among the different supersonic aircraft designs considered.

Changes in atmospheric composition and radiative balance One concern for supersonic aviation is its effects on the ozone layer and the climate. We implement improvements in the global chemistry-transport model (CTM) GEOS-Chem to provide a more accurate representation of the impacts of supersonic aviation. These improvements include the modification of the stratospheric aerosol scheme to represent the formation of large nitric acid trihydrate crystals (Wegner et al., 2013), a new method for determining the boundary conditions for water vapor at the tropical tropopause that prevents non-physical buildup of stratospheric water vapor, and the addition of a methane flux boundary condition that enables calculations of the impact of emissions scenarios on methane concentrations. We then apply this model to simulate how both subsonic and supersonic aviation scenarios affect atmospheric ozone and aerosols and global radiative balance. We also perform sensitivity analyses to quantify the contribution of different emissions, the effect of methane feedbacks, and variation in response due to different aircraft concepts.

Sensitivities of results Since the characteristics of possible supersonic airliners and their potential routes and schedules are uncertain, many scenarios need to be considered to capture the full range of possible environmental impacts. With traditional "forward" modeling of atmospheric chemistry and transport, obtaining these results is computationally expensive since it requires us to run a reference simulation without commercial supersonic services and a scenario simulation with supersonic air services for every scenario. Given the complexity of current CTMs and the spatial and temporal variations in emissions sources, a computationally-efficient alternative is adjoint modeling, a state-of-the-art inverse method that enables rapid computation of the sensitivities of an aggregate objective function to emissions at all points and times. Starting with the GEOS-Chem Adjoint (Henze et al., 2007), we incorporate the forward modeling updates of the GEOS-Chem UCX model (Eastham et al., 2014) into the adjoint model to better represent tropospheric-stratospheric exchanges. After validating the updated GEOS-Chem adjoint, we use the adjoint to evaluate impacts of supersonic aircraft on ozone column and aerosol optical depth for different aircraft and flight restriction scenarios. We further use the approach to attribute the impacts to specific emissions species, to estimate the impact of contrail ice on ozone, and to evaluate the effects of plume-scale chemistry.

Summary By improving and extending a set of tools for evaluating the environmental impact of aviation, we quantify the ozone and climate impacts associated with the roll-out of a fleet of advanced supersonic aircraft. The combination of atmospheric modeling with adjoint methods and a scenario-based approach enables the calculation of both absolute impacts and marginal sensitivities to inputs including fleet size, aircraft performance and emissions, fuel properties, and market adoption. Our models comprise a suite of flexible tools which allow further investigation of the environmental impacts of supersonic aircraft and improve the ability to perform general assessments of the environmental impacts of aviation.

2 Future scenarios for commercial supersonic aviation

Highlights

- In the absence of flight path restrictions, we project a fleet of 130–870 supersonic aircraft to operate up to 2.5% of the seat-kilometers in the global aviation market. This results in a net increase of fuel burn from commercial passenger aviation by up to 7% and of NO_x emissions by up to 10%.
- Between 78% and 100% of the global unrestricted market potentials cannot be addressed when supersonic flight is restricted over land or over areas with a population density of more than 50 inhabitants per square kilometer. Permitting aircraft to fly overland in a Mach cut-off regime can mitigate some losses of market potentials.
- Market potentials vary by a factor of up to 30 (as measured in seat-km) across the notional aircraft under consideration, mainly due to economies of scale in aircraft seat capacity, speed and range.

The atmospheric impacts from supersonic aircraft will differ according to the design parameters of the aircraft, market potentials for and profitability of supersonic aircraft, regulatory restrictions on supersonic flight, and the degree to which supersonic services displace subsonic services. In this section, we present a scenario approach which allows us to develop emissions inventories for future commercial supersonic air services, while considering variability and uncertainty in outcomes with regard to aircraft specification, regulatory scenarios, and market adoption. We choose the year 2035 as our target year, since (1) a mature market for supersonic services can be expected after entry into service (EIS) for commercial supersonic passenger jets in the late 2020s, and (2) widely-used aviation market forecasts are available.

The analysis proceeds as follows. First, we describe our models for estimating market demand and emissions inventories for different notional commercial supersonic aircraft specifications, regulatory scenarios, and economic scenarios (Section 2.1). Second, we summarize the set of scenarios considered in our analysis (Section 2.2). Third, we discuss predicted market outcomes and emissions under the selected scenarios (Section 2.3). Finally, we synthesize our findings and compare them to existing studies (Section 2.4).

2.1 Methods for scenario-based analysis of commercial supersonic services

When estimating market demand and emissions scenarios for a future fleet of supersonic aircraft, we expect our results to be sensitive to: (1) aircraft specification given

Figure 1: Modeling steps for deriving market and emissions scenarios for supersonic aircraft.

its impact on fuel burn, cost, and travel time; (2) regulatory scenarios such as overflight restrictions which can impact on costs and travel time; (3) market conditions such as income and fuel prices; and (4) emissions characteristics of supersonic aircraft engines. To quantify the sensitivity of our results to these input parameters, we build a set of scenarios using the modeling chain outlined in Figure 1. This modeling chain also captures expected time-of-day and seasonality patterns of subsonic and supersonic flight activity since we expect the atmospheric impacts of commercial supersonic flight to vary with these parameters. Each part of the modeling chain is outlined in the following subsections.

2.1.1 Notional aircraft

Significant uncertainty and variability exists with respect to the characteristics of the expected fleet of commercial supersonic aircraft. The only previous commercial supersonic aircraft, the Concorde and the Tu-144, were developed in the 1960s and were taken out of passenger service in 2003 and 1978, respectively. More recent supersonic concepts include designs by Boom (2020), Aerion (2020), and NASA's X-59 QueSST (NASA, 2020) as well as design concepts like the NASA N+2 (Morgenstern et al., 2015). These concepts differ in characteristics such as aircraft size, speed, range, and technologies to avoid or reduce the sonic boom. For example, Boom is developing a commercial aircraft for 55 passengers with a speed of Mach 2.2 and a range of 4,500 nautical miles (nmi). In contrast, Aerion's concept is a supersonic business jet for 10–15 passengers and supersonic cruise speed of Mach 1.4. It is projected to be equipped with "Boomless Cruise" technology, which reduces the noise footprint of the supersonic boom for flights at low Mach numbers ($\leq$ Mach 1.2). Finally, NASA's planned X-59 QueSST is an experimental aircraft which is expected to fly at Mach 1.4 and will feature technology to reduce the sonic boom.

Due to technical progress in almost all aircraft systems over the past decades, one can expect mid-20th century aircraft like the Concorde and the Tu-144 not to represent the performance of future supersonic aircraft. At the same time, little concrete information is known about novel aircraft concepts. In addition, actual configurations of future supersonic aircraft and their associated performance are still subject to uncertainties. The purpose of this study is to assess the sensitivity of environmental outcomes to aircraft design choices, such as how the choice of cruise Mach number—and corresponding cruise altitude—might affect global ozone concentrations. We therefore do not develop detailed aircraft concepts, but define a set of notional aircraft by choosing fundamental design parameters (range, passenger count, and cruise Mach number) which span the design space of interest. We then prescribe L/D, thrust-specific fuel consumption, and weight accordingly, constrained by data from aircraft concepts discussed in the literature.

2.1.1.1 Reference aircraft concepts

Two existing concepts are used as reference aircraft to constrain performance characteristics of the assumed fleet of supersonic aircraft: (1) NASA's Supersonic Technology Concept Aeroplane (STCA) (Berton et al., 2020), a 55-tonne (55t) trijet; and (2) an updated version of the Concorde (Roxburgh, 2004), which incorporates newer aircraft technologies. Table 1 summarizes the characteristics of the two reference aircraft.

These reference aircraft concepts are chosen for three reasons: First, the concepts consider the state-of-the-art in commercial supersonic aircraft technologies. As such, they reflect performance characteristics which can be expected for commercial supersonic aircraft with entry into service over the coming decade. Second, unlike concepts currently developed by industry (e.g. Boom (2020) or Aerion (2020)), detailed performance and configuration data are available for our analysis. Third, the reference aircraft represent two fundamentally different approaches towards designing a supersonic airliner. While Concorde flew at Mach 2.0 and carried 100 passengers, STCA is designed to fly at Mach 1.4 and to carry ∼15 passengers in airliner configuration (8 passengers in a business jet configuration). As such, the two concepts can be used to interpolate aircraft specifications for intermediate designs.

2.1.1.2 Design variables and definition of notional aircraft types

We define a set of commercial supersonic notional aircraft, which enable us to study the sensitivity of market outcomes, emissions, and their atmospheric impacts to different aircraft design parameters. We identify an individual notional aircraft through three design variables: maximum range (in nautical miles, nmi), high-speed Mach number (maximum cruise speed in unrestricted areas) and passenger capacity (N_{seats}). The range of values to investigate is chosen according to the following considerations:

1. *Maximum range*: the maximum range of existing and proposed designs varies

Reference aircraft	Year	MTOW, tonnes	Empty weight, tonnes	Fuel Weight, tonnes	N_{seats}	High-speed Mach	Max. range, nmi	Cruise $\frac{L}{D}$	Cruise TSFC, kg/s/kN
Improved Concorde	2000's	186	84	78	100	2.0	4,100	7.7	0.028
STCA	2020	55	23	31	15	1.4	4,200	7.4	0.027

Table 1: Properties of reference aircraft concepts. We assume the STCA to be a 15 passenger aircraft in an airliner configuration. The improved Concorde includes an increase of 8% in maximum $\frac{L}{D}$ and a decrease of 15% in cruise TSFC (Roxburgh, 2004). MTOW: Maximum Take-Off Weight; TSFC: Thrust Specific Fuel Consumption; $\frac{L}{D}$: Lift-to-Drag ratio.

between 3,500 nmi (Tu-144) and 4,500 nmi (Boom). As such, we consider these values for our analysis. We also evaluate notional aircraft with extended maximum ranges of up to 6,000 nmi, since the additional range allows us to study the sensitivity of our results to the availability of non-stop, supersonic trans-Pacific services (e.g. Seattle to Hong Kong).

2. *High-speed cruise Mach number*: we consider parameter values between Mach 1.4 and Mach 2.2. The minimum value at Mach 1.4 corresponds to the STCA and Aerion's proposed design, while the maximum value of Mach 2.2 corresponds to the Boom design.
3. *Passenger capacity* (N_{seats}): we analyze aircraft with capacity ranging from 20 to 100 seats. The midpoint represents Boom's proposed design (60 passengers), whereas the maximum capacity is similar to the Concorde. The minimum capacity is chosen slightly above the STCA and Aerion's proposed design because Aerion's proposed jet and the STCA are designed as business jets. For commercial operations, we assume that additional seating capacity will be necessary for commercial viability.

From these ranges, we define eight notional aircraft as specified in Table 2. These notional aircraft are chosen to enable us to analyze the sensitivity of our results to each design variable. Throughout the report, we will refer to the SST45-1.6-60 as our supersonic "baseline notional aircraft" (with SST standing for supersonic transport). As characterized by its name, this notional aircraft has a maximum range of 4,500 nmi, a high-speed cruise Mach number of 1.6, and can carry up to 60 passengers. It reflects the mid-point specification for all design variables.

All notional aircraft are modeled using two assumptions for the "low-speed" regime, which is used when the aircraft flies over areas where supersonic cruise is prohibited (e.g. over US land): (1) a "low-speed" Mach number of 0.85, which is similar to cruise speeds of conventional subsonic aircraft; and (2) a "low-speed" Mach number of 1.05, which could enable Mach cutoff (sonic boom not reaching the ground). For this study, we will mark the latter aircraft with an "f" suffix (e.g.: SST45-1.6-60f).

	SST35-1.4-60/f	**SST35-1.6-20/f**	**SST35-1.6-100/f**	**SST35-1.8-60/f**	**SST35-2.2-60/f**	**SST45-1.6-60/f**	**SST55-1.6-100/f**	**SST60-1.6-100/f**
Max. range, nmi	3,500	3,500	3,500	3,500	3,500	**4,500**	5,500	6,000
High-speed Mach	1.4	1.6	1.6	1.8	2.2	**1.6**	1.6	1.6
N_{seats}	60	20	100	60	60	**60**	100	100
Max. h_{cruise}, kft	53	57	57	60	65	**57**	57	57
Max. h_{cruise}, km	16.1	17.4	17.4	18.3	19.8	**17.4**	17.4	17.4

Table 2: Notional aircraft analyzed in this study. The baseline notional aircraft SST45-1.6-60 is highlighted in bold.

2.1.1.3 Mission profiles

Estimation of fuel consumption and flight time for each notional aircraft requires us to model the mission. For this purpose, we adapt the mission profile developed for the NASA N+2 project (Morgenstern et al., 2015). This profile (see Figure 2 and Table 3) assumes (1) constant altitude acceleration at subsonic cruise altitude before reaching supersonic altitudes, which results in a fuel burn peak at approximately 10 km, and (2) constant altitude deceleration before descent. In addition, it considers cruise climb, which results from the combination of a constant lift coefficient with a reduction in aircraft weight during cruise.

The NASA N+2 profile is adapted for each notional aircraft in an effort to reflect the unique characteristics of each of them. This adaptation is a four-step process. Firstly, we impose cruise properties for each notional aircraft based on the design variables. Secondly, we calculate the maximum cruise altitude of each notional aircraft as a function of high-speed Mach number, following Seidel (2020) (see Table 2) and restrict the mission profile accordingly. Thirdly, we model performance characteristics (e.g. thrust specific fuel consumption, $\frac{L}{D}$, aircraft weight) for each cruise segment ("high-speed" and "low-speed") and each notional aircraft as described in Section 2.1.1.4. We use the resulting performance metrics to replace the NASA N+2 values during cruise (e.g. fuel burn, TSFC). Finally, all remaining segments are assumed to be at the same speed and altitude as defined in the NASA N+2 profile. Corresponding specifications (e.g. TSFC and $\frac{L}{D}$) are estimated by applying constant ratios between the cruise specification and relevant mission segment. These ratios are derived from the mission profile for the NASA N+2 aircraft (see Table 3).

2.1.1.4 Performance of notional aircraft

For each notional aircraft, we prescribe performance characteristics, especially "high-speed" and "low-speed" cruise TSFC and $\frac{L}{D}$, and operating empty weight (OEW). Since the goal of this work is not to study specific supersonic aircraft designs, we define constraining relationships between aircraft characteristics and performance using data from our reference aircraft (Section 2.1.1.1) as well as data for other supersonic aircraft concepts and existing subsonic designs where applicable (Seidel,

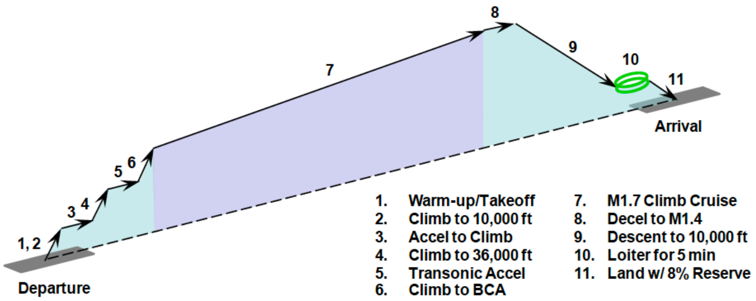

Figure 2: Reference mission profile retrieved from NASA N+2 supersonic project (Morgenstern et al., 2015)

		Initial alt, ft	Initial Mach	Initial weight, lb	Seg. fuel, lb	Seg. distance, nmi	Mission time, min	Average $\frac{L}{D}$	Average TSFC, lb/hr/lbf
1	Take-off	0	0.00	335,000	1,245	0	5.0	/	0.71
2	Climb	0	0.38	333,755	3,391	10	7.2	7.61	0.89
3	Accel.	10,000	0.45	330,364	992	4	7.9	9.68	0.94
4	Climb	10,000	0.66	329,372	7,719	68	16.0	10.20	1.03
5	Accel.	36,000	0.90	321,653	4,992	65	22.4	9.35	1.06
6	Climb	36,000	1.28	316,661	6,773	97	29.2	8.73	1.14
7	Cruise	48,000	1.70	309,888	133,216	5,088	342.3	8.73	0.94
8	Decel.	60,000	1.70	176,672	93	22	343.8	9.21	2.95
9	Descent	60,000	1.42	176,579	1,972	146	363.9	10.47	2.32
10	Loiter	10,000	0.50	174,608	1,341	0	368.9	10.49	0.97
11	Reserve	/	/	/	14,080	/	/	/	/

Table 3: Reference mission profile for the NASA N+2 design (Morgenstern et al., 2015).

	SST35-1.4-60/f	**SST35-1.6-20/f**	**SST35-1.6-100/f**	**SST35-1.8-60/f**	**SST35-2.2-60/f**	**SST45-1.6-60/f**	**SST55-1.6-100/f**	**SST60-1.6-100/f**
Max. range, nmi	3,500	3,500	3,500	3,500	3,500	**4,500**	5,500	6,000
High-speed Mach	1.4	1.6	1.6	1.8	2.2	**1.6**	1.6	1.6
N_{seats}	60	20	100	60	60	**60**	100	100
Max. h_{cruise}, km	16.1	17.4	17.4	18.3	19.8	**17.4**	17.4	17.4
High-speed cruise TSFC, kg/s/kN	0.022	0.028	0.023	0.027	0.031	**0.024**	0.023	0.023
High-speed cruise $\frac{L}{D}$	8.6	6.8	8.9	7.3	6.4	**7.9**	8.9	8.9
OEW, tonnes	42	23	67	51	66	**58**	96	108
MTOW, tonnes	78	51	123	104	148	**123**	206	241

Table 4: Design variables and performance characteristics for notional aircraft. In bold is the baseline aircraft SST45-1.6-60.

2020). Table 4 summarizes the resulting specifications obtained for the notional aircraft.

Figure 3 shows the performance characteristics for each notional aircraft. Furthermore, it compares the characteristics of our notional aircraft to data for past supersonic concepts, and (where applicable) operating subsonic aircraft. For this purpose, we present TSFC and $\frac{L}{D}$, as functions of high-speed Mach number and aircraft capacity, which allow us to specify our notional aircraft in line with existing data. Furthermore, for cruise $\frac{L}{D}$, we apply a modified version of Küchemann's equation (Küchemann, 1978) to facilitate the comparison (Figure 3b). Equivalent parameters for the "low-speed" cruise regime are obtained by scaling the high-speed cruise TSFC and $\frac{L}{D}$, using the ratios reported for the STCA (Berton et al., 2020). Finally, aircraft operating empty weight (OEW) is compared by making OEW a function of maximum fuel and payload weights and leveraging data from operative subsonic designs (see Figure 3c).

For non-cruise mission segments, we infer performance metrics based on the NASA N+2 reference profile (Morgenstern et al., 2015). In particular, we iterate fuel requirements (to meet range requirements) and OEW to estimate the landing weight

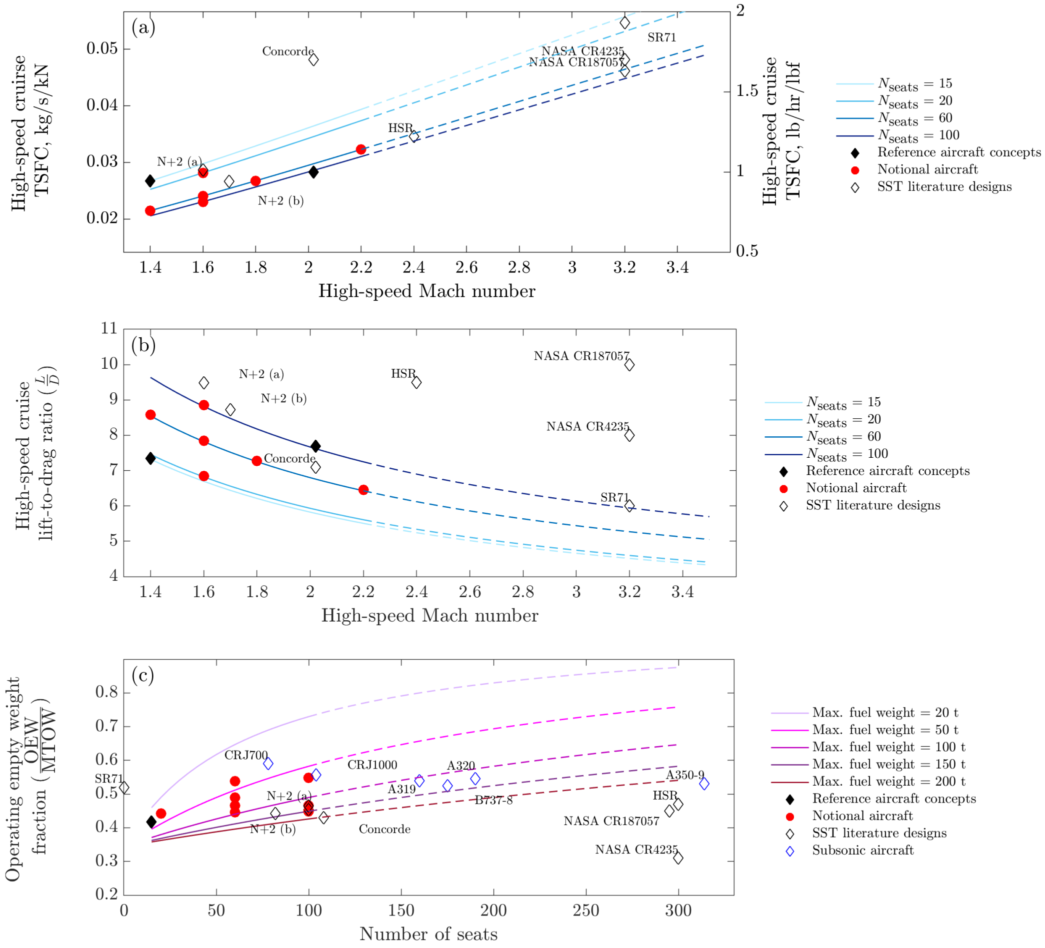

Figure 3: Performance characteristics for each notional aircraft, compared to existing designs. From top to bottom high-speed cruise TSFC, high-speed cruise $\frac{L}{D}$ and the ratio of operating empty weight (OEW) to maximum takeoff weight (MTOW).

for each notional aircraft. Once landing weight is obtained, we can invert the mission profile to calculate fuel consumption and flight time for every origin-destination (O/D) pair at every point of the flight. The latter can account for cruise in both the "high-speed" and "low-speed" regime if needed.

2.1.2 Routing model

For each potential O/D pair, we define the expected routing of subsonic and supersonic aircraft to calculate travel time and fuel burn. Each routing includes (1) the horizontal flight path, which is a two-dimensional trajectory, and the vertical flight profile; and (2) flight speed at each point of the trajectory. The latter indicates if the supersonic aircraft is operated in a "high-speed" or "low-speed" regime. The methods used to define optimal routings are described in the following subsections. We note that our model for calculating fuel burn and flight times accounts for annually averaged wind profiles as given by the GEOS-5 dataset. This allows us to convert between an aircraft's true air speed and aircraft ground speed as a function of spatial location and heading. As a result, flights with a tailwind fly at higher ground speeds which reduces flight times, while ground speed for flights with headwinds are reduced, which results in longer flight times.

2.1.2.1 Routing of subsonic flights

For subsonic aircraft, we use AEIC (Simone et al., 2013; Stettler et al., 2013) to identify routings and to model flight time and fuel burn. AEIC assumes subsonic flight paths between departure and arrival airports to be great circle routes. AEIC assumes empirical lateral inefficiency factors to modify non-LTO fuel burn and emissions to account for inefficiencies in routing. Performance of individual aircraft is computed using look-up tables of true air speed (TAS), fuel flow rate, and rate of climb and descent. The look-up tables are based on Eurocontrol's BADA data. Take-off weights are taken from Eyers et al. (2004) and include empty weight of the airframe, payload, and fuel (reserve, diversion and holding).

2.1.2.2 Unrestricted routings of supersonic flights

In a scenario without flight restrictions, we assume that supersonic aircraft operate on horizontal profiles which resemble great circle routes between origin and destination airport. The vertical profile and flight speed are taken from the mission profile as described in Section 2.1.1.3.

2.1.2.3 Restricted routings of supersonic flights

Regulatory restrictions such as 14 CFR § 91.817 for the United States may restrict or ban commercial supersonic flights over certain areas. We develop an algorithm which identifies optimal flight routes for supersonic aircraft under different flight restrictions. Using global GPW data (Center for International Earth Science Information Network (CIESIN), Columbia University, 2018) on land and population density distribution, we define two regulatory scenarios:

1. No supersonic flight over land areas
2. No supersonic flight over areas with population density higher than 50 inhabitants per km^2 . As shown in Figure 4, this scenario allows supersonic flight over significant areas with low population density. Other population density thresholds can be selected. For example, a threshold at 1,000 inhabitants per km^2 would ban supersonic flight over urban areas in the United States.

We assume buffer zones around the restricted areas. These are defined by estimated carpet width, which is the area where shockwaves from the supersonic boom can reach the ground. While this area would be dependent on aircraft altitude and speed, we assume a fixed carpet width of 95 km which is estimated for maximum altitude (19.8 km) and highest speed (Mach 2.2) of all notional aircraft under investigation (Liebhardt, 2019).

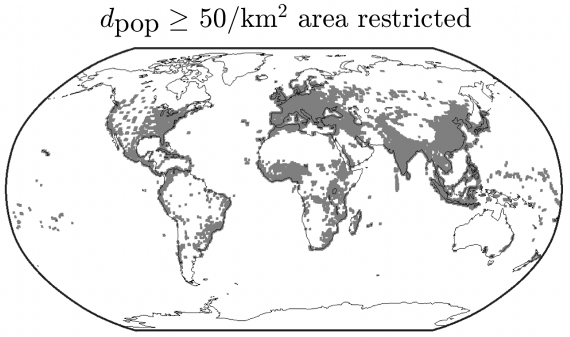

Figure 4: Global map of areas with overflight restrictions under a scenario with flights banned over areas with population density higher than 50 inhabitants per km^2 (shaded in grey, including carpet width).

Under the restricted flight scenarios, we identify an optimal flight path for an O/D pair by minimizing the net generalized travel cost mark-up of a supersonic service (SST) over a subsonic service (SUT) for a given passenger. This objective function aims to estimate flight paths which provide the best balance between cost and time savings from the passenger perspective. When comparing a supersonic flight to a subsonic flight for a given passenger, differences in their generalized travel costs, which are the monetary (e.g. ticket price) and non-monetary (e.g. time costs) costs of travel, result from differences in ticket price as well as from differences in costs associated with flight time. This yields the objective function in Equation 1 , where c are the costs of a flight, t is the time (in hours) spent traveling on a route, and VOT (value of time) is the monetary value a passenger assigns to an hour of travel time saved.

$$\Delta c - \text{VOT} \times \Delta t = (c_{\text{SST}} - c_{\text{SUT}}) - \text{VOT} \times (t_{\text{SUT}} - t_{\text{SST}}) \tag{1}$$

We break down the optimization problem into horizontal profile optimization and vertical profile calculation.

For **horizontal profile optimization**, we use existing algorithms which are designed to find minimum cost paths. Specifically, we apply the A* algorithm (Hart et al., 1968). This algorithm is an improved version of Dijkstra's algorithm (Dijkstra, 1959), a shortest distance graph-based pathfinding algorithm that evolves node by node to calculate distance (here: generalized cost) from node to node until the nodes giving the minimum total distance (generalized cost) are found. In our approach, nodes can be connected through "low-speed" or "high-speed" flight depending on underlying restrictions and generalized cost optimization. The optimization also considers fuel and time required for transitioning between "low-speed" and "high-speed" regimes. The A* algorithm guides the optimization through a heuristic function that estimates generalized cost from the current node to the destination. The heuristic function needs to be admissible (underestimating total cost) for the A* algorithm to identify the optimal route. Therefore, we use generalized cost of a hypothetical unrestricted flight to the destination as our heuristic function.

We implement this optimization on a 0.5° × 0.5° global grid, with an evaluation of 48 points around each of the objective nodes (corresponding to 3 grid levels), to reduce the number of segments obtained per route. This is due to the fact that the original A* algorithm, moving cell by cell, does not provide a suitable route for aircraft operations. The accuracy of the algorithm is verified by using linear distance as the objective function and by comparing routes for unrestricted scenarios with the great circle path. For a set of test routes, the routes identified by the algorithm differ less than 1.5% in length from the great circle path, with the remaining difference being attributable to grid discretization.

The implementation of the algorithm uses the operating cost model to calculate cost mark-ups (see Section 2.1.3.2). Because multiple scenarios need to be modeled, and due to the long computational times required by the algorithm, it is run separately for every restriction and notional aircraft. For each O/D pair, notional aircraft and overflight restriction, we subsequently obtain a set of potential flight paths, one for each assumed VOT. The optimal path is selected from that set by including conditions on "low-speed" performance and economic assumptions.

As mentioned, for each VOT, overflight restriction scenario, and notional aircraft, we obtain a different optimal path for each O/D pair. Figure 5 shows the algorithm results for the route from New York to Mexico City with two different value of time assumptions. The results show that a higher value of time results in longer detours since the the cost increases from higher fuel burn are outweighed by even small time saving from flying a longer distance at supersonic speed.

The vertical profile is determined after horizontal profile optimization is complete. The vertical profile is constructed as discussed in Section 2.1.1.3. This assumes that differences between the assumed and final vertical profile do not lead to significant changes in fuel burn and flight time.

2.1.3 Global market model

In established market forecasts such as Airbus (2019), Boeing (2019), and ICAO (2018), analysts predict future aviation market growth based on projections of drivers of air transportation demand (e.g. income growth) and air transportation supply (e.g. fuel price). In contrast to these market forecasts, the supersonic market model does not aim to predict the size of the market for scheduled aviation services, but sets out to identify routes for which passengers who are committed to traveling are willing to use supersonic services instead of subsonic services. As such, the supersonic market model can leverage existing market forecasts (Airbus, 2019; Boeing, 2019) and estimates the share of customers, who are willing to use supersonic air services instead of "conventional" subsonic air services ("substituted traffic'). Additionally, we follow evidence from other transport modes such as high-speed rail (Goodwin, 1996; Givoni and Dobruszkes, 2013) and consider demand generated by the availability of supersonic air services ("induced traffic"). Such additional growth results from the time savings associated with supersonic flights. For example, executives might decide to join meetings in-person instead of virtually given the lower time commitment associated with a supersonic flight. The resulting market structure and our market model are shown in Figure 6. Each sub-module is described in the following subsections. We note that the market model assumes the market for

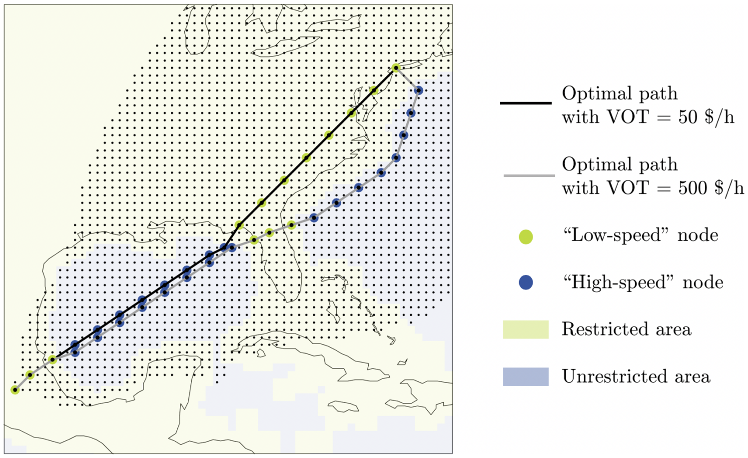

Figure 5: Routing algorithm solutions for the route New York–Mexico City. Two different values of time are assumed, \$50 per hour and \$500 per hour.

supersonic aircraft to reach an equilibrium state in the target year, i.e.: airlines will have access to a fleet of supersonic aircraft which can meet demand for supersonic services.

2.1.3.1 Baseline market projection

Our model requires a projection of scheduled passenger traffic for the year 2035, which we derive in three steps. Firstly, we calculate year-2015 capacity on scheduled passenger air services by route from year-2015 flight schedules as published by OAG. Secondly, we compute future capacity by route through applying the regionalized market forecast as published in Boeing’s year-2016 Market Outlook (Boeing, 2016). This approach allows us to capture expected changes in the global distribution of passenger flows at the regional level. It does not enable us to consider sub-regional changes in network structures, e.g. dispersion of future traffic to new airports and entirely new routes. As such, we limit the resolution of our results to the region-to-region and/or country-to-country level. Thirdly, we correct the target-year capacity estimates obtained in Step 2 for potential changes in load factors. For this purpose, we use data on current regional load factors (ICAO, 2013) and project future load factors through an empirically calibrated model of load factor adjustments calibrated with data for the US market.

We note that our baseline forecast does not account for the current drop in traffic associated with the COVID-19 pandemic. For April 2020, IATA (2020) reports a 94% year-on-year drop in global revenue passenger kilometers. While the shape of the recovery remains unclear (see Molenaar et al. (2020) for an overview), a substantial short-term recovery in 2021 and 2022 is expected (Pierce, 2020; Hader, 2020; InterVISTAS, 2020). In the medium-term, the aviation industry could return to its prior growth path (Pierce, 2020). In fact, existing forecasts often describe reductions in long-term market growth rates as a worst-case scenario (Hader, 2020). As such, the market volumes forecast in this analysis might not be reached in 2035.

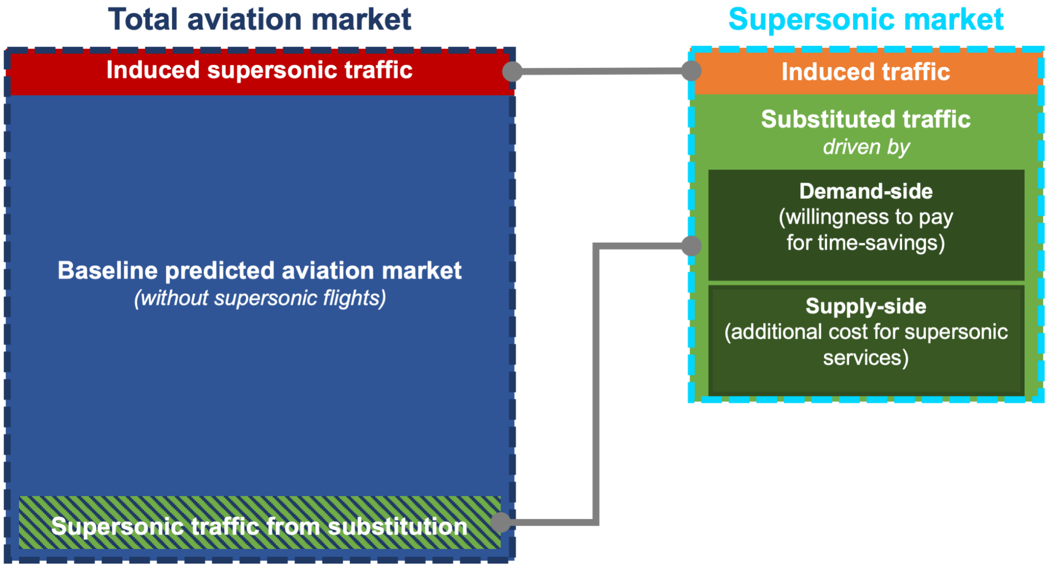

Figure 6: Building blocks of the market model. Left side: Structure of the aviation market; right side: supersonic market and associated models.

Instead, we consider the target year of the forecast to be delayed, with the length of the delay period depending on the shape of demand recovery from the pandemic.

2.1.3.2 Projection of substituted traffic

Substitution of subsonic services through supersonic services can be modeled in the discrete choice framework proposed by Train and McFadden (1978). In this framework, an individual chooses a transport mode (supersonic service (SST) or subsonic service (SUT)) for a given trip while maximizing individual utility U - a measure of satisfaction of needs as a function of consumption - with respect to leisure time L and aggregate (fixed price-level) consumption G. For a given transportation mode i, the simplified optimization problem is represented in Equation 2.

$$\max U(G, L) \;\; s.t. \;\; G + c_i = wW \; and \; L + W + t_i = \tau \tag{2}$$

where c_i $[t_i]$ is the cost [travel time] for transport mode i, W is working time, w is the wage rate and τ is total available time. Following Jara-Díaz (2007), Equation 2 can be solved for each available transport mode by maximizing utility U through the choice of working time W, which leads to the conditional indirect utility function V_i, which describes the maximum attainable utility as a function of the cost and time of travel, in Equation 3.

$$V_i(c_i, t_i) = U(wW^*(c_i, t_i) - c_i\,;\, \tau - t_i - W^*(c_i, t_i)) \tag{3}$$

Assuming a positive marginal utility of consumption and leisure time, a utility-maximizing individual prefers supersonic travel over subsonic travel if $V_{SST} > V_{SUT}$.

As a consequence, utility-maximizing travelers prefer supersonic transportation over subsonic air transport services if Equation 4 is true.

$$c_{SST} - c_{SUT} \leq w(t_{SUT} - t_{SST}) \tag{4}$$

Equation 4 implies that a trade-off between higher ticket prices and time savings drives the share of passengers, who switch from subsonic services to supersonic services. Through approximating the fare premium (supply-side modeling) and passengers' willingness to pay for time savings (demand-side model), we can estimate the share of passengers who substitute subsonic air services with supersonic services.

Demand-side model

The demand-side model focuses on deriving the willingness-to-pay of passengers for travel time savings associated with supersonic flights. While mean or median estimates for the underlying value of time of (air) travelers can be found in the literature (Shires and Jong, 2009; US Department of Transportation, 2014), no global route-specific data on the distribution of the value of time among air travelers is available. In this study, we therefore estimate the distribution of the value of time among passengers on each route.

The economic literature suggests that an individual's value of time on a specific trip depends on characteristics of the trip such as the purpose of travel, travel duration, waiting time and congestion, (Mackie et al., 2001) as well as characteristics of the traveler. For the latter, empirical evidence points towards income being a major predictor of the individual value of time for leisure travelers and individual productivity being correlated with the value of time for business travelers (Abrantes and Wardman, 2011; Börjesson et al., 2012). We therefore use data on income and productivity distributions to approximate the value of time distributions among passengers for each route following a five-step process:

In the first step, we derive county-level income and productivity distributions for the origin and destination market of each route. National income distribution data from the UNU-WIDER database (UNU-WIDER, 2014) and population and GDP data from global statistical databases (United Nations, Department of Economic and Social Affairs, Population Division, 2013; The World Bank, 2014) are used for this purpose. We compute productivity-per-employee distributions from the income distributions through applying labor participation data as provided by The World Bank (2014). Future income and productivity growth are considered by applying (price-adjusted) income growth projections as published in the ERS International Macroeconomic Data Set by the US Department of Agriculture (USDA Economic Research Service, 2016).

In a second step, we truncate and scale the income distributions to reflect changes in travel intensities with income, thereby moving from income and productivity distributions valid for the population to the income and productivity distributions of air travelers. Truncation is considered to (1) set the travel frequency of population with income below 120% of the poverty line plus 2 roundtrip fares to zero; and (2) set the travel frequency of business travelers, whose productivity surplus during a business trip cannot cover the cost of the business trip, to zero. Further scaling of travel frequencies with income and productivity is subject to scenario analysis as discussed in Section 2.1.3.4.

In a third step, the income and productivity distributions are converted into the value of time distributions, by fitting the median income and productivity estimates from the income and productivity distributions to the value of time estimates for leisure and business travelers as recommended in US Department of Transportation (2014). The value of time estimates are subject to scenario analysis as discussed in Section 2.1.3.4.

In a fourth step, we follow existing empirical evidence pointing towards an increasing value of time with travel time (Abrantes and Wardman, 2011; Axhausen et al., 2008). In line with Abrantes and Wardman (2011), we model this impact through the elasticity of the value of time with travel time. We use values for business and leisure travelers proposed by Axhausen et al. (2008). This results in higher adoption rates of faster supersonic services on longer routes. The elasticity of the value of time with travel time is subject to scenario analysis as discussed in Section 2.1.3.4.

In a last step, route specific value of time distributions are derived by weighting the willingness-to-pay distributions for each route end point by market size of each end point. For this purpose, we use data on the geographical distribution of population around each airport (Allroggen et al., 2015) as a proxy for market size and estimate business traveler shares through an empirically calibrated model using data from the US Survey of International Air Travelers (U.S. Department of Commerce, 2013) and the U.K. International Passenger Survey (U.K. Office of National Statistics, 2020).

Since we expect the fares for supersonic air services to be substantially higher than fares for subsonic air services, travelers on supersonic air services will likely have a high value of time. Potential passengers for supersonic air services will, in turn, expect regular frequencies to reduce the schedule adjustment time, which is the time between the desired departure and the scheduled departure. We therefore assume that passengers will expect feasible routes to be operated with at least one flight per weekday.

Supply-side model

The supply-side model computes the price premium per seat for supersonic air services as compared to subsonic air services. We calculate the route-specific full cost per seat, including operating costs, capital expenditures and capital costs, for both subsonic and supersonic services. The cost of capital considers the cost of debt and the cost of equity so that the return requirements of airlines' shareholders is considered in the model. A Weighted Cost of Capital for the Airline Industry at 6.8% (IATA, 2015) is assumed, which is higher than more recent averages for the airline industry at around 5.8% (Damodaran, 2020) reflecting the current low-interest market environment. To quantify the price premium for supersonic flights, we compute the per-seat cost for subsonic services and supersonic services separately.

The **costs of subsonic flights** are calculated by route and notional aircraft using data published by the US Bureau of Transportation Statistics (BTS) (Bureau of Transport Statistics, 2017). Our cost model considers 11 cost categories as shown in Table 5. For each cost category, the total costs as published by BTS are broken down per unit of an associated cost driver. Through modeling route and notional aircraft characteristics, such as the number of seats, total fuel burn or flight duration, we then compute the total operating costs per route and notional aircraft type. We note that the fuel price is subject to scenario analysis (Section 2.1.3.4). The average cost per seat for a return trip on each route is subsequently obtained by weighting the cost for each aircraft type with the service frequency of each type.

To obtain **cost estimates for supersonic air services**, we apply the cost model as outlined above. With the exception of capital costs and aircraft operating

Cost category	**Definition**	**Cost driver**
Fuel costs	Cost for fuel in target year	Fuel consumption (Section 2.1.5) and fuel price (Section 2.1.3.4)
Aircraft operations (without fuel)	Cost for the operation of aircraft (e.g. flight crew, direct maintenance, depreciation)	Flight duration, by aircraft type
Passenger services	Cost for the comfort, safety, and convenience of passengers during flight and flight interruptions (e.g. cabin crew, food)	Seats and flight duration
Aircraft services	Cost for servicing the aircraft (e.g. landing fees, line services)	Seats and flight duration
Traffic services	Cost for e.g. loading and ground handling	Seats
Reservation system	Cost for processing a reservation in a booking system and for maintaining the system	Seats
Advertising and publicity	Cost for advertising	Per flight
Administration	General management overhead	Mark-up on total costs
Depreciation and amortization of maintenance equipment		Mark-up on operating costs (without fuel)
Depreciation and amortization of ground equipment		Mark-up on traffic service costs
(After-tax) capital cost	Cost for equity and debt of airlines	Capital commitment per seat-hour and Weighted Average Cost of Capital

Table 5: Description of cost categories and associated cost drivers for the operating cost model.

costs without fuel, we assume the unit-cost for all cost drivers to remain constant. For the capital costs, we apply a multiplier to the capital commitment per seat-hour of subsonic aircraft, which is subject to scenario analysis (see Section 2.1.3.4). Through this multiplier, we consider the (initially) high capital commitment for supersonic aircraft resulting from R&D costs and production ramp-up, as well as from the complexity and novelty of the supersonic aircraft technology. For hourly aircraft operation cost without fuel, we assume costs per flight hour to be a function of aircraft size. For a 100-seat supersonic aircraft, we assume operating costs (without fuel) at 3,000 USD per hour, which is comparable to Boeing 777 or Airbus A340 aircraft. This high cost reflects the additional cost associated with the increased complexity of a supersonic aircraft. Accordingly, for a 20-seat supersonic aircraft, we assume operating costs (without fuel) costs to decrease to 1,700 USD per hour, which is comparable to Embraer 190 or Bombardier CRJ 900 jets. For intermediate aircraft sizes, direct operating costs are interpolated linearly with seat count.

We validate the resulting cost estimates by comparing the cost per seat mile for our baseline notional aircraft SST45-1.6-60 to Concorde data. Woolley (1972) find the total operating cost per seat-mile for a 106-seat Concorde was 75% higher than the cost per seat-mile of a 344-seat Boeing 747. According to our cost model, the total operating cost per seat for the SST45-1.6-60 on a New York-to-London flight exceeds the per-seat cost for a state-of-the art aircraft such as a year-2035 aircraft type, represented by a Boeing 777-300ER with fuel burn improvement of 1% p.a., by 144%. However, with fuel prices adjusted to the levels of 1972 (in year-2011 dollars), the supersonic service is 83% more expensive per seat than the Boeing 777-300ER. As such, the relative cost difference between supersonic aircraft and a state-of-the-art aircraft falls in line with existing data. We note though that this comparison implies that the cost for the supersonic aircraft has decreased as compared to the Concorde since the assumed hypothetical updated Boeing 777-300ER is more efficient than the Boeing 747-100 which Woolley (1972) used as a reference aircraft for the Concorde.

In addition to the cost estimation, the supply-side model considers **restrictions for opening supersonic routes**. These restrictions result from technical restrictions of the aircraft and economic considerations.

1. Only airports with sufficiently long runways ($\geq 10,000$ ft.) are considered as endpoints for supersonic routes.

2. Airlines prefer to operate services from base airports, where they base crews and maintenance resources (Klein et al., 2015). For an airport to become a base, a critical number of operations is required. Thus, we assume that each feasible route needs to have at least one endpoint where a fleet of 4 supersonic aircraft can be operated for 12 hours per day.

The supply-side model's final module covers the modeling of the fleet of aircraft for the target year. This entails: (1) modeling the aircraft types which are replaced through supersonic services. Assuming that airlines are profit-maximizing companies, we expect airlines to retire the aircraft with the highest operating costs first. As such, we identify the replaced subsonic aircraft through ranking the per-seat costs of all aircraft types operated on each route; (2) providing first-order estimates of the size of the supersonic fleet. The estimation does not consider specific schedule requirements but estimates fleet size by assuming system-level aircraft utilization to be consistent with values for large narrowbody and widebody aircraft of US carriers (MIT, 2020).

2.1.3.3 Projection of induced demand

The economic literature provides evidence that improvements of transport infrastructure or transport services can result in "induced demand", which is not caused by substitution patterns from other transport modes or services. Such effects have been identified for improvements in road infrastructure (Goodwin, 1996; Hymel et al., 2010), as well as for the introduction of high-speed rail services (Givoni and Dobruszkes, 2013).

In light of the significant time savings associated with supersonic air services, we expect supersonic air services to create induced demand. Given potentially high prices for supersonic flights, we expect induced traffic for supersonic services to result from increasing travel intensities of passengers, who substitute subsonic services with supersonic services. As such, we model induced traffic as a "mark-up" on the market volumes, which result from substitution of subsonic services through supersonic services. Since we are not aware of published analyses on induced demand for air transportation, the market share of induced demand is inferred from market share data on high-speed rail services collected after a new service is introduced. In a meta-analysis, Givoni and Dobruszkes (2013) identified induced traffic to account for 10–20% of high-speed rail traffic, which is similar to the results for road transportation obtained by Goodwin (1996). We use these prior findings to calibrate our model, but explicitly consider induced demand growth in our sensitivity analysis (Section 2.1.3.4).

2.1.3.4 Economic scenario analysis and case selection

The model outlined above relies on assumptions about the values of key parameters. However, some of these parameters are volatile or uncertain, but may impact on results. As such, we run scenario analyses on the economic assumptions for nine variables (Table 6) using the following considerations:

1. Radich (2015) forecasts the price for jet fuel to reach 3.31 USD (year-2013) per gallon in 2035 (equivalent to 3.13 USD per gallon in year-2011 USD). This is equivalent to approximately 1.00 USD per kg. We set boundary values at 20% above and below the projected value to account for the uncertainty related to the long-term projection. EIA's year-2020 Annual Energy Outlook (Energy Information Administration, 2020) predicts a broader range of values, with a baseline prediction of 0.85 USD per kg jet fuel and a low [high] estimate at 0.45 USD [1.38 USD] per kg jet fuel under a low [high] oil price scenario. Since the reference estimates overlap, we run the analysis on the initial values, but note that our projections cannot reflect scenarios with very high or very low oil prices.

Variable	**Low, mid and high scenario values**
Fuel price	0.8, 1, 1.2 USD per kg
Capital commitment and depreciation for supersonic aircraft	2, 3, 4.5 times that of subsonic aircraft
Value of time of the median leisure passenger (coupled to value of time of the median business passenger)	28, 32.6, 42 USD per hour
Value of time of the median business passenger (coupled to value of time of the median leisure passenger)	48, 60, 72 USD per hour
Income elasticity of demand (leisure passengers)	0.7, 1.1, 1.2
Income elasticity of demand (business passengers)	0.7, 1.1, 1.2
Travel time elasticity of value of time (leisure passengers) (coupled to time elasticity of value of time for business passenger)	0.2, 0.25, 0.3
Travel time elasticity of value of time (business passengers) (coupled to time elasticity of value of time for leisure passenger)	0.15, 0.2, 0.25
Share of induced demand in supersonic market	0.1, 0.153, 0.2

Table 6: Variables for economic scenario analysis.

2. For supersonic aircraft, we expect the higher complexity of airframe and engines to increase the capital commitment (per seat-hour) and depreciation by a factor of 2 compared to subsonic aircraft. Although data for the Concorde suggests a value of 7 (Woolley, 1972), we use lower values, thereby assuming advances in manufacturing processes and computational R&D approaches. However, to model potentially higher capital costs and depreciation, scenarios with capital commitment factors of 3 and 4.5 are included.

3. We follow the US Department of Transportation's recommendation and apply the low, mid, and high values for the US value of time for air and high-speed rail leisure and business passengers (US Department of Transportation, 2014). For the scenario analysis, we use a coupled approach for choosing the low, mid and high case for leisure and business travelers so that the underlying economic assumptions regarding income and productivity remain consistent. The values are transformed into target year values by applying per-capita income growth from USDA Economic Research Service (2016).

4. In transforming income and productivity distributions of the population to income and productivity distribution of air travelers, we follow empirical evidence suggesting that individual travel frequency increases with income (Alegre and Pou, 2006). This is consistent with evidence on a positive income elasticity of air travel demand (Njegovan, 2006; InterVISTAS, 2007; Fouquet, 2012; Gallet and Doucouliagos, 2014). In our model, we transform the density functions to assume a constant increase of travel frequency as implied by the

marginal income elasticity of air travel demand. In order to consider saturation effects for high-income groups, the values selected are taken from the lower end of the range of values reported by Gillen et al. (2007) and Fouquet (2012).

5. The elasticity of the value of time with travel time for business and leisure travelers is taken from Axhausen et al. (2008), with ranges derived from bounding values of reported variation. Our values are similar in magnitude to the estimates of the distance elasticity of the value of time presented in the meta-analysis by Abrantes and Wardman (2011). We use coupled scenarios for the business and leisure traveler cases to model consistent behavioral trends.
6. As discussed in Section 2.1.3.3, mark-ups for modeling induced demand are taken from Givoni and Dobruszkes (2013).

The resulting analysis generates an ensemble of 2,187 economic scenarios. For each economic scenario, we compute the number of global round-trip operations. Considering all cases, we estimate the density function of the number of supersonic (round-trip) operations through a kernel density approach and through fitting a lognormal distribution. An example of the resulting distribution is shown in Figure 7.

To identify the low, mid and high case for the model run, we compute the 10th, 50th and 90th percentile of the estimated lognormal distribution (Kernel estimates if zero-cases are identified). Based on the estimated percentiles of the number of global round-trip operations, we identify the low, mid and high case by choosing the case with the smallest absolute deviation between the number of supersonic operations as estimated through the particular percentile and the number of supersonic operations as implied by the model.

2.1.4 Scheduling module

Since we expect the atmospheric impacts of supersonic aircraft to be sensitive to seasonality patterns and time-of-day patterns of their operations, we estimate flight schedules for the target year based on the market results as obtained according to the methods described in Section 2.1.3. Most existing schedule and fleet modeling tools such as Rexing et al. (2000) aim to support airline planning and are therefore designed to support precise decision-making. In contrast, our scheduling tools aims to outline scheduling trends only. As such, we rely on heuristics derived from observed distributions of flights for subsonic traffic and a model of time-of-day preferences for supersonic traffic.

2.1.4.1 Subsonic schedule projection

For subsonic flights, we use empirical information from current-day flight schedules to derive future schedules. For this purpose, we characterize each flight through the following components: airport pair, week of the year, weekday, and time of day. For each airport pair, we then capture seasonality and day-of-the-week patterns through obtaining week of the year and weekday density functions from the year-2016 base

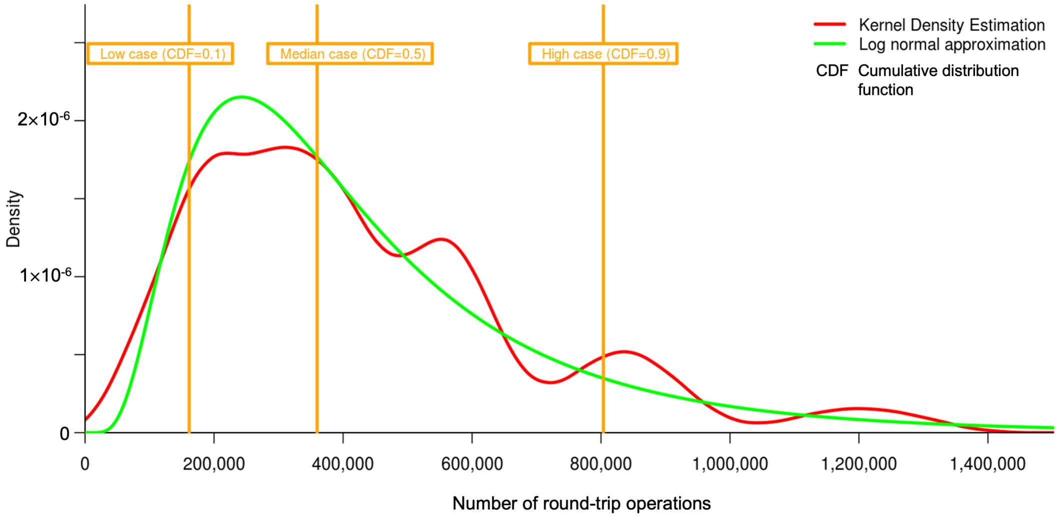

Figure 7: Distribution plot for the number of global supersonic roundtrip operations. Unrestricted routing scenario for SST45-1.6-60.

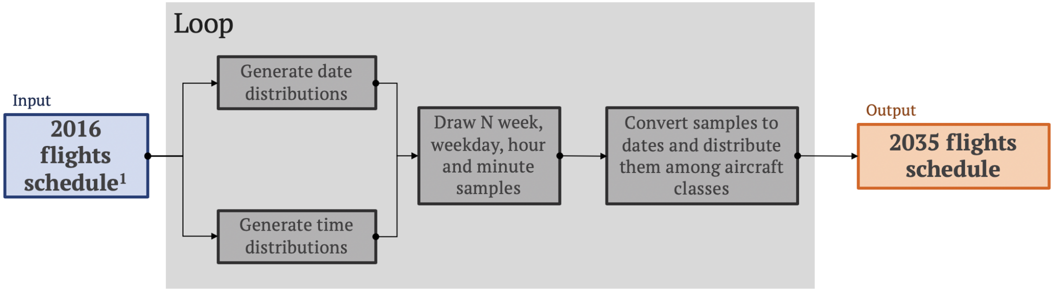

Figure 8: Process to estimate future subsonic schedules for every airport pair with N flights ([1]: constrained to complete weeks (4th Jan 2016–31st Dec 2016))

schedule provided by OAG. If an airport pair is not available in the base schedule, we approximate the density functions by aggregating all flights with identical UTC time zone offset and flight durations within 45 min. To capture time-of-day patterns, we use the same process to generate hourly and per minute density functions, while conditioning on the day of the week. With the simplifying assumption that all flights are independent (with the exception of time of day being conditionally dependent on weekday), we can then sample target-year flight schedules using the market projections outlined above. A simplified representation of our workflow is shown in Figure 8.

2.1.4.2 Supersonic schedule projection

Supersonic schedules are derived by using hypotheses about time preferences of passengers on supersonic air services.

First, given the expected higher costs of supersonic flights as compared to subsonic

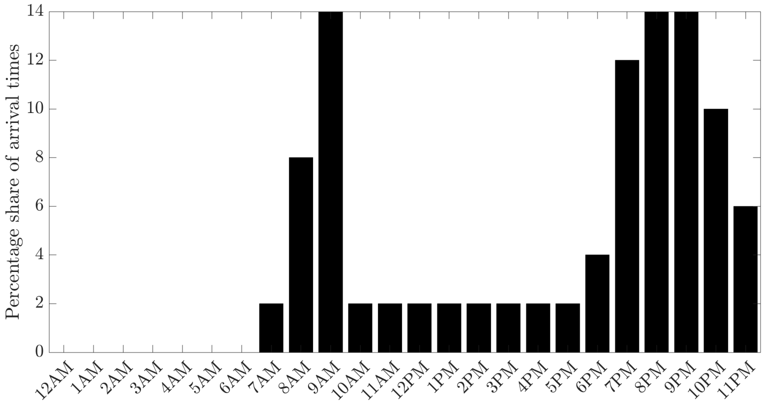

Figure 9: Assumed distribution of arrival times by hour (in local time of the arrival airport). Flights are assumed to land at the o'clock time such as 10AM refers to the portion of flights landing at 10AM.

flights, we identify preferred arrival times, which maximize working time during the day. In turn, we assume higher preferences for arrival times in the morning (to reach a meeting), early evening (to get home) or late evening (for arrival the night before an early-morning meeting). From these preferences, we define a generalized distribution of arrival times (in local time at the arrival airport) as shown in Figure 9.

Second, we assume no seasonality in the demand for supersonic flights. Seasonality for subsonic flights is largely driven by leisure travel demand peaks during vacation seasons, which is not expected to be a major driver for supersonic traffic. As such, we assume a constant number of flights per week for supersonic traffic. Additionally, we disregard the day-of-week distribution since this variation is assumed unlikely to have a significant effect on the environmental impact assessment.

With these assumptions, we compute the number of flights in each week for each route. For each day, arrival times are drawn from the distribution in Figure 9. Considering flight duration as modeled in Section 2.1.1 and time zone offsets between departure and arrival airports, we subsequently calculate the associated take-off time (in local time at the departure airport). If an assumed global night curfew (12am to 6am) prohibits the flight, we move it to the nearest available hour. This yields the number of supersonic flight departures per route and hour of the year (in local times and UTC).

2.1.5 Global emissions estimation

Based on the market outcomes and schedules for different notional aircraft, flight restrictions, and economic scenarios, we model global emissions inventories for both subsonic and supersonic aviation in the target year. These inventories will serve as an input for estimating the atmospheric impacts of supersonic air services. The inventories therefore capture the following emission species: CO_2, H_2O, NO_x, carbon monoxide (CO), hydrocarbons (HC), sulfur oxides (SO_x), and black carbon (BC). To estimate emissions indices, we first develop an engine cycle model to determine combustor operating conditions, and then use those conditions to compute emissions indices using the p_3T_3 method. Global inventories are then obtained using AEIC (Simone et al., 2013; Stettler et al., 2013).

2.1.5.1 Engine cycle model

We use the Numerical Propulsion System Simulation (NPSS) (Lytle, 2000) software to develop an engine cycle model, which estimates the engine performance and emissions of NO_x, CO and HC for given temperatures and pressures at the inlet of the combustor. This engine cycle model is used solely to assess variations in emissions indices (NO_x, HC and CO) during each mission for each notional aircraft (see Figure 10), whereas fuel burn is estimated as presented in Section 2.1.1.4. A two-spool, mixed-flow turbofan engine is modeled with an external compression supersonic inlet for each of the notional aircraft. A reference subsonic engine is modeled based on the CFM56-5B/3 using certification data published in ICAO's Emissions Databank (EDB) (ICAO, 2019). The technology assumptions for the turbo-machinery, represented by their polytropic efficiencies, are taken from the subsonic reference engine. The temperature limits applied to the last stage of the compressor and the turbine inlet are assumed to be equal to those of the reference subsonic engine.

The thrust requirement F_n for each notional aircraft is determined at each point of a design mission is calculated as

$$F_{\mathrm{n}} = W \times \left(\frac{1}{\frac{L}{D}} + \frac{\frac{dh}{dt}}{V} \right) \tag{5}$$

where W is the instantaneous weight, $\frac{dh}{dt}$ is the rate of climb and V is the flight speed at a given point in the mission profile.

The aerodynamic coupling between the airframe and engine imposes a constraint on the engine frontal area in order to avoid excessive nacelle and wave drag. Therefore, for each of the supersonic aircraft, a fan diameter constraint is applied which reflects the engine size constraint for each notional aircraft. We choose the maximum fan

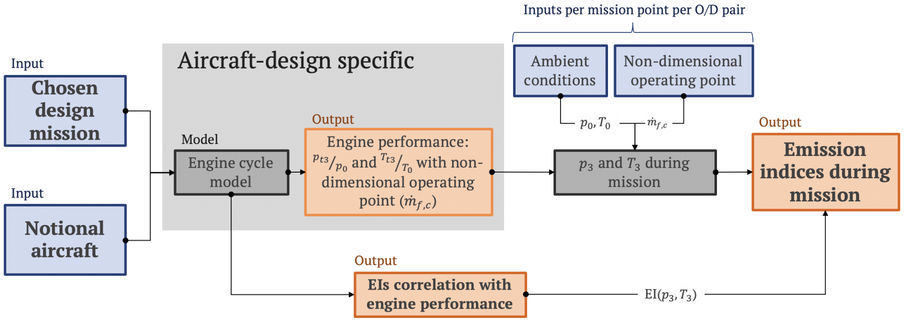

Figure 10: Scheme of NO_x, HC and CO emissions indices calculation process. Engine cycle model is derived from NPSS, EIs correlation is based on "p_3T_3" method.

diameter to vary between 50 and 70 inches ($\sim 1.1\,\mathrm{m}$ to $1.5\,\mathrm{m}$) (see Table 7) depending on aircraft size. The choice of fan diameter determines the feasible fan pressure ratio for a given thrust requirement along with a chosen compressor pressure ratio. For a fixed fan size, increasing thrust requirements imply an increase in specific thrust ($F_n/\dot{m}_a$ where $\dot{m}_a$ is the mass flow rate through the inlet) which leads to an increase in the fan pressure ratio. As a consequence, the compressor exit temperature and pressure increase with higher thrust requirements for a fixed fan diameter.

The engine performance for each notional aircraft, route and mission profile is based on the calculations of the engine model for a single design mission (typically the longest route). Since multiple engines varying in fan and compressor pressure ratios are capable of flying that design mission, we select the engine providing the most similar results in total fuel burn for the mission as compared to our simulated data (Section 2.1.1.4). The total difference between defined engine model per aircraft, and assumed mission profile fuel burn, is of less than 15% for every notional aircraft.

For emissions and performance estimation, the engine is assumed to operate at the same non-dimensional operating point during each mission segment. Therefore, the temperature and pressure ratios $T_{\mathrm{t}3}/T_0$ and $p_{\mathrm{t}3}/p_0$ are functions of the corrected fuel flow. The corrected fuel flow ($\dot{m}_{f,c}$) is a non-dimensional parameter defined as the energy provided by the fuel per unit time (fuel flow, in kg/s, multiplied by fuel heat of combustion) divided by the power required by the aircraft (thrust required multiplied by speed). The conditions at the inlet of the combustor (total pressure $p_{\mathrm{t}3}$ and total temperature $T_{\mathrm{t}3}$) are estimated using the ambient conditions (pressure and temperature) and the temperature and pressure ratios defined above.

2.1.5.2 Emissions indices (EIs) calculation

CO_2 and H_2O emissions indices are 3.15 kg per kg of fuel and 1.26 kg per kg of fuel, respectively, assuming conventional Jet-A. Sulfate and black carbon (BC) emissions are here calculated as being proportional to fuel burn, thereby assuming a fixed emissions index. As a baseline, we use an emission index for BC at 30 mg/kg (Stettler et al., 2013; Agarwal et al., 2019), a fuel sulfur content of 600 ppm, and a sulfur to H_2SO_4 conversion factor of 2% (i.e. the percentage of fuel sulfur emitted as H_2SO_4) (Hileman et al., 2010). We note that with a different type of fuel, such as a paraffinic biofuel, these emissions indices would be significantly different. The sensitivity of the results to these assumptions is explored in Sections 5 and 6.

To estimate emissions indices for NO_x, CO, and HC, we apply the p_3T_3 method (DuBois and Paynter, 2006). In this method, emissions indices for each species are

	SST35-1.4-60	**SST35-1.6-20**	**SST35-1.6-100**	**SST35-1.8-60**	**SST35-2.2-60**	**SST45-1.6-60**	**SST55-1.6-100**	**SST60-1.6-100**
High-speed Mach	1.4	1.6	1.6	1.8	2.2	**1.6**	1.6	1.6
MTOW, kg	78	51	123	104	148	**123**	206	241
Max. h_{cruise}, km	16.1	17.4	17.4	18.3	19.8	**17.4**	17.4	17.4
Max. fan diam., in	50	50	65	60	65	**65**	70	70

Table 7: Characteristics of notional aircraft under consideration. In bold baseline aircraft SST45-1.6-60.

assumed to be functions of the compressor exit temperature and pressure only. We use the NPSS cycle model of the reference engine and emissions measurements from the EDB (ICAO, 2019) to determine the coefficients of the equation for each species. We then use the fits for determining the emissions indices for each notional aircraft. This approach provides a consistent representation of combustor technology across the notional aircraft, and ensures that emissions indices scale appropriately with changing Mach number and cruise altitude.

2.1.5.3 Modeling global distribution of fuel burn and emissions

AEIC—in combination with the notional aircraft specifications (Section 2.1.1), routing module (Section 2.1.2), and schedule module (Section 2.1.4)—is used for estimating a global fuel burn inventory. Emissions are then estimated for each point of flight paths as outlined above. The original version of AEIC (Simone et al., 2013; Stettler et al., 2013) has been adapted to simulate fuel burn and emissions accordingly. AEIC's existing methods for estimating fuel burn and emissions for subsonic aircraft are used. All emissions are gridded at a monthly temporal resolution and a spatial resolution of $1^\circ \times 1^\circ$.

2.2 Summary of scenarios

In Section 2.1, we describe the modeling approach for the scenarios presented as part of this analysis. Figure 11 provides an overview of the different scenario dimensions considered in this study. By combining all dimensions, we obtain 120 emission and market outcome scenarios. These scenarios include 24 market outcome and emissions scenarios with unrestricted flight paths (8 notional aircraft and 3 economic scenarios), and 96 market outcome and emissions scenarios with restricted flight paths (8 notional aircraft types, 2 low-speed scenarios, 2 restricted market scenarios, 3 economic scenarios).

2.3 Results

2.3.1 Forecast of the global subsonic market for 2035

We use year-2015 traffic data published by OAG as the baseline market data for our model. The data covers 33.3 million flight departures with each flight carrying on average 138 seats over 1,315 km. This yields a total of 8.1 trillion seat-km, where a seat-km, here and in the following, is defined as a passenger seat flown one kilometer assuming that the aircraft operates on a direct great circle route between origin and destination of the flight. A break-down of the data by departure world region is shown in Figure 12. To validate the input data, we compare them to the year-2015 statistical data as published by ICAO (ICAO, 2015) finding deviations in traffic not exceeding 2.5%.

The target year baseline forecast, which does not consider the introduction of supersonic services, is derived by combining the regionalized Boeing forecast with the year-2015 traffic data. For the target year, we obtain 18.8 trillion seat-km in the subsonic market, an increase of 132% over the year-2015 data. As compared

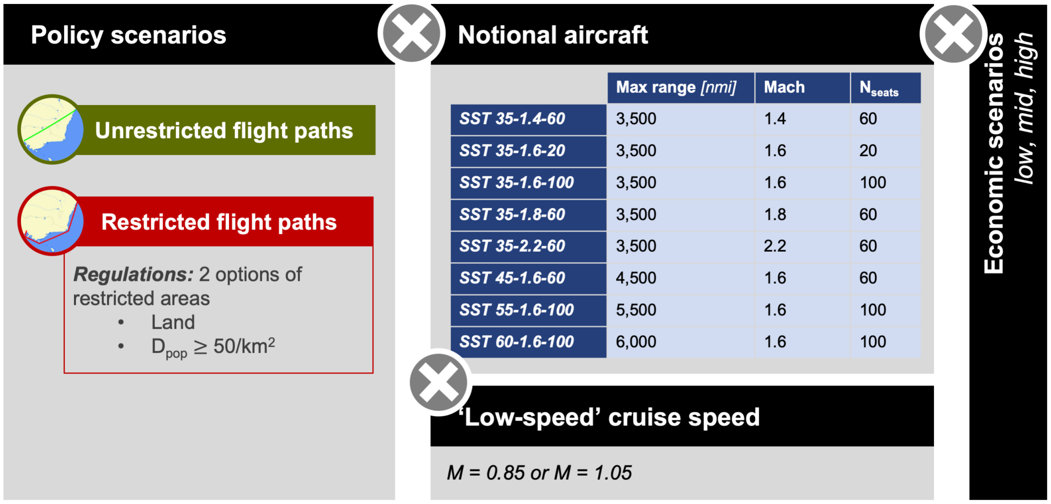

	Max range [nmi]	Mach	N_{seats}
SST 35-1.4-60	3,500	1.4	60
SST 35-1.6-20	3,500	1.6	20
SST 35-1.6-100	3,500	1.6	100
SST 35-1.8-60	3,500	1.8	60
SST 35-2.2-60	3,500	2.2	60
SST 45-1.6-60	4,500	1.6	60
SST 55-1.6-100	5,500	1.6	100
SST 60-1.6-100	6,000	1.6	100

Figure 11: Overview of scenario dimensions considered in this study

to Boeing's RPK growth forecast at 156%, our seat-km growth is lower since our model considers a slow-down in capacity growth due to load factor adjustments. Furthermore, our model expects the number of global aircraft departures to increase by 123% only, indicating rising average aircraft capacity and increasing average flight distance.

2.3.2 Forecast of global supersonic market for 2035 – Unrestricted routing

2.3.2.1 Market projection

Baseline aircraft (SST45-1.6-60)

The low case, mid case and high case market projections for the baseline notional aircraft (SST45-1.6-60; range of 4,500 nmi, Mach 1.6 supersonic cruise speed, 60 seats) are summarized in Table 8. For the mid case, we find a global market for a fleet of 440 to 470 aircraft operating 359,800 round-trip operations per year, thereby producing 0.86% of the system-wide seat-kilometers in the target-year market. The number of related take-offs and landings is similar to the year-2019 number of operations at Los Angeles Airport. This low traffic share results from high costs: the model indicates that passengers on supersonic flights need to value time savings at (average over all supersonic routes) 212 USD per hour or more which is significantly higher than the value of time of the median leisure traveler (33 USD per hour) and the median business traveler (60 USD per hour) (FAA, 2015). As a result, traffic is largely concentrated in high-income countries, specifically the North American and North Atlantic market and parts of Asia (Figure 13), whereas only very few markets can be identified in Central and South America & Caribbean and in Africa. A major driver of costs is fuel burn. For the SST45-1.6-60, fuel consumption per seat-km is approximately 6 times higher than the fuel burn of reference subsonic fleet. As such,

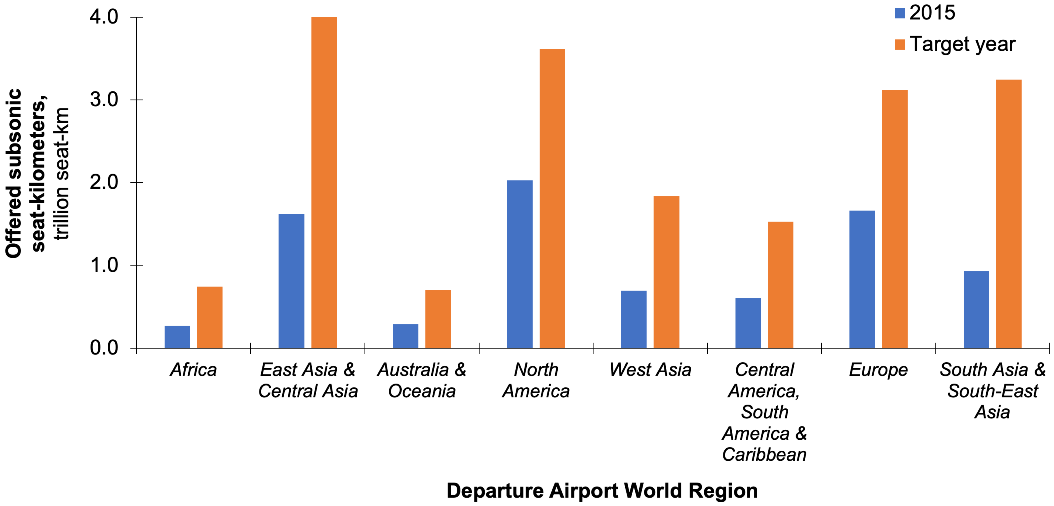

Figure 12: Overview of seat-kilometers offered in the subsonic baseline market for the year 2015 and the target year.

we observe a disproportionate impact on total fuel burn where supersonic services will account for 0.86% of global seat-km, but cause a 4.0% net increase in total fuel burn.

We assess the sensitivity of our results with regard to the variables selected for economic scenario analysis (Section 2.1.3.4). As shown in Table 8 and Figure 14, we find the number of global round-trip operations to be sensitive to the economic assumptions. More specifically, the global market approximately halves [doubles] with more pessimistic [optimistic] assumptions. This sensitivity is largely driven by fuel price assumptions and the assumed capital commitment factor on the supply-side, and the value of time of the median passenger on the demand side. For example, we find higher fuel costs and increasing capital commitments for supersonic aircraft to result in less supersonic flights, since increasing costs reduce the demand potential for supersonic services (less travelers with required willingness-to-pay). This impact is disproportionately large in North America, since short routes dominate the North American market and higher costs increase the likelihood of shorter routes becoming infeasible. In contrast, an increasing value of time of the median passenger increases the potential market for supersonic flights because a higher share of the population will be willing to pay for the time savings associated with supersonic flights at given costs.

We note that SST45-1.6-60 is not assumed to have sufficient range for trans-Pacific nonstop flights. For example, it cannot operate a direct flight from Los Angeles to Beijing. However, it would be possible for the aircraft to serve this route through a flight with a refueling stop, for example in Anchorage, which would increase flight distance by less than 1% (best case for detours). The additional time required for landing, taxiing, re-fueling, taxiing and take-off would limit the total round-trip time saving to 8.5 hours (36% of subsonic travel time; best-case assumptions for the technical stop), while resulting in round trip cost per seat to be 3 times higher than

	Low Case	**Mid Case**	**High Case**
Annual number of supersonic round-trip operations, (*in 1,000 roundtrip operations*)	161.4	359.8	803.7
Annual offered seat-km on supersonic aircraft, *bn seat-km (in percentage of total market)*	81.09 (0.43%)	162.6 (0.86%)	361.8 (1.92%)
Average market share of supersonic services on routes with replacement in percentage of seats	2.9%	4.2%	7.1%
Average value of time threshold, $ per hour	281	212	185
Average time saving per round-trip, hours	4.7	4.3	4.3
Average time saving in percentage of subsonic flight	43.8%	43.2%	43.2%
Estimated fleet size, *# of aircraft*	210 to 230	440 to 470	990 to 1060
Total fuel burn (only SST), Tg	8.14	16.8	37.2
Net fuel burn impact in percentage of BAU	1.9%	4.0%	8.9%
Percentage substitution of subsonic seat-km	0.37%	0.69%	1.63%

Table 8: Global market potential for SST45-1.6-60 without overflight restrictions under low, mid and high economic scenario (BAU: Business as usual).

for a subsonic flight. As such, we estimate the required willingness to pay for an hour of time saving to be 320 USD or higher, which would let us expect the route to be marginal.

Sensitivity of unrestricted market to notional aircraft specification

We assess the sensitivity of the results to notional aircraft specification by comparing the results for the baseline aircraft (SST45-1.6-60) to those for other notional aircraft (Section 2.1.1.2). For simplicity, we focus on our economic mid-case results. Overall, we find the market potential to be sensitive to the specification of our notional aircraft. Global market size as measured by seat-kilometers produced by commercial supersonic aircraft varies by a factor of 30 (Table 9). In contrast, the largest number of round-trip operations is a factor of 7 higher than the smallest number. The difference is attributable to variation in aircraft size and average stage lengths. The geographic distribution of the markets resembles the general trends described for the baseline aircraft (SST45-1.6-60) (Figure 15).

We find the largest market potentials for notional aircraft with maximum seat capacity (100 seats) and lowest range (3,500 nmi). For SST35-1.6-100, we expect a market potential of 754,000 round trip operations served by a fleet of 820 to 870 aircraft. The fleet would produce 2.5% of global seat-kilometers and reach an 11% average market share on routes with replacement. The required mark-up per hour of time saved would be 123 USD per hour which is 42% lower than for the baseline notional aircraft SST45-1.6-60. The latter points towards significant economies of scale which are assumed in our notional aircraft designs. These economies result from both our cost model (decreasing fixed operating cost per seat hour) and, most importantly, our performance assumptions, especially on fuel burn per seat-kilometer. For the 20-seat SST35-1.6-20, we expect fuel burn per seat-kilometer to be 3.3 times

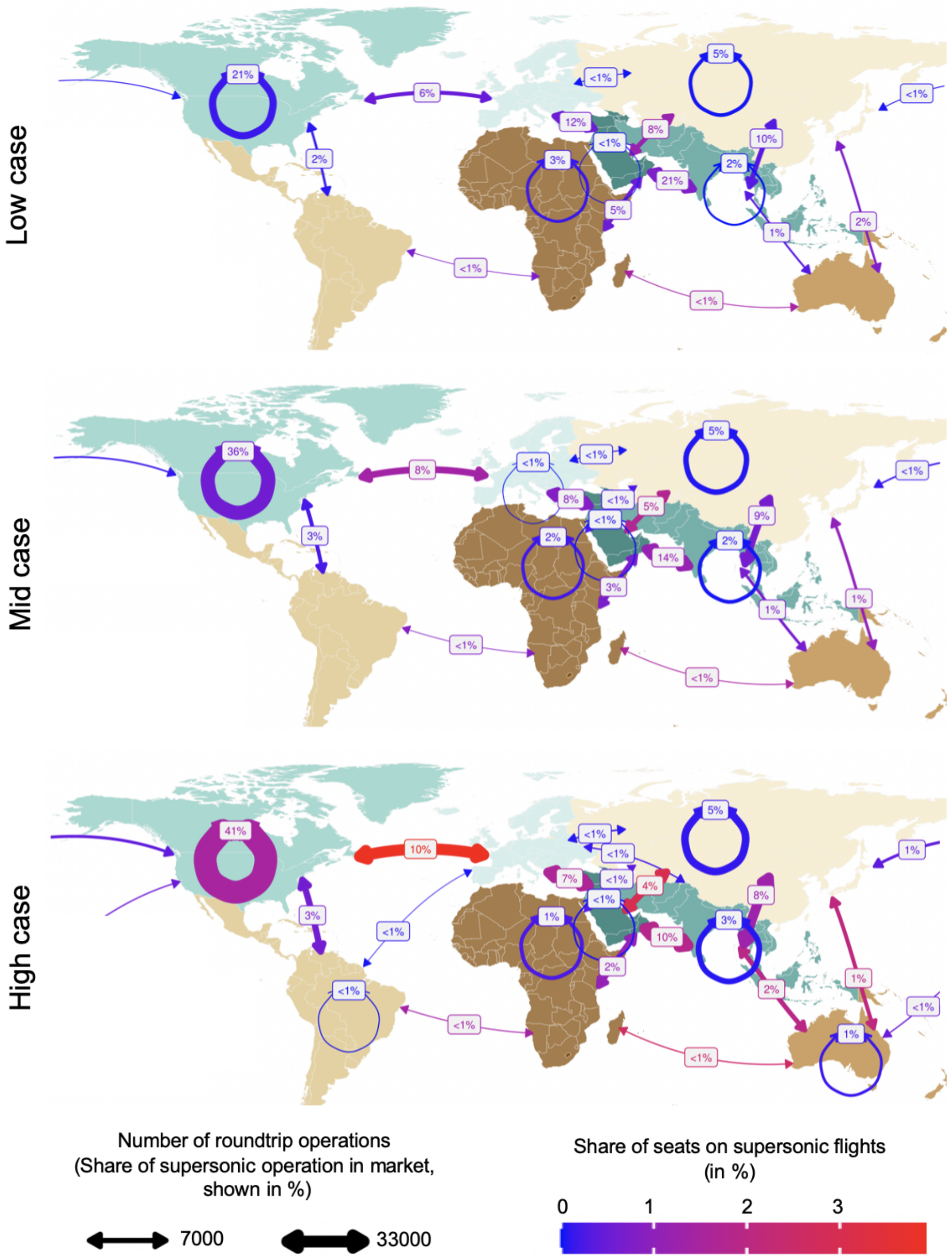

Figure 13: Maps of global commercial supersonic market for baseline notional aircraft in an unrestricted scenario. Baseline aircraft SST45-1.6-60: max. range = 4,500 nmi, $M_{\text{high-speed}} = 1.6$, $N_{\text{seats}} = 60$. Sensitivity to economic assumptions shown from top to bottom: Low, mid and high economic cases.

higher and the required willingness to pay per hour of time saved to be 5.5 times higher than for SST35-1.6.100. SST35-1.6-20 would subsequently achieve the lowest

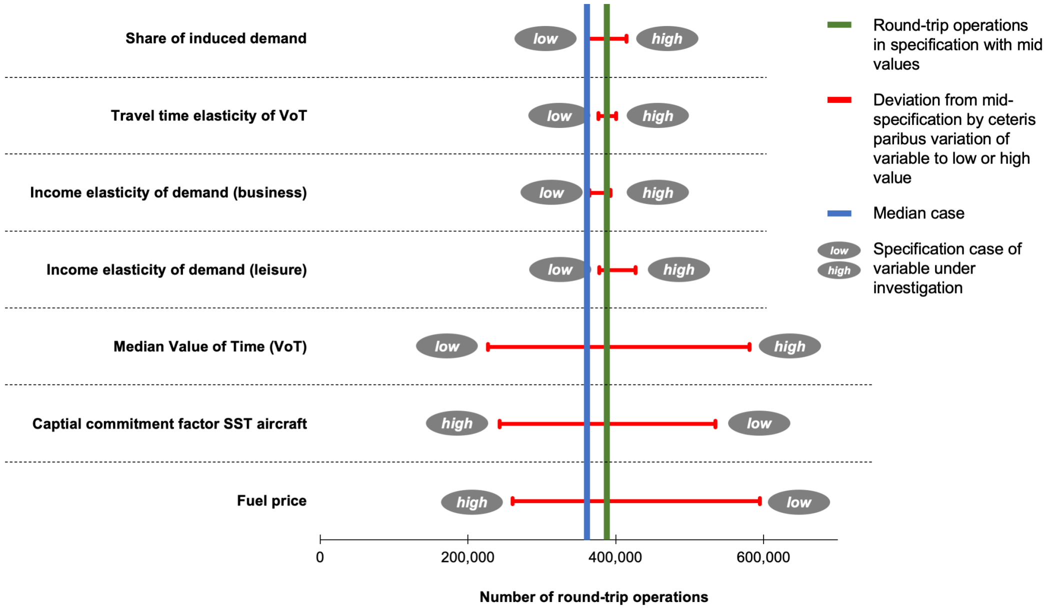

Figure 14: Sensitivity of global market size to variations in economic scenario variables (as described in Table 6 from the mid specification to the low and high specification)

identified market potentials with 103,200 round-trip operations, a fleet of around 130 aircraft, and production of 0.08% of global seat-kilometers. Similar trends are observed in Figure 16, which shows that larger aircraft with economies of scale enable supersonic services on a more diverse set of routes, including to and from medium- and lower-income world regions.

In addition, we find market potentials to be sensitive to the range specification of our notional aircraft. By increasing the range of SST35-1.6-100 from 3,500 nmi to 5,500 nmi [6,000 nmi], the potential number of round-trip operations drops by 34% [46%]. This is despite the added capabilities of the aircraft to serve longer routes. In fact, we find decreases in produced seat-kilometers with range increases (-17% for 5,500 nmi range and -24% for 6,000 nmi range), which are smaller than the reductions in round-trip operations. Taken together, these results suggest that the assumed notional aircraft with longer range will be used on longer flights, but come at the cost of significant losses of markets on shorter routes due to weight increases. This finding is also reflected in the distribution of traffic between world regions (Figure 15). Since the assumed longer-range supersonic aircraft would not be efficient for operations on shorter routes, especially in the North American market, the North American market potentials decrease more substantially with range increases than potentials in other markets. We note that neither the Concorde nor the STCA were designed for ranges of more than 5,000 nmi, so that we consider the uncertainty in our range sensitivity estimates to be significant.

Finally, we find notional aircraft specifications with higher supersonic cruise speed to have lower market potentials. For example, SST35-1.4-60 with supersonic cruise at Mach 1.4 has a 17% [3 times] higher number of projected round-trip operations than the Mach 1.8 SST35-1.8-60 [Mach 2.2 SST35-2.2-60]. While higher speed increases

	SST35-1.4-60	**SST35-1.6-20**	**SST35-1.6-100**	**SST35-1.8-60**	**SST35-2.2-60**	**SST45-1.6-60**	**SST55-1.6-100**	**SST60-1.6-100**
Maximum range, nmi	3,500	3,500	3,500	3,500	3,500	**4,500**	5,500	6,000
High-speed Mach number	1.4	1.6	1.6	1.8	2.2	**1.6**	1.6	1.6
N_{seats}	60	20	100	60	60	**60**	100	100
Annual number of supersonic round-trip operations, × *1000*	484.3	103.2	754.0	413.2	162.7	**359.8**	494.6	403.8
Annual offered seat-km on supersonic aircraft, *bn seat-km (in percentage of total market)*	188.4 (1%)	15.6 (0.08%)	476.1 (2.52%)	173.3 (0.92%)	73.6 (0.39%)	**162.6** **(0.86%)**	393.2 (2.08%)	359.5 (1.91%)
Average market share of supersonic services on routes with replacement in percentage of seats	5.4%	0.9%	11.4%	4.9%	2.8%	**4.2%**	8.1%	6.8%
Average value of time threshold, $ per hour	272	678	123	226	359	**212**	223	233
Average time saving per roundtrip, hours	3.2	4.2	3.6	4.4	5.3	**4.3**	4.5	5
Average time saving in percentage of subsonic flight	37.1%	43.4%	42.4%	47.1%	53.7%	**43.2%**	43.4%	43.7%
Estimated fleet size, *# of aircraft*	580 to 620	130	820 to 870	450 to 480	160 to 170	**440 to 470**	640 to 680	570 to 610
Total fuel burn (only SST), Tg	15.5	3.56	35.0	22.1	15.3	**16.8**	38.4	39.2
Net fuel burn impact in percentage of BAU	2.8%	0.8%	6.0%	4.4%	3.2%	**4.0%**	7.1%	7.3%
Average fleet fuel burn efficiency, kg/seat-km	0.08	0.23	0.07	0.13	0.21	**0.12**	0.10	0.11
Percentage replacement of subsonic seat-km	0.85%	0.07%	2.15%	0.78%	0.35%	**0.69%**	1.78%	1.72%

Table 9: Global supersonic market potentials for different notional aircraft. No overflight restrictions and economic mid scenario are assumed. In bold baseline notional aircraft SST45-1.6-60.

time savings and thereby the willingness to pay for passengers to use supersonic air services, it also results in higher costs. More specifically, the higher thrust requirements increase with flight speed so that fuel burn per seat-kilometer rises from 0.08 kg per seat-km for SST35-1.4-60 to 0.21 kg per seat-km for SST35-2.2-60. In our model specification, this cost effect outweighs the cost savings, which results in lower market potentials. As a result, we find supersonic markets for faster aircraft to be focused on world regions with high-incomes (Figure 16).

When comparing market outcomes with projected fuel burn, we find total fuel burn from supersonic aircraft trends to follow the general trend in market size (Figure 15), with total fuel burn varying between 3.56 and 39.2 Tg (million metric tonnes). This is of the same order as results by Kawa et al. (1999), while accounting for the difference in aircraft speed and size. However, we note that the fuel burn distribution has less variance than the traffic distribution. This is because aircraft with small projected markets are generally less fuel efficient (see Table 9), thereby increasing total fuel burn.

2.3.2.2 Emissions in unrestricted scenarios

Emissions Indices

We first calculate emissions indices for all notional aircraft under consideration. We find average fleet NO_x emissions indices for the notional aircraft under consideration to vary between 6 and 19 $\text{g}_{\text{NO}_x}/\text{kg}_{\text{fuel}}$ (Table 10). At the engine level, this variation is driven by total pressure (p_{t3}) and temperature (T_{t3}) at the combustor inlet, with higher temperature and pressure increasing NO_x EI. These values are dependent on

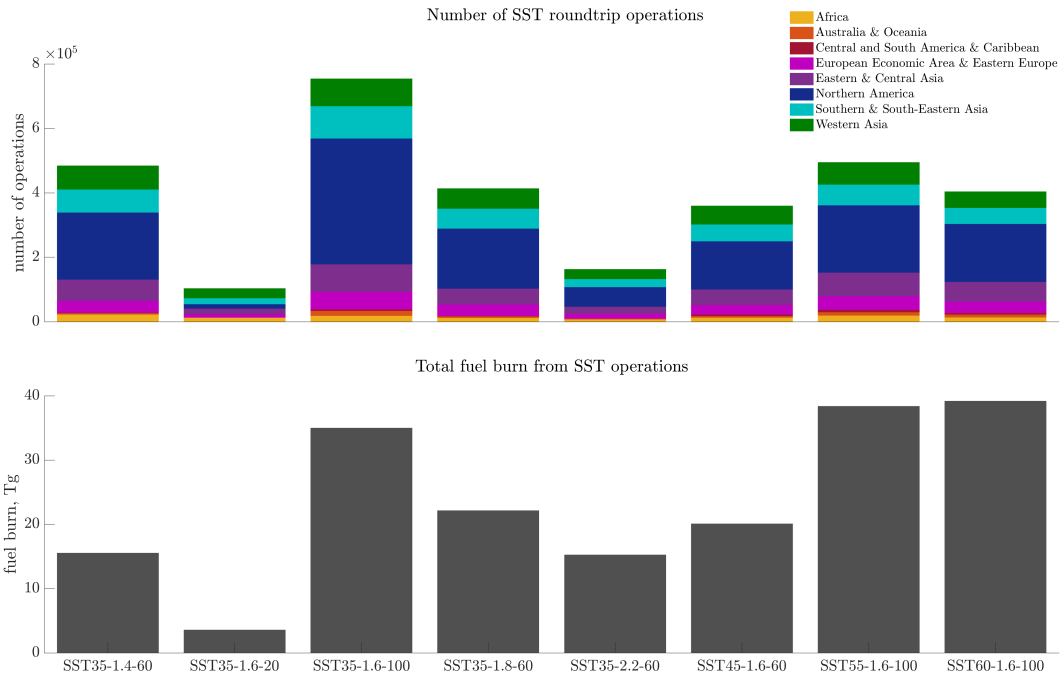

Figure 15: Unrestricted market distribution and total fuel burn of supersonic aircraft for the different notional aircraft tested (mid-economic case).

multiple factors such as ambient conditions, assumed maximum fan diameter and thrust requirements. Fleet average NO_x EI will also be a function of routes due to differing mission thrust requirements. Furthermore, combustor inlet conditions (p_{t3} and T_{t3}) are also drivers of CO and HC EIs. However, the typical low altitude of those emissions limits their stratospheric effects.

Global emissions and their distribution

By combining the market model and fuel burn results with the emissions indices, we derive global emissions inventories. We find global NO_x emissions to vary between 0.02 and 0.76 Tg (Table 11), which is the result of variation in total fuel burn (a

	Subsonic 2035	**SST35-1.4-60**	**SST35-1.6-20**	**SST35-1.6-100**	**SST35-1.8-60**	**SST35-2.2-60**	**SST45-1.6-60**	**SST55-1.6-100**	**SST60-1.6-100**
High-speed Mach	var	1.4	1.6	1.6	1.8	2.2	1.6	1.6	1.6
Max. h_{cruise}, km	var	16.1	17.4	17.4	18.3	19.8	17.4	17.4	17.4
Average h_{cruise}, km	var	15.7	16.4	16.9	17.6	19.1	16.7	16.7	16.7
MTOW, tonnes	var	78	51	123	104	148	123	206	241
max. fan diameter, in	var	50	50	65	60	65	65	70	70
Average fleet fuel weighted NO_x EI, g/kg	15	7.6	6.0	9.3	17	19	**8.8**	13	19
Average fleet fuel weighted CO EI, g/kg	8.3	11	15	6.3	8.3	15	**6.3**	5.0	4.8
Average fleet fuel weighted HC EI, g/kg	1.0	3.4	6.6	1.0	2.7	10	**1.6**	1.4	2.2

Table 10: Average fleet NO_x EI and aircraft characteristics for all notional aircraft under investigation and assuming no flight restrictions. In blue, subsonic 2035 forecast; in green, unrestricted. In bold baseline notional aircraft SST45-1.6-60.

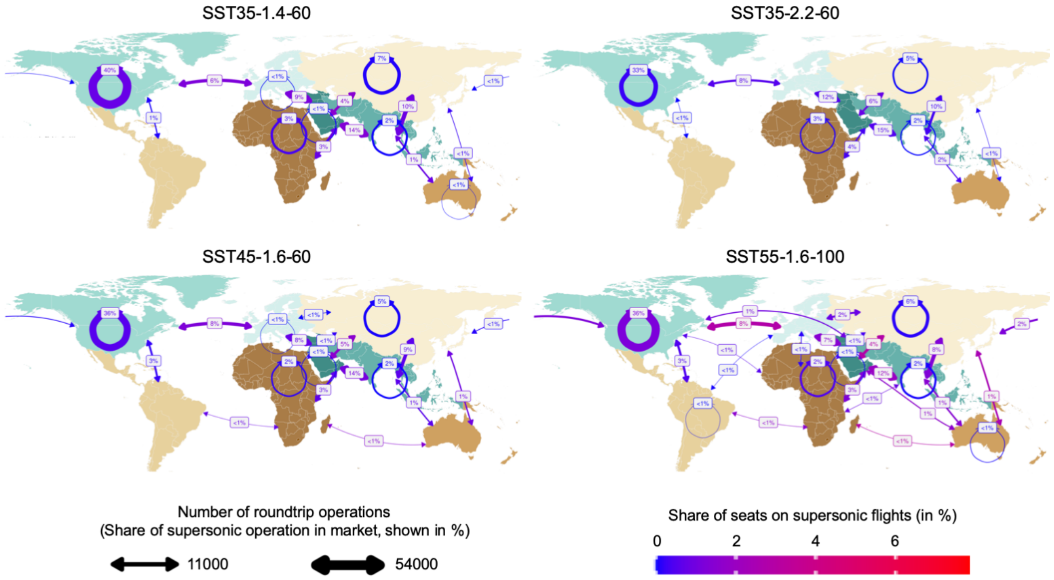

Figure 16: Global market distribution without overflight restrictions for multiple notional aircraft. Top line shows sensitivity to aircraft speed; bottom line shows sensitivity to aircraft maximum range.

factor of 11) in combination with the variation in NO_x EIs (a factor of 3) discussed in Section 2.3.2.2.

The geographical distribution of fuel burn and emissions follows flight corridors in major markets. As a result, 90 to 95% of total fuel burn of SST aircraft is located in the Northern Hemisphere, with approximately two thirds located within 30°N and 60°N (Figure 17). As compared to Kawa et al. (1999), emissions and fuel burn are more evenly distributed in the Northern Hemisphere because Kawa et al. (1999) consider overflight restrictions which impose limits on flights, especially over North America (see Section 2.3.3). For aircraft with longer range and/or higher seat counts, we observe the share of emissions to increase in the Northern Hemisphere beyond 50°N and in the Southern Hemisphere. This is because additional routes can be served with longer range (e.g. connections between Southern America, Southern Africa and Australia) and higher seat capacity results in economies of scale and thereby higher market adoption (Section 2.3.2).

In addition, Figure 17 shows the vertical distribution of emissions. 50% [70%] of global fuel burn [NO_x emissions] is observed above 15 km, with the extreme case of

	SST35-1.4-60	**SST35-1.6-20**	**SST35-1.6-100**	**SST35-1.8-60**	**SST35-2.2-60**	**SST45-1.6-60**	**SST55-1.6-100**	**SST60-1.6-100**
Total NO_x emissions (only SST), Tg	0.11	0.02	0.31	0.37	0.29	**0.17**	0.48	0.76
Total CO emissions (only SST), Gg	153	49	211	177	228	**122**	185	186
Total HC emissions (only SST), Gg	50	22	32	57	152	**30**	52	86

Table 11: Total emissions from SST aircraft for each notional aircraft for unrestricted conditions under economic mid-scenario.

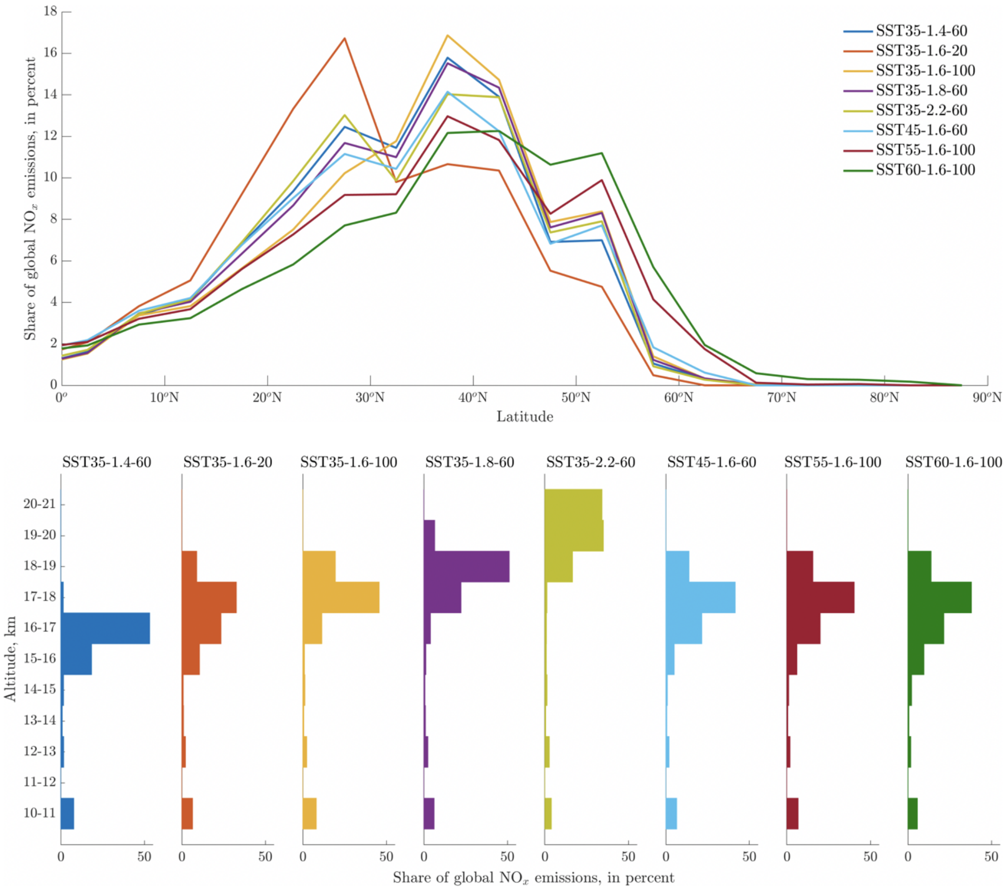

Figure 17: Distribution of NO$_x$ emissions of SST aircraft for each notional aircraft without overflight restrictions. Top plot: latitudinal distribution of NO$_x$ emissions, in percent; bottom plot: vertical distribution of NO$_x$ emissions, in percent.

SST35-2.2-60 with 55% [69%] of fuel burn [NO$_x$ emissions] above 19 km. In addition, our results indicate fuel burn peaks at cruise altitudes which varies between 15.7 km (for SST35-1.4-60) and 19.1 km (for SST35-2.2-60) (see Table 10). Small peaks are observed at lower altitudes and are related to the most demanding phases of the mission, including constant altitude accelerations (i.e. the one at approximately 10 km), see Figure 2.

2.3.3 Forecast of global supersonic market for 2035 – Restricted routing

2.3.3.1 Impact of overflight regulations on routings

We apply the routing algorithm described in Section 2.1.2 to gain insights into how overflight restrictions would change flight paths for supersonic aircraft. Overflight restrictions would either force supersonic aircraft to fly in a "low-speed" regime over restricted areas or to fly detours to avoid areas with restrictions. As described in Section 2.1.2.3, we consider two scenarios: (1) no flight over land areas; and (2) no flight over areas with population density higher than 50 inhabitants per km^2. These scenarios are compared to the case without overflight restrictions discussed in the previous subsection.

Figure 18 shows a subset of optimized flight paths for supersonic aircraft in South-East Asia and Australia (left column) and in Europe and the Middle East (right column) for the unrestricted flight scenario, the scenario with land-area restrictions, and the scenario with population-density restrictions, considering the baseline aircraft (SST45-1.6-60). Under flight restrictions over land, we find aircraft to be re-routed over water, where over-water flight paths with reasonable detours exist (e.g. flights to and from Australia). If these paths do not exist, we find flight

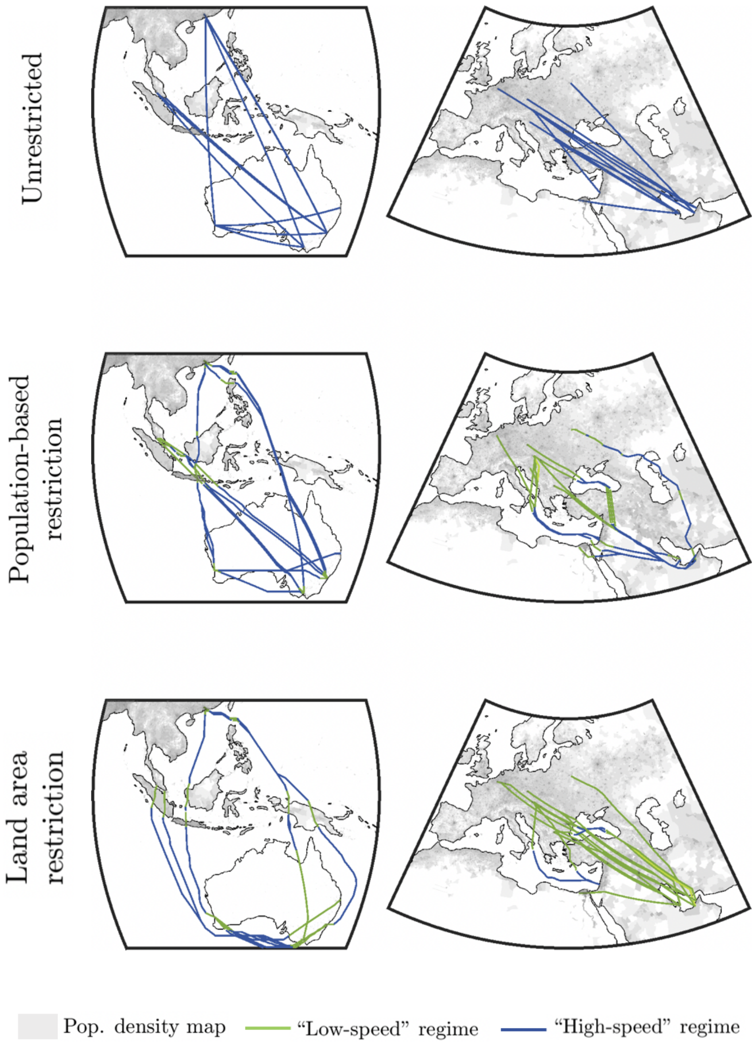

Figure 18: Subset of flight paths under different overflight restrictions for the baseline aircraft (SST45-1.6-60) and economic mid scenario. Left column: South-Eastern Asia and Australia, right column: Europe and Middle East. Overflight restrictions varying from top to bottom: no restrictions, land area restricted, area with population density higher than 50 people per km^2 restricted.

paths to be largely unaffected (e.g. Middle East to Western Europe), which would force supersonic aircraft to fly in their "low-speed" regime over restricted areas. Under population-density restrictions, similar patterns can be observed, though the less stringent restrictions can open up (1) more direct flight paths, e.g. over the Australian continent; or (2) new flight paths over low-density land areas which can be operated at supersonic speed but require detours compared to the more direct paths operated in the "low-speed regime", e.g. between the Middle East and Eastern Europe.

Overall, we find flight restrictions to increase fuel burn and flight times for the SST45-1.6-60 aircraft by 38.6% and 43.9% respectively for land-area restrictions and by 27.0% and 29.5% respectively under population-density restrictions. As shown in Table 12, these circuity values are sensitive to the notional aircraft designs. For faster and larger aircraft, we find time advantages and/or improved economies of scale to improve the economics of detours, while smaller and slower aircraft will use more direct routes in the "low speed regime" due to a lack of achievable time savings and/or high costs of operations for detours.

2.3.3.2 Market projections

We analyze market potentials under overflight restrictions in two steps. Firstly, the analysis is run for the baseline aircraft (SST45-1.6-60), considering two "low speed" regimes (Mach 0.85 and Mach 1.05). Secondly, we analyze the sensitivity of the results to the different notional aircraft with both "low speed" regimes (Mach 0.85 and Mach 1.05).

Baseline aircraft (SST45-1.6-60)

Table 13 shows the market potentials under the economic mid case for SST45-1.6-60 with Mach 0.85 and Mach 1.05 "low speed" regime and both overflight restriction scenarios. The overflight restrictions reduce annual round-trip operations by 81.5% to 96.7% as compared to the unrestricted scenario. Fleet size estimates drop from 440 to 470 aircraft for the unrestricted scenario to 20 to 110 aircraft, which would produce between 0.03% and 0.18% of global seat-kilometers. The market potentials become marginal so that the low economic scenarios under overflight restrictions

	Restriction	**SST35-1.4-60**	**SST35-1.6-20**	**SST35-1.6-100**	**SST35-1.8-60**	**SST35-2.2-60**	**SST45-1.6-60**	**SST55-1.6-100**	**SST60-1.6-100**
Δ fuel burn	land	36.5%	30.1%	44.5%	47.1%	58.6%	**38.6%**	45.6%	46.9%
	$d_{\text{pop}} \geq 50/\text{km}^2$	26.7%	25.4%	33.3%	34.2%	40.4%	**27.0%**	30.3%	31.3%
Δ flight time	land	36.8%	46.9%	46.0%	52.5%	66.1%	**43.9%**	44.3%	44.2%
	$d_{\text{pop}} \geq 50/\text{km}^2$	26.2%	31.0%	32.8%	34.0%	39.8%	**29.5%**	29.3%	29.2%

Table 12: Impact of routing restrictions on fuel burn and flight time by notional aircraft. All O/D pairs with unrestricted markets considered. Algorithm is run for central economic case (fuel price equal to 1 USD per kg and capital multiplier at 4) and Mach 0.85 cruise speed in the "low-speed" regime. In bold: baseline notional aircraft SST45-1.6-60.

	SST45-1.6-60	**SST45-1.6-60**	**SST45-1.6-60f**	**SST45-1.6-60**	**SST45-1.6-60f**
Area restricted	none	land	land	$d_{\text{pop}} \geq 50$/kr	$d_{\text{pop}} \geq 50/\text{km}^2$
Annual number of supersonic round-trip operations, *× 1000*	359.8	11.9	32.2	35.3	66.6
Annual offered seat-km on supersonic aircraft, *bn seat-km (in percentage of total market)*	162.6 (0.86%)	6.2 (0.03%)	16.7 (0.09%)	18.2 (0.1%)	33.4 (0.18%)
Average market share of supersonic services on routes with replacement in percentage of seats	4.2%	1.5%	1.8%	2.1%	2.4%
Average value of time threshold, $ per hour	212	428	391	446	334
Average time saving per roundtrip, hours	4.3	3.4	3.9	3.9	3.9
Average time saving in percentage of subsonic flight	43.2%	31.4%	34.9%	35.7%	36.2%
Estimated fleet size, *# of aircraft*	440 to 470	20	50	50 to 60	100 to 110
Total fuel burn (only SST), Tg	16.8	0.92	2.38	2.55	4.69
Net fuel burn impact in percentage of BAU	4.0%	0.19%	0.48%	0.51%	0.95%
Average fleet fuel burn efficiency, kg/seat-km	0.12	0.15	0.14	0.14	0.14
Percentage replacement of subsonic seat-km	0.69%	0.03%	0.07%	0.09%	0.15%

Table 13: Global market potential for the baseline aircraft (SST45-1.6-60) for mid-economic scenario and different overflight restrictions. We include the different "low-speed" regimes considered. In green, unrestricted; in red, restricted scenarios.

may not result in traffic on a single route. Figure 19 shows that these reductions in market potentials result from losses around the globe. Most importantly, the North American market entirely collapses with flight restrictions over land under a Mach 0.85 "low speed" regime.

The reductions in market potentials are driven by cost increases and reductions in travel time savings which result from the introduction of overflight restrictions. In particular, passengers' required willingness to pay for an hour of time saving increases from 212 USD per hour for the unrestricted scenario to 334 to 446 USD per hour for the scenarios with overflight restrictions.

Market potentials are smallest when flight over land is restricted; they almost triple when supersonic flight is restricted over land with population density above 50 inhabitants per square km. This result is in line with lower increases in flight time and lower fuel burn increases (Table 12) for the population-based restrictions. Most importantly, we find that the North American market becomes viable under the population-based restrictions.

Improvements of low-speed cruise speed from Mach 0.85 to Mach 1.05 are found to have positive impacts on market potentials under overflight restrictions. Upgrading the "low-speed" regime from Mach 0.85 to Mach 1.05 would increase global market potentials by a factor of 2.7 under the overland flight restrictions and by 1.9 under the population-based restriction. This is because supersonic aircraft could generate time savings even in the "low speed" regime, since a cruise speed of Mach 1.05 is higher than for existing commercial subsonic aircraft. We note that a higher Mach number in the low-speed regime strongly benefits the North American market potentials given the significance of flights over restricted areas (Figure 19). In addition, the impact of improved "low-speed" performance is larger for the more restrictive scenarios, because routings rely more heavily on the "low-speed" regime.

Changes in total fuel burn of SST aircraft closely follow the traffic trends. However, the average fuel burn per seat-kilometer increases, from 0.12 kg per seat-kilometer in the unrestricted scenario to approximately 0.14 kg per seat-kilometer in any restricted scenario. This is due to additional fuel burn associated with flying detours as well as with changes between "high-speed" and "low-speed" regimes.

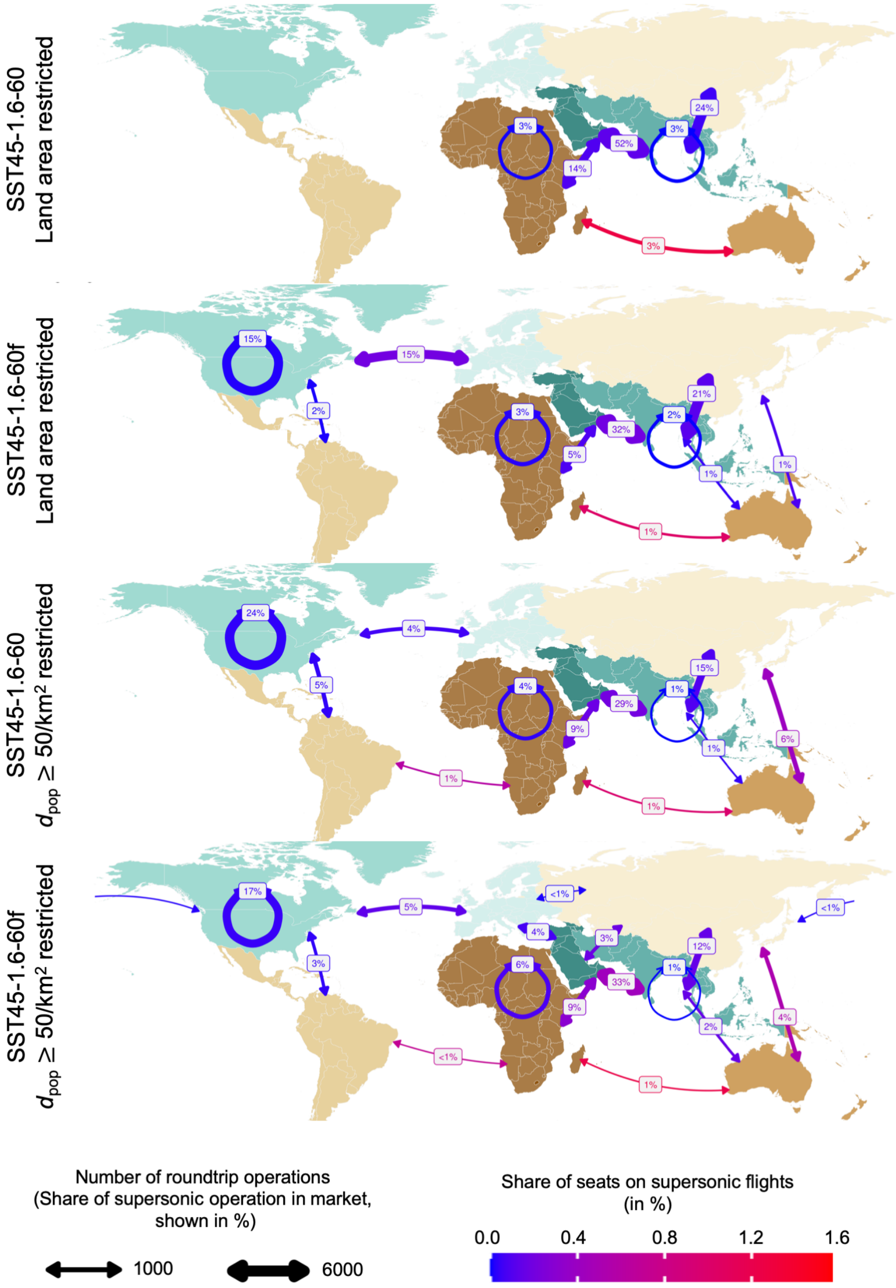

Figure 19: Maps of global commercial supersonic market potentials for the baseline aircraft (max. range = 4,500 nmi, $M_{\text{high-speed}} = 1.6$, $N_{\text{seats}} = 60$) under different overflight restrictions and "low-speed" regimes.

Sensitivity of restricted market to aircraft design

As shown in Figure 20, the market potentials under overflight restrictions are sensitive to the notional aircraft under consideration. All notional aircraft show the strongest reduction in market potentials under overland flight restrictions (-89 to -100% of unrestricted market potentials measured in seat-km with $M_{\text{low-speed}} = 0.85$), whereas under population-density-based restrictions, 5 to 12% of seat-km from the unrestricted market can still be addressed. Similar to the trends for SST45-1.6-60, improved "low-speed" performance improves market potentials for all notional aircraft. Projected fuel burn scales according to market potentials and fuel efficiency, though the increased circuity values for faster and more efficient aircraft increase their fuel burn relative to the traffic increases.

Since overflight restrictions induce detours, they increase costs through fuel burn and reduce time savings given the additional distance flown. As such, it is not surprising that the losses of market potentials are smallest for the most fuel-efficient aircraft (large aircraft), and that particularly slow aircraft lose significant market potentials. Furthermore, aircraft with low supersonic cruise speed benefit the most from increased "low-speed" performance.

2.3.3.3 Emissions in restricted scenarios

We find global emissions totals of commercial supersonic aircraft to decrease by up to 100% with the introduction of overflight restrictions alongside the decreases in market potentials discussed above. For the baseline aircraft (SST45-1.6-60), global fuel burn is reduced by 77% to 95% under overflight restrictions and emissions of all species are being reduced by a same order of magnitude. As such, given the small market under overflight restrictions, global NO_x, CO and HC emissions from commercial supersonic aircraft account for up to 0.6%, 0.6% and 1.8% of forecast subsonic emissions respectively, for the baseline design. While we do not observe significant impacts of overflight restrictions on EIs, we note that overflight restrictions increase the average fuel burn per seat-kilometer by 15–20%. This leads to an average fleet fuel burn per seat-kilometer, which is 3.7–12 times higher than for the the subsonic fleet.

2.4 Synthesis of results and literature comparison

Previous studies of market potentials and emissions of commercial supersonic aircraft have relied on (1) an assumed fixed aircraft design and fleet size (Prather et al., 1992; Kawa et al., 1999; Dutta et al., 2005; Kharina et al., 2018; Jain et al., 2020); and/or (2) estimations of market potentials by assuming fixed shares of passengers who are willing to substitute subsonic air services with supersonic air services (Grewe et al., 2007; Burgos et al., 2020; Wen et al., 2020). These approaches can be combined with additional criteria, including minimum time savings (Wen et al., 2020; Jain et al., 2020) or minimum fleet sizes (Prather et al., 1992). Our study adds to the existing literature by simultaneously (i) estimating market potentials endogenously from market characteristics (e.g. income distribution of passengers) and aircraft

Figure 20: Global commercial supersonic market potentials and total fuel burn (only from SST) for the different notional aircraft, overflight restrictions and "low-speed" regimes.

characteristics (e.g. speed, costs); (ii) considering different scenarios with overflight restrictions for supersonic aircraft and their impacts on market outcomes; and (iii) estimating the sensitivity of our results to different notional aircraft. As such, our approach allows us to analyze the market response to different overflight restrictions (e.g.: over land and over land with certain population density thresholds) and aircraft specifications.

The notional aircraft considered in this study are informed by recent developments and proposals including efforts by Boom and Aerion (Boom, 2020; Aerion, 2020), aircraft studies by NASA (Morgenstern et al., 2015; Berton et al., 2020), and an updated Concorde design (Roxburgh, 2004). As such, the notional aircraft under consideration differ from the aircraft studied in previous work. First, previous studies have often focused on aircraft with very long ranges. For example, Prather et al. (1992) investigated supersonic aircraft with ranges of up to 9,000 nmi. More recently, Kawa et al. (1999) considered notional aircraft with a range of 5,000 nmi and Grewe et al. (2007) analyze aircraft with ranges between 5,400 and 6,000 nmi. However, the latter ranges are still higher than the more recent proposals outlined above. We here focus on notional aircraft with ranges between 3,500 nmi and 6,000 nmi. Second, previous studies have focused on larger aircraft with up to 250 to 300 seats (Kawa et al., 1999; Grewe et al., 2007). While our results suggest such aircraft likely have larger market potentials, recent proposals would suggest that such large aircraft are unlikely to enter into service in the coming decade. We therefore focus on notional aircraft with 20 to 100 seats. Third, past studies have assumed supersonic cruise speeds at the upper end of current trends (e.g. values higher than Mach 2.0) (Kawa et al., 1999; Grewe et al., 2007; Kharina et al., 2018; Jain et al., 2020; Wen et al., 2020). We here include a wider range of Mach numbers (1.4 to 2.2), thereby

	2035 subsonic	**SST45-1.6-60**	**SST45-1.6-60**	**SST45-1.6-60f**	**SST45-1.6-60**	**SST45-1.6-60f**	**SST55-1.6-100**	**SST55-1.6-100**	**SST55-1.6-100f**	**SST55-1.6-100**	**SST55-1.6-100f**
Area restricted	none	none	land	land	$d_{\text{pop}} \geq 5$	$d_{\text{pop}} \geq 5$	none	land	land	$d_{\text{pop}} \geq 5$	$d_{\text{pop}} \geq 50$
Low-speed Mach	/	/	0.85	1.05	0.85	1.05	/	0.85	1.05	0.85	1.05
Percentage replacement of subsonic seat-km	0%	0.69%	0.03%	0.07%	0.09%	0.15%	1.77%	0.13%	0.20%	0.24%	0.39%
Annual number of supersonic round-trip operations, × *1000*	37,091	359.8	11.9	32.2	35.3	66.6	494.6	24.9	43.4	54.6	98.3
Total fuel burn (only SST), Tg	425	19.3	0.92	2.36	2.53	4.65	37.3	3.02	4.72	6.36	9.99
Average fleet fuel burn efficiency, kg/seat-km	0.02	0.12	0.15	0.14	0.14	0.14	0.09	0.11	0.11	0.11	0.11
Average fleet fuel weighted NO_x EI, g/kg	15	8.8	8.7	8.5	7.9	8.6	13	13	11	13	11
Total NO_x emitted (only SST), Tg	6.45	0.17	0.008	0.02	0.02	0.04	0.48	0.04	0.05	0.08	0.11
Total CO emitted (only SST), Gg	3,520	122	6.48	11.2	19.5	22.7	186	15.5	15.5	33.0	35.7
Total HC emitted (only SST), Gg	420	30.3	2.57	2.16	7.49	4.67	52.2	7.28	2.72	15.6	6.53

Table 14: Impact of overflight restrictions on total emissions. In blue, subsonic 2035 forecast; in green, unrestricted; in red, restricted scenarios.

representing all known aircraft currently under development. Finally, we provide insight on the impact of Mach cutoff performance over restricted areas, with our modeled "low-speed" regime at Mach 1.05. A recent study also assumes a different performance over restricted areas, however, their assumption is optimistic considering potential "low-boom" cruise at Mach 1.6 (Burgos et al., 2020).

In the scenarios with unrestricted flight paths, we find supersonic aircraft to operate between 103.2 and 754.0 round-trips, thereby producing between 15.6 and 476.1 billions seat-kilometers (up to 2.52% of the global market). However, our analysis shows that between 78% and 100% of these market potentials cannot be addressed when supersonic flight is restricted over land or over areas with a population density of more than 50 inhabitants per square-kilometer. As such, considering the feedback of overflight restrictions on market outcomes (e.g. through increasing costs and flight times) reduces market potentials significantly. In contrast, other studies have used optimistic assumptions for estimating market size: Burgos et al. (2020) assume a 50% market share, and Wen et al. (2020) assume a substitution potential of 5 to 10%. Our detailed model indicates that such substitution potentials are only achievable on trunk routes without overflight restrictions (0.9 to 11.4% of seats replaced on routes where commercial supersonic service is feasible), whereas we do not find such substitution to be feasible under overflight restrictions (1.5% to 2.4% of subsonic seat-kilometers replaced for the baseline design). However, supersonic aircraft can achieve 2 to 3 times higher market adoption under overflight restrictions, when the flight speed in the "low-speed" regime is increased from Mach 0.85 to Mach 1.05. This is because the "low-speed" regime then allows for speeds which are higher than for subsonic aircraft, so that supersonic aircraft can create time savings even over restricted areas.

Our results suggest that the cost premiums of supersonic services, especially due to fuel burn penalties, limit the market potentials of commercial supersonic aircraft—even in the absence of overflight restrictions. More specifically, we find fuel burn per seat-km to be a factor of 3.2 to 10 higher for our notional supersonic aircraft than for subsonic flights. This result is similar to Kharina et al. (2018), who obtain a 5 to 7 times higher fuel consumption per seat-km for commercial supersonic aircraft as compared to the subsonic fleet.

While the supersonic market share is low ($\leq$2.5%) even under unrestricted conditions, we find that the introduction of commercial supersonic aircraft increases total aviation fuel burn by up to 7% compared to a situation where all routes are being served with subsonic aircraft only. This increase considers replacement of subsonic air services. The contribution of supersonic aircraft to global aviation-related fuel burn can reach up to 7.3%, in unrestricted conditions. These results fall in line with Grewe et al. (2007), who obtain values between 5% and 15%, and Kawa et al. (1999), who analyze a jet carrying 300 passengers flying at Mach 2.4 and obtain an 11% to 24% increase in total fuel burn for a fleet of 500 to 1000 supersonic aircraft.

Emissions from supersonic aircraft have been calculated using different approaches. Some previous studies estimate NO_x emissions indices as a function of combustor technology (Prather et al., 1992), while other studies (Kawa et al., 1999; Dutta et al., 2005) assume constant EIs often informed by EI NO_x targets. Studies considering other emissions like CO and HC assume EIs for these species to be constant (Kawa et al., 1999). In contrast, we have estimated NO_x, CO and HC emissions indices as a function of specific combustor technology for each aircraft design. This explains the variation of our results with aircraft design. We find NO_x EIs to vary between 6.0 and 19, which is in line with Grewe et al. (2007); in contrast, Kawa et al. (1999) assume future low-NO_x technology, which limits NO_x EI to 5 g/kg of fuel. As such, they find net reductions in NO_x emissions with the introduction of supersonic flights. However, we obtain an increase of total aviation NO_x emitted by up to 10% if supersonic aviation is introduced. This may be due to the combination of two factors: (1) fuel consumption of commercial supersonic aircraft is 3.2 to 10 times higher per seat-km than for subsonic aircraft; (2) NO_x EI which can be up to 27% higher (SST35-2.2-60) or up to 60% lower (SST-1.6-20) than for the subsonic fleet. The altitude of emissions varies with maximum cruise altitude (16 to 20 km or 53 to 65 kft). This is in line with values used by Grewe et al. (2007) and Kawa et al. (1999). Other reports have used wider ranges of flight altitude; for example, Dutta et al. (2005) vary it from 13 km to 21 km for analyzing ozone sensitivity.

Given the variability in market outcomes between our scenarios, the report will in the following sections focus on presenting results normalized by a standardized output metric. Seat-kilometers are used for this purpose, as they capture both the capacity of the aircraft and transport distance as the major service provided by commercial air services. We note that a seat-kilometer is defined as a passenger seat flown one kilometer of great circle distance between origin and destination.

3 Plume-scale effects

Highlights

- High concentrations of reactive chemical species in aircraft exhaust plumes lead to non-linear effects that are not typically captured in global-scale models.
- Accounting for plume-scale effects decreases the estimated ozone impact of subsonic aviation and supersonic aviation at Mach numbers below ~ 1.8.
- At higher Mach numbers (and cruise altitudes), accounting for plume-scale effects shows additional ozone destruction compared to an instant dilution approach.
- Heterogeneous chemistry on contrail ice particles contributes up to 10% of the plume ozone impacts, with the greatest effects at high altitudes.

The chemical effects of aircraft emissions are typically simulated using global, Eulerian, 3-D atmospheric chemistry transport models (CTMs). These models simulate aircraft exhaust as being released instantaneously into homogeneously-mixed grid cells that are orders of magnitude larger than the aircraft plume (Brasseur et al., 1998; Meijer et al., 2000; Eyring et al., 2007). This approach does not explicitly capture the high initial species concentrations within the plume, including the effects of non-linear chemistry in the early stages or the formation (and chemical effects) of aerosols and ice crystals (i.e. contrails) in the exhaust plumes. Shortly after release into the atmosphere, species concentrations in the aircraft plume can be several orders of magnitude larger than their background levels. For example, NO_x concentrations at cruise altitude can exceed values up to 20 ppbv in the early stages of the plume, whereas background NO_x levels are typically between 0.007 ppbv and 0.15 ppbv in flight corridors such as the North Atlantic Flight Corridor (NAFC) (Schumann et al., 1998).

The impact of plume-scale modeling of aircraft wakes has been investigated over the past decades mostly because of its relevance to the environmental impact of aviation (Hidalgo, 1974; Thompson et al., 1996). Paoli et al. (2011) summarize the different approaches to model plume scale effects, including approaches which incorporate plume-scale processing of aircraft emissions into global chemistry-transport models. Prior studies have explicitly modeled the gas-phase components of the plume and have shown that the “instant dilution” approach results in inaccurate estimation of the plume’s chemical effects on the environment (Petry et al., 1998; Kraabøl et al., 2000; Cariolle et al., 2009; Huszar et al., 2013).

Furthermore, the effects of interactions between contrail ice and the plume chemistry—including as a surface for rapid heterogeneous chemistry—have not yet been quantified. Field measurements over the past decades, such as the SUCCESS (Toon and Miake-Lye, 1998), POLINAT (Schumann et al., 2000) and SULFUR experiments (Schumann et al., 2002), measured the microphysical characteristics of both liquid aerosol and ice particles (contrails) in aircraft plumes. Contrail modeling efforts based on these measurements have shown that these aerosols are sensitive to ambient relative humidity, fuel sulfur content, and the amount of emitted solid particles (Kärcher, 1998; Wong and Miake-Lye, 2010). In the early stages, non-volatile aerosols take up a significant amount of the emitted water vapor through condensation and heterogeneous freezing, potentially leading to the formation of liquid aerosols and ice crystals. During the plume expansion regime, gas species react and diffuse, potentially reacting with one another through heterogeneous chemistry on their surface. This suggests that the formation of ice in aircraft exhausts may result in additional chemical processing that is not captured in either global atmospheric models or gas-phase aircraft plume models.

An improved understanding of plume-chemistry effects also affects assessment of new fuels for aviation. For example, while biofuels have been identified as an option to reduce aviation's climate impacts, they are also expected to produce less black carbon (Speth et al., 2015) and to have zero sulfur content (in the case of a neat biofuel) (Gupta et al., 2010; Rojo et al., 2015). The effect that these fuels will have on aircraft plume chemistry and contrail evolution—and therefore on the total environmental impact of aircraft emissions—depend on the microphysical response of the plume. As such, the atmospheric effects of changing from conventional jet fuel to alternative fuels are not yet fully understood.

To address these issues we developed the Aircraft Plume Chemistry, Emissions, and Microphysics Model (APCEMM) (Fritz et al., 2020). APCEMM is applied under a variety of conditions to simulate the influence of changes in environmental conditions, aircraft characteristics, and fuel properties on in-plume chemistry and aerosol size distribution. Finally, the effects of these changes are presented in terms of their impact on large-scale properties such as net 24-hour ozone production, end-of-lifetime NO_x partitioning, and contrail optical thickness.

3.1 Plume-scale chemistry and dynamics

APCEMM models the growth and chemical evolution of a single aircraft plume. Chemical concentrations and aerosol characteristics are calculated for a 2-D cross-section of the plume, perpendicular to the flight path. Dynamics, chemistry, and microphysics are explicitly modeled within the plume. In the following, we provide a detailed description of the methods used to establish an aircraft plume model. We first go over the different plume regimes and timescales from the engine exit plane to the long-term plume evolution (Section 3.1.1). In Section 3.1.2, we introduce the chemical mechanism used for the study of in-plume chemical conversions. Section 3.1.3 describes the microphysical representation adopted in APCEMM.

3.1.1 Plume dynamics

Observations and high-resolution modeling of aircraft wakes has shown three dynamical regimes in the first few minutes after emission (early jet, jet and vortex regimes), before the wake develops into a "mature" plume.

Over the first few minutes, the plume cools rapidly to ambient temperatures (~220 K) from an initial temperature of 500–600 K, leading to a spike in ice and liquid water saturations approximately 100 ms after emission and triggering a range of microphysical processes (Kärcher et al., 2015). During this period, formation of sulfate aerosols, freezing on solid nuclei, condensation, heterogeneous nucleation, and coagulation also occur. Since previous studies suggest that homogeneous freezing is unlikely in aircraft plumes given the number of pre-existing nuclei (Wong and Miake-Lye, 2010), we do not consider homogeneous freezing of particles in this work. This is because combustion particles can acquire an ice coating at temperatures much higher than cruise temperatures, implying that ice crystals formed in the vicinity of the engines freeze by virtue of heterogeneous nucleation. In APCEMM, the plume is assumed to be well mixed during the first three regimes—the "early plume phase". We model this early plume as a uniform, well-mixed air mass evolving through time. In the following, we refer to this early-plume representation as a "box model".

The output of this box model is then provided as the initial condition for the model of the long term diffusion regime. This regime begins when the aircraft-induced vortices break apart and the plume expands in ambient air. The rate of diffusion is controlled by the vertical stratification of the atmosphere and by the vertical gradient of the wind speed (wind shear). Unlike the early plume phase, spatial heterogeneity of the plume is explicitly accounted for in APCEMM during the diffusion regime, thereby allowing for cross-plume concentration gradients. For the first hour of this regime, we simulate an upward motion of the plume. This is because the vortex sinking, modeled as a simple vertical displacement, results in adiabatic compression of the plume. In a stably-stratified atmosphere, this causes the plume to be warmer than its surroundings. The resulting buoyancy and radiative imbalance causes the plume to rise back to its original emission altitude, which we simulate as taking place over a one-hour timescale (Heymsfield et al., 1998).

In APCEMM, we use an operator splitting method that allows us to treat the chemical kinetics terms separately from the turbulent diffusion terms, and to apply optimized solution methods for these different processes. For chemistry calculations, the domain is represented using a set of fixed concentric elliptical rings (Figure 21). The central ring (semi-major and semi-minor axis of 75 m and 30 m respectively) is initialized using chemical concentrations and aerosol properties as calculated at the end of the "early plume" stage, and after accounting for losses due to vortex sinking. All other rings are initialized with ambient air. Each ring is further discretized into a lower and upper half-ring to allow for vertical variations in temperature, and to account for sedimentation of aerosols.

Diffusion and advection of pollutants relative to the plume centerline (due to wind shear), in addition to sedimentation of aerosols and buoyant motion, are simulated on a regular, rectilinear grid with a horizontal and vertical grid spacing of 100 m horizontally and 5 m vertically. Prior to these "transport" processes, concentrations of constituents in the rings are mapped to the rectilinear grid. Following transport, the constituents are mapped back to the ring discretization.

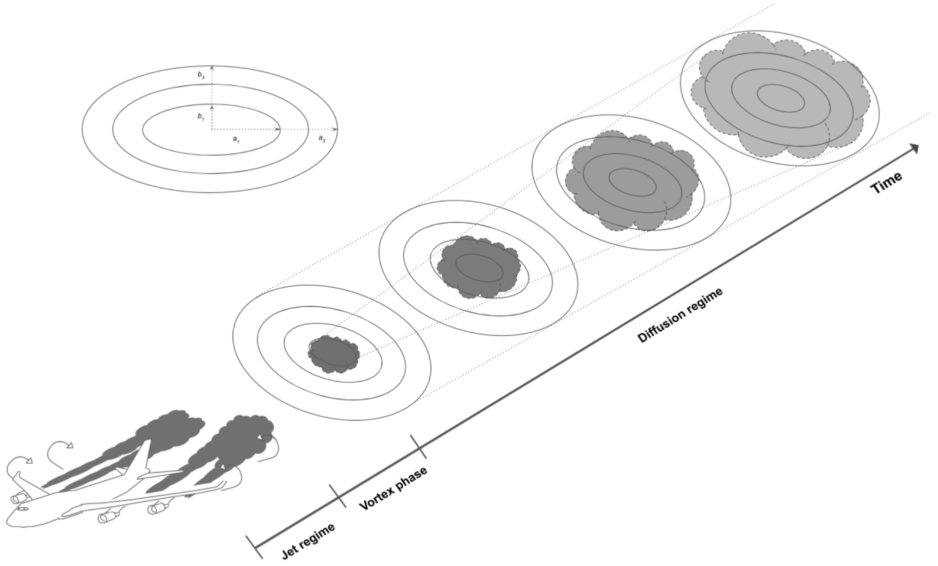

Figure 21: Schematic of the discretized ring approach used in APCEMM. The rings' major and minor axes are denoted by a_i and b_i respectively.

3.1.2 Gas-phase plume chemistry

Gas-phase in-plume chemistry is modeled by distinguishing between the early plume gas-phase chemistry (Section 3.1.2.1) and the long-term chemical conversions in the mature plume (Section 3.1.2.2). Section 3.1.2.3 describes the metric used to compare the chemical outcome of the plume.

3.1.2.1 Early plume gas-phase chemical conversions

In the early stages of the plume, oxidation of NO and NO_2 results in the formation of HONO and HNO_3. As described in Kärcher (1999), conversion efficiencies of NO, NO_2 and SO_2 depend on the exit plane hydroxyl radical concentration. Tremmel et al. (1998) inferred initial OH concentrations at the combustor and engine exit through measurements of NO, HONO, HNO_3 as well as CO_2 to account for plume dilution. Their results indicate that the OH emissions index ranges between 0.32 and 0.39 $\text{g/kg}_{\text{fuel}}$ for the JT9D-7A, which corresponds to an engine exit mixing ratio between 9.0 and 14.4 ppmv. Conversion efficiencies used in APCEMM are depicted in Table 15. Even though the conversion efficiencies remain of the order of a few percent, they increase monotonically with the OH engine exit mixing ratio, as more radicals are available for the following reactions (Kärcher et al., 1996).

Oxidation of SO_2 to gaseous H_2SO_4 is limited during this period. This process mostly occurs in the engine's turbines and only a negligible fraction is converted in the young aircraft plume (Lukachko et al., 1998; Tremmel and Schumann, 1999).

3.1.2.2 Chemistry during mature plume phase

NO	→	HONO	1.5%
NO_2	→	HNO_3	4.0%
SO_2	→	H_2SO_4	0.5%
OH	→	H_2O_2	2.0%

Table 15: Assumed immediate gas-phase conversion efficiencies of NO_x and SO_2 to secondary species

The gas-phase chemistry mechanism is taken from GEOS-Chem v11 (Eastham et al., 2014). Heterogeneous halogen, N_2O_5 and HO_x chemistry, as well as formation and evaporation of stratospheric aerosols are considered. Due to their long lifetimes, reactions involving CFCs and HCFCs are neglected. The set of chemical reactions is solved numerically with the Kinetic Pre-Processor (KPP) (Damian et al., 2002). KPP generates code to integrate the differential equations and compute the time evolution of chemical species with a numerical integration scheme from a set of chemical reactions and rate coefficients.

3.1.2.3 Metrics of the chemical response

To evaluate the error resulting from neglecting non-linear plume chemistry, we compare results from the instant dilution approach to results from APCEMM. The discrepancies between both models are first compared in terms of total ozone mass per unit length in flight direction (kg/km). In addition, the conversion of short-lived nitrogen oxides to reservoir species affects long-term ozone production, heterogeneous chemistry, particle formation and/or growth, with known long-term impacts on air quality (Eastham and Barrett, 2016). The evolution of nitrogen partitioning is therefore computed for both models.

The total emitted NO_y (E_{NO_y}) is a conserved quantity throughout the plume lifetime and is equal to the plume-integrated NO_y perturbation,

$$E_{\mathrm{NO}_y} = \Delta\left(\mathrm{NO}_y\right) = \iint_A \left([\mathrm{NO}_y] - [\mathrm{NO}_y]^{\mathrm{Amb}} \right) dA, \tag{6}$$

where the notation $[\cdot]^{\mathrm{Amb}}$ refers to ambient conditions.

At any given instant, the perturbation of all nitrogen reservoir species ($\Delta\left(\mathrm{NO}_y\right)(t)$) amounts to the initial emission of nitrogen oxides ($\Delta\left(\mathrm{NO}_x\right)(t=0)$), which is proportional to the NO_x emissions index. Averaging the perturbation due to aircraft emissions allows us to compute the time-dependent chemical conversions from one species to another. The emission conversion factor of species X, ECF_X, is then defined as shown in Equation 7.

$$\mathrm{ECF}_X(t) = \frac{1}{E_{\mathrm{NO}_y}} \iint_A \left([X](t) - [X]^{\mathrm{Amb}}(t) \right) dA. \tag{7}$$

The emission conversion factor quantifies how many moles of species X are obtained per one mole of emitted NO_y. For ozone, this is similar to the ozone production efficiency (OPE), although the ECF is time-dependent and does not include ozone that has been produced and later destroyed. Given that nitrogen oxides are converted to reservoir species over the plume lifetime, $\mathrm{ECF}_{\mathrm{NO}_x}$ decreases with time.

3.1.3 Microphysical modeling

The microphysics modeling covers aerosol formation and evolution throughout the plume lifetime. As the plume cools down and mixes with ambient air, aerosols begin to form, thereby supplementing those that were emitted originally from the engine (e.g. black carbon particles). This modifies the local chemical concentrations and changes the initial aerosol size distribution during the second phase of the plume. Four microphysical processes are explicitly considered: freezing of liquid particles into solid ones, condensation of gas onto liquid particles, nucleation of new liquid particles, and coagulation of both solid and liquid particles. Section 3.1.3.1 focuses on the methods used to model formation and evolution of liquid sulfate aerosols and ice particles in the first few minutes after the engine exit plane. Section 3.1.3.2 describes the long-term evolution of ice crystals and sulfate aerosols in the plume.

3.1.3.1 Early plume representation

We first consider growth of an existing particle population. The microphysical model for growth of ice particles is adapted from Kärcher (1998). According to Kärcher and Yu (2009) and *in situ* measurements of black carbon number emissions at cruise altitude (Petzold et al., 1999), the plume is in a "soot-rich" regime, favoring freezing of water around black carbon cores rather than freezing of liquid and ambient particles. We thus assume that solid particles (black carbon and metal) emitted by the aircraft serve as condensation nuclei for water vapor. Under supersatured conditions, deposition induces ice crystal growth, thereby depleting gaseous water vapor. During this initial phase, ice crystals are treated as mono-disperse (single size) and are considered spherical. Under these assumptions, we only consider the growth of a single "representative" particle, rather than analyzing the population as a whole. Because of the low ambient temperatures, water that condenses is assumed to freeze instantaneously, such that ice crystals grow by deposition of water molecules onto their surface. The rate of change in the ice mass of a particle, m_p, is then given by Equation 8.

$$\frac{dm_p}{dt} = H_p^{\mathrm{act}}(m_p) \times 4\pi C_p D_{\mathrm{v,eff}} \left(p_{\mathrm{H_2O}} - p_{\mathrm{H_2O}}^{\mathrm{sat}}\right), \tag{8}$$

where $H_{\mathrm{p}}^{\mathrm{act}}$ is a function accounting for nucleus activation, C_p is the ice crystal capacitance (equal to the particle radius r_p for spherical nuclei), $D_{\mathrm{v,eff}}$ is the effective water vapor diffusion coefficient in air, and $p_{\mathrm{H_2O}}$ the water partial pressure. Assuming that each ice particle is nucleated on a black carbon particle with a dry radius of 20 nm, and using a fixed mass density for ice of 916.7 kg/m^3, this calculation also gives the rate of change of radius of solid particles in the plume. Black carbon and ice particles can also grow by condensation of water vapor, sulfuric acid, and nitric acid into a partial liquid surface layer. The growth of this layer is related to the condensation (or evaporation) rate of H_2O, H_2SO_4 and HNO_3, calculated as shown in Equation 9.

$$\frac{dN_{k,p}}{dt} = 4\pi r_p D_k \beta(r_p) \left(\frac{p_k - p_k^{\text{sat}}}{k_B T} \right) \times \theta, \tag{9}$$

where $N_{k,p}$ is the number of molecules of type k on a particle of type p, D_k is the gas diffusivity in m^2/s, and p_k and p_k^{sat} are the partial and saturation pressures of species k, respectively, expressed in Pa. The function β accounts for changes in uptake in different gas regimes. Experimentally-derived deposition coefficients for heteromolecular condensation, used in the calculation of β, are taken from Kärcher (1998). On black carbon particles, θ describes the fractional surface coverage of the particle liquid coating and is calculated according to Kärcher (1998). For all other particles, this limitation is ignored and θ is set to unity. Gas diffusivities for H_2SO_4 and HNO_3 are taken from Tang et al. (2014).

Similar to sulfur, organic compounds in the upper troposphere have been found to alter the freezing behavior of aerosols and the black carbon coating fraction, θ, even under natural conditions (Cziczo et al., 2004; Kärcher and Koop, 2005; Murray et al., 2010). In aircraft plumes, the formation of condensable organic species originates in the production of electrically charged clusters (chemi-ions) (Kärcher et al., 2015). These organic compounds have been found to be either aqueous aerosols or soluble in aqueous H_2SO_4 solutions (Yu et al., 1999; Kärcher et al., 2015). Their high solubility makes organic matter a prime contributor to the mass of ultrafine plume particles and could also enhance the black carbon particle coating (Rojo et al., 2015). Previous studies estimated the mass of particulate organic matter in aqueous form to be approximately 20 $\text{mg}/\text{kg}_{\text{fuel}}$ (Kärcher et al., 2000). The theory which could explain the role of organics on particle growth and their chemical speciation is still limited.

In addition to growth of existing particles, new liquid particles can form through binary homogeneous and heterogeneous nucleation. Several nucleation parameterizations have been established to simulate binary homogeneous nucleation in a sulfur-rich environment (Jaecker-Voirol and Mirabel, 1989; Napari et al., 2002; Vehkamäki et al., 2002). Jung et al. (2008) have computed different sensitivities using these models and provided further validation of the models cited previously, comparing the results to field measurements. Given the range of ambient conditions relevant to an aircraft plume, we calculate cluster size, composition, and nucleation rate using the parameterization from Vehkamäki et al. (2002). While this model is only considered valid between 230.15 K and 305.15 K, we expect that most nucleation of fresh sulfate aerosol will occur while the plume is still cooling down within this temperature range. Liquid aerosols are assumed to remain liquid throughout the plume lifetime. Previous studies (e.g. Kärcher, 1998; Tabazadeh et al., 1997) have quantified the freezing behavior of sulfate aerosols and liquid sulfur coating at low temperatures and found that freezing of sulfate aerosols requires an ice supersaturation of about 1.5 at 210 K. Additionally, Kärcher et al. (1998) conclude that heterogeneous freezing on coated black carbon particles drives the contrail formation phase. We thus neglect the freezing of sulfate aerosols similarly to Wong and Miake-Lye (2010).

The number concentration of aerosol particles in the plume can also change through coagulation, as emitted and entrained particles collide and coalesce. During the early plume phase, we consider only the coagulation of liquid aerosols, and the scavenging of liquid aerosols by ice and black carbon particles. Self-aggregation of ice and black carbon particles on the time scale of the early plume is assumed to be negligible. Since all aerosols during this phase are likely to be small, all collisions are assumed to result in coagulation (a coalescence efficiency of unity) (Jacobson, 2011). Particle breakup and shattering is neglected for the same reason (Beard and Ochs III, 1995; Jacobson, 2011). The effect of coagulation on the number concentration of aerosols in size bin k, covering the size interval $[r_k, r_{k+1}]$, is modeled as shown in Equation 10.

$$\frac{dn_k}{dt} = \frac{1}{2}\sum_{j=1}^{k-1} K_{j,k-j} n_j n_{k-j} - \sum_{j=1}^{+\infty} K_{k,j} n_k n_j, \tag{10}$$

where n_k is the number density of particles in bin k and $K_{i,j}$ is the coagulation kernel appropriate to collisions between size bins i and j, which represents the physics of the problem. A full description of the coagulation kernel and its calculation is presented by Fritz et al. (2020). Equation 10 states that the rate of change in the number density in bin k corresponds to the rate at which smaller particles of size $k - j$ coagulate with particles of size j minus the rate at which the particles of size k are lost due to coagulation with particle of all sizes.

During the early plume phase, liquid aerosols are modeled using 64 size bins, from a minimum radius of 0.1 nm to a maximum of 0.5 µm. Ice and black carbon aerosols are considered to have a single size, as estimated based on Equations 8 and 9. Instead of solving Equation 10 directly for every size bin, aerosol coagulation is computed using a semi-implicit, non-iterative, volume-conserving and unconditionally stable numerical scheme described in Jacobson et al. (1994). This model has been used extensively in aerosol modeling and aircraft plume simulations (Paoli et al., 2008). The rate of particle coagulation peaks shortly after emission and then significantly reduces as entrainment of ambient air into the plume decreases the number of aerosol particles present per unit volume of air.

The number and size of the aerosol particles present at the end of the early phase is used to provide the initial conditions for the mature plume phase, with one adjustment. The downward movement induced by the aircraft wake vortices (Unterstrasser et al., 2008) increases the depth of the contrail, while adiabatic heating and turbulent temperature fluctuations result in crystal losses through sublimation. These losses are represented using a survival fraction, which we compute using a parameterization based on large eddy simulations (Unterstrasser, 2016). This survival fraction is typically of the order of 0.5, such that the initial aerosol population for the mature plume phase includes roughly half the number of aerosol particles as compared to the number present at the end of the early phase.

3.1.3.2 Aerosol modeling in the mature plume

The aerosol distributions in the mature plume phase are initialized based on the output from the early-plume module. The distribution of sulfate aerosols is unchanged while ice particles are distributed assuming a log-normal distribution, using the mean ice particle radius and a geometric standard deviation of 1.6 (Goodman et al., 1998; Jensen et al., 1998a). The log-normal distribution reflects data from *in situ* measurements (Schröder et al., 2018) and has been used in previous work to initialize the contrail ice particle size distribution (Jensen et al., 1998b; Picot et al., 2015).

As the plume expands, the ice crystal size distribution changes due to growth, sublimation, gravitational settling and coagulation. Even without the application of a log-normal distribution, a polydisperse distribution would have to be assumed due to coagulation and the different meteorological conditions throughout the plume. Particle growth is modeled using a moving-center size structure (Jacobson, 1997) and ice crystal growth is characterized by the "advection" of the particle density distribution across diameter space (Jacobson, 2003).

Ice crystal growth modifies the particle volume but leaves the number of particles constant. Sublimation mechanisms lead to a loss of ice crystals and act as a source of water vapor, modifying the cell's relative humidity and release a dry particle core that is then considered "deactivated" and unable to take up water vapor as ice. The extent of sublimation is moderated by the size of the droplet cores, as larger particles can persist in subsaturated air. Evaporation and sublimation are both endothermic processes that cool down the surface of an ice crystal. The equilibrium surface temperature is obtained through an iterative process that allows us to compute the particle sublimation rate (Jacobson, 2003).

Aggregation of ice particles uses the same algorithm and the same coagulation kernel described previously for sulfate aerosols. Following the approach from Sölch and Kärcher (2010), we assume a constant aggregation efficiency for ice particles.

Gravitational settling causes the ice particles to fall vertically, thus entering warmer regions. Ice particle terminal velocities are computed according to Stokes law, accounting for the slip correction, as in Pruppacher and Klett (1997). The settling velocity of an ice crystal depends on its size, with larger particles falling faster. Different parts of a contrail have different crystal sizes, meaning that they settle at different speeds (Unterstrasser et al., 2016). This differential settling effect is often neglected in contrail models.

3.2 Limitations of the instant dilution approach

We first simulate the evolution of an aircraft plume by using APCEMM and compare the results to those obtained from using an instant dilution assumption (single, well-mixed box). Figure 22 shows the time series of the ozone and NO_x perturbations over the first 24 hours after emission for both approaches.

The chemical evolution of the plume can be split into three regimes, which are distinct from the dynamical regimes described in Section 3.1.1 (Song et al., 2003; Vinken et al., 2011). The first regime is characterized by very high NO_x mixing ratios (>1 ppmv), causing ozone titration. In this period, typically lasting 10 minutes, high mixing ratios of nitric oxide (NO) rapidly deplete local ozone concentrations, resulting in a burst of NO_2 production through reaction [A1] (see Table 16). In this regime, HO_x ($= OH + HO_2$) production is suppressed by the lack of ozone (reactions [A5-A6]).

As the plume dilutes and NO_x mixing ratios fall below 1 ppmv, the plume enters the second regime. With little ozone remaining, HO_2 reacts with the remaining NO (reaction [A4]), producing OH and NO_2 without depleting ozone. This leads to increased OH levels and enhanced ozone production. Meanwhile, photolysis of NO_2 through reaction [A2] results in the recovery of ozone, which had been depleted during the first regime. Between one and two hours after emission, ozone has been restored to its background value. Reactions [A7] through [A10] lead to conversion of emitted NO_x to nitrogen reservoir species.

A few hours after emission, the third regime begins, characterized by NO_x mixing ratios below 1 ppbv. Reaction [A4] and reactions including organic peroxides (such as [A12]) cause increasing levels of ozone and additional conversion to reservoir species. Aircraft plumes, similarly to ship plumes, are characterized by a high NO_x to volatile organic compound (VOC) ratio, therefore favoring termination reactions (e.g. [A7]) over catalytic ozone formation (Song et al., 2003).

Differences between the instant dilution approach and APCEMM are dominated by the behavior during the first two regimes. Explicitly modeling the plume allows the initial ozone destruction to be captured because the highly-concentrated plume is resolved. Although a recovery in ozone is later simulated once the plume diffuses, additional production that would have occurred during the early plume is prevented.

In the instant dilution model, this ozone destruction and production cut-off is not captured. Because ozone is not locally depleted, the instant dilution model instead simulates a prolonged period of net ozone production, as HO_x concentrations remain close to background values. The instant dilution approach, unlike APCEMM, bypasses the first two HO_x-limited regimes and is therefore in a NO_x-rich, HO_x-rich environment, favoring daytime ozone production and conversion of NO_x to reservoir species. Additionally, instant dilution of aircraft emissions results in shorter NO_x lifetimes.

The net result is that, after 24 hours, the instant dilution approach estimates that the aircraft plume has produced ∼1.2 kg of ozone per kilometer flown, compared to ∼0.2 kg per kilometer estimated by APCEMM for a NO_x emissions index of 11.5 g/kg_{fuel}. By this stage in the simulation both models show similar chemical behavior, as the plume has become sufficiently diluted to be well-represented by the instant dilution model. However, the simulation of ozone production in the initial phase leads to a persistent and significant error in the net ozone production of the plume in the instant dilution model.

This discrepancy between APCEMM and an instant dilution model is affected by local meteorology. Increased diffusion, or equivalently higher wind shear, dilutes the plume with a larger mass of air, which minimizes ozone depletion. Therefore, total ozone production scales directly with mixing parameters. Table 17 shows the remaining NO_x and total mass of produced ozone after 24 hours as a function of the local diffusion coefficients. The results for instant dilution are shown in the last row. As diffusion rates increase and dilution becomes faster, the discrepancy between APCEMM and the instant dilution model decreases towards zero. Errors in global simulation of aircraft impacts will therefore be maximized in regions with low diffusion and/or wind shear.

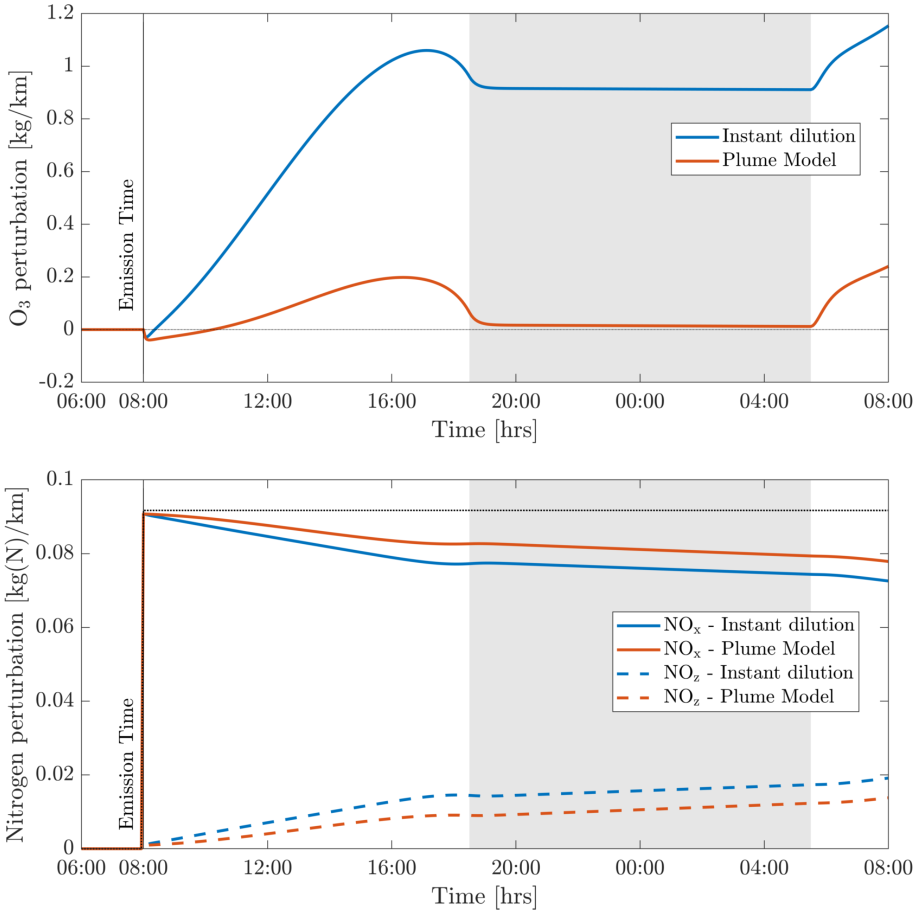

Figure 22: Perturbations in ozone (O_3), nitrogen oxides (NO_x) and the nitrogen reservoir species (NO_z) according to simulations using an instant dilution approach and the plume model. Emissions are released at 8:00 AM local time in a polluted environment. The black dotted line represents all nitrogen species (NO_y), which is a conserved quantity. The shaded areas correspond to nighttime.

3.3 Parameterization of plume-scale effects

The atmospheric response to aircraft emissions also varies as a function of the pressure and latitude of the emission. Although latitude is not a physical parameter of the model, it is equivalent to defining the amount of sunlight received, which affects photolysis rates and background conditions. We simulate pressures from 150 hPa to 750 hPa and latitudes from 0°N to 90°N. Temperature data is taken from monthly-averaged MERRA-2 meteorological data, for 2013. To capture variation of a single flight's emission conversion factors with geographic location and altitude, background conditions and photolysis rates are taken from GEOS-Chem. To also capture seasonal effects, simulations are carried out for emissions taking place on the winter and summer solstices as well as during the spring equinox. We perform simulations using both models. The resulting ozone and NO_x emission conversion factors are presented in Figure 23. Isolines of the discrepancy between both models are plotted on Figure 23 for O_3 and NO_x.

The results show a link between ozone production efficiency and latitude and

Reaction #	Reaction		
[A1]	$NO + O_3$	$\longrightarrow$	$NO_2 + O_2$
[A2]	$NO_2 + h\nu$	$\longrightarrow$	$O(^3P) + NO$
[A3]	$O(^3P) + O_2$	$\longrightarrow$	O_3
[A4]	$NO + HO_2$	$\longrightarrow$	$NO_2 + OH$
[A5]	$O_3 + h\nu$	$\longrightarrow$	$O(^1D) + O_2$
[A6]	$O(^1D) + H_2O$	$\longrightarrow$	$2OH$
[A7]	$NO_2 + OH + M$	$\longrightarrow$	$HNO_3 + M$
[A8]	$NO_2 + O_3$	$\longrightarrow$	$NO_3 + O_2$
[A9]	$NO_3 + NO_2$	$\longrightarrow$	N_2O_5
[A10]	$N_2O_5 + H_2O$	$\xrightarrow{\text{Aerosol}}$	$2HNO_3$
[A11]	$CH_4 + OH$	$\longrightarrow$	$CH_3O_2 + H_2O$
[A12]	$CH_3O_2 + NO$	$\longrightarrow$	$HCHO + \ldots$
			$HO_2 + NO_2$
[A13]	$CO + OH$	$\longrightarrow$	$CO_2 + H$
[A14]	$H + O_2 + M$	$\longrightarrow$	$HO_2 + M$
[A15]	$RH + OH$	$\xrightarrow{O_2}$	$RO_2 + H_2O$
[A16]	$RO2 + NO$	$\longrightarrow$	$RO + NO_2$

Table 16: Dominant $O_3/NO_y/HO_x$ reaction pathways in APCEMM.

pressure. Increasing pressure enhances the ozone emission conversion for the same amount of emitted NO_x, given sufficient sunlight. The amount of sunlight drives ozone production, as little ozone is generated in the most northern latitudes during winter. At high flight altitudes or in cold regions, the daytime NO_x-driven ozone production is of the order of magnitude of the ozone loss at dusk and the early titration effect. This cancellation leads to a small in-plume ozone perturbation of varying sign as shown previously (Vohralik et al., 2008).

The instant dilution approach consistently overestimates the amount of ozone produced at cruise altitudes (∼150 to ∼240 hPa). In absolute terms, the instant-dilution approach performs worst during summertime when ozone production is enhanced across the Northern Hemisphere and the discrepancy in the ozone emission conversion factor is larger. The maximum ozone discrepancy reaches values around 5 in all seasons, corresponding to a relative error of approximately +200%.

NO_x conversion shows different sensitivities to location than the ozone ECF. As shown in the right panels of Figure 23, the NO_x ECF is positively correlated with ambient temperature but is insensitive to the amount of sunlight and season. As the temperature decreases with increasing altitude in the troposphere, the conversion of NO_x to NO_y is lowest at high altitude, going from an average value of 0.3 at 700 hPa to approximately 0.75 at 150 hPa. Greater conversion occurs in warmer air, around the equator and the tropics. Furthermore, the instant-dilution approach

Shear [1/s]	Diffusion coefficients $[\mathrm{m}^2/\mathrm{s}]$	Remain. NO_x [%]	O_3 perturbation [kg/km]
0.000	$D_\mathrm{h} = 05,\ D_\mathrm{v} = 0.05$	88	0.063
	$D_\mathrm{h} = 10,\ D_\mathrm{v} = 0.10$	86	0.17
	$D_\mathrm{h} = 15,\ D_\mathrm{v} = 0.15$	85	0.26
	$D_\mathrm{h} = 20,\ D_\mathrm{v} = 0.20$	84	0.34
	$D_\mathrm{h} = 25,\ D_\mathrm{v} = 0.25$	83	0.41
0.003	$D_\mathrm{h} = 05,\ D_\mathrm{v} = 0.05$	86	0.078
	$D_\mathrm{h} = 10,\ D_\mathrm{v} = 0.10$	84	0.21
	$D_\mathrm{h} = 15,\ D_\mathrm{v} = 0.15$	83	0.31
	$D_\mathrm{h} = 20,\ D_\mathrm{v} = 0.20$	82	0.42
	$D_\mathrm{h} = 25,\ D_\mathrm{v} = 0.25$	82	0.47
	Instant dilution:	79	1.3

Table 17: Influence of diffusion parameters and wind shear on in-plume chemistry

underestimates the amount of remaining NO_x at high altitudes but overestimates at lower levels. The crossover point varies significantly with season and latitude.

3.4 Particle emission and formation

In this Section, we present the results of the aerosol representation in APCEMM. Section 3.4.1 describes the formation and evolution of sulfate aerosols early-on in the plume and the sensitivity of different aerosol modes to the fuel sulfur content (FSC). Section 3.4.2 presents the in-plume microphysical and dynamical evolution resulting from a non-persistent contrail.

3.4.1 Sulfates

Figure 24 describes the sensitivity of the sulfate aerosol distribution to the fuel sulfur content and its evolution throughout the first few minutes. In three experiments, we set the fuel sulfur content (FSC) to 50, 500 and 5000 ppm. Two regimes appear. In the low sulfur emission case, very few liquid particles are formed at the nucleation mode (∼0.5 nm). In this regime, coagulation is slow and the shape of the aerosol distribution is dictated by the dilution and the entrainment of background aerosols whose mode is not represented in Figure 24, given their larger size and smaller concentrations. In the high sulfur emissions scenario, coagulation is more efficient and leads to the apparition of a second mode (∼3 nm). After 100 seconds, the two modes have approximately the same number of particles. At later times, the rate of particle formation is reduced, thus promoting the coarser mode. At intermediate FSC values, the two modes still coexist but the larger mode contains more particles.

3.4.2 Contrail formation

This section describes the evolution of the aerosol size distribution during the early plume phase, from the engine exit plane to approximately 15 minutes after initial

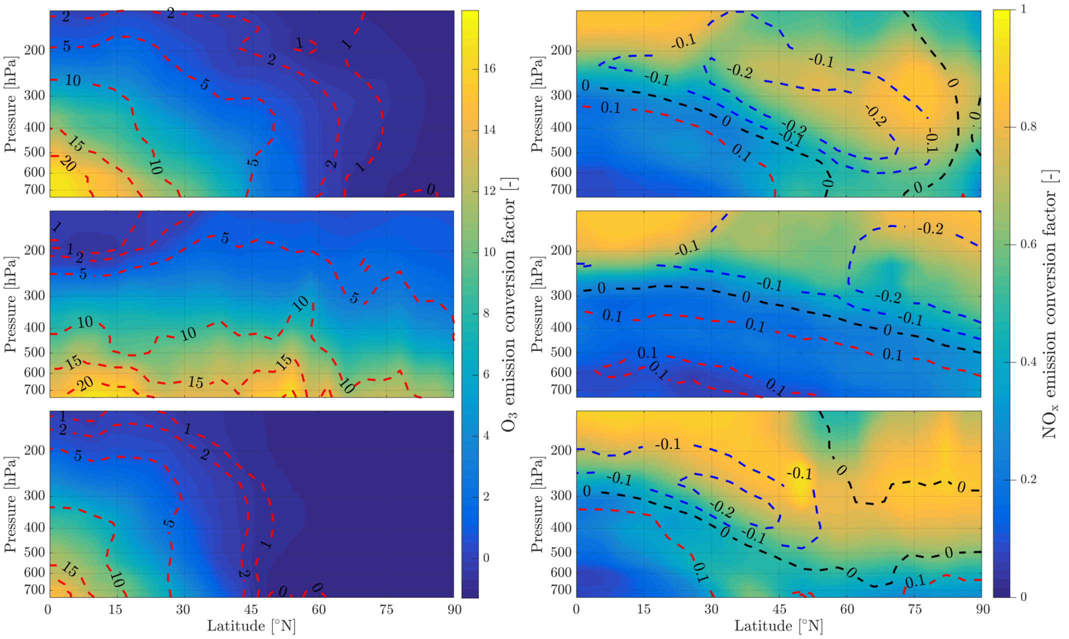

Figure 23: Contour plots of O_3 (left) and NO_x (right) conversion emission factor, 24 hours after emission from APCEMM. The isolines represent the discrepancy between the instant dilution approach and APCEMM. Blue isolines represent cases where the species ECF is underestimated, whereas the red isolines signify that the quantity is overestimated by instant dilution. Simulations have been carried out for emissions at 8:00 on March 21st, June 21st and December 21st (from top to bottom).

emission. We then quantify one potential effect of organic species on plume chemistry and aerosol size distribution through their effect on black carbon surface composition, by varying the initial fractional coating between 0 and 25%.

Figure 25 displays the evolution of the early plume over different timescales. The air at the exit plane of the engine is assumed to be at a temperature of ~550 K. The plume undergoes rapid cooling in the jet phase and fresh ambient air is entrained into the warm plume. As the temperature decreases, the plume reaches saturation and remains saturated for ~2 seconds. During this time, rapid deposition of water increases the particle radius of ice nuclei (as shown in the upper-right plot). As plume mixing continues, fresh, dry air enters the plume. As the relative humidity with respect to ice falls below saturation, the particles start to sublimate. The loss of ice mass serves to maintain the plume's relative humidity at 100% with respect to ice. This continues until all ice mass has melted, after which point mixing drives the plume relative humidity to the background humidity.

The history of the plume can be displayed as a "mixing line" (on the bottom-right plot in Figure 25) on which the water partial pressure is plotted against plume temperature. The line starts in warm and moist conditions at the engine exit. The dilution of the plume, which responds similarly to changes in temperature and water mixing ratio, leads to a straight mixing line until the plume becomes supersaturated. Uptake of gaseous water onto aerosol then reduces the gaseous water partial pressure. Further mixing brings the plume to background state.

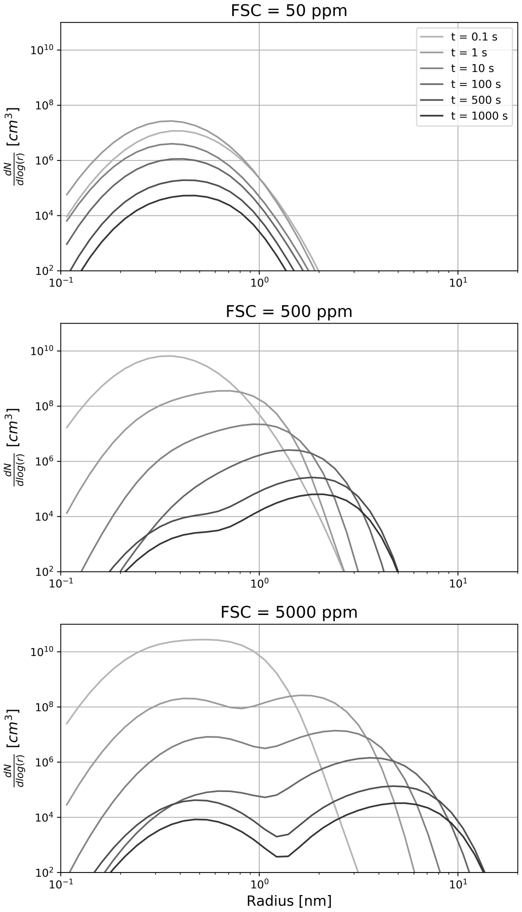

Figure 24: Time evolution of the sulfate aerosol distribution as a function of the fuel sulfur content. From top to bottom, the fuel sulfur content is set to 50, 500 and 5000 ppm on a mass basis. The color shading depicts the time evolution, with lighter shading corresponding to a younger plume.

Some fraction of the fuel sulfur, which is released in the engine combustor, is converted to gaseous H_2SO_4 and quickly condenses. This results in both liquid sulfate aerosol particles, but also coats existing particles (including engine-emitted black carbon particles). The bottom-left plot in Figure 25 shows the coating fraction of black carbon particles over time. This fraction is the result of both adsorption (gas-phase H_2SO_4 condensing onto black carbon directly) and scavenging (collision with existing liquid droplets) as described in Kärcher (1998). In the absence of organic matter, the fractional coating is dominated by sulfuric acid. Adsorption of sulfur particles is initially the prevailing pathway to the formation of a black carbon coating. The coating fraction attributed to adsorption plateaus after ∼0.1 seconds as the gaseous molecular concentration of sulfuric acid becomes negligible. The remaining growth in the coating fraction is attributed to the scavenging of liquid sulfur aerosols onto black carbon particles.

As described in Section 3.1.3.1, organic matter can influence the black carbon fractional coating. Given the short timescales associated with formation of particulate

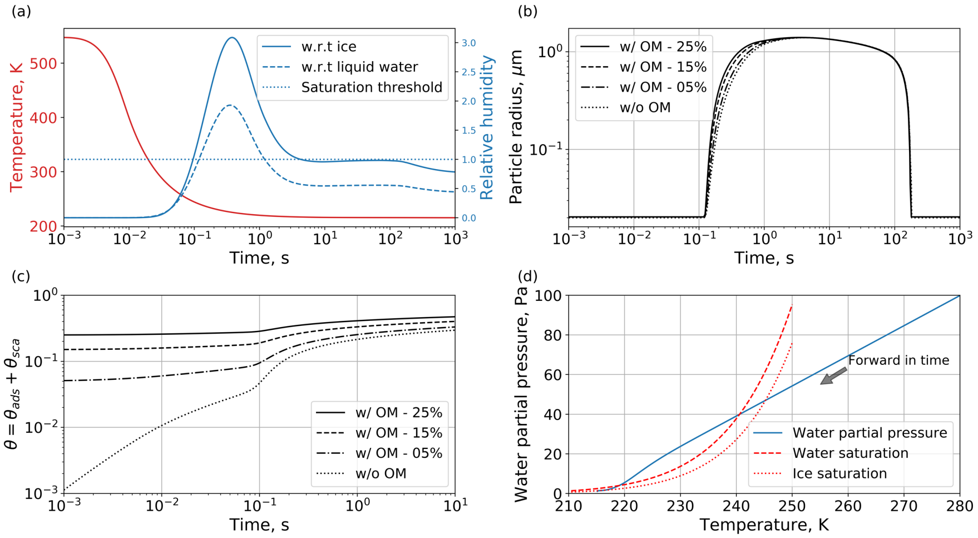

Figure 25: Time evolution of contrail properties simulated by APCEMM. (a) plume temperature and relative humidity, (b) particle radius, (c) black carbon fraction coverage, and (d) water mixing line. "OM" refers to the percentage coating by organic matter.

organic matter, we assume that the black carbon particles are partially coated with condensable organic compounds in the first few milliseconds. As a sensitivity test, we vary the coating fraction attributable to organic species between 0 and 25%. The bottom-left plot of Figure 25 shows the effect on total fractional coating. Our simplified treatment of organic species shows that the inclusion of organic compounds results in faster particle growth, affecting the transient regime in the first second after emission, but does not have any effect on particle radius (upper-right) after approximately one second. Similarly, the gaseous chemical composition is unaffected by the condensation of organic compounds onto black carbon particles, even under supersaturated conditions.

3.5 Contrail persistence

We model how changes in black carbon emissions affect the properties of the contrail. We simulate an aircraft plume in which the black carbon mass emissions indices are varied between 10 and 60 $\mathrm{mg/kg_{fuel}}$, compared to 10 to 14 $\mathrm{mg/kg_{fuel}}$ estimated using the $\mathrm{SN-C_{BC}}$ method for the GEnx engine. All other aircraft and engine emissions parameters are fixed for this sensitivity analysis. As a comparison, Stettler et al. (2013) estimate a fleet-wide average black carbon mass emissions index of 28 $\mathrm{mg/kg_{fuel}}$ while *in situ* observations at cruise altitude have shown that different engines are estimated to have emissions indices between 11 to 100 mg/kg fuel (Petzold et al., 1999). Each simulation assumes a flight-level temperature and relative humidity of 217 K and 110% respectively, and a post-vortex sinking updraft of 5 cm $\mathrm{s^{-1}}$.

We calculate optical thickness by integrating the extinction χ, as defined by Ebert and Curry (1992). Figure 26 shows the temporal evolution of the optical thickness, integrated over the vertical and horizontal (perpendicular to the flight path) axes.

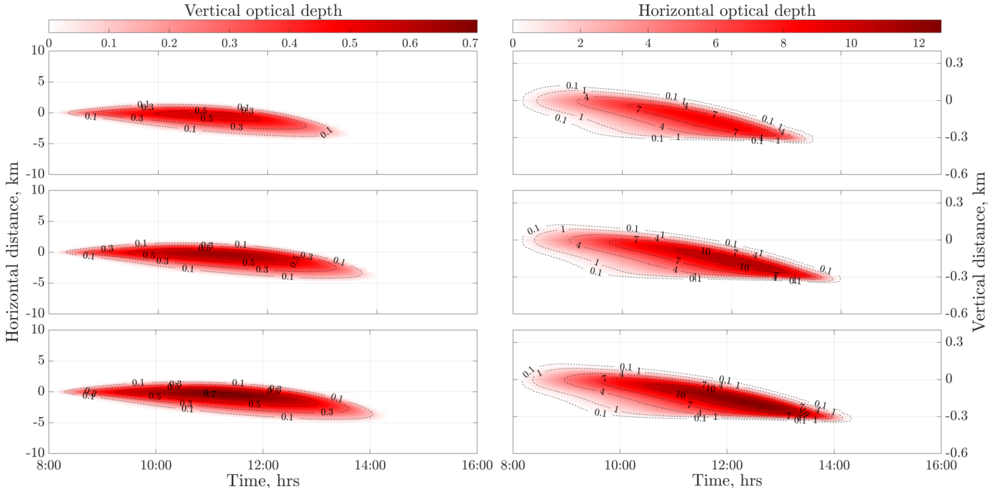

Figure 26: Effect of black carbon emissions index on contrail optical properties. Contours of optical thickness along the vertical (left) and horizontal (right) direction for black carbon mass emissions indices of 20 (top), 40 (center), and 60 mg/kg$_{\text{fuel}}$ (bottom) respectively. The horizontal axis is centered on the flight location. The vertical axis represents the distance with respect to the altitude after vortex sinking. The flight altitude before vortex sinking is at a pressure altitude of 10.6 km. Vortex sinking caused the plume to settle at a new altitude, 112 m lower, corresponding to the origin of the vertical axis. We apply a wind shear of 0.002 s^{-1}, causing the contrail to move left of the initial center line while sinking. An optical depth of 0.1–0.2 is usually given as a contrail detection threshold through satellite sensing (Kärcher et al., 2009).

The ice water content is identical in the first few hours for all simulations, meaning that a scenario with a large particle number has a larger total crystal surface area. This means that reducing the black carbon emissions index decreases both the optical depth of the contrail and its lifetime. This is shown in Table 18, which quantifies the "predominant" optical depth as defined in Equation 11.

$$\tau_{\text{pre}}(t) = \frac{\displaystyle\int \tau^2(x,t)dx}{\displaystyle\int \tau(x,t)dx}. \tag{11}$$

Equation 11 follows the formulation of Unterstrasser and Gierens (2010). Table 18 shows how optical depth varies over time for each scenario. In all cases, the predominant optical depth increases with the black carbon emissions index, with the relative difference between scenarios increasing over time until 4 hours after emissions. After this time, the cases with the lowest black carbon emissions indices have almost fully sublimated. Scaling the emitted black carbon by a factor 2 with respect to the baseline case (set to 20 mg/kg$_{\text{fuel}}$) increases the 2-hour predominant optical depth by 14%. Further enhancement of the black carbon emissions index yields smaller increases in τ_{pre}, although we find no reversal in trend for EIBC up to 3 times the baseline value.

By aggregating these results, we find that doubling the black carbon mass emissions index from the baseline case increases the peak ice mass by approximately 24% and delays the time at which the peak occurs by up to 1 hour. This translates

EIBC (mg/kg_{fuel})	30 min	1 hour	2 hours	5 hours
10	0.11 -20%	0.22 -16%	0.32 -15%	0 -100%
20	0.13 -	0.26 -	0.38 -	0.15 -
40	0.16 +20%	0.30 +15%	0.43 +14%	0.30 +105%
60	0.18 +32%	0.32 +26%	0.47 +24%	0.39 +165%

Table 18: Predominant optical depth for different black carbon mass emissions scenarios. Percentage changes are with respect to the baseline values corresponding to a black carbon mass emissions index of 20 mg/kg_{fuel}.

to a larger climate impact. Reducing the amount of released black carbon particles could instead cut down the contrail-cirrus radiative forcing; halving the black carbon emissions index decreases the optical depth after two hours by ∼15%.

3.6 Coupling of aerosol microphysics and chemistry

In addition to changing the optical properties of the contrail, black carbon emissions affect the chemical impact of the plume. Table 19 shows how the 24-hour emissions conversion factors for O_3, NO_x, and NO_y reservoir species change for different soot emissions indices assuming subsonic cruise conditions. The comparison is here made with respect to a case where no contrail forms, thus yielding the contrail-related chemical perturbation.

Contrail-induced impacts on ozone production are small, with an overall difference of ∼10% with respect to the pure gas-phase response. The NO_y partitioning is affected to a greater extent. The ice crystal surface area in the plume provides a surface for rapid, heterogeneous conversion of N_2O_5 to HNO_3. The descending, crystal-dense contrail therefore rapidly converts NO_x into reservoir forms, with the overall rate and extent of conversion increasing with black carbon emissions. At a black carbon mass emissions index of 20 mg/kg_{fuel}, HNO_3 concentrations are 170% greater after 24 hours than for the baseline case. We also find that concentrations of NO_x, corresponding to the overall NO_x "survival fraction", are lower after 24 hours with higher black carbon emissions due to the heterogeneous reactions on the surface of ice crystals.

Chemical species have an asymmetric profile across the contrail height. A greater aerosol surface area in the lower side of the plume leads to larger chemical rates through heterogeneous chemistry. The extent of the asymmetry depends on ice crystal microphysical parameters and therefore on meteorological conditions as well as aircraft parameters.

We run an additional simulation to quantify how the radiative and chemical impact of contrails differs when contrails form in the stratosphere instead of the troposphere. While contrails in the stratosphere are unlikely to survive the initial

EIBC (mg/kg_{fuel})	ECF_{O_3}	ECF_{NO_x}	ECF_{HNO_3}	$ECF_{N_2O_5}$
0*	0.68 -	0.78 -	0.12 -	0.041 -
10	0.62 -8.8%	0.73 -6.4%	0.32 +170%	-0.042 -200%
20	0.60 -12%	0.72 -7.7%	0.38 +220%	-0.063 -250%
40	0.58 -15%	0.71 -9.0%	0.45 +280%	-0.093 -330%
60	0.56 -17%	0.70 -10%	0.50 +320%	-0.11 -370%

* A black carbon mass emissions index of 0 mg/kg_{fuel} denotes a case in which no contrail forms.

Table 19: Effect of changing the black carbon mass emissions index on emission conversion factors in the upper troposphere. Percentage changes are relative to the baseline case where no contrail forms.

formation stage due the dry conditions, we expect any surviving contrails to persist for longer periods due to the low mixing rates in this region of the atmosphere. In this additional simulation, the relative humidity profile is kept identical.

We find that the lower temperature lapse rate in the stratosphere leads to a smaller contrail ice mass, with optically thinner contrails. This is explained by lower temperatures in the lower part of the contrail core and in the fallstreak. As explained by Unterstrasser and Gierens (2010), a lower temperature reduces the effective crystal radius and optical thickness of the contrail. In the stratosphere, we find that contrails reach horizontal dimensions of 8 to 15 km compared to 5 to 10 km in the upper troposphere after 4 hours.

The nitric acid emission conversion factors are also greater in the stratosphere compared to the troposphere. In some cases, the HNO_3 ECF reaches values above one as ambient, short-lived N_2O_5 is converted to long-lived HNO_3. At a pressure of 100 hPa, a black carbon mass emissions index of 10 mg/kg_{fuel} leads to greater absolute contrail-induced impacts compared to typical subsonic altitudes. The relative changes are however smaller, corresponding to a 73% and -69% change in the HNO_3 and N_2O_5 perturbations as compared to the baseline case. The same change in emission causes a decrease of the ozone perturbation per unit of NO_x emitted by 21% compared to 12% for the tropospheric case.

Aircraft-induced stratospheric cirrus clouds are found to have shorter lifetimes and lead to a smaller optical thickness compared to tropospheric altitudes assuming similar relative humidity profiles. Heterogeneous chemistry on ice crystals gains greater importance at lower pressures and shifts the N_2O_5-HNO_3 local equilibrium.

4 Contrails

Highlights

- Mach 1.6 supersonic aircraft flying at 17 km are one third as likely to form persistent contrails compared to subsonic aircraft flying at 9–12 km.
- The likelihood of persistent contrail formation varies with latitude, with aircraft flying at 17 km twice as likely to form contrails when flying in the tropics, compared to subsonic aircraft.
- Although contrails forming at higher altitude may have longer lifetimes, displacement of subsonic travel by supersonic travel is expected to result in a net decrease in contrail impacts.

4.1 Motivation

Condensation trails, or contrails, are line-shaped ice clouds that form behind aircraft engines under sufficiently cold and humid atmospheric conditions. They have been estimated to contribute up to half of aviation's annual average radiative forcing (RF) (Kärcher, 2018). However, this is subject to large uncertainties given the dependence of contrail RF on uncertain factors including black carbon emissions (Agarwal et al., 2019; Teoh et al., 2019; Zhang et al., 2019), atmospheric conditions (Rädel and Shine, 2010), and the underlying models that capture the physics of contrail evolution (Schumann, 2012; Burkhardt and Kärcher, 2009; Bock and Burkhardt, 2016; Chen et al., 2012; Yi et al., 2012; Caiazzo et al., 2017).

We have already discussed the plume-scale differences in chemistry and microphysics that might be expected in contrails forming behind subsonic and supersonic aircraft (Sections 3.4.2 and 3.5). However, expanding this assessment to a global-scale evaluation requires an accurate representation of upper tropospheric and stratospheric atmospheric conditions. Previous studies of contrail formation have relied on estimates from sources such as meteorological renalysis, which uses observational data to constrain numerical simulations of the atmosphere (Schumann, 2012; Burkhardt and Kärcher, 2009; Bock and Burkhardt, 2016; Chen et al., 2012; Yi et al., 2012; Caiazzo et al., 2017). However, these reanalyses are not optimized to reproduce contrail-relevant quantities at the altitudes typical for subsonic and supersonic aircraft cruise. As a result they may introduce large errors when estimating contrail formation and evolution, both in absolute terms (for subsonic and supersonic aircraft) and in relative terms when comparing between them (Jiang et al., 2015; Ovarlez et al., 2000).

We use observational data directly to capture trends in atmospheric conditions which would affect the formation and persistence of contrails behind subsonic and supersonic aircraft. For this purpose, we use radiosonde observational data provided by the Integrated Global Radiosonde Archive (IGRA) (Durre et al., 2006; Durre and Yin, 2008). The IGRA comprises a global dataset of radiosonde observations including over 2,700 stations. The data includes regular observatoins from 1905 through to the present day. IGRA is thus suitable for assessing global and temporal variations in atmospheric conditions and contrail formation.

4.2 Method

We use IGRA V2 data from 2012 to 2016 (Durre et al., 2006; Durre and Yin, 2008). The soundings are provided from 2,788 stations globally, 1,081 of which contribute between 2012 to 2016. The instruments used in each sounding can vary depending on year and country. To be consistent between stations and times, we use only those stations which use the Vaisala RS92 sensor. This choice is a compromise between the need for a widely-used sensor — to ensure sufficient coverage — and the need for accurate readings. The RS92 is used at 360 of the 1,081 contributing stations, providing excellent global coverage (see Figure 27). It has also been shown to measure temperature and relative humidity—the two critical measurements for contrail formation and persistence—with errors of less than ±1 K and 10% respectively (Miloshevich et al., 2009). Further information on the sensors used at each station is available from the World Meteorological Organization (WMO, 2020).

The number of RS92 sonde launches from each station globally between 2012 and 2016 is shown in Figure 27. The 360 stations using the RS92 and providing humidity readings globally launched 930,091 sondes ("profiles") in this time period. The distribution of stations and profiles varies by latitude as seen in Figure 27, with 48.5% of profiles concentrated in the northern mid-latitudes (30°N to 60°N) and 75% in the Northern Hemisphere. The annual trend in number of profiles separated by latitude band and season is also shown in Figure 28. The number of profiles decreased by around 8% from 2012 to 2016 and that the number of profiles varies by less than 4% between seasons.

Humidity measurements in the IGRA V2 data are provided as a dew point depression ($T - T_\mathrm{d}$), which measures the difference between the ambient temperature T and dew point temperature T_d. The dew point temperature measures the temperature to which the air must be cooled to become saturated with respect to water vapor. The dew point temperature can be converted to the water vapor partial pressure as

$$p_\mathrm{wv} = a_1 \exp\left(\frac{a_2 T_\mathrm{d}}{a_3 + T_\mathrm{d}}\right) \tag{12}$$

where $a_1 = 611.2\,\mathrm{Pa}$, $a_2 = 17.67$ and $a_3 = 243.5\,\mathrm{K}$ are fitted coefficients (Bolton, 1980). This is converted to a relative humidity by estimating the saturation water vapor partial pressure as

$$\begin{aligned} p_\mathrm{wv}^\mathrm{sat} = 100 \exp\bigg(& -\frac{6096.9385}{T} + 16.635794 - 0.02711193T \\ & + 1.673952 \times 10^{-5} T^2 + 2.433502 \log T \bigg) \end{aligned} \tag{13}$$

where $p_\mathrm{wv}^\mathrm{sat}$ is the saturation water vapor partial pressure in Pascal and T is the ambient temperature in kelvin (Sonntag, 1990).

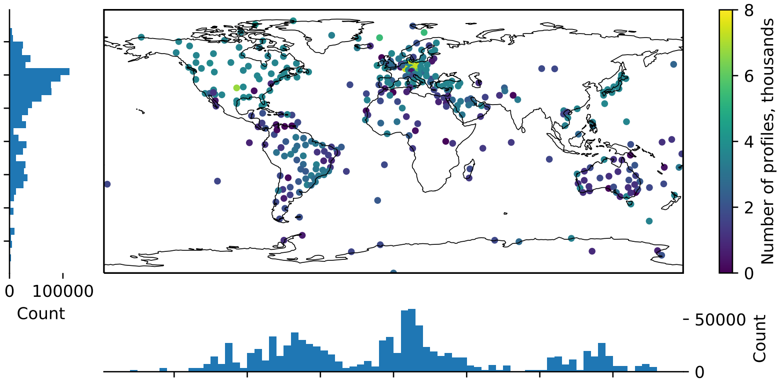

Figure 27: Global distribution of IGRA stations. Each circle is colored according to the number of sonde launches ("profiles") between 2012 and 2016. Left and lower panels show the distribution of profiles by latitude and longitude bands in thousands.

We estimate altitude based on pressure data. Each data point is considered to represent a layer with constant temperature from the lower to upper edge. A layer is defined by the geometric mid-point between consecutive observations. The barometric formula with constant temperature (Equation 14) is used to estimate the difference in altitude between the upper and lower edge of the layer. The altitude is initialized assuming the highest recorded pressure value is at the surface. We therefore calculate

$$z_+ = z_- + \frac{RT}{gM_{\mathrm{air}}} \log\left(\frac{p_-}{p_+}\right) \tag{14}$$

where z_+ and z_- are the altitude of the upper and lower edge of the layer respectively, $R = 8.3145\,\mathrm{J\,mol^{-1}\,K^{-1}}$ is the universal gas constant, $g = 9.81\,\mathrm{m\,s^{-2}}$ is the gravitational acceleration at the surface of earth, $M_{air} = 0.028\,\mathrm{kg\,mol^{-1}}$ is the average molecular mass of air and p_+ and p_- are the pressure at the upper and lower edge of the layer respectively.

To quantify the likelihood of contrail formation and persistence, we define a persistent contrail criterion (PCC). The PCC identifies whether a contrail can form and persist in the local conditions. Satisfying the PCC means satisfying three conditions: (a) the air must be supersaturated with respect to ice ($\mathrm{RH_i} > 100\%$); (b) the relative humidity with respect to water must be above the critical ambient relative humidity with respect to water ($\mathrm{RH_w} > \mathrm{RH_{w,C}}$); and (c) the relative humidity with respect to water must be below 100% ($\mathrm{RH_w} < 100\%$).

$\mathrm{RH_i}$ is calculated as

$$\mathrm{RH_i} = \mathrm{RH_w} \frac{p_{\mathrm{wv}}^{\mathrm{sat}}}{p_{\mathrm{wi}}^{\mathrm{sat}}} \tag{15}$$

where $\mathrm{RH_w}$ is the measured relative humidity with respect to water, and $p_{\mathrm{wi}}^{\mathrm{sat}}$ is the estimated saturation partial pressure with respect to ice. This is approximated

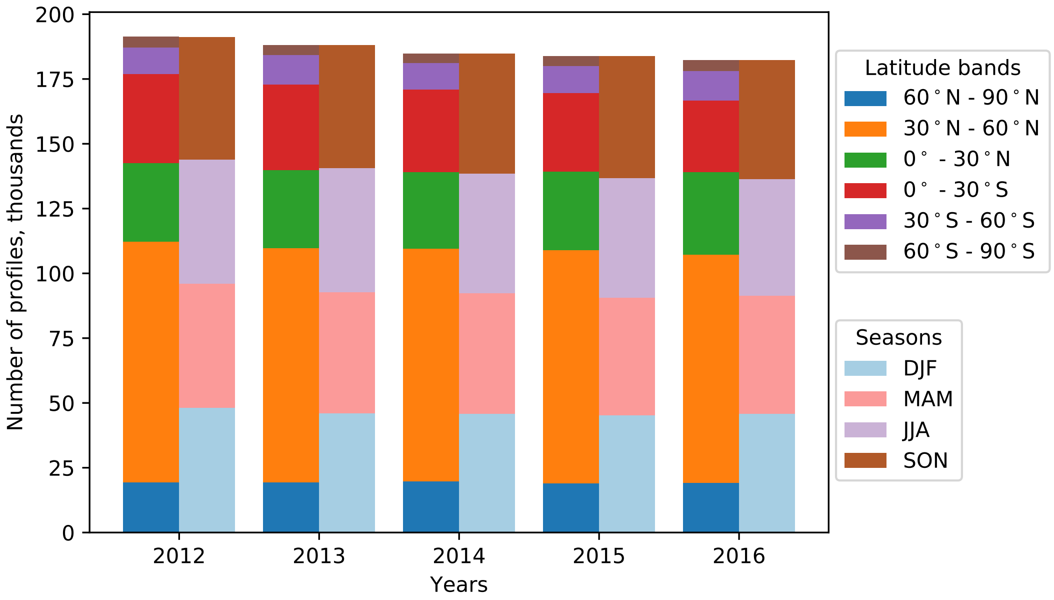

Figure 28: Annual number of IGRA profiles for each year. Each bar is colored by latitude band and season. Seasons are represented as: DJF = December, January, February; MAM = March, April, May; JJA = June, July, August; SON = September, October, November.

following Sonntag (1990) as

$$p_{\mathrm{wi}}^{\mathrm{sat}} = 100 \exp\Bigg(-\frac{6024.5282}{T} + 24.7219 + 0.010613868T - \\ 1.319883 \times 10^{-5} T^2 - 0.49382577 \log T \Bigg) \quad (16)$$

where T is the local, measured air temperature in kelvin. The $\mathrm{RH}_{\mathrm{w,C}}$ is formulated in the Schmidt-Appleman Criterion (SAC) (Schumann, 2000; Schmidt, 1941; Appleman, 1953), which is a thermodynamic condition requiring the exhaust plume to locally reach water supersaturation as it mixes with the ambient air. It is calculated as

$$\mathrm{RH}_{\mathrm{w,C}} = \frac{G \cdot (T - T_{\mathrm{LM}}) + p_{\mathrm{wv}}^{\mathrm{sat}}(T_{\mathrm{LM}})}{p_{\mathrm{wv}}^{\mathrm{sat}}(T_{\mathrm{LM}})} \quad (17)$$

where G is the gradient of the line representing the temperature and water vapor partial pressure of the exhaust plume as it mixes with ambient air in $\mathrm{Pa\,K^{-1}}$, $p_{\mathrm{wv}}^{\mathrm{sat}}(T)$ is the saturation pressure defined above but calculated at temperature T. T_{LM} is the maximum threshold plume temperature when $\mathrm{RH}_{\mathrm{w}} = 100\%$ as the plume mixes in °C. T_{LM} is calculated as

$$T_{\mathrm{LM}} = -46.46 + 9.43 \log(G - 0.053) + 0.72 \log^2(G - 0.053) \quad (18)$$

It is calculated as

$$G = \frac{c_{\mathrm{p}} p \mathrm{EI}_{\mathrm{H_2O}} M_{\mathrm{air}}}{M_{\mathrm{H_2O}} \mathrm{LHV} \left(1 - \eta_{\mathrm{o}}\right)} \tag{19}$$

where $c_{\mathrm{p}} = 1,004\,\mathrm{J\,K^{-1}\,kg^{-1}}$ is the specific heat capacity of air, p is the ambient pressure, $\mathrm{EI}_{\mathrm{H_2O}} = 1.23\,\mathrm{kg\,kg_{fuel}^{-1}}$ is the water emissions index, $M_{\mathrm{air}} = 28.97\,\mathrm{g\,mol^{-1}}$ and $M_{\mathrm{H_2O}} = 18.02\,\mathrm{g\,mol^{-1}}$ are the molecular masses of air and water respectively, $\mathrm{LHV} = 43.13\,\mathrm{MJ\,kg^{-1}}$ is the lower heating value of jet fuel and η_{o} is the engine overall efficiency. η_{o} is equal to the propulsive efficiency (η_{p}) multiplied by the thermal efficiency (η_{t}).

Since the PCC is a function of aircraft efficiency (as used in the SAC), we calculate it for multiple efficiency values that are representative of the subsonic and supersonic (nominal) aircraft considered for this report (see Table 2). The scenario/nominal aircraft choices and efficiencies chosen are shown in Table 20. The specific choice of efficiency is stated for each plot.

In addition to individual observations of the PCC, we identify contiguous PCC observations, referred to as PCC regions. The depth of PCC regions is defined as the difference between the upper and lower altitude. A deeper PCC regions is expected to allow contrails to persist to a lower altitude, leading to a longer lifetime.

The PCC provides an estimator of whether a persistent contrail will form if an aircraft flies through the region at a specific space and time. Multiplying the PCC at a given altitude (averaged over time) by the likelihood of a flight passing through that altitude therefore gives a metric of the frequency with which contrails will form at the location. For a given vertical profile, we can use the vertical distribution of aviation fuel burn as a proxy for the likelihood that aircraft will be present at that altitude. Accordingly, we calculate the fuel burn weighted PCC, F_{PCC}, at any given time t as

$$F_{\mathrm{PCC}} = \frac{\displaystyle\int P_{\mathrm{PCC}}\left(z\right) F\left(z\right) dz}{\displaystyle\int F\left(z\right) dz} \tag{20}$$

	Engine overall efficiency, η_{o}
Subsonic	0.35
SST35-1.6-20 SST35-1.4-60	0.40
SST45-1.6-60 SST35-1.8-60 SST35-1.6-100	0.45
SST35-2.2-60 SST55-1.6-100 SST60-1.6-100	0.475

Table 20: Mapping between engine overall efficiency values used for contrail simulations and nominal aircraft.

where P_{PCC} is the proportion of space-time that satisfies the PCC, F is the fuel burn profile, and z is the vertical coordinate. F_{PCC} thus represents the proportion of the vertical fuel burn profile in a region that could lead to a contrail forming. In all cases we use an annual average fuel burn profile as this is not expected to vary significantly by region. $F_{\text{PCC}}(t)$ therefore corresponds to the proportion of the annual average fuel burn profile that could lead to a persistent contrail.

4.3 Results

We first evaluate the likelihood of persistent contrail formation due to the background atmospheric conditions by looking at the vertical distribution of the PCC globally, by latitude band and by season. The effect of the vertical fuel burn profile and higher cruise altitude of supersonic aircraft is accounted for in the fuel burn weighted PCC. Next, we study the effect of notional SST design and over-land flight restrictions on the fuel burn weighted PCC. Finally, we discuss the major sources of uncertainty with using sonde data in this context.

4.3.1 Central case

Figure 29 shows the proportion of samples at each altitude which satisfy the PCC (right) for all IGRA locations from 2012 to 2016, using an overall efficiency $\eta_{\text{o}} = 0.35$. These results show that PCC likelihood peaks at around 10 km, with the PCC being satisfied approximately 5% of the time. This peak is typical of the cruise altitude of subsonic aircraft. Flying at higher altitudes, as expected for supersonic aircraft, could therefore reduce the number of contrails that form. For example, for an SST with a cruise altitude of 16 km, the annual mean PCC percentage across all stations is lower by a factor of 5.9 compared to an altitude of 10 km. This reduction is consistent with expectations from prior assessments of contrails due to SSTs (Kawa et al., 1999; Grewe et al., 2007). Grewe et al. (2007) modeled the effect of supersonic aircraft on linear, short-lived ($<$ 30 minutes) contrails, finding that contrail coverage would reduce by 1.6%.

The left panel of Figure 29 shows the depth of PCC regions, defined as the difference between the upper and lower extent of contiguous PCC observations, versus the altitude at the midpoint of the PCC region. Results are only shown where sufficient data is available. This shows the depth of PCC regions tends to remain constant until 12 km, before increasing with altitude until 15 km. As deeper PCC regions are associated with longer lasting contrails, this data suggests that contrails forming above 12 km could persist for longer periods before evaporating than contrails forming below this altitude. For a fleet of supersonic aircraft with a cruise altitude of 16 km, the PCC depth is approximately 1,700 m, 2.2 times larger than that at subsonic cruise altitudes of 10–11 km. A greater PCC depth means a contrail forming in this region can survive to a lower altitude and is thus expected to have a longer lifetime. For this reason, we would expect SSTs to lead to fewer persistent contrails forming than for subsonic aircraft, but also expect that these contrails might last for longer periods.

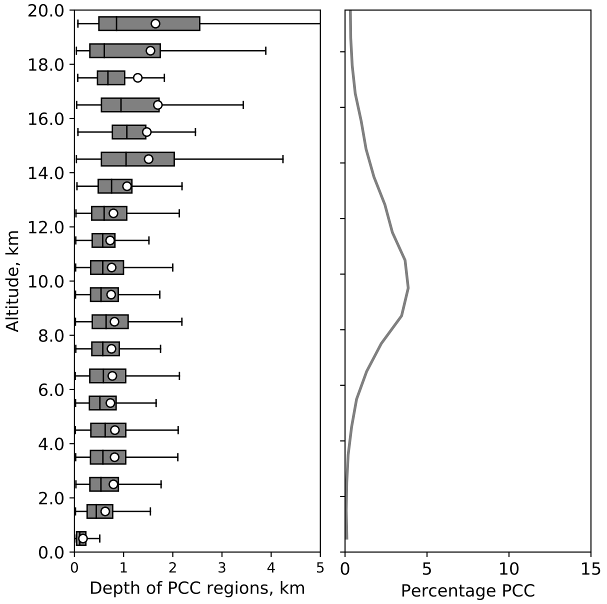

Figure 29: Global distribution of PCC depth and percentage PCC. Box plot showing distribution of the depth of PCC regions (left) and the percentage satisfying the PCC (right) by altitude for all IGRA locations from 2012 to 2016 for $\eta_o = 0.35$. The box represents the 25% and 75% range (interquartile range (IQR)), the whiskers reach 1.5 times the IQR, the vertical black line represents the median and the white dots the mean.

These results are averaged across all stations, but significant differences in contrail formation and persistence are expected between, for example, the tropics and extratropics (Grewe et al., 2007). We therefore decompose the data by latitude, region, season, and year to understand how these factors could affect contrail impacts resulting from a fleet of supersonic aircraft.

Figure 30 shows the altitude distribution of PCC regions, separated by latitude band. Although the IGRA dataset includes locations in the Southern Hemisphere, we only show results for the Northern Hemisphere as we project 88% of projected subsonic and projected supersonic fuel burn to be in this region. The right most plot shows the percentage PCC by altitude for each latitude band. This shows that the altitude of maximum PCC proportion moves upwards from 8.5 km at the Arctic to 12.5 km at the tropics. The peak proportion satisfying the PCC however decreases by 58%, from 0.12 at the Arctic to 0.05 in the tropics. This trend was also found by Grewe et al. (2007), that showed contrail coverage from linear, short-lived (< 30 minutes) contrails for a mixed subsonic-supersonic fleet would reduce by around 10% in the northern mid-latitudes, but increase by 5% in the tropics.

The trend seen in the percentage PCC is also evident in the depth of PCC regions. The range of altitudes in which PCC regions appear increases from 0–13 km in the Arctic to 0–15 km in the mid-latitudes and to 9–19 km in the tropics. The PCC depth and its trend with altitude is similar in the mid-latitudes and Arctic. In the tropics, the mean PCC depth is around two times greater than the other regions. These results imply that supersonic aircraft in the tropics would lead to longer-lasting contrails than supersonic aircraft in other latitude bands. We also expect more contrails to form at SST cruise altitudes in the tropics. Contrails may also form during the transition from subsonic to supersonic speeds (around 11 km) in other latitude bands.

The trend by latitude for each season (DJF: December, January, and February; MAM: March, April, and May; JJA: June, July, and August; and SON: September, October, and November) is shown in 31. The percentage PCC tends to be at lower altitudes in JJA compared with DJF. In the tropics, the altitude of peak PCC proportion moves downwards between these two seasons, from 14.5 km to 12.5 km. A similar shift occurs in the mid-latitudes with the peak moving from 11.5 km to 9.5 km, and in the Arctic, moving from 10.5 km to 9.5 km. These results are consistent with radiosonde water vapor measurements from earlier SST assessments (Prather et al., 1992), which showed the peak water vapor in the upper troposphere, lower stratosphere to be higher in JJA than DJF. The value of the peak percentage PCC between JJA and DJF varies between region, however. In the tropics, the peak increases from 3.0% in DJF to 6.2% in JJA. In comparison, the peak decreases from 6.5% in DJF to 3.9% in JJA in the mid-latitudes and from 17% in DJF to 9.5% in JJA in the Arctic. This suggests that there are strong seasonal cycles in contrail formation, especially in the northern mid-latitudes and Arctic.

We quantify inter-annual trends in Figure 32. The peak percentage PCC has increased by approximately 40% from 2012 to 2016. The increase is greatest at approximately 17 km. This data suggests that the percentage PCC has been increasing with time above approximately 8 km. However, this increase could represent changes in the location of sonde profiles. In addition we only consider a period of five years, which is not sufficient to study long-term trends in the atmosphere. Additional years need to be analyzed to confirm these trends. In comparison, Irvine and Shine (2015) find a long-term decrease of one-third in the global, annual average area of cold ice supersaturated (CISS) regions, which is expected to coincide with the PCC, from an average value in 1979–2005 to 2100. This decrease is concentrated in the tropics, while the mid-latitudes and Arctic show an increase in CISS of 1% and 5%. Bock and Burkhardt (2019) estimate the PCC and find a similar decrease in the tropics at approximately 10 km from 2006 to 2050, with no significant change outside the tropics. At higher altitudes, there is an approximately 1% increase in CISS in the Arctic and mid-latitudes.

An important caveat is that all the discussion thus far has been based on estimates using a single value of $\eta_o = 0.35$. The effect of this assumption is quantified in Section 4.3.2.

Temporal trends are studied by calculating a monthly rolling median of PCC depth at 10, 14, 17 and 20 km is shown in Figure 33, requiring a minimum of 10 observations. In all latitude bands, the median PCC depth at 20 km does not appear, since there are fewer than 20 observations in a given month. This is representative of the $< 1\%$ likelihood of a PCC region at this altitude (see Figure 30).

The median PCC depth in the Arctic exhibits a weak seasonal dependence varying from approximately 1 km in NH winter to approximately 0.5 km in NH summer. This 0.5 km seasonal trend decreases to approximately 0.2 km by 2016. This effect is expected to be caused by changes in stations operating over this time period. In the mid-latitudes, a seasonal trend at 14 km occurs in NH summer with PCC regions

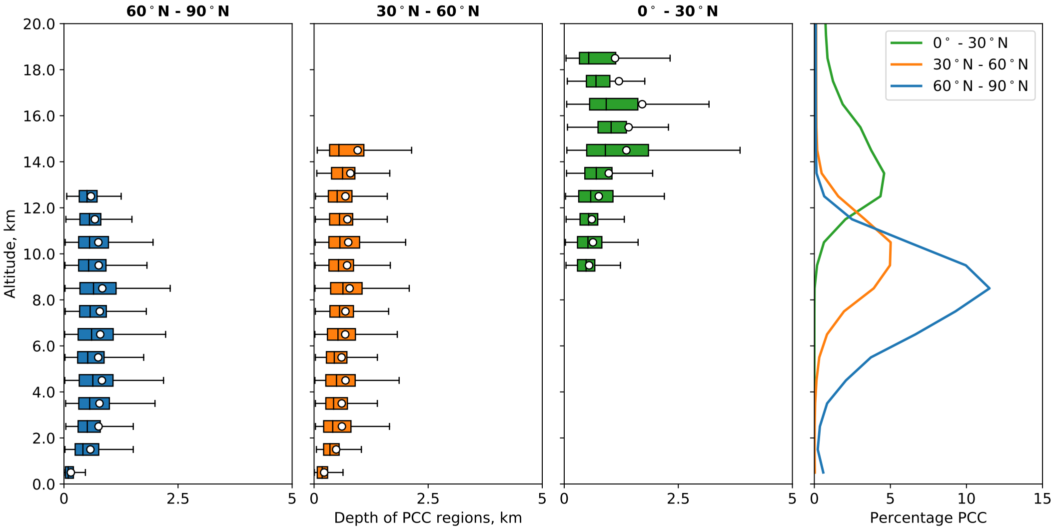

Figure 30: PCC depth and percentage PCC by latitude band. Box plot showing distribution of the depth of PCC regions (left) and the percentage satisfying the PCC (right) by altitude from 2012 to 2016 for $\eta_o = 0.35$ separated by latitude band. A box plot is included only if sufficient data are observed.

appearing in NH summer with a depth of 0.5–1 km. In the tropics, PCC regions at 17 km appear with a depth of 0.5–1.5 km.

Figure 34 shows the percentage of fuel burn in a PCC region for the 2035 baseline subsonic case, and for the baseline supersonic scenario (notional aircraft SST45-1.6-60, no restrictions). The SST case has 68% less fuel burn in a PCC region than the subsonic cases. There is a strong dependence by latitude band and subsonic fuel burn in the Arctic have more than six times the fuel burn in a PCC region than in the tropics, and 1.5 times that in the mid-latitudes. In comparison, the maximum variation in fuel burn weighted PCC for supersonic flights is only 56% between latitudes. This means the supersonic flights in the tropics would have a 25% higher likelihood of a persistent contrail forming than subsonic flights in the tropics. In comparison, in the Arctic, supersonic flights would have a 77% lower likelihood of a persistent contrail forming than subsonic flights.

4.3.2 Sensitivity analysis

In this section, we study the effect of supersonic aircraft design, overland flight restrictions, and efficiency on the proportion of fuel burn in a PCC region.

Figure 35 shows the effect of latitude on the fuel burn weighted PCC for each supersonic aircraft design. As in the baseline case, supersonic aircraft generate more contrails in the tropics than at other latitudes. The variability of the fuel burn weighted PCC is also greater in the tropics. Comparing between designs, the fuel burn weighted PCC is 44% to 178% greater than the subsonic value in the tropics. In the mid-latitudes and Arctic, this range reduces to a 73% to 80% decrease and 74% to 82% decrease respectively relative to the subsonic case. This difference between cases is driven by the differences in cruise altitude for each aircraft design (see Table

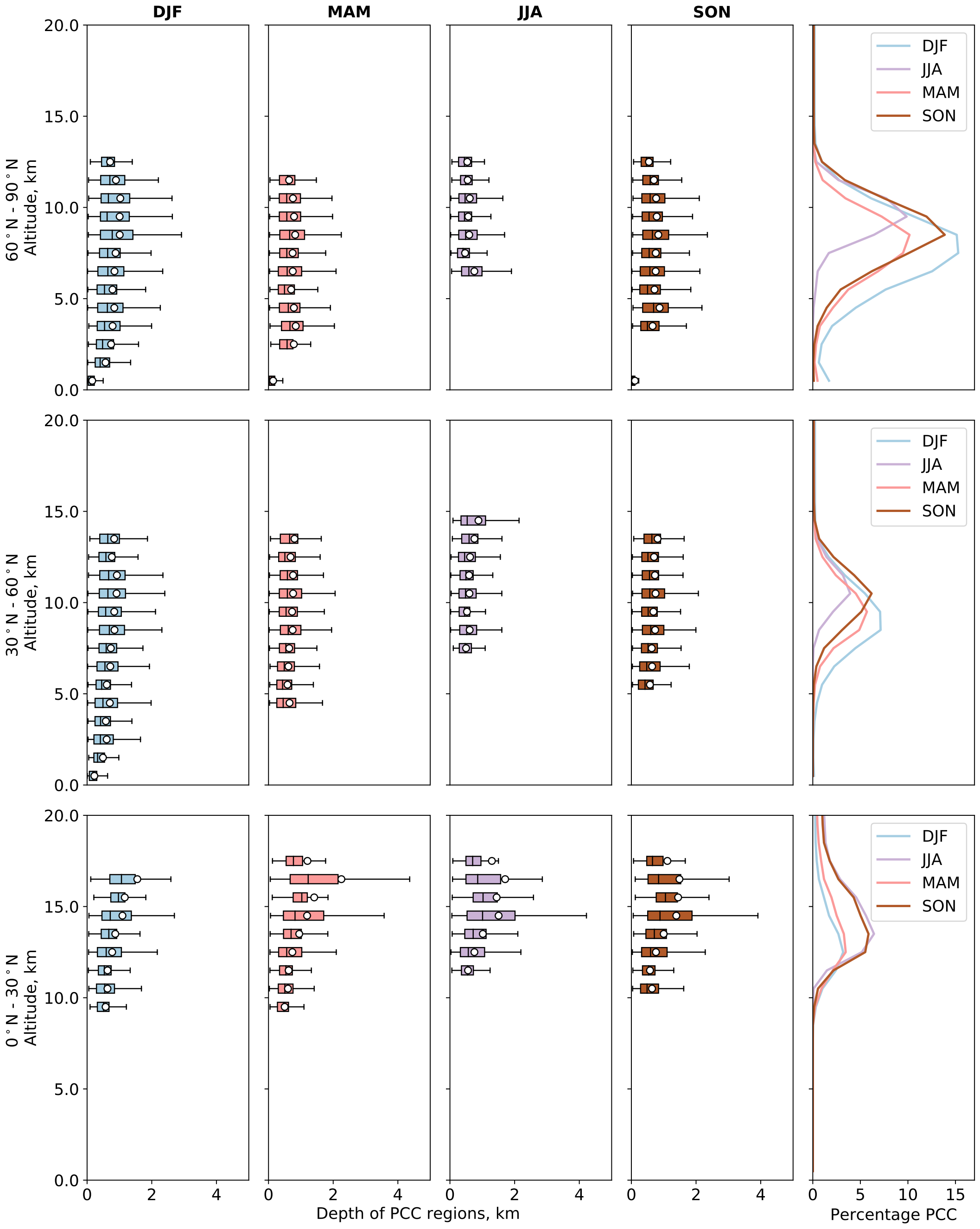

Figure 31: Seasonal and latitudinal variation of PCC depth and percentage PCC. Box plot showing distribution of the depth of PCC regions (left) and the percentage satisfying the PCC (right) by altitude from 2012 to 2016 for $\eta_o = 0.35$ separated by latitude band (rows) and season (columns). Seasons are defined by DJF: December, January and February; MAM: March, April and May; JJA: June, July and August; SON: September, October and November. A box plot is included only if sufficient data are observed.

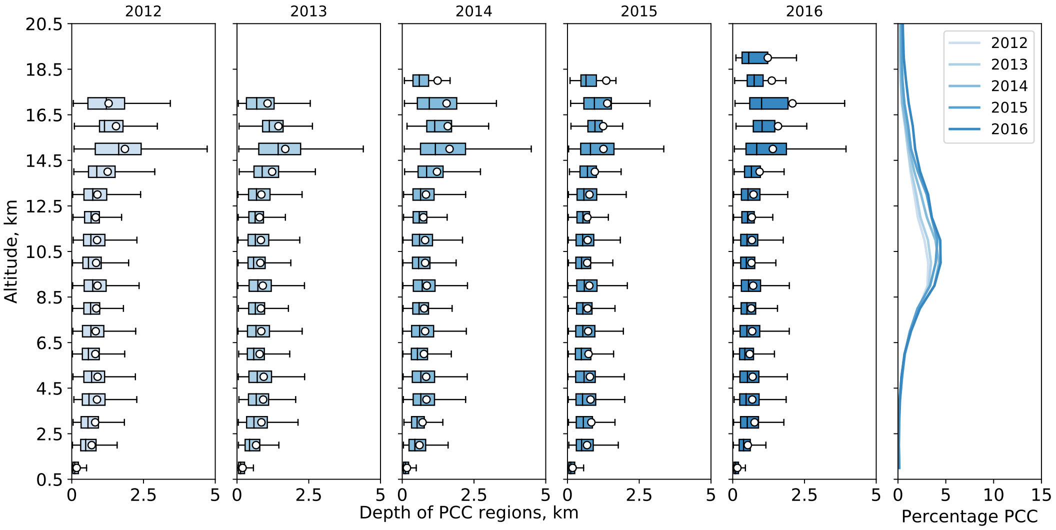

Figure 32: Inter-annual variation of PCC depth and percentage PCC. Box plot showing distribution of the depth of PCC regions (left four panels) and the percentage satisfying the PCC (right) by altitude for $\eta_o = 0.35$ separated by year. A box plot is included only if sufficient data are observed.

2). The average cruise altitude can vary from 15.7 km to 19.1 km and the PCC proportion varies by more than 200% between these altitudes in the tropics compared with <1% in the mid-latitudes and Arctic. The dependence of altitude was also found by (Grewe et al., 2007), who found that lowering supersonic cruise altitudes from 17.5 km to 16 km could decrease linear, short-lived ($<$ 30 minutes) contrail coverage by around 12%.

The overall efficiency for each supersonic aircraft design varies from 0.40 to 0.475 (see Table 20). The PCC depends on the efficiency, which an increase in efficiency leading to an increase in the likelihood of a persistent contrail forming. For this reason, we isolate the SST aircraft engine overall efficiency by calculating the fuel burn weighted PCC for a fixed $\eta_o = 0.40$ in Figure 35. A baseline of 0.40 is chosen as this is the lowest overall efficiency for all SST designs.

Across all designs, the efficiency causes up to a 15% increase in the fuel-burn weighted PCC, which occurs for the SST55-1.6-100 design ($\eta_o = 0.475$). Above approximately 12 km, the absolute effect of efficiency in proportion PCC is less than 0.1% and this leads to the small difference in fuel burn weighted PCC for supersonic aircraft design.

The choice of low-speed Mach number (0.85 versus 1.05) and the regulation on where SSTs may fly at supersonic speeds is estimated using the fuel burn weighted PCC as shown in Figure 36. Restricting flights could lead to a higher percentage of the fuel burn leading to contrails by 18% to 42%. At the low-speed Mach number of 0.85, relative to the no restriction scenario, land area restrictions lead to a 42% increase in the fuel burn weighted PCC and the population density restriction a 21% increase. In comparison, the high-speed Mach number of 1.05 leads to a 26% and 18% increase, respectively. The low-speed Mach number has a strong effect on fuel burn weighted PCC because of the altitude flow at this speed. At a low-speed Mach

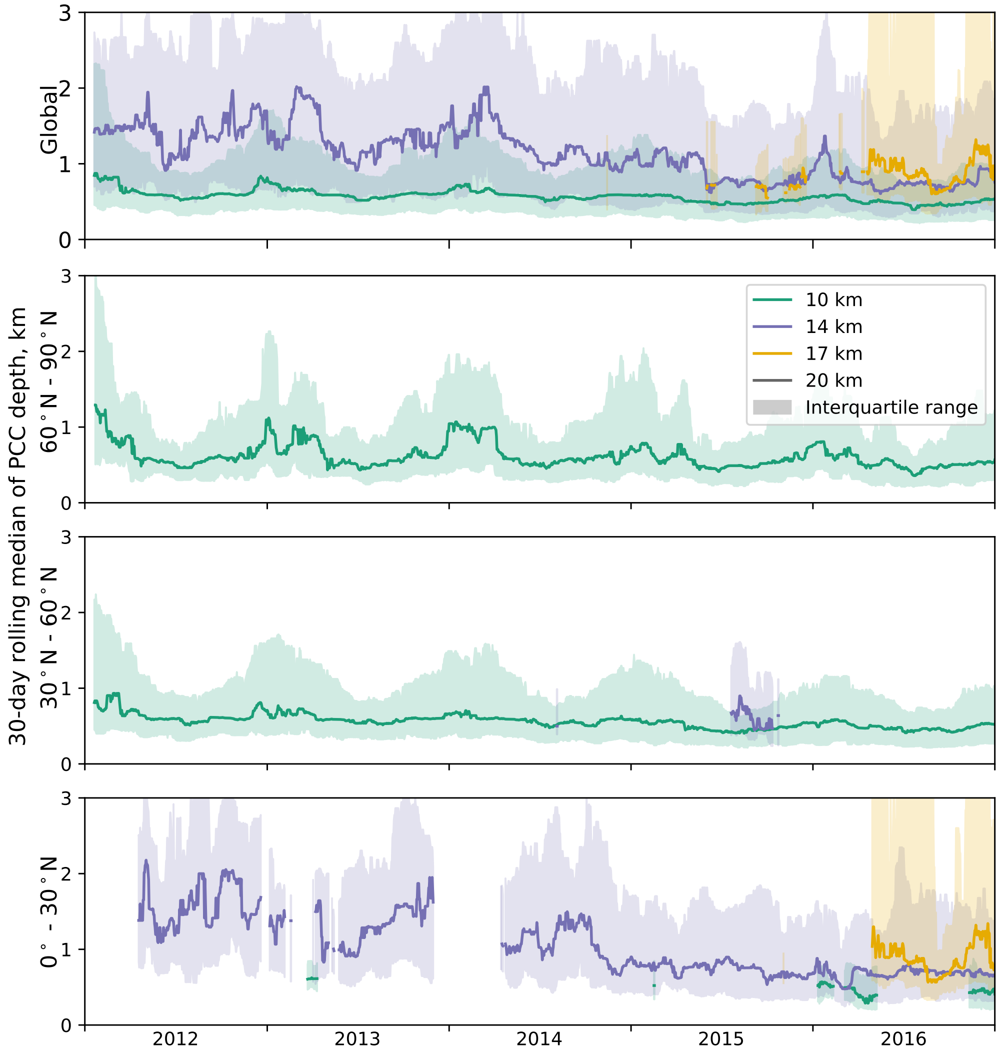

Figure 33: Time evolution of PCC depth at 10, 14, 17 and 20 km altitude separated by latitude band. 1 month rolling median (solid lines) and inter-quartile range (shaded areas) of PCC region depth with region mid-altitude at 10, 14, 17 and 20 km (±0.5 km) for $\eta_o = 0.35$. Top panel shows global results and subsequent panels shows results separated by latitude band. Results not shown if fewer than 10 observations available for the given day.

number of 0.85, the flight altitude is approximately 10 km, compared with 12.5 km at a low-speed Mach number of 1.05. Between these two altitudes, the global, annual average percentage PCC reduces by 35% from 3.7% to 2.4%. We also note that the fuel burn weighted PCC only provides information on the proportion of the vertical fuel burn profile that could lead to a persistent contrail forming. The total number that form is also dependent on the total number of SST operations, which is up to a factor of 30 higher in the no restriction case than other overflight restrictions.

The choice of SST notional aircraft can affect the median PCC depth by up to a factor of 3.5 as shown in Figure 37. In addition to SST efficiencies and altitudes, we also include the subsonic case in blue. These results show that there are very few

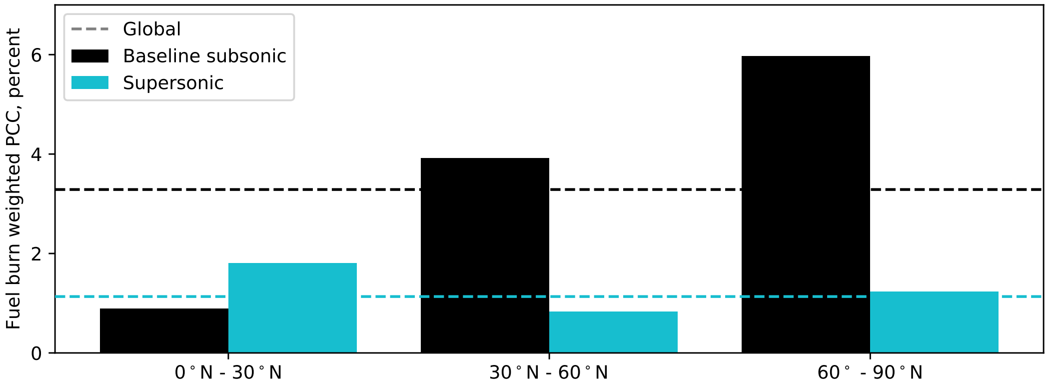

Figure 34: Latitudinal variation in contrail formation likelihood for subsonic and supersonic aircraft. Proportion of fuel burn in PCC regions globally (dashed lines) and separated by latitude band. Colors represent baseline subsonic (black), subsonic with replacement (blue) and supersonic baseline case (aircraft design SST45-1.6-60, no restrictions, orange). Global results for subsonic with replacement (blue dashed line) is hidden by global baseline subsonic results (black dashed line). In each case, the global fuel burn profile is used, but PCC proportions according to each region. Engine overall efficiencies are used according to each case as defined in Table 20.

PCC occurrences at SST cruise altitudes. Only at an altitude of 17.5 km are PCC occurrences found, and the PCC depth is around a factor of two deeper that at 10.5 km.

To further isolate the effect that engine overall efficiency, Figure 38 shows the PCC depth and the percentage satisfying the PCC for η_o ranging from 0.30 to 0.475. As expected from the definition of the SAC, a higher η_o leads to a higher percentage PCC. The greatest absolute change occurs at 8.5 km, where a change in efficiency from 0.30 to 0.475 results in a 0.009 increase in PCC likelihood—a relative change of 30%. The minimum relative effect of efficiency occurs at an altitude of 13.5 km (4%). This increases to 9% at 16.2 km, 14% at 17.4 km and 19% at 18.3 km.

4.3.3 Sources of uncertainty

There are a number of uncertainties that are important to consider. The first and most significant is the instrument measurement uncertainty. We have selected stations using the RS92 sensor only, since it is a high performing and widely used sensor. However, there are uncertainties and biases present that can affect the results presented earlier. Dirksen et al. (2014) provide a detailed overview of the major shortcomings and uncertainties. The temperature sensor design results in a positive bias during the day as the sensor is heated by ambient radiation. The increase in temperature leads to a negative bias in the relative humidity. The humidity sensor, in addition to being affected by the temperature bias, suffers from an additional dry bias from ambient radiation drying the sensor. The average dry bias varies by altitude, between around 30% at 10 km to 50% at 15 km (Dirksen et al., 2014; Miloshevich et al., 2009; Wang et al., 2013; Vömel et al., 2007). Together, these may lead to an underestimate in the PCC, especially at supersonic cruise altitudes. Finally, the humidity sensor has a slow response at cold temperatures (up to approximately

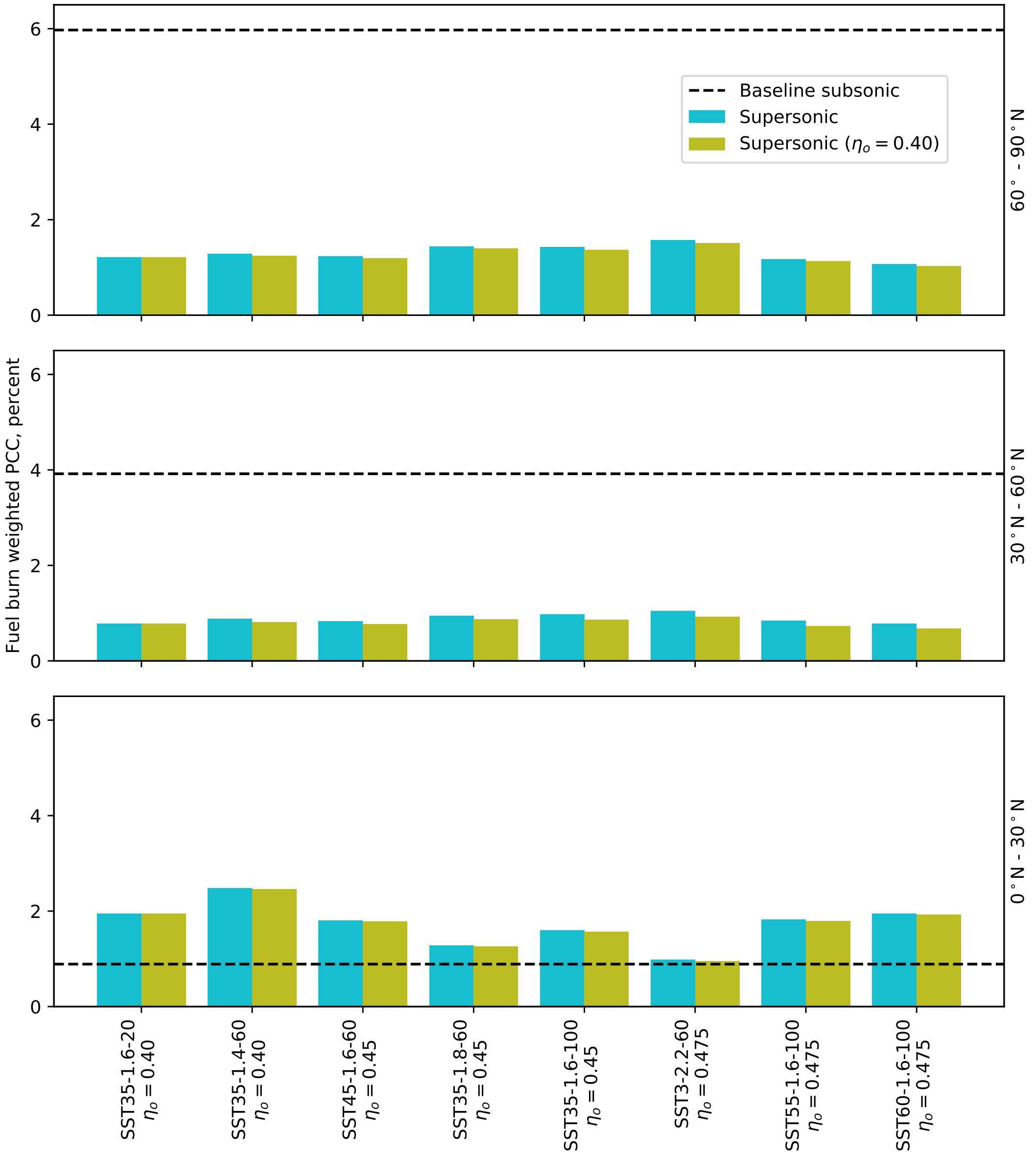

Figure 35: Fuel burn weighted PCC for each nominal SST design separated by latitude band. Proportion of fuel burn in PCC region by latitude band. Colors represent subsonic with replacement (blue), supersonic cases at engine efficiency as in Table 20 and supersonic cases at a fixed efficiency, $\eta_o = 0.40$. Black dashed line represents baseline subsonic result for given latitude band. In each case, the global fuel burn profile is used, but PCC proportions according to each region.

two minutes at −80°C), which can lead to a time lag-associated uncertainty in the humidity, especially at temperatures below −40°C. Since the IGRA data is averaged before storage, we do not expect this to lead to significant biases in our results.

Finally, when statistically analyzing the data, there is a potential for results to be biased due to the differing number of profiles for a given station. An example of this can be seen in comparing the global results in Figure 29 with the results by latitude

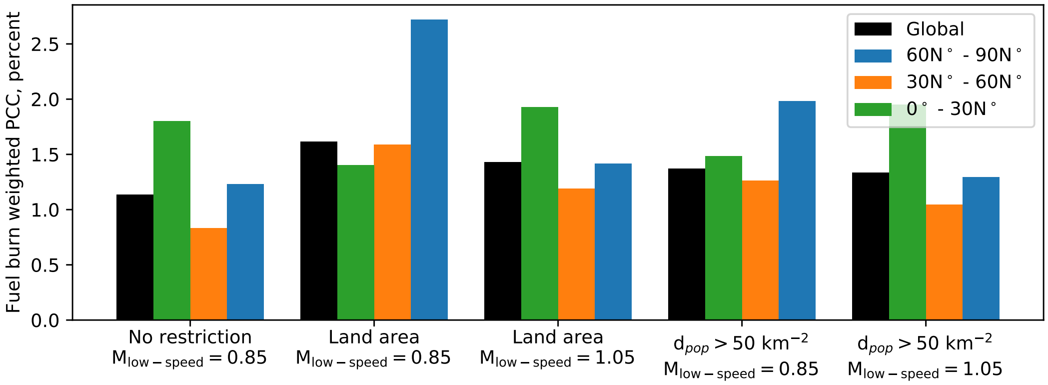

Figure 36: Fuel burn weighted PCC for each overland restriction and low-speed Mach number, separated by latitude band. Percentage of fuel burn in a PCC region by latitude band. Colors represent different latitude bands and each grouping of bars the SST low-speed Mach number or flight restriction.

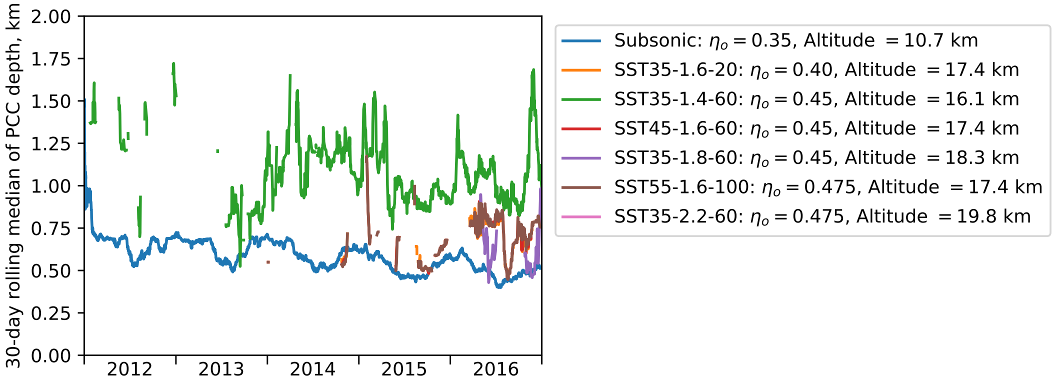

Figure 37: Evolution of PCC depth at the cruise altitude and engine overall efficiency of each nominal SST design. Time series of rolling median PCC depth for each SST aircraft design. Results are presented only if sufficient data are observed.

band in Figure 30. The global results are skewed by the large number of profiles in the northern mid-latitudes. By breaking the data into multiple segments (primarily altitude, season and latitude band), these effects should be avoided, however there could be intra-segment differences between profiles that are not captured. Differences resulting from the changing distribution of stations over time are also not analyzed in this report.

4.4 Synthesis

Our results show that the percentage PCC globally reaches a peak at around 10 km, where the PCC is satisfied approximately 5% of the time. This reduces by a factor of 5.9 at 16 km, the baseline SST cruise altitude studied in this report. There is also a strong latitude-based trend in these results. The altitude of maximum percentage PCC is approximately 4 km higher in the tropics (12.5 km) than in the Arctic (8.5 km). The maximum likelihood of persistent contrail formation, however, decreases

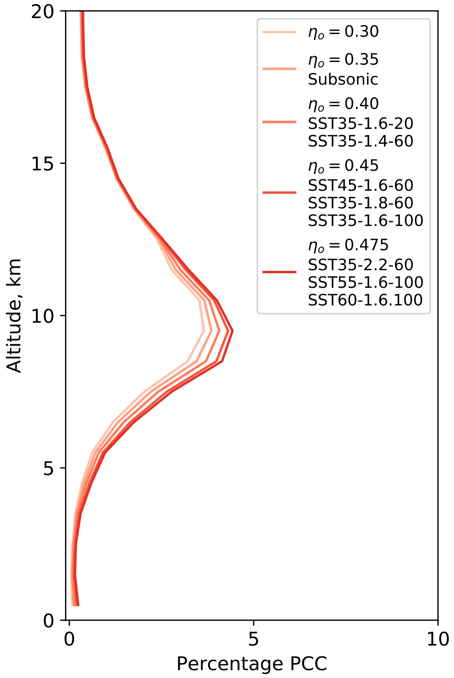

Figure 38: Percentage PCC as a function of altitude at five engine overall efficiencies. The nominal design code is included under the closest matching engine overall efficiency.

by 58% between these regions suggesting that SSTs could lead to contrails in the tropics but at a lower likelihood than subsonic flights in the mid-latitudes and Arctic.

Seasonal trends were also considered and it was found that the maximum PCC proportion occurred at lower altitudes in Northern Hemisphere summer than winter by one to two km. The value of this maximum, however, varies by region. In the tropics, the maximum decreases by more than 50% from northern hemispheric summer to winter, while increasing by 67% and 79% in the mid-latitudes and tropics respectively over the same period.

Finally, we compared across each SST nominal aircraft using the fuel burn weighted PCC. These results showed that the choice of nominal aircraft is highest in the tropics, with a 153% difference between the highest and lowest fuel burn weighted PCC. This difference is due to changes in the supersonic cruise flight altitudes, which control the percentage PCC. We also showed the effect of over-land flight restrictions, which could lead to a higher percentage of the fuel burn in a persistent contrail forming region. This occurs because a higher proportion of over-land supersonic flights happen in the low-speed cruise mode, where the percentage PCC is highest.

Although further work will be needed to produce an comprehensive estimate of contrail coverage due to projected supersonic aviation, these results suggest broadly that supersonic aircraft will produce approximately 96% fewer contrails than subsonic aircraft in the northern mid-latitudes. This difference is driven by the difference in flight altitude—10.5 km for subsonic aircraft and 17.5 km for the baseline supersonic aircraft studied in this report. This result is highly dependent on the latitude of flight activity. For example, supersonic flights in the tropics could lead to 95% more contrails per unit distance flown than subsonic flights.

5 Changes in atmospheric composition and radiative balance

Highlights

- Non-CO_2, non-contrail radiative forcing from a notional Mach 1.6 supersonic aircraft is estimated to be $-20 \times 10^{-3}\,\mathrm{mW\,m^{-2}}$ per billion seat-km flown, compared to a positive forcing of $1.3 \times 10^{-3}\,\mathrm{mW\,m^{-2}}$ per billion seat km for subsonic aviation.
- Higher-altitude flight with a notional Mach 2.2 aircraft results in a net positive radiative forcing, at $26 \times 10^{-3}\,\mathrm{mW\,m^{-2}}$ per billion seat-km flown. This reversal in sign is due to the greater relative increase in the contribution of positive forcing components (e.g. ozone, water vapor) compared to negative forcing components (e.g. aerosols).
- Per seat-km flown, ozone destruction due to the modeled supersonic aircraft fleets is one to two orders of magnitude greater than the ozone production resulting from subsonic aircraft emissions.
- Emissions of sulfur and NO_x contribute around 90% of the ozone destruction due to supersonic aviation. Desulfurizing fuel or using sulfur-free biofuels could reduce ozone loss resulting from Mach 1.6 supersonic aviation by half.

One of the most prominent concerns for supersonic aviation has been, and continues to be, its effects on the ozone layer and the climate. We use global chemistry modeling to estimate how atmospheric composition might change in response to supersonic aviation. We use a global chemistry-transport model (Section 5.1) to simulate how both subsonic and supersonic aviation would affect atmospheric ozone and aerosols and global radiative balance (Section 5.2). We also perform sensitivity analyses to quantify the contribution of different emissions, the effect of methane feedbacks, and variation in response due to different aircraft concepts (Section 5.2.4). More comprehensive sensitivity analyses, including sensitivity of results to the full set of potential aircraft concepts, are conducted in Section 6 using the GEOS-Chem UCX adjoint.

5.1 Simulating the atmospheric response

Estimates of changes in atmospheric composition are obtained by using the GEOS-Chem global atmospheric chemistry-transport model. GEOS-Chem incorporates unified tropospheric and stratospheric chemistry from the surface to the stratopause (Eastham et al., 2014). The model enables estimation of the changes in global atmospheric composition resulting from changes in subsonic or supersonic aviation, as described in Section 2.1.5.

Although the stratospheric extension to GEOS-Chem underwent validation against observations in Eastham et al. (2014), GEOS-Chem has since incorporated additional improvements in its representation of atmospheric chemistry and physics. For this study, we took as our base model GEOS-Chem v11, and implemented further improvements designed to provide a more accurate representation of the impacts of supersonic aviation on parameters such as stratospheric ozone burden, aerosol depth, and the atmospheric radiative balance.

Firstly, we modified the stratospheric aerosol scheme, following Wegner et al. (2013). This scheme allows for the formation of large crystals of nitric acid trihdydrate (NAT) by prescribing a particle number density of 10^{-2} cm^{-3} on the basis of CALIOP observations. The amount of HNO_3 which is partitioned into NAT in any grid cell is also limited to $\leq 20\%$, thereby preventing excessive polar denitrification. Furthermore, we implement a new method to estimate aerosol settling velocities which accounts for the aerosol size distribution (Chen et al., 2013).

Secondly, previous reports on the atmospheric impacts of supersonic aviation have found that water vapor emissions could contribute significantly to overall impacts. As a result, having reliable background water vapor concentrations in the stratosphere is important to ensure that the model delivers valid results. GEOS-Chem prescribes tropospheric concentrations of water vapor to match those in the meteorological product driving the simulation, and permits water vapor concentrations to evolve freely in the stratosphere. However, this results in excessive water vapor entering the stratosphere through the tropical tropopause. As a consequence, the model is prone to gradual buildup of stratospheric water vapor. We therefore implement a prescribed annual cycle for the water vapor mixing ratio at the tropical tropopause. Between 30°S and 30°N, we identify the coldest grid cell below 7.5 hPa in each column. The water vapor mixing ratio at all locations below this cell is reset to the value provided in the meteorological data. The water vapor mixing ratio in the "cold-point" cell is prescribed based on an annual cycle, varying sinusoidally between a minimum of 3.0 ppmv around June 4th, and a maximum of 4.8 ppmv around November 22nd. This approach has been applied previously to provide a stable and realistic oscillation in stratospheric water vapor which recreates the observed "water vapor tape recorder" (McCormack and Siskind, 2002).

Finally, we implemented an option to use methane emissions in place of prescribed near-surface volumetric mixing ratios (VMRs). Fixed surface VMRs facilitate a stable chemical simulation by ensuring that the methane available in the simulation closely matches observational data. This is important given the role that methane plays in promoting tropospheric ozone and as a source for stratospheric water vapor. However, the use of a fixed surface VMR can also act to dampen changes in tropospheric ozone. Although aviation emissions are thought to increase ozone concentrations in the short term, this increase is expected to reduce tropospheric methane concentrations, thereby reducing a global source term for tropospheric ozone. In simulations where the surface methane VMR is prescribed, this feedback cannot occur, since the accelerated methane loss is compensated for by an effective increase in surface emissions of methane. To account for this, we implemented a system where we first perform a "business-as-usual" calibration simulation. This simulation uses a fixed surface VMR for methane, which forces concentrations of methane in the planetary boundary layer to match a reference concentration. At each time step, the effective methane flux resulting from enforcement of the boundary condition is archived, aggregated zonally into four equal-area latitude bands: 90°S–30°S, 30°S–0°, 0°–30°N, and 30°N–90°N. Monthly averages of these emissions are then taken and stored for use in future simulations in place of a forced surface VMR. This enables the effects of long-term methane feedbacks to be quantified.

Meteorological input data are supplied by the Modern Era Retrospective analysis for Research and Applications (MERRA). To allow for inter-annual variability, simulations are run for 28 model years, repeating the 14-year record of meteorological data for January 1, 2000 to December 31, 2014. To accomplish this, the output from the end of December 31, 2014 from the first pass through is used to re-initialize the second simulation on January 1, 2000.

5.1.1 Evaluation of the GEOS-Chem UCX model

In light of the newly implemented functionality for GEOS-Chem, we establish the accuracy and limitations of the GEOS-Chem UCX model for simulating the atmospheric impacts of supersonic aviation by first assessing its ability to represent the historical atmosphere.

For validation, we compare our results from GEOS-Chem simulations of year-2000 to year-2014 (using historical emissions) to observations of multiple species from the Ozone Monitoring Instrument (OMI) and Microwave Limb Sounder (MLS) instruments aboard the NASA Aura sun-synchronous, low Earth orbit satellite. MLS takes vertically-resolved observations under both day and night conditions, while OMI takes full column measurements once per day during daylight conditions. Unless otherwise noted, comparisons to MLS data are shown using average of day- and night-time observations. Data processing and interpretation is performed based on the most recent available recommendations from the MLS team (Livesey et al., 2020).

In particular, we show data only over the range of altitudes in which MLS observations are recommended for scientific use. MLS and GEOS-Chem estimates are shown on their native vertical grids, averaged over each season and over a full year. All seasonal data are for the target year only, with the exception of winter (DJF) which is the average of December 2005 to February 2006. The annual average is taken from December 2005 to November 2006, inclusive. When differences are shown, this is after remapping the GEOS-Chem data to the MLS vertical coordinate, applying pressure weighting.

We first evaluate typical transport-relevant constituents—nitrous oxide (N_2O) and water vapor (H_2O). Figure 39 shows the comparison between GEOS-Chem and the MLS for N_2O in 2006. The vertical gradient approximately overlaps, with N_2O mixing ratios falling from a background tropospheric value of around 300 ppbv to almost zero at a 45 km altitude. MLS N_2O observations are known to have a high bias below 20 km, so we assume the high gradient of MLS-observed N_2O across the 20 km boundary to be an artifact. Therefore GEOS-Chem's lower stratospheric N_2O is biased high by 10% across all seasons. This bias is near zero in the tropics and rises towards the poles. In contrast, at higher altitudes, GEOS-Chem is biased low, reaching a maximum annual average bias of 10% at altitudes of 30–35 km.

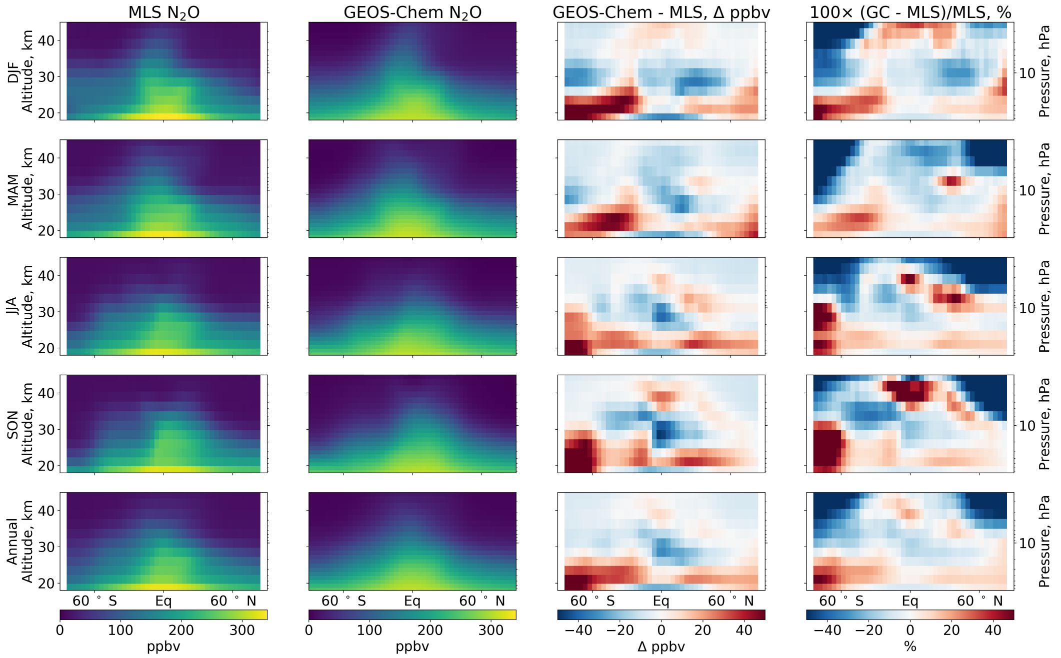

Figure 39: Comparison of GEOS-Chem's estimate of N_2O concentrations to observations from MLS. Each row shows a different time period from December 2005 through November 2006. From left to right: observed N_2O from MLS; estimated N_2O from GEOS-Chem; the absolute difference between the two, after remapping GEOS-Chem data to MLS pressure levels; percentage difference of GEOS-Chem relative to MLS.

These biases are likely due to two factors. Firstly, the MERRA-1 fields used in this study have previously been shown to produce high estimates of the age of air in the mid- and upper-stratosphere when compared to other meteorological reanalyses (Chabrillat et al., 2018). Simultaneously, the horizontal resolution used for this work ($4° \times 5°$) is 8× lower than the resolution at which MERRA-1 was originally produced, and the associated averaging will dampen vertical transport. The combination of these two factors is expected to result in a reduction in vertical transport and excessive horizontal transport in the lower stratosphere, as the upper branches of the Brewer-Dobson circulation are "short-circuited".

The transport biases described above are also visible when comparing simulated water vapor (H_2O) to observations (Figure 40). As in the case of N_2O, biases are small near the tropical tropopause, albeit of mixed sign. This is in part due to the simplified boundary condition which we now apply in this region. However, GEOS-Chem's estimate of mid- and upper-stratospheric water vapor are biased low by up to 20%, averaged over the year.

A possible cause for the lower bias at higher altitudes is the simulation of transport. We simulate horizontal gradients in water vapor in GEOS-Chem than is observed in the MLS data, suggesting excessive horizontal mixing and weak vertical transport. However, the error in vertical gradient appears to be greater for H_2O than is the case for N_2O. This could be due to insufficient methane reaching the

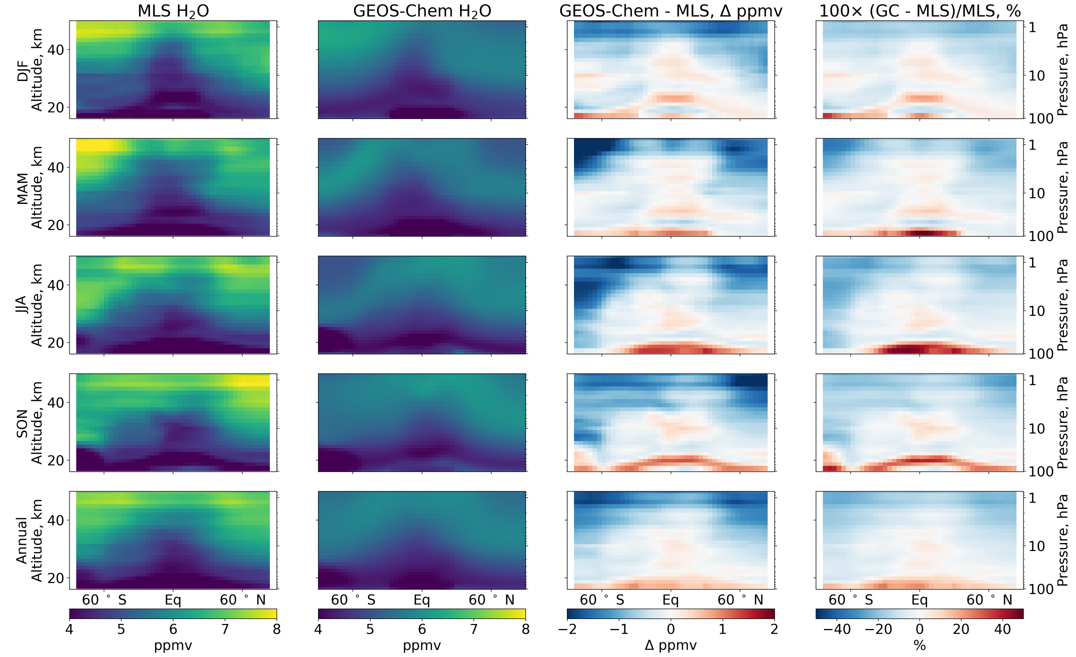

Figure 40: Comparison of GEOS-Chem's estimate of water vapor concentrations to observations from MLS. Layout is the same as in Figure 39.

mid- and upper-stratosphere, resulting in too little water being produced from water oxidation.

Figures 41 and 42 show the same plots for nitric and hydrochloric acid (HNO_3 and HCl), respectively. Errors in the former are inversely correlated with errors in N_2O, as expected based on the ability of the UCX to reproduce tracer-tracer correlations in the stratosphere (Eastham et al., 2014). Seasonal variations in the relative concentrations of HNO_3 at the North and South Pole are reproduced by GEOS-Chem, as is the presence of high concentrations of gas-phase HNO_3 over the South pole in austral winter. However, denitrification in the Antarctic spring is not well captured. Sensitivity simulations performed with the previous representation of nitric acid trihydrate (NAT) formation were better able to reproduce the observed denitrification. The new approach limits NAT formation to 20% of available HNO_3 and characterizes NAT as being made up of large "NAT rocks". Although this will compromise the representation of Antarctic ozone depletion, it is not expected to significantly degrade the simulation of the stratosphere elsewhere.

Similarly, the simulation of HCl also shows weaker horizontal gradients than are observed by MLS. Simulated HCl is positively biased in the tropical lower stratosphere but negatively biased elsewhere in the stratosphere. Simulated ClO is also biased low (not shown) by 10–20% throughout the stratosphere. This may reflect inaccurate CFC boundary conditions.

Finally, Figure 43 shows the comparison of GEOS-Chem's ozone simulation to MLS. The same transport errors which affected the prior species will also affect ozone.

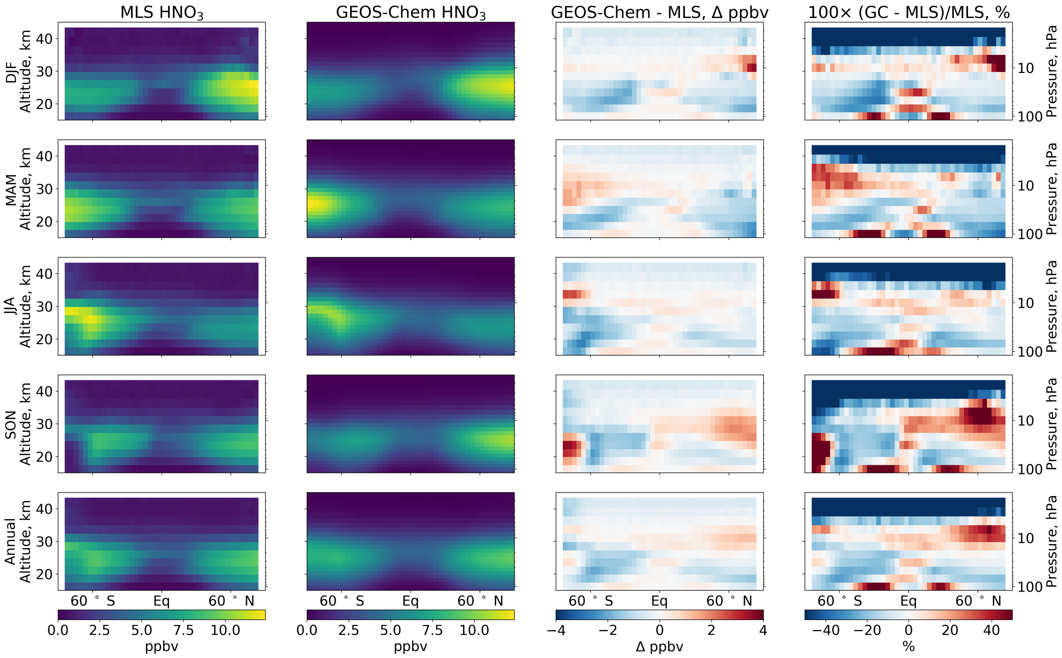

Figure 41: Comparison of GEOS-Chem's estimate of gas-phase nitric acid (HNO_3) concentrations to observations from MLS. Layout is the same as in Figure 39.

This is likely part of the reason for the negative bias (5%) in mid-stratospheric ozone across all seasons. We also observe high bias in tropical lower-stratospheric ozone. Percentage biases in this region are high, in part due to the high vertical gradients in ozone in this region.

Considering instead the total column, Figure 44 shows the daily mean total ozone column as measured by the Ozone Monitoring Instrument (OMI) aboard the Aqua satellite, and as estimated by GEOS-Chem. The bias in simulated column ozone varies in sign by latitude, with a positive bias in the tropics and high Southern latitudes but a negative bias at high northern latitudes. We also find that, while there is significant ozone depletion during Antarctic winter which is captured by GEOS-Chem, this depletion is smaller than in the observed column, resulting in a bias of up to +50%.

5.1.2 Experimental design

We use the GEOS-Chem UCX to simulate conditions in 2035 with and without supersonic aviation. We assume that global anthropogenic non-aviation emissions are consistent with RCP 4.5 for 2035. We also assume that the fixed surface volumetric mixing ratio boundary conditions for CFCs and other long-lived species are consistent with the RCP 4.5 projection for 2035, with the exception of methane which we discuss in more detail below.

For natural emissions, we use standard GEOS-Chem inventories. This includes the online calculation of emissions of lightning NO_x (Murray et al., 2012), dust

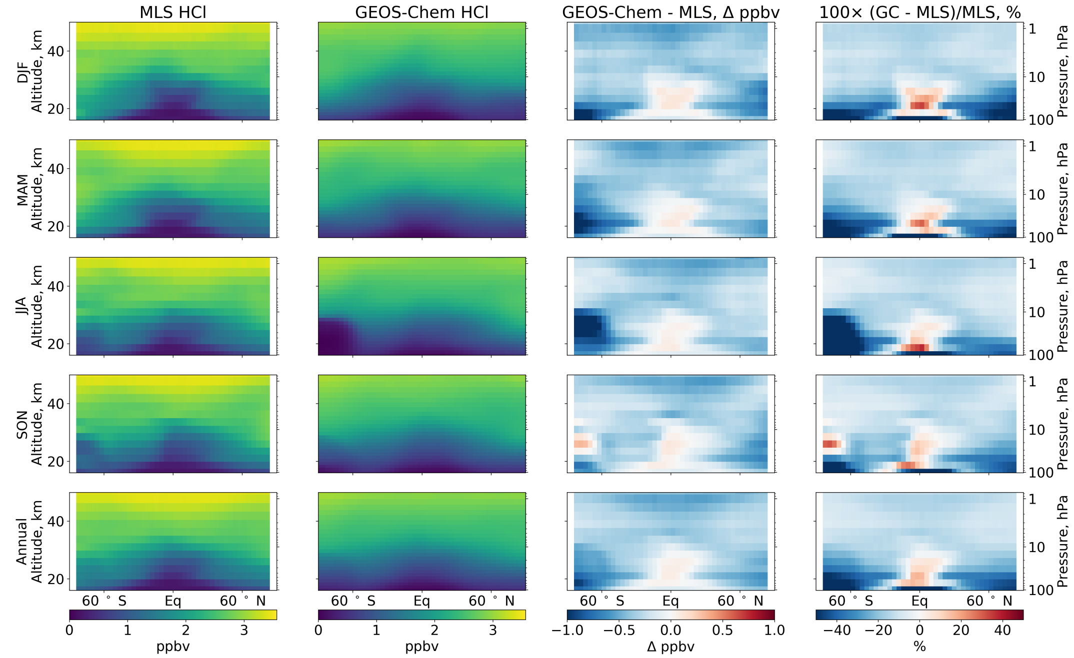

Figure 42: Comparison of GEOS-Chem's estimate of HCl concentrations to observations from MLS. Layout is the same as in Figure 39.

via the DEAD scheme (Fairlie et al., 2007), biogenic species through the MEGAN model (Guenther et al., 2012), sea salt (Jaeglé et al., 2011), and soil NO_x (Hudman et al., 2012). Volcanic emissions are disabled, likely increasing the sensitivity of stratospheric ozone to sulfur emissions (Weisenstein et al., 1996). We use 14 years of meteorological data from MERRA-1 covering the period January 1, 2000 through December 31, 2013 which allows us to reduce the effects of inter-annual variability. Methane emissions are estimated in a single calibrating run, for which a fixed surface volumetric mixing ratio of 1835 ppbv was used. All results are then calculated using a methane flux boundary condition which is consistent across all simulations unless otherwise stated. This means that methane feedbacks on atmospheric ozone are captured. These feedbacks are quantified separately alongside other sensitivity analyses in Sections 5.2.2 and 5.2.4.

In each scenario, aviation emissions are updated once per month. The underlying Aircraft Emissions Inventory Code (AEIC) model (Simone et al., 2013) is used to estimate total fuel burn and emissions of NO_x, CO, and unburned hydrocarbons. SO_2 and H_2SO_4 aerosol emissions are calculated by assuming 600 parts sulfur per million parts fuel, by mass, and a 2% conversion rate of SO_2 to H_2SO_4 before the exhaust plume expands to grid scale. Water vapor emissions are estimated using a factor of 1.321 kg H_2O per kg of fuel burned. Emissions of black and organic carbon (BC and OC) are calculated differently for sub- and supersonic aviation. Subsonic BC emissions are estimated using the FOX model (Stettler et al., 2013), and a constant emissions index of $20\,\mathrm{mg\,kg^{-1}}$ is used for OC. For supersonic emissions, we assume

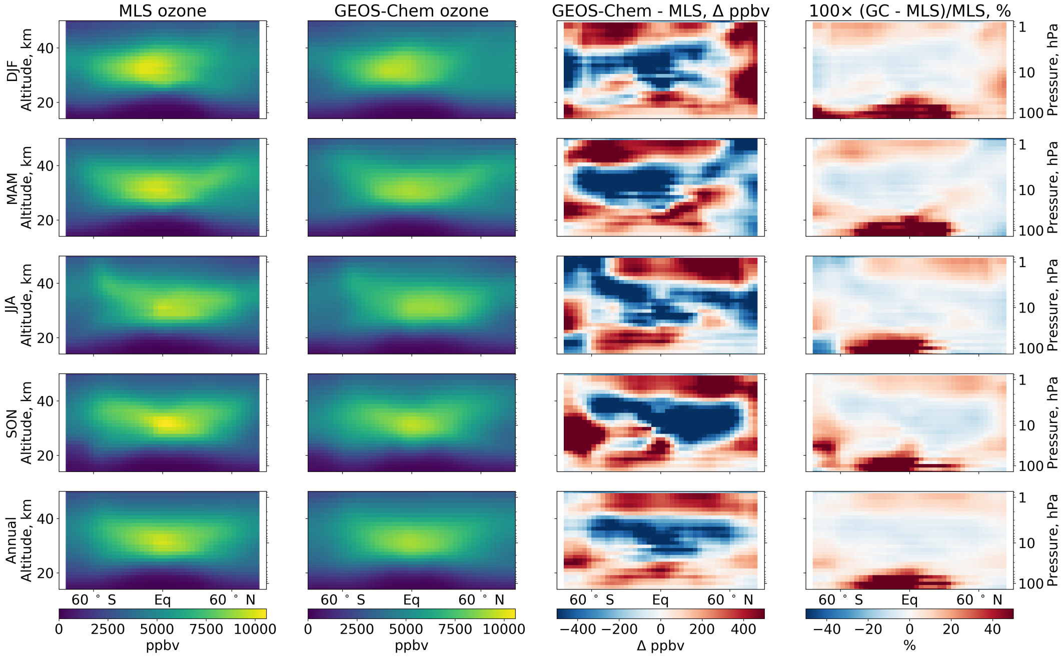

Figure 43: Comparison of GEOS-Chem's estimate of ozone concentrations to observations from MLS. Layout is the same as in Figure 39.

constant emissions indices of 30 mg kg^{-1} for both BC and OC. Further details on these assumptions are given in Section 2.1.5.

For the majority of this analysis, we focus on two scenarios. The first is a "business-as-usual" subsonic aviation scenario, in which year-2015 subsonic aviation is projected forward to 2035 as described in Section 2. This results in 19 trillion seat-km of flight by subsonic aircraft, requiring 420 Tg of fuel burn and emitting 6.5 Tg of NO_x (on an NO_2 mass basis). Impacts on atmospheric composition and radiative forcing are calculated by subtracting the results of a simulation with no aviation emissions.

Here, we aim to provide quantitative information regarding the relative impacts of different design and regulatory choices for supersonic aircraft. However, it is prohibitively computationally expensive to explicitly simulate all possible scenarios, even when considering only those shown in Section 2. We therefore focus our analysis on a "central" scenario, corresponding to aircraft design SST45-1.6-60 (range 4,500 nmi, cruise speed of Mach 1.6, with 60 seats). This design has a mean cruise altitude of around 16 km. Impacts from supersonic aviation are calculated by subtracting the results of a simulation that includes aviation-related emissions from only the subsonic aircraft in this scenario, such that the impacts calculated for supersonic aircraft are only those resulting from supersonic flights. This means that changes in subsonic aviation due to the inclusion of supersonic aircraft, while they affect the background conditions under which supersonic aviation operates, are not included in the reported effect of supersonic flights.

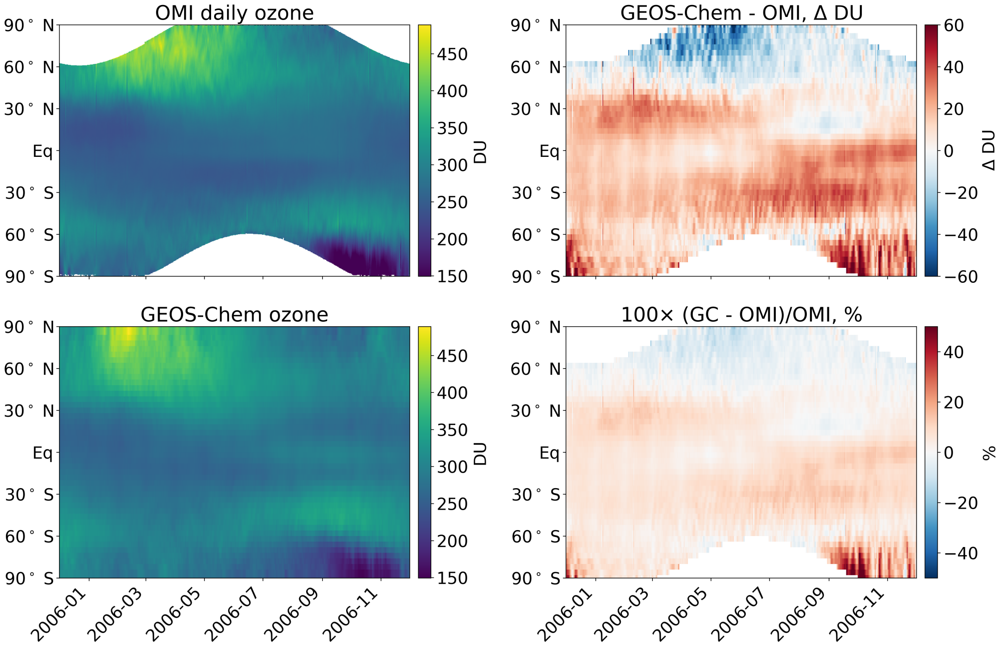

Figure 44: Comparison of GEOS-Chem's estimate of total ozone column concentrations to observations from OMI. Lower left: GEOS-Chem daily column ozone, averaged over all longitudes for 2005-12-01 to 2006-12-01, in 4° latitude bands (model resolution). Upper-left: OMI daily column ozone, averaged over all longitudes for the same period, in 1° latitude bands. Upper right: the difference between GEOS-Chem and OMI, after regridding OMI data to the GEOS-Chem model resolution. Lower right: as before, but now in percentage terms relative to the OMI observations.

Section 5.2 quantifies changes in ozone and aerosols in these two scenarios, while Section 5.2.2 quantifies the associated radiative forcing. Finally, Section 5.2.4 decomposes these impacts based on the contribution of different emissions, as well as performing sensitivity analysis regarding the effect of changing the notional aircraft design Mach number and the role of methane feedbacks. Broader sensitivity analysis is performed in Section 6 using the GEOS-Chem UCX adjoint.

Our analysis of impacts is divided into two sections: changes in atmospheric composition (Section 5.2), and the radiative forcing associated with aviation (Section 5.2.2). In each Section, we first analyze the impacts of subsonic aviation in 2035. This is followed by analysis of the central supersonic case (SST45-1.6-60), followed by limited sensitivity analysis to quantify the contribution of black carbon, NO_x, sulfur, and water vapor emissions to the impacts in the central case. We also compare the results when using an aircraft design with a higher cruise Mach number of 2.2 compared to the baseline 1.6. A more detailed sensitivity analysis is given in Section 6.3.2 using linearized sensitivities from the UCX adjoint. Finally, we also compare the results from simulated aviation when ignoring or including methane feedbacks, as detailed in the opening to Section 5.2.

5.2 Results

We first evaluate the effect of subsonic aviation in 2035, to provide a baseline for evaluation of the potential impacts of supersonic aviation. As described in Section 2 our baseline subsonic aviation scenario includes 420 Tg of fuel burn, resulting in 19 trillion seat-km of travel. The distribution by latitude and altitude is not significantly different from aviation in the 2000s and early 2010s, but global fuel burn and NO_x emissions are 2.4 times greater than year-2005 values (Simone et al., 2013).

When comparing cases and designs, we present results in terms of the change due to aviation emissions "per billion seat-km traveled" thereby normalizing all impacts per unit of output produced (see Section 2.4). The resulting metrics are presented alongside total impact metrics and the impacts normalized per unit of fuel burn if useful. Unless otherwise stated, all results are shown in terms of the long-term impact. This means that we average over the last fourteen years of a 28-year simulation, allowing us to capture inter-annual variability.

5.2.1 Changes in ozone and aerosols

Figure 45 shows the change in column ozone by latitude and time of year in each scenario. In absolute terms, subsonic aviation results in an average of 0.061 mDU of ozone per billion seat-km, or an increase of 1100 mDU (i.e. 1.1 DU) in total ozone for the year 2035. This corresponds to a 0.37% increase in global mean ozone for the year, or 580 mDU per Tg of N emitted as NO_x. This is a lower sensitivity than found by (for example) Köhler et al. (2008), who found that 0.68 Tg of aviation N emitted as NO_x resulted in a 820 mDU increase in global column ozone. However, our calculation includes the contribution of aviation sulfur, whereas the study by Köhler et al. (2008) considered aviation NO_x only. Our approach also includes methane feedbacks which significantly reduce the net production of ozone due to aviation (see Section 5.2.4).

The increase in column ozone due to subsonic aviation varies by latitude and time of year, but the largest distinction is between the Northern and Southern Hemispheres. In the Northern Hemisphere, column ozone increases by an average of 0.096 mDU per billion seat-km traveled globally, compared to 0.025 mDU in the Southern Hemisphere.

Whereas aviation emissions yield an increase in column ozone, emissions from supersonic aviation (design SST45-1.6-60) result in decreases in ozone for all seasons and latitudes. The global mean ozone column is reduced by 140 mDU due to supersonic aircraft emissions, or 12% of the increase resulting from subsonic aviation emissions. However, per billion seat-km traveled, supersonic aircraft emissions result in 0.85 mDU of ozone loss, a factor of 14 greater in magnitude than the increase (per billion seat-km) resulting from subsonic aviation emissions. This is in spite of the lower simulated NO_x emissions index used for some supersonic aircraft considered in this study relative to the subsonic fleet. Northern Hemisphere impacts are 2.0 times those in the Southern Hemisphere, lower than the factor of 3.9 for subsonic aviation.

These changes in column ozone are caused by the different sensitivities of column ozone to NO_x emissions at different altitudes. Figure 46 shows the zonal mean

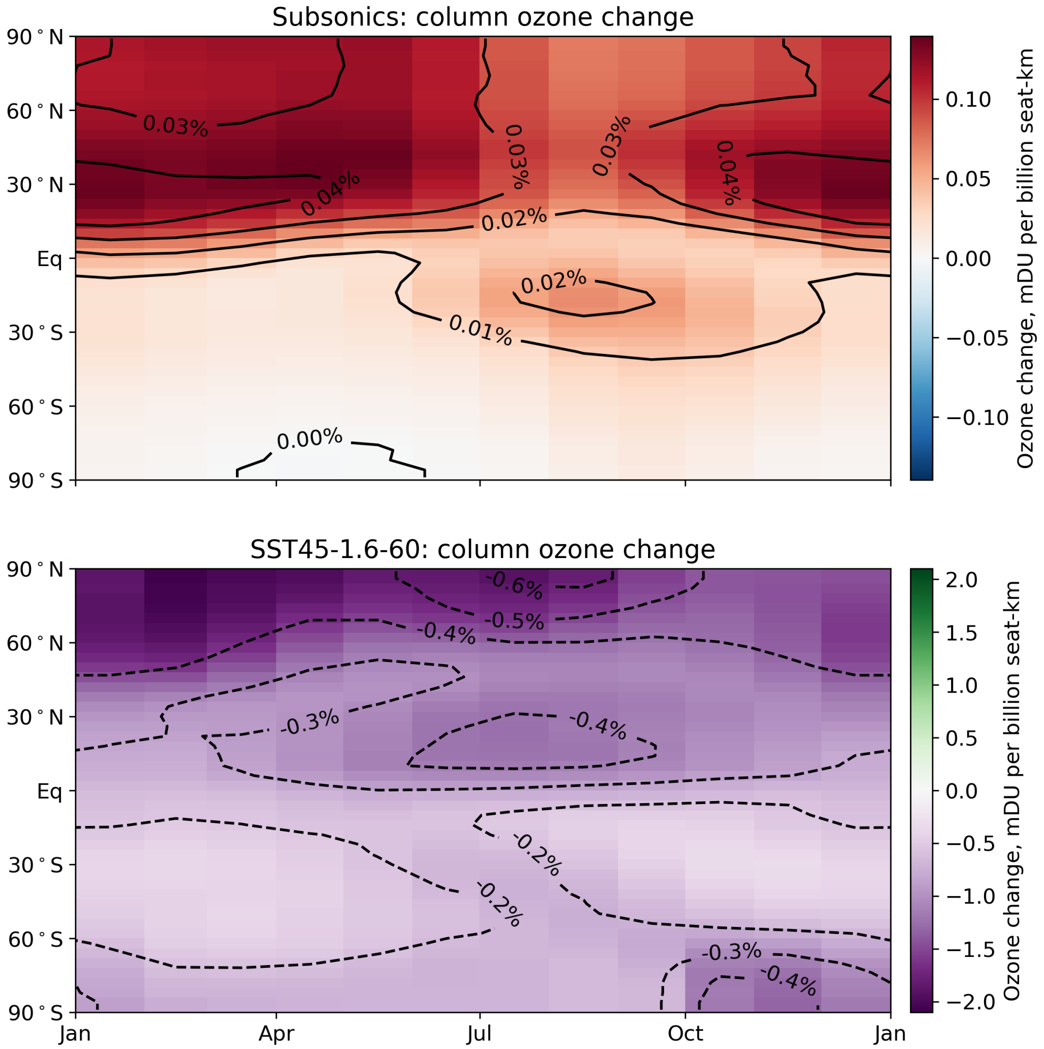

Figure 45: Changes in column ozone attributable to aviation, averaged over the last fourteen years of simulation. Upper panel: changes due to subsonic aviation in 2035. Lower panel: changes due to supersonic aviation with the SST45-1.6-60. Color is used to indicate the change per billion seat-km traveled. Contours show the percentage change in ozone relative to a baseline (no-aviation) scenario per billion seat-km. Different color maps are used to indicate different scales.

response of ozone volumetric mixing ratios to aviation emissions. Subsonic aircraft emissions result in an increase in tropospheric ozone concentrations, with the greatest absolute increases occurring near cruise altitudes between 30 and 90°N. The relative increase is greater at lower altitudes, reaching a maximum in the descending branch of the Hadley cell.

In the stratosphere, the sign of the ozone response is mixed. At lower altitudes (up to 20–25 km) the overall response is an increase in ozone, due to typical tropospheric NO_x-VOC chemistry. However, at higher altitudes, the sign is negative, as catalytic ozone destruction reactions begin to dominate. Although this is 10 or more kilometers above cruise altitude for subsonic aviation, a small fraction of the exhaust products reaches these altitudes, causing ozone depletion. The more symmetrical pattern of ozone loss in the stratosphere is likely because aviation-attributable NO_x and SO_x are being injected into the stratosphere in the tropics, from which they spread equally North and South through the Brewer-Dobson circulation. However, due to the low air densities at these altitudes relative to the troposphere, the change in ozone column shown in Figure 45 due to subsonic aviation is dominated by the lower-altitude increases in ozone.

The zonal pattern in ozone change due to supersonic emissions is instead dominated by ozone destruction in the mid-stratosphere. For SST45-1.6-60, the typical cruise altitude is approximately 17 km (see Table 2). This results in a significant fraction of cruise-altitude emissions being re-injected into the tropical stratosphere. These emissions result in depletion of zonal mean tropical stratospheric ozone of up to 0.69×10^{-3} ppbv per billion seat-km. However, this is a small relative change. In this region, background ozone concentrations are of the order of several thousand ppbv.

Due to the larger magnitude of stratospheric ozone depletion and smaller magnitude of tropospheric ozone production from supersonic aviation compared to subsonic aviation, the change in column ozone is instead negative. The dominance of the stratospheric signal is visible in Figure 45. The greatest impact of subsonic emissions on column ozone is at northern mid-latitudes, near to the emissions themselves. The reduction in column ozone due to supersonic emissions is more diffuse, and spread more evenly over the northern extratropics. In this case, the impacts of advected NO_x and SO_x have accumulated. The relative contribution of NO_x and SO_x is explored in more detail in Section 5.2.4, and more broadly in Section 6.

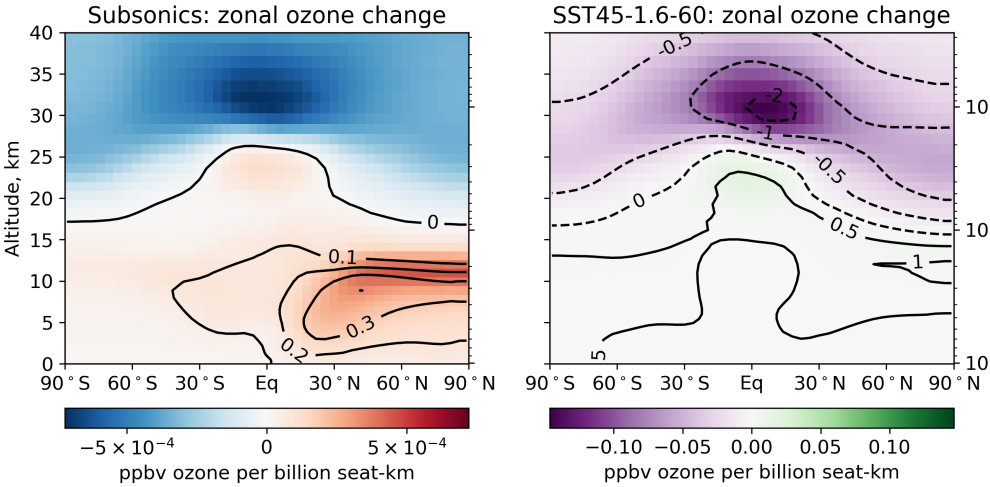

Figure 46: Changes in zonal mean ozone due to aviation, averaged over the last four years of simulation. Left: changes due to subsonic aviation in 2035. Right: changes due to supersonic aviation, using the SST45-1.6-60 design. Color is used to indicate the change per billion seat-km traveled. Contours show the change in ozone relative to a baseline (no-aviation) scenario, in thousandths of a percent per billion seat-km traveled. Different color maps are used to indicate the different scales in use.

Finally, Figure 47 shows the effect of subsonic and supersonic aviation emissions on black carbon aerosol optical depth. Black carbon has no chemical sources, and thus serves as a useful tracer of transport and deposition processes. In the case of subsonic aviation, the area-weighted mean increase in optical depth in the Northern Hemisphere is 2.2×10^{-9} per billion seat-km traveled. There are also sharp changes in optical depth associated with geographical features such as the Himalayas, and the change in the Northern Hemisphere is 3.1 times that in the Southern Hemisphere.

The pattern for supersonic aviation is again different, with supersonic aviation resulting in 20 times larger changes in optical depth in the Northern Hemisphere (per seat-km traveled) than subsonic aviation. This is due to the longer lifetime of black carbon in the stratosphere. In addition, we observe a clear North-South divide for black carbon aerosol optical depth resulting from supersonic aviation. Whereas clear geographic features are visible for changes due to subsonic aviation, for supersonic aviation, the coverage is much more homogeneous. However, the Northern Hemisphere changes are still a factor of 2.5 greater than in the Southern Hemisphere. This is within 27% of the factor for column ozone changes from this design, in spite of a different spatial pattern. We know that soluble gases and aerosols are removed efficiently by wet scavenging, whereas ozone and NO_x are not. As such, the majority of the emitted black carbon will be scavenged after it enters the tropopause and before it can be reinjected into the stratosphere through upwelling motions in the tropics, whereas the same would not be true for ozone and NO_x. The similarity in spatial pattern for SST45-1.6-60's changes in ozone and black carbon therefore hint at the dominant factors in ozone loss, as will be discussed in detailed in Sections 5.2.4.3 and 6.3.

For the scenario evaluated here, the effect of subsonic aviation on global column ozone is still 8.3 times greater in magnitude than from supersonic aviation in 2035. However, per seat-km traveled, supersonic aviation causes changes in column ozone which are 14 times as great in magnitude as for subsonic aviation. We also observe that, whereas subsonic aviation causes an increase in northern hemispheric ozone, supersonic aviation decreases ozone at all latitudes. This implies the possibility of an "ozone-neutral‘' cruise altitude. At this altitude, increases in tropospheric and lower-stratospheric ozone would be equaled by decreases in mid-stratospheric ozone, at least on average and in terms of the overall ozone column. This possibility is explored in more detail in Section 6.

5.2.2 Radiative forcing

We quantify the changes in radiative forcing (RF) associated with subsonic and supersonic aviation emissions. RF calculations are performed using the Rapid Radiative Transfer Model for Global simulations (RRTMG) code incorporated into GEOS-Chem (Heald et al., 2014). This code was extended to calculate the contribution of atmospheric water vapor and methane to changes in longwave and shortwave radiation. We modified RRTMG to output radiative fluxes at the tropopause.

Radiative transfer is simulated for the first day of each month in years 11 to 14 of each simulation. This restricted range of years is used because of computational constraints. We then average across the resulting 48 samples to derive an estimate of

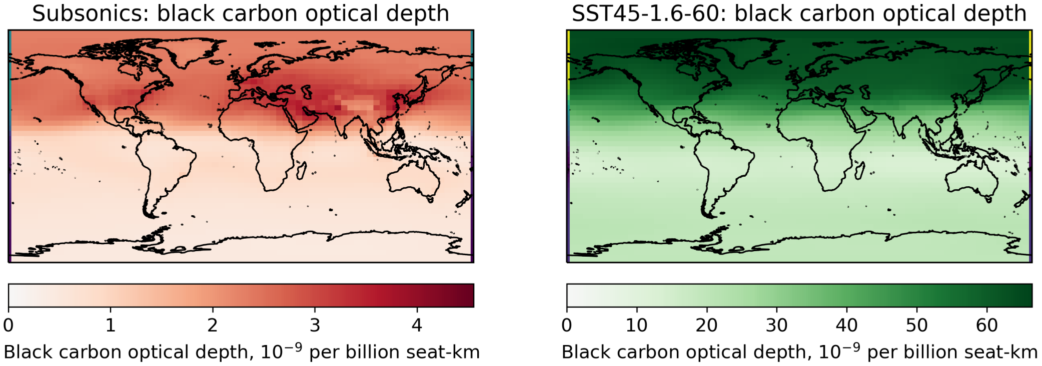

Figure 47: Changes in column total black carbon aerosol optical depth due to aviation, averaged over the last fourteen years of simulation. Left: changes due to subsonic aviation in 2035. Right: changes due to supersonic aviation, using the SST45-1.6-60 design. Changes are per billion seat-km traveled.

annual mean radiative forcing. Unless otherwise stated, all RF values are calculated with "stratospheric adjustment" which allows stratospheric temperatures to reach radiative equilibrium using a fixed dynamical heating assumption (Fels et al., 1980). This is accomplished by archiving longwave and shortwave heating rates for each time step in a reference simulation with no supersonic aviation and 2035-projected subsonic aviation. For all other simulations, the longwave and shortwave heating rate is calculated for every stratospheric grid cell during the radiative transfer calculation, and the radiative heating from the reference simulation is subtracted. Assuming that dynamical heating is unchanged between the two simulations, this yields a net heating rate. As long as the magnitude of this heating rate is greater than 1.0 mK/day, the temperature adjustment is integrated forward in time using a Runge-Kutta 4th order approach. During this adjustment process only changes in longwave fluxes and heating are calculated, as shortwave RF is relatively insensitive to temperature and its recalculation would incur significant additional computational expense (Maycock et al., 2011).

The stratospheric temperature adjustment process is performed while incorporating all atmospheric constituents. The contribution of each constituent to the resulting longwave and shortwave fluxes is calculated as the difference in flux which results when excluding that constituent from all calculations. During these single-component evaluations, stratospheric temperatures are not readjusted. RFs are then calculated as the difference in this single-constituent contribution between a two simulations (e.g. with and without subsonic aviation).

Figure 48 shows how aerosol, ozone, and methane contribute to RF per seat-km, with and without long-term (decadal-scale) methane feedbacks. Contrail impacts are not shown, since they are discussed separately in Section 4. RF due to carbon dioxide is not quantified, as it will occur on a much longer timescale than these other components and will scale with total fuel burn. For reference, the subsonic fleet in 2035 is projected to burn 0.023 kg of fuel per seat-km, compared to 0.12 kg per seat-km for the SST45-1.6-60 notional aircraft supersonic fleet.

We focus our discussion on RFs calculated when including methane feedbacks,

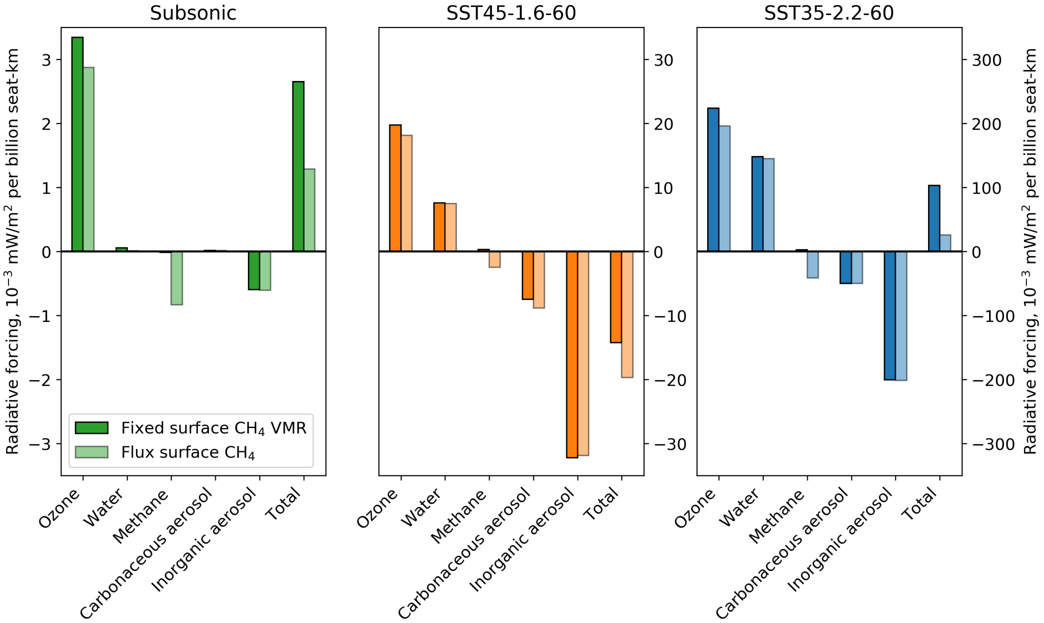

Figure 48: Radiative forcing per seat-km, averaged over a four-year period from simulation years 11–14. Changes are in mW/m^2 per billion seat-km traveled. Different vertical scales are used for each chart due to the different orders of magnitude. Darker bars show the RF evaluated when excluding methane feedbacks. Lighter bars show the RF when including methane feedbacks. The "methane" bar corresponds to the RF resulting from changes in methane concentrations.

using the case without feedbacks to explain the effect of methane.

For subsonic aviation, ozone is the dominant contributor to the overall non-CO_2 impact, resulting in ozone-attributable RF impacts of $2.9 \times 10^{-3}\,\mathrm{mW\,m^{-2}}$ per billion seat-km traveled. This includes a 14% reduction in ozone's effects due to long-term methane feedbacks. This feedback occurs because the increased ozone resulting from aviation NO_x emissions results in faster depletion of atmospheric methane, which is itself a source of ozone. This negative feedback reduces the amount of ozone which forms as a consequence of aviation, and therefore the ozone-related radiative forcing. Since methane is itself a greenhouse gas, the depletion of methane resulting from aviation emissions provides an additional direct negative radiative forcing of $0.83 \times 10^{-3}\,\mathrm{mW\,m^{-2}}$ per billion seat-km traveled. This is accompanied by a $0.61 \times 10^{-3}\,\mathrm{mW\,m^{-2}}$ negative forcing per billion seat-km from inorganic (sulfate, nitrate, and ammonium-based) aerosol.

Combined, we find a net positive RF of $1.3 \times 10^{-3}\,\mathrm{mW\,m^{-2}}$ per billion seat-km traveled, 52% lower than if methane feedbacks are neglected (including both the reduction in ozone and the direct methane forcing). Recalculating this impact without including stratospheric adjustment has a negligible effect. Calculating the change in fluxes at the top of the atmosphere reduces this by $0.36 \times 10^{-3}\,\mathrm{mW\,m^{-2}}$ per billion seat-km as the absorption of shortwave radiation in the stratosphere is then counted as a positive radiative forcing. In this context, the presence of additional carbonaceous aerosol also results in a small additional positive radiative forcing of $0.35 \times 10^{-3}\,\mathrm{mW\,m^{-2}}$ per billion seat-km traveled.

The response to supersonic aviation with the lower-altitude (SST45-1.6-60) supersonic notional aircraft is different in magnitude and composition. Ozone RF remains a large component, resulting in $18 \times 10^{-3}\,\mathrm{mW\,m^{-2}}$ per billion seat-km, or 6.3 times the ozone-attributable radiative forcing per seat-km resulting from subsonic aviation. Water vapor, accumulating in the stratosphere as a direct consequence of emission from supersonic aircraft, contributes an additional $7.5 \times 10^{-3}\,\mathrm{mW\,m^{-2}}$ per billion seat-km. However, the combined positive forcing from ozone and water vapor are exceeded in magnitude by a negative RF at $41 \times 10^{-3}\,\mathrm{mW\,m^{-2}}$ from carbonaceous and inorganic aerosol which absorb and scatter downwelling shortwave radiation, respectively. The net result is a (non-CO_2) RF of $-20 \times 10^{-3}\,\mathrm{mW\,m^{-2}}$ per billion seat-km traveled due to supersonic aviation. This includes the effect of long-term methane feedbacks, which reduce ozone-related radiative forcing by 8.1% compared to a case in which methane feedbacks are not simulated. The direct methane radiative forcing is $-2.4 \times 10^{-3}\,\mathrm{mW\,m^{-2}}$ per billion seat-km traveled, or around 12% of the total net forcing.

Comparing by component, the response to higher-altitude supersonic aviation (SST35-2.2-60) is larger. The trends are the same as for the lower-altitude design, with ozone and water vapor having positive impacts on radiative forcing, and aerosols contributing negative radiative forcings. However, water vapor contributes a larger fraction of the positive forcing, providing 43% of the positive signal, compared to 29% in the case of SST45-1.6-60. The magnitude of the forcing from each component is also an order of magnitude greater per seat-km traveled. This is partially due to the lower fuel efficiency of the SST35-2.2-60 design, which burns 2.2 times as much fuel per seat-km as the SST45-1.6-60 design. However, the remaining difference is the result of different atmospheric sensitivities. Finally, the increase in ozone and water vapor RF for the higher-altitude emissions exceeds the increase in negative RF due to aerosol, resulting in a net positive, rather than negative, radiative forcing.

If methane feedbacks are neglected (green bars), the result is $100 \times 10^{-3}\,\mathrm{mW\,m^{-2}}$ per billion seat-km traveled. However, comparing between the three plots, inclusion of methane feedbacks has the largest effect on net radiative forcing for SST35-2.2-60. This is not because the effects of methane are themselves large. The negative radiative forcing resulting from methane feedbacks, and the reduction in ozone-related positive radiative forcing, are each several times smaller than the contribution from water vapor or inorganic (mostly sulfate) aerosols. However, because the net RF is the result of a large positive component being mostly canceled by a large negative component, the additional negative forcing due to methane feedbacks reduces the net RF to $26 \times 10^{-3}\,\mathrm{mW\,m^{-2}}$ per billion seat-km. This is 25% of the value when excluding methane feedbacks, and similar to the value for the lower-altitude SST45-1.6-60 notional aircraft.

5.2.3 Other contributions to radiative forcing

The results discussed in the previous section do not include two components of radiative forcing which are significant for subsonic aviation—CO_2 and aviation-induced cirrus (“contrails”) (Lee et al., 2009). For CO_2, the calculation of radiative forcing requires consideration of timescale (Kawa et al., 1999). At the same time, the altitude of emissions is not significant, since the emitted CO_2 will be mixed homogeneously into the atmosphere for most of its lifetime (Pitari et al., 2008). No significant difference is therefore anticipated between the radiative forcing resulting from one unit of fuel burn for subsonic and supersonic aircraft. However, the higher fuel burn per seat-km of the supersonic designs results in increases of the total CO_2 radiative forcing per seat-km by a factor of three to nine as compared to subsonic aviation.

For contrails, we do anticipate significant differences in the radiative forcing—and therefore climate impact—resulting from contrails formed by supersonic aircraft (Grewe et al., 2007). Section 4 discusses in detail the likely differences in contrail formation and persistence which will result from flying aircraft at higher altitudes. However, we expect differences in the radiative forcing from contrails if occurring at higher altitudes. In a perturbation experiment, we simulate the radiative forcing resulting from an increase in cirrus coverage at different altitudes and latitudes (Figure 49). At each altitude, a 1-km thick cirrus layer is simulated, covering 1% of the latitude band. As for the prior radiative forcing calculations, we calculate the stratospherically-adjusted radiative forcing (red). The instantaneous forcing (green) and shortwave and longwave components thereof (yellow and blue) are also shown.

These results do not account for differences in contrail formation or persistence between scenarios, but they demonstrate that, as long as a contrail is present, its altitude and latitude may change the radiative forcing resulting from it. If supersonic aircraft are likely to result in the formation of high, tropical contrails rather than lower, extratropical contrails, these sensitivities suggest that this may result in a reduced radiative forcing.

5.2.4 Decomposition of changes in ozone and the effects of methane feedbacks

To better understand the calculated radiative forcings and changes in ozone column, we perform an additional set of sensitivity simulations. To provide a baseline, Figure 50 shows the change in global mean ozone column for two scenarios: subsonic aircraft emissions, and flights with SST45-1.6-60.

Ozone changes in response to subsonic emissions reach a steady state within about one year, at +0.061 mDU per billion seat-km (averaged over years 15–28). This change shows little seasonal or inter-annual variability, apart from a gradual decline due to methane feedbacks which is explored below. In this time period, the annual mean change in ozone has a standard deviation of 3.8×10^{-3} mDU per billion seat-km, or 6.2% of the mean over this period. The net impact is positive because most of the ozone impact from subsonic aviation is the generation of low-altitude (tropospheric and lower-stratospheric) ozone.

Ozone changes due to emissions from the SST45-1.6-60 design are different than subsonic emissions in four ways.

Firstly, they take significantly longer to reach a steady state. Initially, ozone increases in response to the emissions, reaching a monthly mean peak of 0.30 mDU per billion seat-km. However, after one year the ozone response begins to decrease

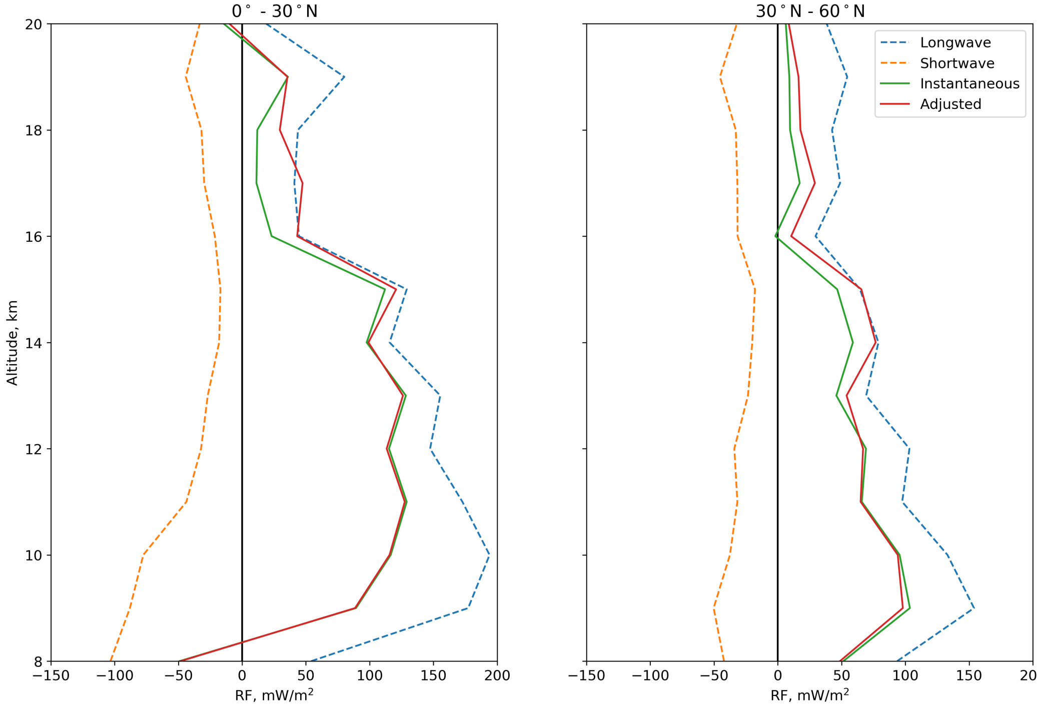

Figure 49: Radiative forcing per unit of additional cirrus cloud cover, as a proxy for the sensitivity to contrail cirrus. Radiative forcing is shown in red; instantaneous radiative forcing in green; and components of the instantaneous radiative forcing as dashed lines. Left: sensitivity in the tropics (0 to 30°N). Right: sensitivity in northern mid-latitudes (30 to 60°N).

and it becomes negative after around two years. This decrease continues until approximately the tenth year of integration.

Secondly, there is greater seasonal variability in the ozone impacts of SST45-1.6-60. Once the steady state response has been established, the standard deviation of the month-to-month change in ozone column is 5.0% of the mean. This is calculated as the standard deviation of the difference between the monthly average column and that year's annual average. Impacts are smaller in the northern hemispheric winter and greater in the summer. This reflects that the ozone change is a contribution of a positive tropospheric and lower-stratospheric contribution, and a negative mid- to upper-stratospheric change. As in the case of subsonic aviation emissions, the positive contribution is maximized during winter (Gilmore et al., 2013; Eastham and Barrett, 2016).

Thirdly, there is significant inter-annual variability in the ozone response to high-altitude emissions, in comparison to the response to subsonic aviation. Once the initial 10-year transient has passed, the net effect on the global, annual mean ozone column continues to vary significantly. Over the year 15–28 period, we calculate a standard deviation which is 16% of the long-term mean. This demonstrates the need not only for long chemical integrations, but also for considering multiple meteorological years when evaluating the impacts of supersonic aviation. Several prior studies, including several of the models used by Kawa et al. (1999), used

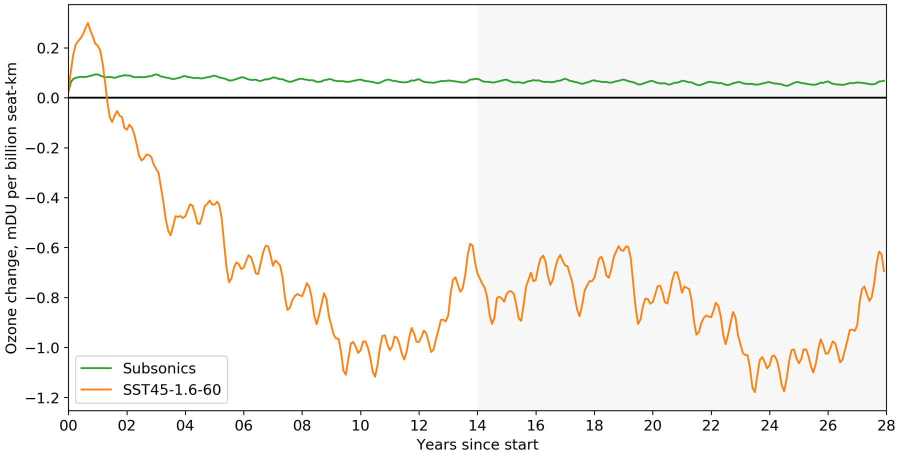

Figure 50: Change in global mean ozone due to subsonic or supersonic aviation. Each data point shows the monthly average. Estimates are calculated by repeating 14 years of meteorological data. The averaging period used for evaluation of mean changes is highlighted in gray.

repeating annual climatologies to represent atmospheric circulation. These studies may therefore not be able to address this aspect. However, this may be of limited importance given the sensitivity to cruise altitude as discussed below.

Finally, the magnitude of the change is greater—per billion seat-km traveled—than for subsonic emissions. Averaging over years 15–28, the mean change is -0.85 mDU per billion seat-km, 14 times greater in magnitude than the positive perturbation from subsonic aircraft. The greater magnitude of depletion compared to the response to subsonic emissions is in part due to the lower efficiency of the SST45-1.6-60 design compared to the subsonic fleet, burning 5.3 times as much fuel (on average) per seat-km. Per unit fuel burn, the total impact of this design is therefore only 2.6 times that for subsonic aircraft, albeit of opposite sign.

5.2.4.1 Differences in response by design cruise altitude

To test the sensitivity of the ozone response to the design cruise altitude, we repeated our simulations using the higher-speed SST35-2.2-60 notional aircraft, which has a cruise altitude of 19 km compared to the 17 km cruise altitude of SST45-1.6-60 (Figure 51).

Per seat-km, and averaged over the year 15–28 period, we find a 38 times greater net change in ozone column than for the lower-altitude SST45-1.6-60 design. As in the case of SST45-1.6-60, the transient response appears to stabilize within around 10 simulation years, and there is month-to-month variability of 4.4% (compared to 5.0% for SST45-1.6-60 for this period). The inter-annual variability is 4.9%, lower than the 16% estimated for SST45-1.6-60. This is because the atmospheric sensitivity to emissions is of mixed sign at the lower altitudes, and varies year-by-year. The response at the higher altitudes flown by the SST35-2.2-60 notional aircraft is more stable.

The greater impacts calculated for the supersonic fleets are not exclusively due

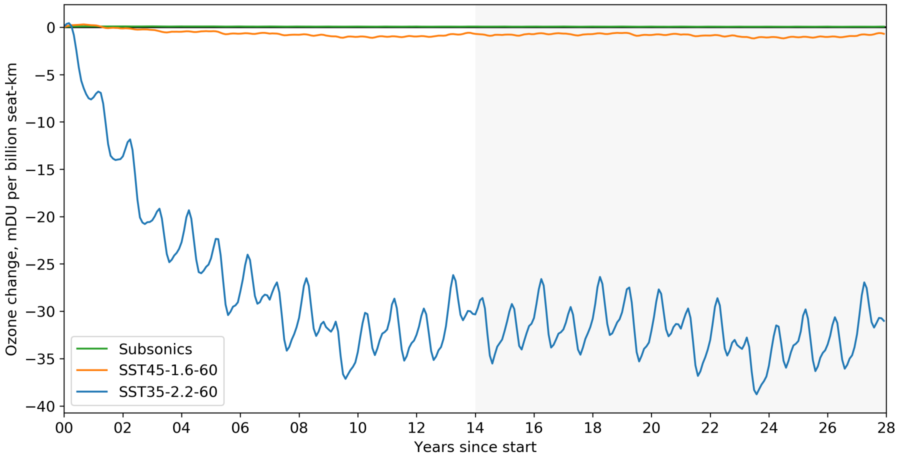

Figure 51: Change in global mean ozone due to subsonic or supersonic aviation, now including SST35-2.2-60.

to higher atmospheric sensitivities to emissions at these altitudes. The supersonic designs proposed here also burn more fuel per seat-km than the subsonic fleet, further increasing the change in ozone per seat-km. The same results can be expressed per unit of fuel burn to produce the impacts in terms of pure atmospheric sensitivity without factoring in the lower efficiency expected from a supersonic fleet. As such, the higher-altitude SST35-2.2-60 design results in a net decrease of 160 mDU per Tg fuel burn, compared to a loss of 7.1 mDU per Tg fuel burn for SST45-1.6-60, and a net production of 2.7 mDU per Tg fuel burn for the subsonic fleet.

5.2.4.2 Methane feedbacks

We perform a series of additional simulations in which we fix surface concentrations of methane to 1835 ppbv, to quantify the role of methane feedbacks in the response of atmospheric ozone to sub- and supersonic aircraft emissions. Figure 52 compares the results of these simulations (dashed lines) to those in which methane feedbacks are included (solid lines).

As has been described in detail elsewhere, inclusion of long-term methane feedbacks results in a reduction in the net increase in ozone from subsonic aviation due to the reduced methane lifetime (e.g. Khodayari et al. (2015) and Holmes et al. (2011)). Relative to the case with no feedbacks, we find that methane feedbacks reduce net ozone production by 29% over the year 15–28 averaging period, or 0.025 mDU per billion seat-km traveled.

For SST45-1.6-60, methane feedbacks also result in a negative effect on the ozone response. However, in this case, supersonic aviation already reduces ozone concentrations. The net effect when including methane feedbacks is an additional 0.85 mDU of ozone depletion per billion seat-km when averaging over years 15–28. Relative to a case with no feedbacks, this is a 10% increase in depletion, or 0.094 mDU per billion seat-km.

The relative magnitude of these changes is subject to the choice of metric. If

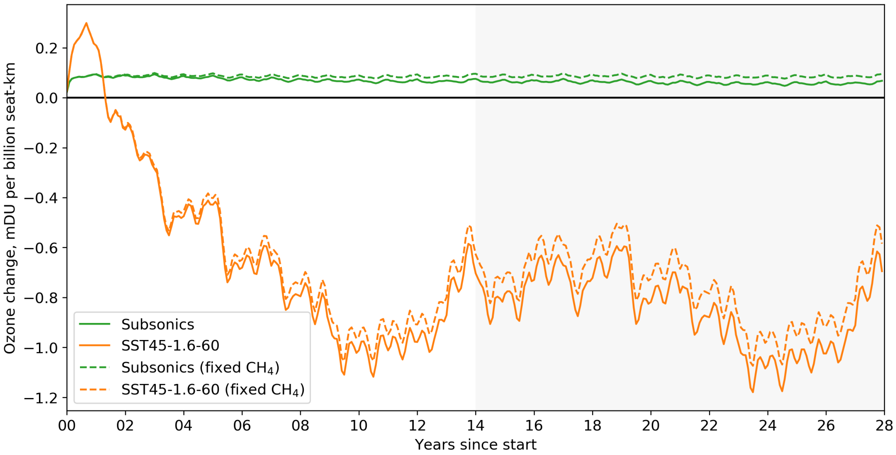

Figure 52: The effect of methane feedbacks on ozone changes due to aviation. Solid lines show the change in global mean ozone column density when including methane feedbacks. Dashed lines show the results when methane feedbacks are excluded, instead using a fixed surface VMR.

changes are quantified per unit of fuel burn, the absolute effect of methane feedback is of a similar order of magnitude, causing a change of -1.1 mDU per Tg of fuel burned by subsonic aviation and -0.79 mDU per Tg of fuel burned by SST45-1.6-60. This is in spite of the lower emissions index of 9.0 g NO_x per kg of fuel for notional aircraft SST45-1.6-60, compared to an average of 15 g per kg fuel burn for the simulated subsonic fleet.

5.2.4.3 Decomposition by exhaust product

We perform additional sensitivity simulations by reducing the emissions index of different species in the supersonic aircraft exhaust based in the baseline notional aircraft (SST45-1.6-60). This allows us to estimate the contribution of each component to the overall impact of supersonic aviation on atmospheric composition and climate. In each simulation, one emissions index is reduced while all others are held constant. The simulations are as follows:

1. Zero NO_x: Reduce NO_x emissions by 100%
2. Zero H_2O: Reduce water vapor emissions by 100%
3. Zero SO_x: Reduce SO_x emissions by 100%
4. Zero BC: Reduce emissions of non-volatile particulate matter by 100%

The effect of each of these changes is shown in Figure 53 as the difference between a simulation with all emissions included, and that where an emission has been set to zero.

Based on the average of simulated impacts for years 15–28, we find that a 100% NO_x reduction would result in a 35% reduction in ozone impacts, implying that NO_x contributes around 35% of the total impacts from the SST45-1.6-60 design.

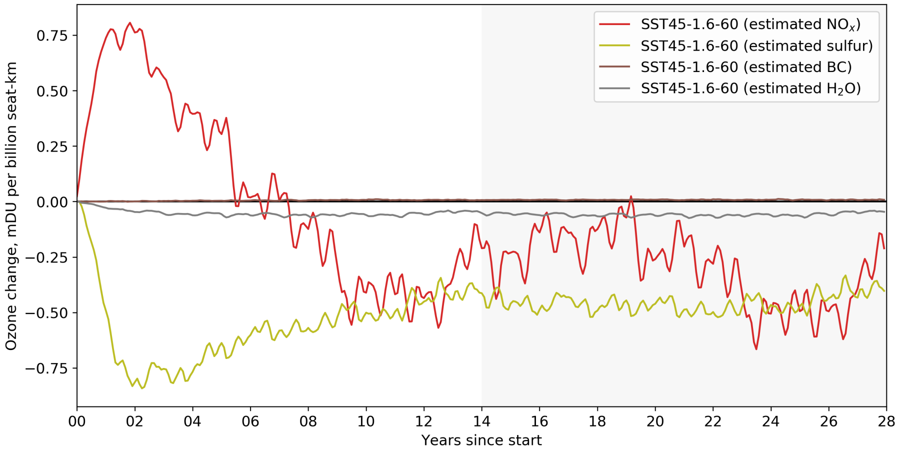

Figure 53: Estimated contribution of NO_x, sulfur, water vapor, and black carbon to ozone losses for the baseline aircraft.

Removing water vapor would reduce ozone impacts by 6.9%. This small contribution is in part due to the low altitude of the emission. Whereas NO_x can cycle through the troposphere and be re-injected into the stratosphere, this is not true for water vapor. The quantity of water vapor entering the stratosphere from the troposphere is controlled by the temperature of the tropical tropopause "cold point", where excess water vapor condenses and is rained out (Solomon et al., 2010) This prevents water vapor emitted at low altitudes from having significant effects at higher altitudes or in the other Hemisphere. The potential for additional ozone depletion resulting from contrail formation is discussed in Section 6.3.3.

Sulfur emissions are found to contribute 54% of the total ozone depletion associated with supersonic aviation. Stratospheric sulfur forms sulfate aerosol, which can persist for several years and catalyze ozone depletion. The sulfur content of aviation fuel (simulated at 600 parts per million by mass, consistent with current-day fuels (Hileman et al., 2010)) therefore constitutes a significant cause of ozone depletion in a supersonic aviation scenario.

Finally, we find that black carbon (non-volatile particulate matter) increases the ozone column density, offsetting 0.96% of the depletion resulting from other supersonic emissions. This is likely due to its role as a surface for chlorine deactivation and sequestration of NO_x. However, this is subject to significant uncertainty due to the lack of information regarding black carbon heterogeneous chemistry in the stratosphere. This also does not account for the role of black carbon and other particles in forming condensation trails, which may have significant climate and atmospheric composition impacts as discussed in Sections 3, 4, and 6.3.3.

5.3 Synthesis and literature comparison

5.3.1 Comparison of results to previous studies

The impacts of supersonic aviation, especially on stratospheric ozone, have been assessed several times. Here, we compare our results to the last two major reports by NASA (Kawa et al., 1999; Dutta et al., 2005). Comparison with these studies is complicated by the different underlying assumptions. In particular, both prior studies focused on a series of scenarios described in the IPCC 1999 report, using fuel burn and emissions estimates described by Baughcum et al. (2003). The (Kawa et al., 1999) study focused on an aircraft design which cruised at 18–20 km, compared to the 17 km cruise altitude used for our the SST45-1.6-60. The Dutta et al. (2005) study, although it did explore multiple different cruise altitudes, did not include sulfur emissions.

In broad terms, our findings agree with the results from both studies. As discussed by Kawa et al. (1999), emissions from supersonic aircraft at high altitudes result in net ozone depletion. We find the same broad pattern, of decreased ozone above around 25 km altitude, and increased ozone below this altitude.

Considering NO_x, we find a sensitivity of global column ozone to NO_x emissions which is greater than that reported by Kawa et al. (1999) but consistent with that from Dutta et al. (2005). Based on comparison of our "all emissions" and "no NO_x" SST45-1.6-60 scenarios, we estimate a sensitivity of 280 mDU of ozone depletion per Tg of NO_x emissions (on an NO_2 mass basis), or a loss of 0.09% of the global ozone column per Tg of NO_x. By contrast, Kawa et al. (1999) found that NO_x was a minor contributor to ozone depletion in most simulations, with water vapor instead providing the majority of the ozone depletion potential. However, the report by Dutta et al. (2005) finds a sensitivity of -0.04% per Tg of NO_x for an aircraft with a cruise altitude of 15–17 km, and -0.13% per Tg NO_x for an aircraft with a cruise altitude of 17–19 km.

Consistent with Kawa et al. (1999), we find that sulfur emissions may significantly increase total ozone depletion. However, we find that this depletion will occur even for low rates of conversion of fuel sulfur, due to the long-term conversion of emitted SO_2 to sulfate aerosol. The previous assessment found a high sensitivity of total column ozone depletion to the gas-to-particle conversion rate, and stated that a conversion rate of 10% could double the overall depletion. We find that the presence of sulfur (as SO_2 and H_2SO_4 in the fuel is likely to contribute significantly to ozone depletion. The relative contribution of each component is quantified in Section 6.

The sulfur dependence found by Kawa et al. (1999) is based on results which are explored further by Weisenstein et al. (1996). Their model used a size-resolving aerosol model, which enables a more complex investigation of changes in surface area density due to stratospheric emissions. By contrast, the GEOS-Chem UCX model assumes that aerosol surface area density increases with sulfate mixing ratio according to an empirical relationship described by Grainger et al. (1995). We therefore likely do not fully capture the nuances of changes in surface area density associated with different gas-to-particle conversion ratios. However, Weisenstein et al. (1996) also find a high sensitivity of total ozone depletion to sulfur emissions of any kind. Under a relatively low NO_x emissions scenario of $5\,\mathrm{g\,kg^{-1}}$, they find that inclusion of sulfur emissions (assuming pure SO_2) increases the column ozone depletion at 47° N by a factor of four, while the same sulfur emission for a fleet with a higher NO_x emissions index of $10\,\mathrm{g\,kg^{-1}}$ instead results in a 50% increase. Our finding of a doubling in ozone depletion due to sulfur emissions (relative to the impact when sulfur emissions are excluded) is therefore within the range of previous assessments.

The most significant difference between the results of this work and those of prior studies is the reduced sensitivity of both ozone and radiative forcing to water vapor emissions. This is for two reasons. Firstly, our findings of a large ozone depletion due to sulfur increase the relative contribution of ozone depletion to all calculated radiative forcings. This in turn has reduced the relative contribution of water vapor. Secondly, the relatively low cruise altitude of SST45-1.6-60 at 17 km results in significantly less accumulation of water vapor in the stratosphere. The simulated peak increase in annual mean, cruise-altitude water vapor is up to 36 ppbv, or 1.9 ppbv per Tg of fuel burned for SST45-1.6-60 (given 19 Tg of annual fuel burn). The total resulting forcing attributable to water vapor is then estimated to be $1.2\,\mathrm{mW\,m^{-2}}$, or $0.063\,\mathrm{mW\,m^{-2}}$ per Tg of fuel burn.

In the Kawa et al. (1999) report, the peak increase in water vapor varies between models but is approximately 200–600 ppbv, centered on the higher cruise altitude of 18–20 km. This results from a total fuel burn of around 100 Tg—an increase of 2–6 ppbv per Tg of fuel burned. The associated total forcing is $100\,\mathrm{mW\,m^{-2}}$, or around $1\,\mathrm{mW\,m^{-2}}$ per Tg of fuel burn—16 times greater than in this report. This difference is the result of the difference in cruise altitude. When using the SST35-2.2-60 design, with a cruise altitude of 19 km and 15 Tg of fuel burn, we find a larger peak change of 23 ppbv of water vapor (at cruise altitudes) per Tg of fuel burn. This is associated with a radiative forcing of $11\,\mathrm{mW\,m^{-2}}$, or $0.72\,\mathrm{mW\,m^{-2}}$ per Tg of fuel burned. This is consistent with a multi-model assessment by Grewe et al. (2007), which found a radiative forcing of 16–$34\,\mathrm{mW\,m^{-2}}$ due to water vapor resulting from 60 Tg of fuel burn from supersonic aircraft cruising at 16–20 km.

5.3.2 Synthesis

We find that, for a projected year-2035 atmospheric composition, a fleet of Mach 1.6 supersonic aircraft results in 0.85 mDU of ozone column depletion for each billion seat-km traveled. This is a factor of 14 greater than the increase in ozone that results per seat-km of subsonic aviation. We find that 54% of this depletion is the result of sulfur emissions, 35% is the result of NO_x emissions, and the remainder is due to a combination of water vapor, black carbon, and other emissions. Methane feedbacks also contribute significantly, being responsible for 10% of the change in ozone when compared to a case with no such feedbacks.

Whereas subsonic emissions result in a positive non-CO_2, non-contrail radiative forcing of $1.3 \times 10^{-3}\,\mathrm{mW\,m^{-2}}$ per billion seat-km traveled, supersonic emissions by this design result in a negative forcing of $20 \times 10^{-3}\,\mathrm{mW\,m^{-2}}$ per billion seat-km. This is a combination of a positive forcing from ozone and water vapor and a larger negative forcing from carbonaceous and sulfate aerosols, with a small negative contribution from methane depletion. Flying at higher altitudes (19 km) would reverse the sign, resulting in around $26 \times 10^{-3}\,\mathrm{mW\,m^{-2}}$ per billion seat-km. This is the result of cancellation between several components of different sign with magnitudes of up to $200 \times 10^{-3}\,\mathrm{mW\,m^{-2}}$ per billion seat-km, implying a high level of uncertainty in the sign and magnitude of the net response.

Based on these results, both the sign and magnitude of ozone and climate impacts resulting from supersonic aviation are highly sensitive to the design cruise altitude and emissions indices. In particular, the use of desulfurized fuel for Mach 1.6 supersonic aircraft could reduce the resulting ozone depletion by up to 54%, at the cost of removing a significant negative radiative forcing component.

6 Sensitivity of atmospheric composition to aircraft design and emissions

Highlights

- Cruise at 14 km could be net neutral with regards to changes in the ozone column.
- The net neutral cruise altitude will increase if fuel sulfur content is decreased.
- Although around half of the ozone loss due to Mach 1.6 aircraft operations is due to sulfur, net ozone destruction rises non-linearly as flight altitude is increased beyond 15 km, largely due to NO_x emissions.
- Emissions of water vapor are a minor contributor to net ozone loss.

The previous section used “forward-based sensitivities” to quantify the atmospheric response to individual scenarios. This approach is computationally expensive and provides limited flexibility. Over the past two decades, adjoint-based models of three-dimensional regional and global CTMs have been developed to address this issue, among others (Menut et al., 2000; Menut, 2003; Sandu et al., 2005; Hakami et al., 2007; Henze et al., 2007). Adjoint models quantify the sensitivity of an outcome, such as global column ozone, to any change in inputs, including arbitrary changes in the spatial distribution, chemical composition, and magnitude of an emissions source. Adjoint models have been used successfully to estimate quantities such as the sensitivity of global mean population ozone and particulate matter exposure with respect to changes in emissions (Schmidt and Martin, 2003; Henze et al., 2009), including those from subsonic aviation (Gilmore et al., 2013; Koo et al., 2013; Ashok and Barrett, 2016).

Most of the recent work on adjoint-based CTMs has been focused towards estimating surface population exposure or constraining ground emission sources. Few existing studies have quantified sensitivities of stratosphere-oriented objective functions. Errera and Fonteyn (2001) have developed a four-dimensional variational (4D-Var) assimilation system but their study uses a simplified chemical model and only heterogeneous reaction on sulfate aerosol is considered. Other aerosols are not represented. Additionally, the integration time is limited to a few weeks, much shorter than typical stratospheric lifetimes.

The introduction of the Unified Chemistry eXtension (UCX) in GEOS-Chem (Eastham et al., 2014) offers the potential to capture long-term stratospheric responses and to better represent tropospheric-stratospheric exchanges. However, the UCX is implemented only in the forward version of the code. For this project, we implemented the UCX into the adjoint of the GEOS-Chem model, enabling us to estimate the sensitivity of key atmospheric quantities to arbitrary changes in any input parameter.

Previous sensitivity analyses of the effects of supersonic transport focused on forward-derived sensitivities (Kawa et al., 1999; Dutta et al., 2005). For each forward model run, this approach gives the spatial and temporal response to a set of emissions inventories. For a number N of emissions sets, this approach requires $N + 1$ forward runs (for each emissions scenario and a baseline case). Adjoint modeling enables the evaluation of sensitivities of an aggregated objective function. An estimate of the total impact of emissions from any given scenario can be obtained by taking an inner product of the sensitivities obtained from a single adjoint run with the emissions inventory of the respective scenario. Adjoint sensitivities are thus used here as a linearized, multi-scenario assessment tool, to evaluate the environmental response of the aviation scenarios described in Section 2.3.3.2.

In this section, we first describe the model itself (Section 6.1). This is followed by an evaluation of the model's performance in reproducing results from forward modeling approaches when simulating increases or decreases in aviation emissions (Section 6.2). We then quantify how emissions from supersonic aviation, as described by this study's notional aircraft, is expected to affect the global ozone layer and total aerosol optical depth (Section 6.3). This includes calculation of the sensitivity of these quantities to emissions indices, fuel sulfur content, latitude and altitude of flight, and contrail formation. Finally, we incorporate the plume-scale modeling approaches from Section 3 to quantify how sub-grid, plume-scale chemistry changes the long-term impacts of aviation emissions, and how this effect varies between notional aircraft (Section 6.4).

6.1 Description of the GEOS-Chem Adjoint

6.1.1 Adjoint modeling description

The adjoint of GEOS-Chem computes gradients of a cost function J with respect to a set of model parameters. Examples of cost functions are total ozone column, or the mean ozone mixing ratio in the Antarctic stratosphere. Here, we calculate gradients of an outcome J with respect to emissions of any species at any time, latitude, longitude, and altitude. The adjoint-derived sensitivities $\frac{\partial J}{\partial E}$ thus represents how an emission E (e.g. one kilogram of NO_x emitted at 15 km over Europe in early December) would affect outcome (e.g. global, annual mean ozone column).

Calculation of the full, five-dimensional sensitivity array $\frac{\partial J}{\partial E(\lambda,\phi,z,t,s)}$ (where λ is longitude, ϕ is latitude, z is altitude, t is time, and s is the emitted species) is computationally expensive, but only needs to be performed once to provide the sensitivity of the outcome with respect to any change in emissions. The total impact of an emissions change, such as introduction of supersonic aircraft, can then be calculated by multiplying the array of sensitivities by the corresponding array of emissions, discretized by time, location, and species.

6.1.2 Adjoint modeling approach

The GEOS-Chem Adjoint consists of a forward model and its "inverse". The latter evaluates sensitivities around the "base" state of the atmosphere as computed by the forward model.

A detailed explanation of this theory is given in Hakami et al. (2007), with the example of implementation for tropospheric chemistry described by Henze et al. (2007).

6.1.3 Parameters used for the GEOS-Chem model

For the simulations performed in Section 5, we use GEOS-Chem v11. This version has some features which are not available or are implemented differently in the forward model embedded in GEOS-Chem's adjoint. As a result, the model parameters are not identical between the two sets of simulations. We describe here the key parameters used in the GEOS-Chem adjoint which differed from the simulations performed in Section 5

For all simulations using the GEOS-Chem UCX Adjoint, we use World Meteorological Organization (WMO) projections for greenhouse gases and CFC boundary conditions rather than RCP 4.5, used in the forward modeling approach. For the methane boundary condition, we use a prescribed surface volume mixing ratio of 1805 ppbv. This compares to a value of 1835 ppbv in the Section 5.1. We did not implement a flux condition for surface methane in the GEOS-Chem UCX Adjoint. For natural emissions, we use standard GEOS-Chem inventories, as described in Section 5.1.2. Aviation emissions are computed from AEIC (Simone et al., 2013) and updated monthly. These aviation emissions inventories include aircraft fuel burn, NO_x, CO, and hydrocarbons emissions. Black carbon, organic carbon, sulfur and water vapor emissions use the same emissions indices as in Section 5.1.2. SO_2 and H_2SO_4 aerosol emissions are calculated by assuming 600 parts sulfur per million parts fuel, by mass, and a 2% conversion rate of SO_2 to H_2SO_4, again as in Section 5. The role of further plume-scale sulfur conversion is studied in Section 6.4.

In the GEOS-Chem UCX Adjoint, the representation of stratospheric aerosols uses the original UCX description, as in Eastham et al. (2014). This differs from the forward modeling approach, which uses an updated parameterization. We use the same prescribed, sinusoidal, annual cycle for the water vapor mixing ratio at the tropical tropopause as the forward modeling approach, as described in Section 5. The UCX implementation allows water vapor to freely evolve in the stratosphere, while tropospheric H_2O mixing ratios are derived from relative humidity, read in from meteorological products.

All GEOS-Chem Adjoint simulations use the GEOS-5 forward product rather than MERRA-1. Unless otherwise specified, we compute nine-year adjoint sensitivities, using meteorology for the 2004 to 2013 time period.

In all other respects, the GEOS-Chem forward model (and its inverse) used in this section is functionally identical to that used for the forward simulations in Section 5. Other differences, such as in the length of the simulations performed, are described in the relevant subsections below.

6.2 Evaluation of the GEOS-Chem UCX Adjoint

The implementation of the UCX into GEOS-Chem Adjoint requires modification to both the forward and inverse models. We here provide a brief description of the implementation of the UCX into the GEOS-Chem adjoint forward (or "base") model (Section 6.2.1). We also perform tests to verify that the sensitivities produced by the adjoint model reproduce linearized forward sensitivities, and quantifying any disagreement between the two (Section 6.2.2).

6.2.1 Updates to the base model

Forward simulations were performed covering a six year period with the aim of comparing the adjoint "base" model before and after the implementation of the UCX, as well as to evaluate the results against observations. Figure 54 shows total column ozone, longitudinally-averaged, as a function of time and latitude. From top to bottom, we show: results from the unmodified forward model within the adjoint (v35f); the results from the adjoint after implementation of the UCX; and observations from the Ozone Monitoring Instrument (OMI). Total ozone column is here chosen to demonstrate the improved stratospheric modeling. The updated forward model provides a more accurate representation of the seasonality and latitude-dependence of the observed column, including the Antarctic spring, characterized by a rapid drop in ozone column within the polar vortex. This sudden loss, which is a consequence of the formation of polar stratospheric clouds and heterogeneous chemistry, was not captured in GEOS-Chem before the introduction of the UCX.

Although this is an improvement over the prior capabilities, this does not resolve existing limitations of the UCX in simulating ozone, as highlighted by Eastham et al. (2014). For example, the magnitude of the Antarctic ozone hole is not exactly reproduced compared to ozone observations from sonde data, and Arctic ozone depletion is underestimated. Additionally, Eastham et al. (2014) notes a positive bias exists in the HNO_3 to O_3 correlation, in addition to sharp increases in the NO_y/O_3 ratio around the equator which may exceed those in reality.

An additional comparison (not shown here) was performed with GEOS-Chem v11-01. A mean error of 2.5% in zonally-averaged column ozone was observed for a five-year run.

6.2.2 Comparison of adjoint sensitivities to forward simulations

Henze et al. (2007) describe the development process and validation of the GEOS-Chem Adjoint. The validation of individual components (aerosol thermodynamics, chemistry, convection, advection) as well as combined performance are presented in detail in Henze et al. (2007). Validation tests through inverse modeling (by perturbing emissions inventories) are also presented. Evaluation of the GEOS-Chem Adjoint has so far been focused on the study of surface or tropospheric objective functions, as the GEOS-Chem Adjoint has lacked the representation of stratospheric processes.

By implementing the UCX into the GEOS-Chem Adjoint, both tropospheric and stratospheric chemistry are handled in a consistent fashion. Although we have

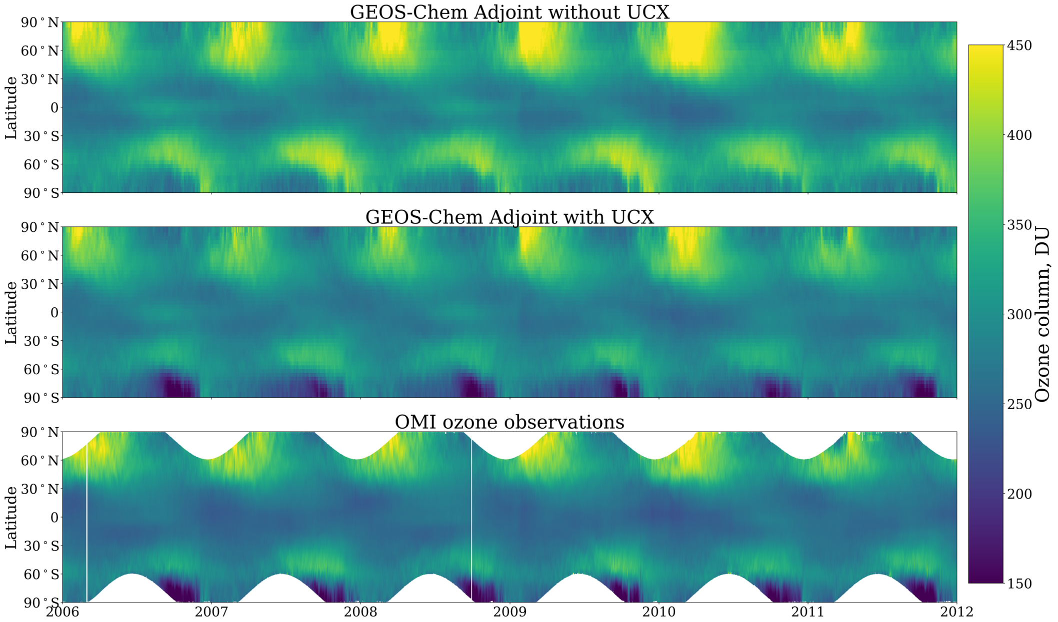

Figure 54: Validation of total ozone column. From top to bottom, forward model GEOS-Chem Adjoint results without the UCX (top), forward model with UCX (middle), OMI observations (bottom).

evaluated (in Section 6.2.1) the performance of the forward component, we also need to ensure that the inverse model can accurately estimate atmospheric sensitivities. The evaluation of the GEOS-Chem UCX Adjoint requires the evaluation of upper-tropospheric and stratospheric-oriented objective functions (e.g. total ozone column). We calculate forward sensitivities by taking the difference between two simulations using the forward model component. We then validate the GEOS-Chem UCX Adjoint by comparing adjoint and forward sensitivities of multi-year runs.

Given that our focus is on aviation impacts, we evaluate the accuracy of adjoint-derived sensitivities by simulating the effects of representative subsonic and supersonic aviation emissions scenarios. The emissions scenarios used for validation purposes differ from those presented in Section 2. Results using the finalized scenarios are presented in Section 6.3.

The test subsonic emissions scenario spans 0 to ∼12 km and includes 400 Tg of fuel burn, with a fleet-wide average NO_x emissions index of 15 g per kg of fuel (on an NO_2 mass basis). The test supersonic emissions scenario includes 25 Tg of fuel burn, with a NO_x emissions index of 10 g per kg of fuel (again on an NO_2 mass basis). This supersonic aircraft emissions scenario has a cruise altitude of ∼20 km, higher than the cases evaluated elsewhere. We estimate the sensitivity of global column ozone to a scaling of each inventory from total removal up to a doubling (i.e. ±100%). These inventories fully span the emissions range of all the scenarios used in this report, enabling us to test the extended tropospheric-stratospheric chemistry.

We perform this analysis for a scaling in subsonic aviation emissions and for supersonic aviation emissions independently (Section 6.2.2.1 and Section 6.2.2.2). As discussed in Section 5.2.4.3, NO_x and sulfur emissions from aviation are expected to have the greatest impacts on ozone column. We therefore use scalings of emissions of these species to test the adjoint's ability to reproduce simulated forward model results.

6.2.2.1 Testing the model by scaling subsonic aviation emissions

In this section, we compare forward and adjoint sensitivities to changes in subsonic aircraft emissions. We apply a scaling in aviation emissions for NO_x and sulfur between ±100% of baseline emissions. The following two model tests were conducted to evaluate simulation accuracy.

Model test: scaling of subsonic nitrogen oxides emissions

Figure 55 displays the forward and adjoint-derived changes in averaged ozone column, expressed in Dobson Units (DU), to a scaling in subsonic aircraft NO_x emissions. The estimated yearly adjoint sensitivities reproduce the results from GEOS-Chem with a maximum error of 50 mDU, corresponding to a relative change of 8%. Using a spline fit for the forward results, we obtain a root mean square error of 18 mDU for the emission range considered, spanning up to 7.5 Tg of emitted NO_x (on an NO_2 mass basis). The right axis of Figure 55 displays the normalized ozone response with respect to a 1% scaling in aviation NO_x. Since the adjoint sensitivities are based on first-order gradients, discrepancies between the adjoint-derived and forward-derived results are in part an indicator of the presence of chemical non-linearities.

Both forward and adjoint approaches estimate that aviation emissions lead to an increase of ∼208 mDU per Tg of emitted NO_x (on an NO_2 mass basis) around the baseline scenario. The forward model response is slightly concave with respect to the annual aviation NO_x emissions, meaning that the gradient is greater at reduced emissions compared to the adjoint-derived sensitivity.

Figure 55 allows us to quantify the impact of aviation nitrogen oxides emissions on total ozone column. We find that including aircraft NO_x emissions results in an increase of ∼600 mDU (compared to a simulation with no aircraft emissions), corresponding to a globally-average increase of 0.21% in total ozone column mass, consistent with prior estimates from Eastham and Barrett (2016). These results were obtained using a single-year adjoint simulation (for 2007), during which we expect the response to aviation to not yet be in steady state. This explains the smaller increase in column ozone than is calculated for the longer-term simulations shown earlier. Long-term feedbacks on upper-tropospheric and stratospheric ozone are captured in longer, five-year simulations.

Model test: scaling of subsonic sulfur emissions

Given the role of sulfate aerosols in stratospheric chemistry, accurately reproducing the sensitivity of ozone to sulfur emissions is important. Heterogeneous chemistry is the main stratospheric ozone depletion pathway for sulfur emissions. Comparing forward model-derived sensitivities by scaling aircraft sulfur emissions to adjoint

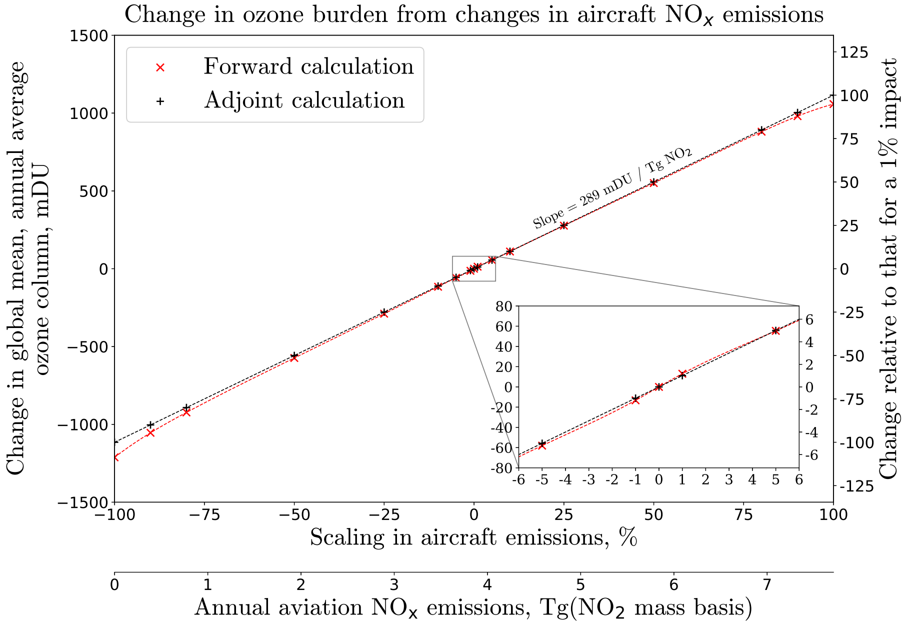

Figure 55: Comparison of forward and adjoint sensitivities with respect to a scaling in aircraft NO_x emissions

sensitivities allows us to validate the adjoint of sulfate aerosol thermodynamics (both liquid binary solutions and supercooled ternary solution) and heterogeneous chemistry, which was until now not included in the GEOS-Chem Adjoint.

Figure 56 shows the forward and adjoint-derived results for a one-year run in which subsonic aviation sulfur emissions are scaled between -100% and +100% of baseline values. Aviation sulfur emissions are derived from aviation fuel burn assuming a fuel sulfur content of 600 ppm on a mass basis and a sulfur to H_2SO_4 conversion factor of 2%. Both adjoint and forward models predict that subsonic aviation sulfur emissions lead to a reduction in total ozone column of 140 mDU per Tg of emitted H_2SO_4. We calculate a root mean squared error of 0.15 mDU between both approaches.

6.2.2.2 Testing the model by scaling supersonic aviation emissions

This section evaluates the accuracy of computed lower and mid-stratospheric sensitivities through a scaling in supersonic aviation emissions. We here focus on the role of nitrogen oxides and sulfur emissions. As discussed in Section 5, the stratospheric behavior of these species is expected to significantly differ from that in the troposphere. Five year adjoint simulations were performed to capture long-term stratospheric responses to supersonic aviation emissions. The following two model tests were conducted to evaluate simulation accuracy.

Model test: scaling of supersonic NO_x emissions

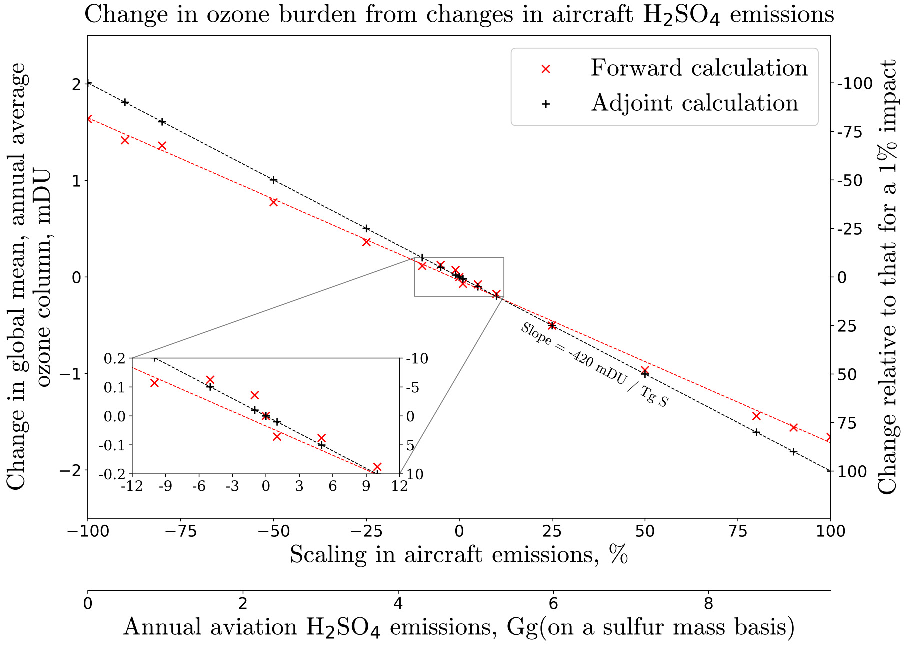

Figure 56: Response of total ozone column to a scaling in subsonic aircraft H_2SO_4 emissions according to GEOS-Chem (red) and using atmospheric sensitivities from GEOS-Chem UCX Adjoint (black). Red data points show the results of a series of forward model simulations, in which the aircraft emissions are scaled, from an annual baseline of ∼15 Gg.

Figure 57 compares the five-year adjoint and forward responses to a scaling in NO_x emissions from supersonic aviation. The adjoint model is able to reproduce the results of the forward model, however with a steeper trend. High altitude NO_x emissions have a greater potential for stratospheric depletion compared to subsonic emissions. The adjoint-derived sensitivities indicate that this supersonic emissions scenario, with a cruise ceiling at 20 km, leads to 2.8 DU of depleted ozone per Tg of emitted NO_x on an NO_2 mass basis (approximately corresponding to 28 mDU/(Tg fuel burn/year)).

The slope of the ozone response from aviation NO_x emissions shows a strong dependence on the cruise ceiling. Sensitivities of ozone column to NO_x emissions reverse at ∼15 km at northern mid-latitudes, going from positive to negative. The altitude of this reversal also depends on season, varying from 13.5 km in July to 16 km in January.

Model test: scaling of supersonic aircraft sulfur emissions

Figure 58 displays the five-year mean ozone response to a scaling in supersonic sulfur emissions, simulated as a change in the fuel sulfur content with a fixed 2% conversion factor. The forward and adjoint models agree with a root mean square error of 29 mDU.

Both models estimate the ozone response to scale linearly with the amount of emitted sulfur, with a slope of -19.5 DU per Tg of elemental sulfur per year, for

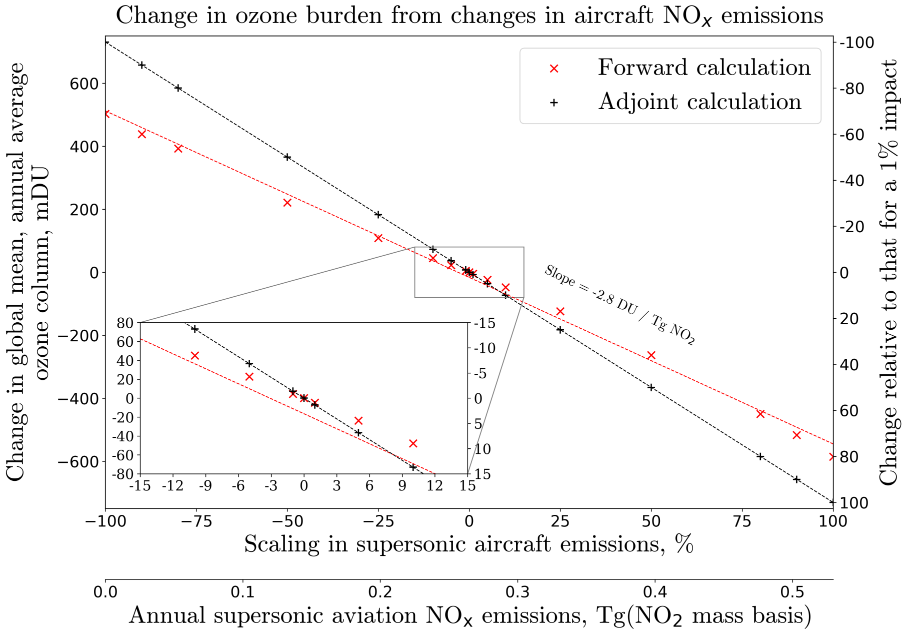

Figure 57: Response of total ozone column to a scaling in supersonic aircraft NO$_x$ emissions according to GEOS-Chem (red) and using atmospheric sensitivities from GEOS-Chem UCX Adjoint (black). Red data points show the results of a series of forward model simulations, in which the supersonic aviation emissions are scaled, from an annual baseline of 0.26 Tg (on a NO$_2$ mass basis). The right axis displays the normalized impact with respect to a 1% scaling in aircraft NO$_x$ emissions.

emissions at 20 km. In the 15–20 km band, sensitivities to SO$_2$ and H$_2$SO$_4$ emissions are approximately 10 times larger than sensitivities to NO$_x$ emissions.

Altitude and latitude play a key role in determining the role of sulfur on ozone column. Figure 59 displays zonally-averaged adjoint sensitivities of ozone column to sulfur emissions. Sulfur has a limited impact in the troposphere. In the stratosphere, sulfur emissions leads to ozone depletion due to the heterogeneous reactions taking place on the aerosol surface, converting reservoir chlorine (e.g. ClONO$_2$) to active chlorine, which catalytically depletes ozone. The amount of ozone depletion from sulfur emissions is expected to reduce with decreased stratospheric chlorine loading.

The magnitude of sulfur-induced ozone depletion varies with altitude and latitude, peaking at -15 mDU per Gg SO$_2$ per year in the extra-tropics. Figure 59 shows that the equatorial region is characterized by lower sensitivities to sulfur emissions.

6.2.3 Summary of evaluation

Comparisons of forward and adjoint-derived sensitivities show good agreement ($r^2 \geq 0.95$). Based on these results, we are confident that the introduction of the UCX in the GEOS-Chem Adjoint enables the accurate calculation of stratospheric sensitivities without compromising existing tropospheric capabilities.

Some limitations remain. The GEOS-Chem Adjoint allows the evaluation of first-order gradients of a user-defined objective function. However, atmospheric chemistry includes non-linear processes, so we can only expect that the adjoint-

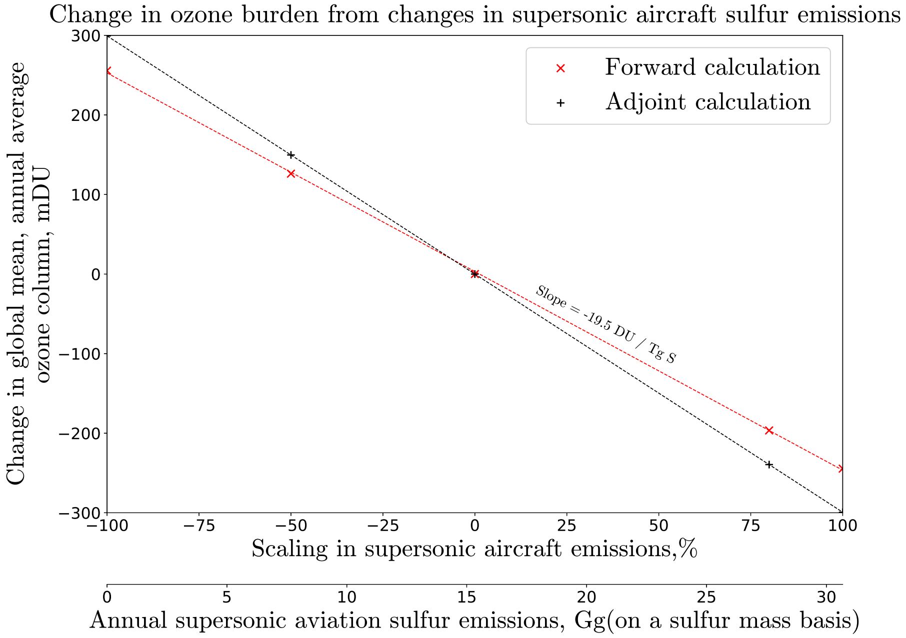

Figure 58: Changes in the response of total ozone column to a scaling in supersonic aircraft sulfur emissions (released as SO_2 and H_2SO_4) according to GEOS-Chem (red) and using atmospheric sensitivities from GEOS-Chem UCX Adjoint (black). Red data points show the results of a series of forward model simulations, in which the supersonic aviation emissions are scaled, from an annual baseline of ∼15 Gg of sulfur.

derived sensitivities are valid over a limited range of values for the emissions.

Additionally, multi-year adjoint integrations are required to capture both inter-annual variability in the response, and the long response and stabilization period of the stratosphere. Stability of the adjoint calculation is difficult to guarantee over these long integration periods, as we note that highly non-linear atmospheric events, such as the Antarctic spring, have led to unreasonably large sensitivities.

6.3 Sensitivity of global atmospheric composition to design choices

Changes in ozone column resulting from different aviation scenarios are calculated in this section using nine-year tropospheric-stratospheric sensitivities derived from GEOS-Chem UCX Adjoint. We use the results from the GEOS-Chem Adjoint as a rapid assessment tool. The adjoint sensitivities enable the evaluation of environmental changes from a wide range of scenarios for the aviation industry.

For these simulations, we use meteorology from the GEOS-5 dataset, archived by the GEOS-Chem community, from the period 2004–2013. As discussed in Section 6.1.3, this differs from the MERRA reanalysis used in Section 5, which may result in some differences between the two analyses. Additional differences will also be driven by the model differences described earlier.

We also use a shorter integration period of nine years compared to the 14 used in Section 5. This is primarily due to computational limitations. The adjoint simulation requires the generation of continuous checkpoints, and a nine-year adjoint simulation

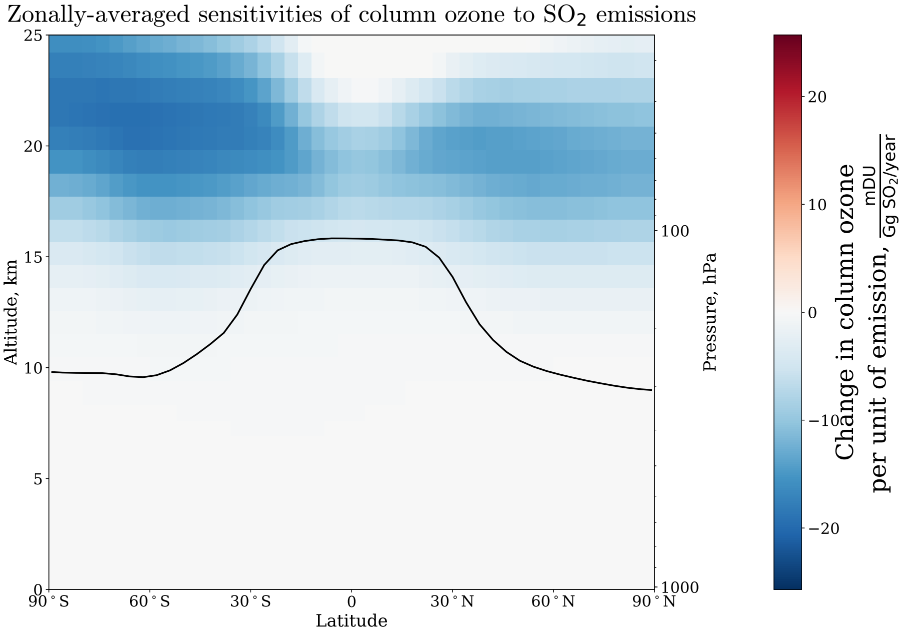

Figure 59: Zonally-averaged sensitivities of total ozone column to changes in sulfur concentrations. The continuous black line represents the annual mean tropopause altitude.

requires 30 TB of storage space for a horizontal resolution of 4° × 5°. A nine year integration period was therefore chosen as a compromise between accuracy and cost. This will result in additional discrepancies between the results shown here and those from the forward modeling assessment. However, one advantage of using a shorter integration period is that it places additional weight on the nearer-term response to emissions, which may be more relevant in the context of a rapidly growing industry—which aviation has historically been.

6.3.1 Decomposition of central case impacts

In this section, we present the total impact on ozone column and aerosol optical depth, as estimated by GEOS-Chem Adjoint, for each of the scenarios previously described. This allows us to evaluate, to a greater level of detail than was previously possible, the exact contribution of emissions of each chemical species, in each time and location, to the overall atmospheric impacts of aviation.

6.3.1.1 Column ozone response

Figure 60 shows the adjoint-derived mean ozone column responses to the baseline subsonic scenario and each unrestricted supersonic scenario considered in this report. Additional cases representing different land restrictions are also displayed in Figure 60 for scenario SST45-1.6-60. As in Section 5.2, the responses are normalized by the total available seat kilometers, expressed in mDU per billion seat kilometers (mDU/bn seat-km).

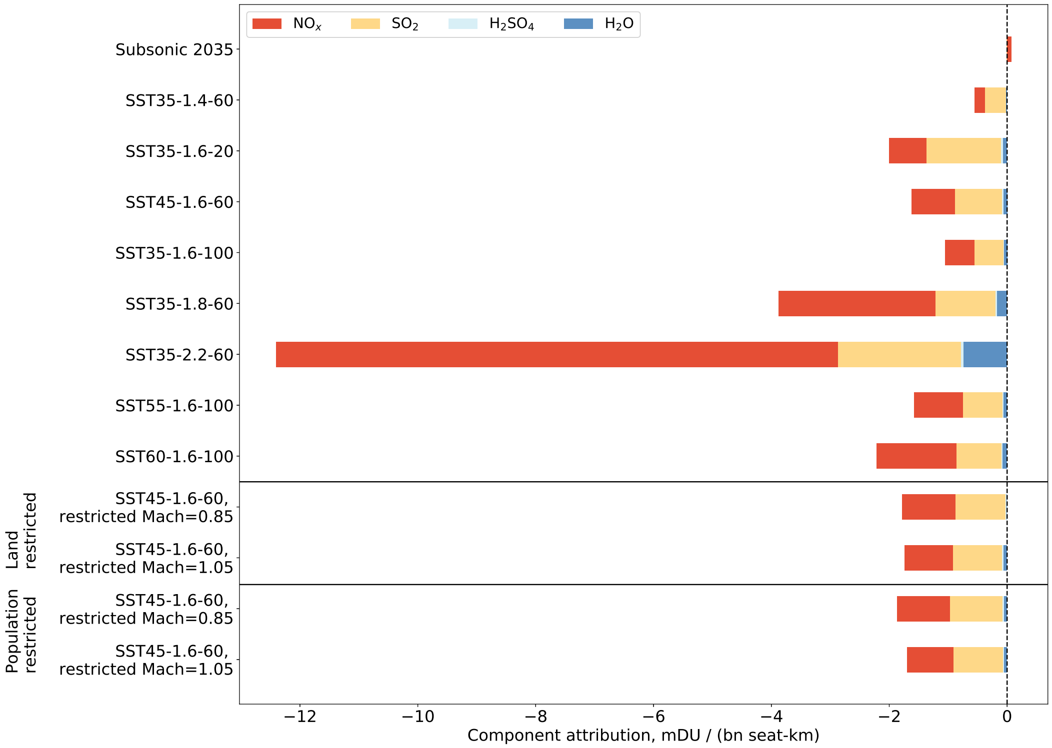

Figure 60: Emission component attribution to column ozone.

Subsonic aviation leads to a positive response of ∼1.3 DU, corresponding to a normalized 0.071 mDU/bn seat-km. These values compare to 1.6 DU and 0.086 mDU/bn seat-km for the forward model results, as described in Section 5.2. The 20% discrepancy observed between the forward and adjoint modeling approach is likely to be the results of the differences in MERRA and GEOS-5 fields for the period considered. Additionally, the adjoint response was computed using nine-year adjoint sensitivities from 2004 to 2013, while the forward model response used the last fourteen years of a 28-year simulation, although this is unlikely to be a significant factor for subsonic emissions as discussed in Section 5.2.4.

While subsonic aviation leads to a positive column ozone response, the nine-year averaged ozone responses are negative for all supersonic scenarios considered, and range between -0.54 and -12.4 mDU/bn seat-km, for scenarios SST35-1.4-60 and SST35-1.8-60, respectively. On a per seat-km basis, the supersonic aviation column ozone response are 7 to 175 times greater in magnitude compared to the subsonic emission response. This is explained in part by the lower fuel efficiency of the supersonic aircraft, but this covers a factor of nine at most. The remaining difference is driven almost entirely by the reversal in chemical sensitivities between the subsonic and supersonic altitudes considered, since the emissions indices are approximately identical (or slightly lower in the case of nitrogen oxides) for supersonic engines compared to subsonic.

The differences between each supersonic scenario are predominantly the consequences of differences in the altitude ceiling, and thus high-speed Mach number.

Using adjoint sensitivities, we find that the low-altitude scenario SST35-1.4-60 leads to the lowest normalized column ozone response out of all supersonic scenario, with a magnitude five times greater than the baseline subsonic scenario on a per seat-km basis. On the other hand, we find the high-altitude scenario SST35-2.2-60 leads to the largest ozone response followed by SST35-1.8-60. These two scenarios correspond to the highest-flying supersonic aircraft, with cruise altitudes of 19.8 and 18.3 km, respectively. Other considered scenarios have a high-speed Mach number of 1.6 and cruise at 17.4 km. Their responses range between -1.58 and -2.21 mDU/bn seat-km, based on the aircraft designs. A reduced aircraft range or higher number of seats lead to a lower ozone response per flown seat-km.

We estimate that SST45-1.6-60 results in a normalized column ozone response of -1.5 mDU/bn seat-km, broadly consistent with the value of -0.85 mDU per billion seat-km calculated using forward modeling methods. For scenario SST35-2.2-60, we find a normalized column ozone response of -12.4 mDU/bn seat-km over the nine-year integration period, approximately eight times greater than the response from scenario SST45-1.6-60. The forward modeling approach finds a 36 times greater net change in ozone column between the high-altitude SST35-2.2-60 and low-altitude SST45-1.6-60 designs. This discrepancy arises due to the limited time integration of the adjoint simulations. Longer adjoint runs (10 years or more) would be needed to capture the feedback from emissions at 20 km, and allow the sensitivities to reach a quasi-steady state at 20 km.

Figure 60 shows the effect of implementing overland flight restrictions for scenario SST45-1.6-60. Land restrictions reduce the potential of supersonic aviation, thus lowering the market share and increasing the normalized environmental impact from -1.5 to -1.78 mDU/bn seat-km. This can be explained by a decrease in fleet-wide fuel efficiency for restricted scenarios as shown in Table 8. We also observe that a higher restricted Mach number reduces the magnitude of the normalized ozone response. This is the consequence of larger fleet fuel burn inefficiencies when considering land restrictions (compared to population restrictions) or lower Mach numbers (see Table 8).

Finally, adjoint sensitivities allow the evaluation of the ozone response for each emission component. Figure 60 presents the normalized ozone column response for each emission component. The response to subsonic aviation is almost entirely driven by NO_x emissions, corresponding to 90% of the column ozone response. This is explained by low sensitivities to sulfur, water and other emissions components in the upper troposphere and lower stratosphere compared to the mid and upper stratosphere. Subsonic sulfur emissions account for 9% of the column ozone response. For the supersonic scenarios, NO_x and sulfur are the emission components with the largest contribution. The ratio of contributions between NO_x and sulfur depends on the cruise altitude. Supersonic NO_x emissions account for 31% to 76% of the column ozone response, at low cruise altitude (scenario SST35-1.4-60) and high cruise altitude (scenario SST35-2.2-60) respectively. Supersonic water vapor emissions also contribute to the total ozone depletion up to 6% for scenario SST35-2.2-60 (with a high-speed cruise altitude of 19.8 km) but do not exceed 5% for the other scenarios considered.

The share of sulfur in the total ozone depletion from supersonic aviation varies between 16% and 64% for scenarios SST35-2.2-60 and SST35-1.4-60 respectively. At 16 km, the sulfur attribution is the greatest because the sensitivities to NO_x emissions reverse sign, thus making the NO_x contribution minimal. At 20 km, the negative sensitivities to sulfur reach a local maximum in magnitude, with approximately 3 times the magnitude of the sensitivity to NO_x. However, the cruise altitude NO_x emissions indices are greater than the sulfur emissions index by an order of magnitude, making nitrogen oxides the dominant component at 20 km.

Black carbon and CO emissions are not significant contributors to the mean ozone column response for the subsonic and supersonic cases studied here.

The forward model results presents a decomposition of the impact by exhaust product, described in Section 5.2.4.3. For the scenario SST45-1.6-60, emissions from NO_x, sulfur and water vapor are found to contribute to approximately 40%, 51%, and 5.9% of the column ozone response respectively, according to the forward model results. Using adjoint sensitivities, we find that the component share is 45%, 50%, and 4.2%. Black carbon emissions are found to contribute to 0.8% based on adjoint sensitivities, compared to 0.7% for the forward model results. The forward model predicts a lower contribution of nitrogen oxides compared to the adjoint model for this particular design. This discrepancy is most likely due to the longer integration period used in the forward model. However, it will also be in part due to differences in background meteorology and other model parameters.

The prior discussion focuses on nine-year average responses, but the nature of the adjoint allows us to understand the evolution of an emission's aggregated impact over time. We calculate the contribution of each year of the nine-year adjoint run to the temporally-averaged mean ozone column. The results are presented in Figure 61. The aggregated sensitivities for a given year (e.g. 2010) display the effect of a single-year (e.g. 2010) emission pulse on the time-averaged (over the 2004–2013 time interval) ozone response. The cumulative sum of the effects from yearly individual pulse yield the total time-averaged sensitivity.

The ozone response to nitrogen oxides emissions is steadily-increasing over the first two years and starts to decrease in year three. The magnitude of the NO_x-attributable perturbation grows with time, indicating that the ozone response to NO_x emissions has not reached steady-state after the nine-year GEOS-Chem Adjoint simulation. Based on the adjoint sensitivities, the cumulative response to NO_x emissions becomes negative in year four.

At the altitudes considered, the sensitivities to sulfur emissions leads to ozone depletion and the magnitude of the sulfur attributable ozone response grows steadily over the full time period of the simulation. Unlike the response from nitrogen oxides, the sulfur-induced perturbation does not reverse sign at any point throughout the simulation. The water vapor emissions lead to ozone depletion, whose magnitude levels off after two years.

Based on this information, we conclude that nine-year adjoint sensitivities are sufficient to estimate a steady-state response of water vapor emissions, but longer adjoint runs are needed to capture the full response associated to NO_x emissions. However, the contribution of sulfur levels off after seven years, and these nine year sensitivities are sufficient to provide insight into the relative impacts of aircraft flying at different altitudes.

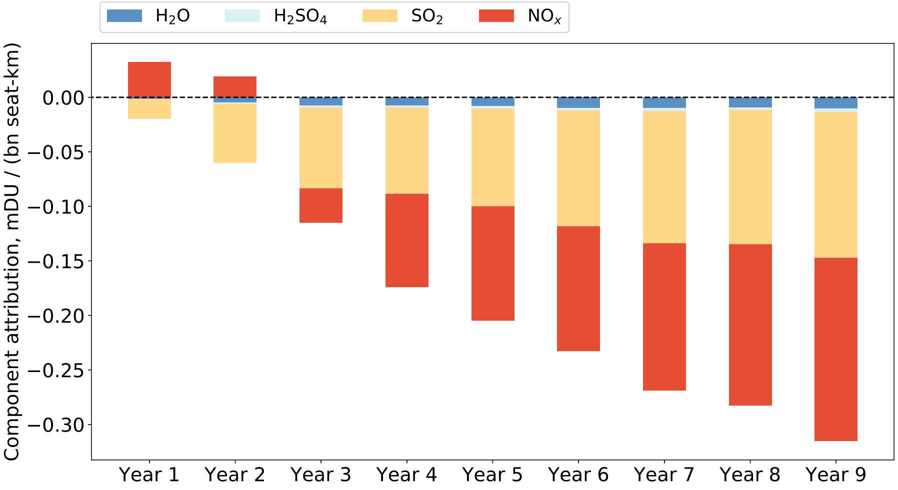

Figure 61: Yearly contribution to the nine-year mean ozone column response to emissions from scenario SST45-1.6-60 with an altitude ceiling of 17.4 km.

6.3.1.2 Total aerosol optical depth response

Figure 62 presents the emission component attribution for the total aerosol optical depth (AOD). When evaluating the objective function, the aerosol optical depth is weighted by the grid-cell area. The results are expressed in changes in AOD per billion available seat-km.

For each scenario considered in this study, sulfur emissions are the major contributor to the aerosol optical depth. The release of sulfur in the form of SO_2 and sulfate aerosols leads to a positive change in the aerosol optical depth and is responsible for up to 94% of the response. This sulfur-attributable response reaches 68% for subsonic aviation, where nitrogen oxides play a greater relative role compared to the supersonic scenarios considered here.

We find that black carbon is a minor contributor to the induced change in aerosol optical depth with contributions of up to 4%. The changes in total aerosol optical depth vary between 1.0×10^{-8} and 4.8×10^{-8} per billion seat-km—corresponding to scenarios SST-35-1.4-60 and SST-35-2.2-60, respectively. Black carbon has no chemical sinks other than deposition processes, which efficiently scavenge black carbon aerosols and prevents its reinjection in the stratosphere through tropical upwelling. Black carbon emissions at higher altitude thus leads to greater sensitivities of AOD, as they remain in the atmosphere for longer. Scenario SST45-1.6-60 is characterized by a total AOD increase of 1.32×10^{-6} per billion seat-km, with a black-carbon attributable change of 2.0×10^{-8} per billion seat-km, consistent with Section 5.2. As a comparison, subsonic aviation leads to an increase in total AOD of 3.6×10^{-8} per billion seat-km, with black carbon being responsible for a change of 1.3×10^{-9} per billion seat-km. This compares to a forward model-derived black carbon-induced change in AOD of 2.2×10^{-9} per billion seat-km. This can be explained by differences in meteorology between GEOS-5 and MERRA-1, leading to different values of age of air and black carbon lifetime in the stratosphere. We also find that the black carbon

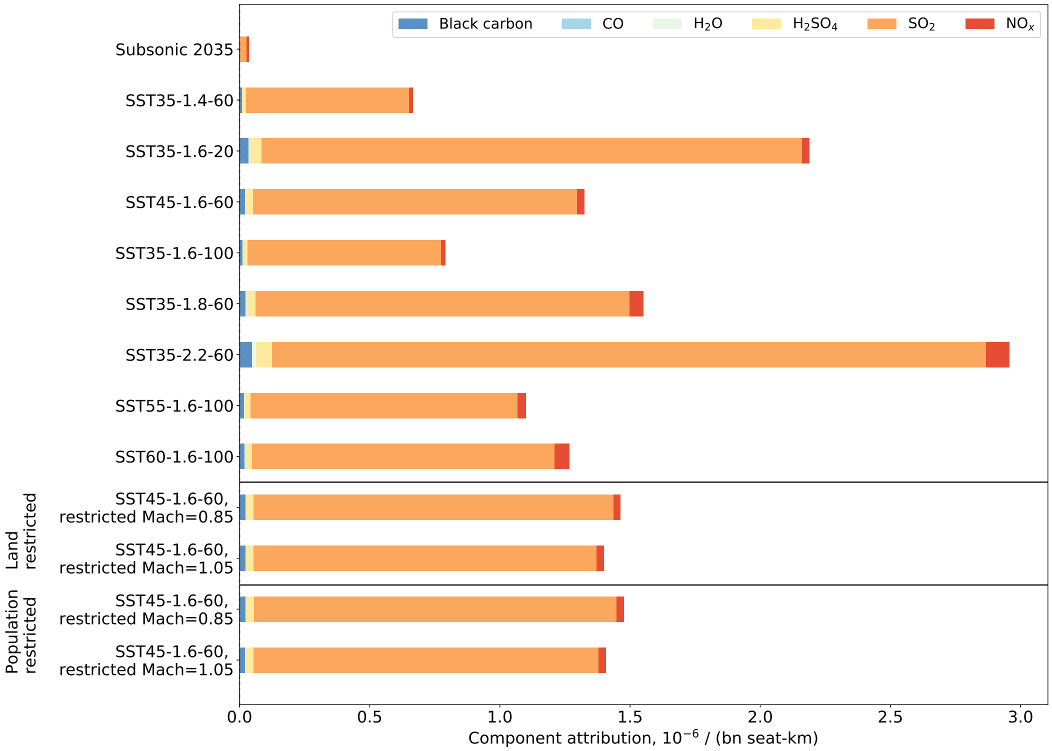

Figure 62: Emission component attribution to area-weighted aerosol optical depth.

contribution to AOD is 15 times greater for scenario SST45-1.6-60 compared to the baseline subsonic scenario on a per seat-km basis. The forward model approach estimates this ratio to be approximately 20, as described in Section 5.2. Emission species other than sulfur and black carbon have negligible contributions to total aerosol optical depth.

Figure 62 shows that the cruise altitude is a dominant factor in the aviation-attributable AOD response. The scenario with the highest cruise altitude leads to a larger AOD perturbation.

Additionally, we find that flight restrictions increase the AOD response, by up to 12% (on a per bn seat-km basis), with land-restricted scenarios having a slightly reduced response compare to the scenarios with population-restricted flight areas. This is the consequence of lower fleet fuel efficiencies for restricted scenarios, as shown in Table 13.

6.3.2 Sensitivity to latitude and altitude of emissions on averaged ozone column

Figure 63 displays the time evolution of zonally-averaged adjoint sensitivities to nitrogen oxides emissions used for this analysis. The sensitivities cover different altitude bands, representing subsonic and supersonic cruise altitudes ($\sim$11 km and $>$14 km respectively). Sensitivities to NO_x emissions vary by two orders of magnitude between the near-surface and 25 km. Two color scales are hence used to distinguish

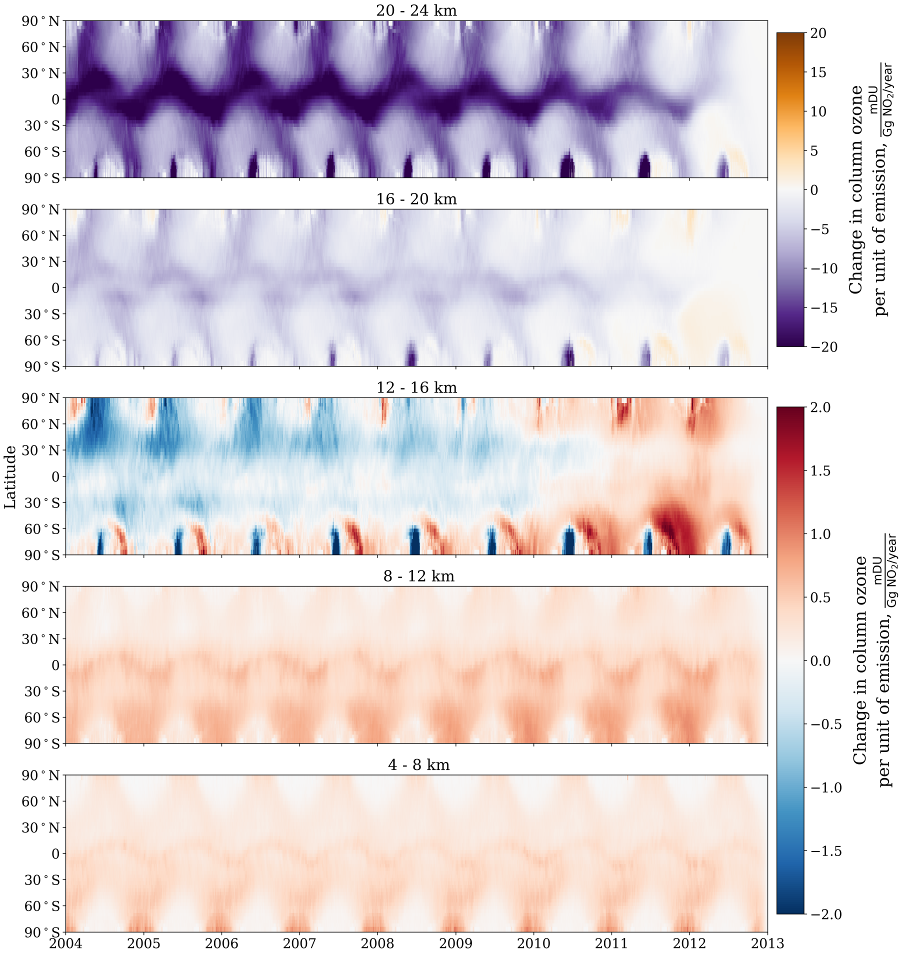

Figure 63: Temporal evolution of zonally-averaged sensitivities of total ozone column to NO_x emissions for different altitude bands. Different color scales are used to differentiate between the low altitude (<16 km) and higher altitude behaviors. Commercial subsonic aviation typically cruises between 10 and 12 km.

between low altitude (<16 km) and higher altitude behaviors.

In the troposphere, we observe an asymmetry in the sensitivities between hemispheres. Sensitivities are greater in the less polluted Southern Hemisphere; a greater ozone response is expected in a cleaner environment for the same amount of NO_x emissions. The polar nights are characterized by sensitivities close to zero in the troposphere. No significant interannual variability is observed in the lowest altitude band, despite the variations in meteorological conditions. This signifies that tropospheric sensitivities have reached a steady-state.

Above 12 km, the hemispheric asymmetry disappears, seasonal patterns, such as the Antarctic winter and spring seasons, appear and the interannual variability becomes significant. Stratospheric timescales are usually of the order of multiple years. Obtaining steady-state sensitivities thus means that a multi-year simulation is required to evaluate adjoint sensitivities to stratospheric-oriented objective functions.

In the mid-stratosphere (20-24 km band in Figure 63), sensitivities to nitrogen

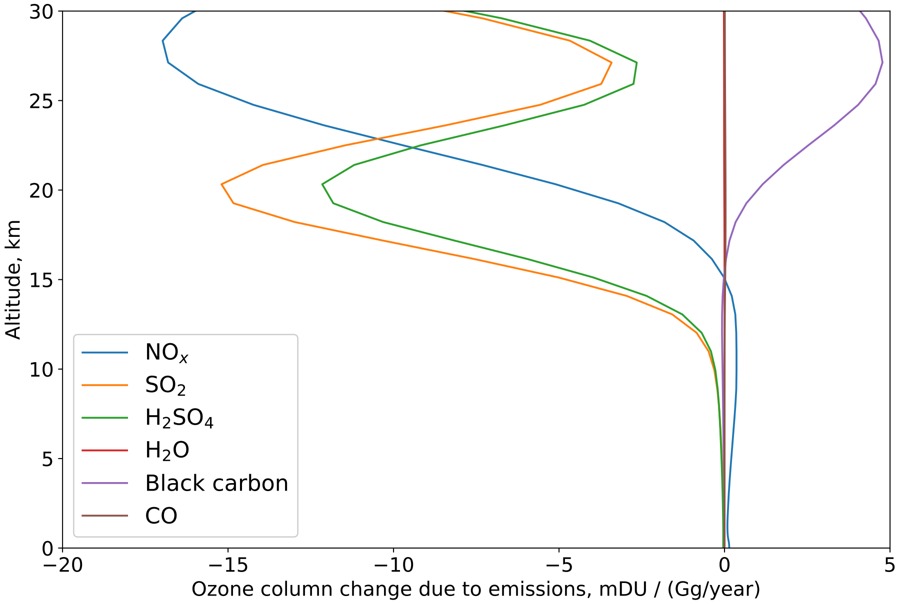

Figure 64: Aggregated sensitivities as a function of altitude for each emission component.

oxides reach a quasi-steady state after an initial time of one year (adjoint integration time is backwards). After the first few years of adjoint integration, the ozone-depleting NO_x cycles lead to a negative sensitivity in the tropics and the sunlit poles of approximately -15 mDU/(Gg NO_x/year). As a reference point, this value compares to an average of +0.23 mDU/(Gg NO_x/year) in the four to eight km band.

Figure 64 displays averaged sensitivities for each aviation emission component as a function of altitude. In the upper troposphere and lower stratosphere, where subsonic commercial aviation cruises, NO_x is the dominant contributor to column ozone.

Above 12 km, sulfur leads to ozone depletion and becomes increasingly important. For the fuel sulfur content and subsonic fleet mean cruise emissions indices used here, sulfur emissions are the dominant contributor to the mean ozone column response in the 16–18 km band, where the sensitivities to NO_x emissions reverse.

The sensitivities to black carbon are negligible at altitudes lower than 20 km. Above 20 km, any increase in black carbon will lead to additional ozone. Given the low mass of emitted black carbon, the contribution from soot particles is negligible compared to the other emission component. On the other hand, the sensitivity to water vapor is relatively small on a per kg basis, but H_2O emissions contribute up to 10% to the ozone response in the stratosphere because of the large amount of water vapor released compared to NO_x and sulfur.

Based on the subsonic fleet mean cruise-level emissions indices, we derive sensitivities with respect to aviation fuel burn and we find that the 13–15 km altitude band is approximately column ozone neutral, consistent with previous studies (Dutta et al., 2005). This is the result of the balance between NO_x-driven ozone production and sulfur-induced ozone depletion. We also find that the column ozone-neutral altitude depends on the NO_x to sulfur emission ratio, with lower NO_x emissions

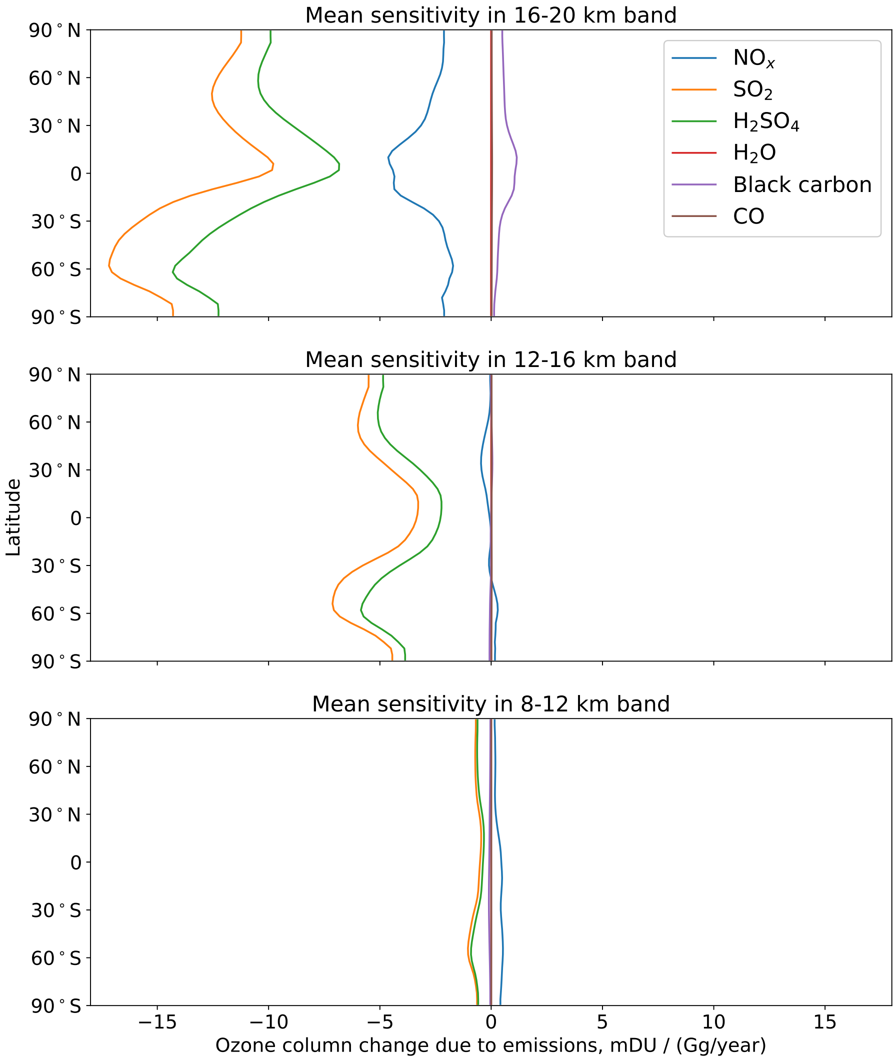

Figure 65: Aggregated sensitivities as a function of latitude for each emission component.

indices driving the neutral altitude downward.

Figure 65 shows the zonally integrated sensitivities at different altitude bands for each emission component as a function of latitude. In the 8–12 km band, little variation in the adjoint sensitivities with respect to latitude is observed. A slight increase in sensitivities can however be noticed in the less-polluted Southern Hemisphere.

Above 12 km, latitudinal variations become important. The sensitivities to sulfur peak in the extra-tropics and are lower near the equator by a factor of 2 compared to the 30°–60°N average.

In the 16–20 km band, the sensitivities of total ozone column to nitrogen oxides display an opposite behavior, where the sensitivities are larger in equatorial regions compared to the extra-tropics. The sensitivities in both regions vary by a factor of 3.

The sensitivity to black carbon becomes positive in the equatorial 16–20 km band.

However, it does not contribute significantly to the mean ozone column response due to the low black carbon emissions.

6.3.3 Sensitivity to ice surface area

Contrails are an important climate forcer and have been the subject of a number of previous assessments. Their representation in global climate model and chemistry transport models is, however, still limited due to modeling shortcomings and for reasons described in Section 4.

Adjoint models offer the possibility to estimate sensitivities of an objective function without a priori knowledge on emissions inventories. We use the GEOS-Chem Adjoint to estimate the sensitivity of total ozone column, in mDU, to a change in ice surface area density, expressed in mm^2/cm^3.

Figure 66 displays the sensitivity of total ozone column to changes in ice aerosol surface area density expressed in $\text{mDU}/((\text{mm}^2/\text{cm}^3)/\text{year})$. The two panels show the averaged sensitivity for the 8–12 km and 12–16 km altitude bands respectively. The column ozone sensitivity to changes in ice aerosol surface area is negative. Any positive change in ice surface area (e.g. from contrails) leads to a net ozone depletion.

We find an average sensitivity of -0.64 and -16 $\text{mDU}/((\text{mm}^2/\text{cm}^3)/\text{year})$ for the 8–12 km and 12–16 km altitude bands. However, seasonal patterns are significant for each Hemisphere and are tied to local winter events, with sensitivities reaching up to -1.1 and -1400 $\text{mDU}/((\text{mm}^2/\text{cm}^3)/\text{year})$ for each altitude bands. Additional aerosol surface area during polar nights leads to enhanced conversion of reservoir species to active chlorine and bromine, which catalytically deplete ozone once polar night ends. Outside of the polar nights, the sensitivities reach background values of -0.1 and -1 $\text{mDU}/((\text{mm}^2/\text{cm}^3)/\text{year})$ for 8–12 and 12–16 km bands.

The latitudinal variations of the sensitivities to ice aerosol surface area are significant as well. The extra-tropical region is characterized with the largest sensitivities, while sensitivities are negligible around the equator.

Using APCEMM, described in Section 3, we estimate the impact on total ozone column from a single contrail. We find that the total contrail aerosol surface area typically ranges between 10^3 and 5×10^3 m^2 per meter of flight path. The total contrail length is estimated from the literature. Using infrared channels from the Advanced Very High Resolution Radiometer, Mannstein et al. (1999) find an average contrail length of 20 km, with contrail streaks varying from 2.4 to 600 km. Releasing a single contrail in an extra-tropical grid box leads a total surface area density of $\sim 8 \times 10^{-7}$ mm^2/cm^3. Using adjoint sensitivities, we estimate the nine-year column ozone impact of a single contrail to be -6×10^{-7} mDU for the 8–12 km band. For the 12–16 km band, we find that the impact ranges up to -6×10^{-4} mDU during polar night, with a mean value -1×10^{-5} mDU. However, more work is needed to establish a spatial and temporal contrail ice inventory.

6.4 Effects of plume-scale chemistry

Section 3 shows that instant dilution of emissions, as performed in CTMs, leads to non-physical ozone production and does not capture the plume-scale conversion

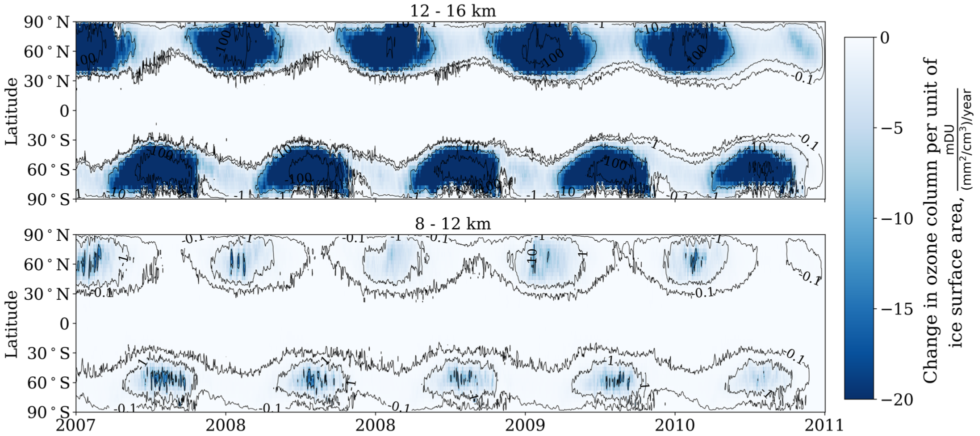

Figure 66: Sensitivities of total ozone column to changes in ice surface area density expressed in mDU/((mm^2/cm^3)/year) for the 8–12 km (bottom) and 12–16 km (top) altitude bands respectively. Contour lines display the magnitude and range from -0.1 to -100, varying by a factor of 10 between each level.

of nitrogen oxides to reservoir species. Additionally, sulfur oxidation in the plume converts SO_2 to sulfate aerosols. This conversion step is driven by reaction with OH which becomes limited in the first hours after emission.

In this section, we quantify how the inclusion of the effects of plume-scale chemistry affects the aviation-attributable ozone response. Using APCEMM, we estimate season and altitude-dependent variations in the NO_x to NO_y partitioning and on the sulfur to H_2SO_4 conversions occurring throughout the first 24 hours after emissions. The derived conversion factors are applied to aircraft emissions, above 300 hPa and below 55 hPa, corresponding to a pressure-altitude of ∼9 km and 20 km respectively. Outside of that range, aircraft emissions are considered without any plume processing. We use adjoint-derived sensitivities to capture how changes in the NO_y and sulfur partitioning, as computed by APCEMM, could affect the ozone response.

Figure 67 displays the adjoint-derived column ozone response, without and with plume-scale results. We note that the inclusion of plume-scale effects reduces the total column ozone impact by up to 6.3%, except for the higher altitude scenarios SST35-1.8-60 and SST35-2.2-60, for which the impact is increased by 0.6% and 2.5%, respectively. For the baseline subsonic scenario, the column ozone response is reduced by 4.6% when including plume-scale effects.

For all scenarios, the share of H_2SO_4 in the aviation-attributable ozone perturbation increases owing to the conversion of sulfur dioxide to sulfates. Similarly, the NO_x-attributable response decreases, except for scenario SST35-2.2-60.

At subsonic altitudes, between 30% and 80% (during local summer and winter respectively) of the initial NO_x emissions remains in the plume and approximately 20% and 15% of it is converted to HNO_3 and HO_2NO_2 respectively after 24 hours, in agreement with Vohralik et al. (2008). We find that sensitivities of column ozone to HNO_3 are lower than the sensitivities to NO_x, on a molar basis, thus explaining the reduction in the subsonic response. At higher altitudes, a large fraction (greater than

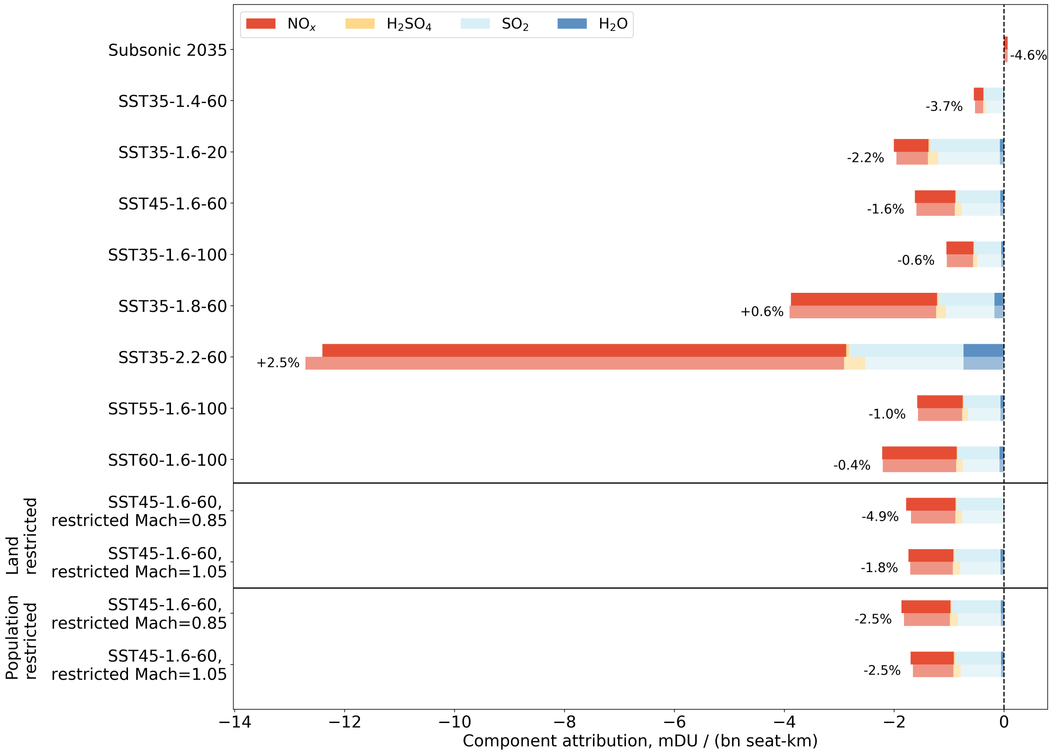

Figure 67: Emission component attribution to column ozone, including a plume-scale processing of emissions. For each scenario, the results are displayed without (top) and with (bottom) plume-scale processing of emissions. The percentage values represent the total change in the aviation-attributable response owing to plume-scale processes.

50% and up to 90%) of nitrogen oxides is still present in the plume. The remaining fraction is a combination of HNO_3, HO_2NO_2 and N_2O_5. The resulting effect is to decrease the NO_y-attributable response, except for scenario SST35-2.2-60, in which the high cruise altitude corresponds with lower sensitivities to NO_y reservoir species, compared to NO_x.

6.5 Synthesis and literature comparison

6.5.1 Previous studies

The environmental damages from a fleet of supersonic aircraft have been estimated in previous reports. In Section 5 of this assessment, we provide an updated estimate, which is compared to forward modeling approaches described in previous NASA reports (Kawa et al., 1999; Dutta et al., 2005). In this section, we use adjoint modeling to calculate sensitivities of total ozone column and aerosol optical depth. The derived adjoint sensitivities allow us to assess with reasonable precision the environmental impacts of a wide range of possible future scenarios.

Previous reports have evaluated forward model-derived sensitivities. Using adjoint modeling, we find that the sensitivities to NO_x, sulfur and water vapor emissions critically depend on the aircraft cruise altitude. This agrees with findings from Dutta et al. (2005).

Looking at NO_x emissions, we obtain sensitivities of +50, -250, and -950 mDU of ozone column change per Tg of NO_x emissions (on a NO_2 mass basis) for cruise altitudes of 15, 17.5, and 20 km, respectively. These values translate to a change of +0.01%, -0.08%, and -0.32% change in column ozone per Tg of NO_x for 15, 17.5, and 20 km, respectively. Dutta et al. (2005) found a sensitivity of -0.04% per Tg of NO_x for the 15–17 km altitude band, and -0.13% per Tg of NO_x for the 17–19 km altitude band, broadly consistent with our own results. Similarly, Kawa et al. (1999) found that nitrogen oxides emissions are not a major contributor to column ozone; however, they found that water vapor emissions are dominant, which is in conflict with this report.

We find that sulfur emissions could explain up to 64% of the total ozone depletion from supersonic aviation, depending on the deployment scenario. In broad terms, this is in agreement with Kawa et al. (1999), which found a high sensitivity to sulfate aerosols emissions. Dutta et al. (2005) did not find that sulfur was a major contributor to ozone depletion, as they assumed that sulfur will be eliminated from the fuel in the coming decades. In this study, we assumed a constant fuel sulfur content of 600 parts per million on a mass basis. Based on forward and adjoint modeling studies, we find that sulfur, whether in the form of SO_2 or in sulfate aerosol, contributes to ozone depletion, with similar sensitivities. The inclusion of plume-scale effects, converting emitted SO_2 to sulfate aerosol, does not change the contribution of sulfur to the net column ozone impact significantly.

According to our study, water vapor emissions contribute between 2 to 6% of the ozone response attributable to supersonic aviation. Larger sensitivities to water vapor emissions are obtained at higher altitudes. The obtained sensitivities to water vapor are smaller in this study compared to previous NASA reports.

We conclude that reducing the cruise altitude by approximately 1.7 km (from scenarios SST35-2.2-60 to SST35-1.8-60) reduces the ozone depletion effects by 70% on per seat-km basis. This is in agreement with Kawa et al. (1999), who found that decreasing the cruise altitude from approximately 19 km to 17 km reduces the absolute ozone impact by ∼50%.

Flight restrictions were not considered in previous NASA assessments. We find that land and population flight restrictions increase the normalized ozone response, leading to a reduced supersonic aviation market, but increased ozone column change on a per seat-km basis. This is the result of higher fleet fuel burn inefficiencies when flight restrictions are enforced.

No previous studies of the role of contrail ice on total column ozone was found at the global scale. Using adjoint sensitivities, we are able to assess the column ozone change from additional ice surface area. We find that the sensitivities are season-dependent and are tied with local polar events in both hemispheres.

Combining adjoint sensitivities to plume modeling, we estimate that the role of plume-scale processes reduce the net column ozone impact by approximately 5%, except for the high-flying scenarios SST35-1.8-60 and SST35-2.2-60, for which the inclusion of plume processes increases the responses by 0.6% and 2.5%, respectively. Kraabøl et al. (2002) found that the total ozone perturbation decreased by 15–18% at northern middle and high latitudes for subsonic aviation. The adjoint approach used in this report only allows us to obtain the global average ozone response. Looking at the seasonal cycle presented in Kraabøl et al. (2002), the annual average due to the inclusion of plume-scale effects lies between -20 and -150 mDU. Using adjoint sensitivities, we find that the impact of subsonic aviation is lowered by 4.6% when including plume-scale effects, corresponding to a reduction of approximately 55 mDU, consistent with Kraabøl et al. (2002). However, Kraabøl et al. (2002) did not consider further conversion of SO_2 to sulfate particles in the plume.

6.5.2 Synthesis

We have introduced the Unified Chemistry eXtension (UCX) into the GEOS-Chem Adjoint, allowing us to evaluate environmental responses to a wide-range of high-altitude emissions scenarios. Using nine-year adjoint sensitivities, we find that the introduction of a fleet of supersonic aircraft leads to a net ozone depletion, with magnitudes ranging from -0.54 to -12.4 mDU per billion seat-km traveled, 7 and 175 times greater in magnitude compared to the subsonic ozone response. The supersonic aircraft cruise altitude is the most critical aircraft parameter influencing the ozone and aerosol optical depth response to emissions.

We also estimate that sulfur plays a critical role in the column ozone response to supersonic aviation emissions, reaching contributions up to 64% for a cruise altitude 16 km. This share is maximal in the 15–16 km band. Because of the reversal in the sensitivity of column to NO_x emissions, we validate the possibility of an column ozone-neutral cruise altitude. This neutral altitude depends on the ratio of sulfur to nitrogen oxides emissions indices and lies in the 13–15 km altitude band, assuming conventional emissions indices.

We provide one of the first estimates of the impact of contrail ice surface area density on ozone column. We find that the sensitivities to contrail ice display large seasonal and latitudinal dependencies, with large negative sensitivities tied to local polar winters. During such events, the sensitivities reach -1 and -1400 mDU/((mm^2/cm^3)/year) in the 8–12 and 12–16 km altitude bands respectively. Using the plume modeling presented in this study, we find that a single subsonic or supersonic contrail could lead to a net ozone depletion of up to 6×10^{-7} and 6×10^{-4} mDU for both altitude bands.

We combine the results of the plume modeling section with adjoint sensitivities to yield the adjoint-derived effects of plume-scale chemistry for subsonic and supersonic aviation. We conclude that the inclusion of plume-scale effects reduces the column ozone by approximately 5% for all subsonic and supersonic scenario, except for the high-altitude scenarios SST35-1.8-60 and SST35-2.2-60.

7 Conclusions and future work

In this report, we have evaluated the atmospheric and climate impacts of notional commercial supersonic aircraft which are similar to designs currently being proposed or developed. Considering a notional 60-passenger aircraft capable of cruising at Mach 1.6 with a range of 4500 nautical miles (SST45-1.6-60) with no restrictions on overland flight, we identify a potential market for supersonic travel comprising 0.86%

of total seat-km. The aircraft would be responsible for 4.4% of fuel burn and 2.6% of NO_x emissions from commercial aviation, with the additional emissions occurring at a typical cruise altitude of 17 km. The emissions from this supersonic fleet would decrease the global mean ozone column by 140 mDU (-0.045%), compared to an increase of 1600 mDU (+0.52%) for the forecast 2035 subsonic fleet. However, the size of the supersonic fleet, the emissions, and the resulting impacts all depend upon uncertain design parameters and policy considerations.

Market outcome and global emissions estimation When no overflight restrictions for supersonic aircraft are imposed, we find a small global market for supersonic flights (up to 2.5% of global aviation) which is largely focused on high-income countries due to the high costs of commercial supersonic flights. The market potentials are sensitive to aircraft design, with global seat-km varying by a factor of 30 across the notional aircraft under consideration in this study. Aircraft seat capacity is the strongest driver of this variability given economies of scale. Introduction of commercial supersonic services is expected to increase aviation fuel burn by up to 7% and NO_x emissions up to 10% under the unrestricted scenarios.

We find that 78 to 100% of the potential market without flight restrictions would not be served if overflight restrictions are in place globally, due to increases in flight duration and costs. Reducing the stringency of overflight restrictions (e.g. to overflight restrictions for areas with population density higher than 50 inhabitants per sq. km only) can make supersonic routes viable in significant markets (e.g. North America) which would not see commercial supersonic services otherwise. Furthermore, higher speeds in the “low-speed” regime can provide some competitive advantage for supersonic aircraft even when overflight restrictions exist, especially when aircraft are not optimized for very high supersonic cruise speeds. With reduced restrictions and improved “low-speed” performance, supersonic aircraft could account for up to 0.6% of aviation seat-km, or up to 2.8% of global aviation fuel burn.

Since the market potential for supersonic aircraft exhibits a high sensitivity to operational costs (and hence fuel burn per seat-km) and flight times, re-assessments of the market size may be warranted for any future aircraft designs with performance differing from the notional aircraft considered here. In addition, the approach to market modeling taken here cannot capture the market for private supersonic aircraft. As such, a different modeling approach would be warranted to model the market for private supersonic jets.

Plume-scale chemical effects We develop and use an aircraft plume model, APCEMM, to quantify the role of plume-scale processes on the long-term impacts of aircraft emissions. This is because the instant dilution of emissions into large grid cells, as conventionally implemented in CTMs, leads to a positive bias in ozone production and in NO_x to NO_y conversion rates. In absolute terms, the bias in the instant-dilution approach is largest during summertime when ozone production is enhanced across the Northern Hemisphere.

APCEMM is also able to capture the formation and evolution of condensation trails. We find that heterogeneous chemistry on the surface of ice crystals leads to a different partitioning of nitrogen species, thereby depleting NO_x and ambient N_2O_5 to longer-lived HNO_3. Contrail-induced impacts on ozone production are small, with an overall difference of ~10% with respect to the pure gas-phase response. Heterogeneous chemistry on ice crystals gains importance at lower pressures and shifts the N_2O_5-HNO_3 local equilibrium.

In this study, we have incorporated the impact of plume-scale chemistry on global atmospheric impacts through the use of adjoint sensitivities. However, further coupling between APCEMM and GEOS-Chem could be pursued as a means to capture these effects in "forward" model runs.

Contrails Assessing contrail impacts from both subsonic and supersonic aviation at a global scale requires an accurate representation of upper tropospheric and stratospheric conditions. For this purpose, we use sonde profiles from the Integrated Global Radiosonde Archive to evaluate the percentage of each sonde profile satisfying the persistent contrail condition (PCC).

The sonde observations show that, on global average, the percentage of the vertical atmospheric profile satisfying the PCC peaks at 3.9% at approximately 10 km and decreases by a factor of 8.8 at 17 km (cruise altitude for Mach 1.6 notional aircraft), and by a factor of 11.9 at 19 km altitude (cruise altitude for Mach 2.2 notional aircraft). The altitude of the peak PCC region decreases with increasing latitude, from 8.5 km in the poles to 13.5 km in the tropics. Overall, this results in the likelihood of persistent contrail formation being (1) a factor of 1.9 higher at 17 km than at 10.5 km (typical subsonic cruise altitude) in the tropics; and (2) a factor of 105 lower between the same altitudes near the poles. Using the fuel-burn weighted PCC as a metric, the flight altitude has the strongest effect on potential persistent contrail formation from SSTs. Among the different notional supersonic aircraft, the variation between highest and lowest fuel burn weighted PCC is 153% in the tropics and less than 50% in the mid-latitudes and near the poles. In the mid-latitudes and near the poles, this is because the high fuel consumption during climb and the transition from subsonic to supersonic speeds drives the fuel burn weighted PCC. In comparison, in the tropics, the variability is driven by contrails forming at supersonic cruise altitudes.

There are also seasonality trends in the PCC, and the maximum percentage PCC occurs at 1–2 km higher altitudes in northern hemispheric winter. This altitude shift could lead to seasonal trends in the number of contrails forming from supersonic flights.

Further work is needed to extend the evaluation of both subsonic and supersonic contrails to include lifetime, microphysical properties, and climate impacts. While the APCEMM model is suitable for modeling individual contrails, it is not computationally feasible to use APCEMM to model all contrails at a global scale. This motivates the development of simplified or reduced-order models that can capture the sensitivities of contrail properties to aircraft parameters and atmospheric conditions.

Long-term changes in atmospheric composition and radiative forcing We estimate emissions from subsonic commercial air services in 2035 to produce a non-

CO_2, non-contrail radiative forcing of $1.3 \times 10^{-3}\,\mathrm{mW\,m^{-2}}$ per billion seat-km flown. In contrast, we find a net negative radiative forcing of $20 \times 10^{-3}\,\mathrm{mW\,m^{-2}}$ from introducing the SST45-1.6-60 fleet. This negative radiative forcing is attributable to the long lifetime of emitted sulfur compounds, and the low (relative to prior studies) positive forcing estimated for water vapor.

The notional baseline aircraft is associated with a 140 mDU reduction in the global mean ozone column per billion seat-km traveled, compared to the 1100 mDU increase per billion seat-km for subsonic aviation (neglecting long-term methane feedbacks). Sulfur emissions are responsible for 54% of net ozone depletion. NO_x emissions cause 35% of net global ozone depletion, with the remainder resulting from water vapor, carbonaceous aerosols, and non-methane volatile organic compounds.

Changes in global column ozone and radiative balance attributable to emissions from supersonic aircraft take up to a decade to reach steady-state. Even when allowing 14 years of spin-up and averaging over a further 14 years, we find seasonal and interannual variability, with a standard deviation of 16% in the annual mean ozone depletion. This suggests that studies using single, repeating years of meteorology may not capture the mean magnitude and potentially the sign of some elements of the atmospheric response. This long equilibration period is due to the long lifetime of stratospheric emissions. Long-term methane feedbacks, which offset 41% of the ozone increase resulting from subsonic aviation after 15–28 years, contribute only 11% of the total ozone depletion calculated for SST45-1.6-60 in the same period.

These results are highly sensitive to the design Mach number. A higher Mach number—and therefore cruise altitude—will result in a net positive radiative forcing due to greater positive radiative forcing from depletion of ozone and the accumulation of stratospheric water vapor. Not including methane feedbacks, the higher-altitude SST35-2.2-60 aircraft produces a net radiative forcing of $100 \times 10^{-3}\,\mathrm{mW\,m^{-2}}$ per billion seat-km traveled, compared to $-14 \times 10^{-3}\,\mathrm{mW\,m^{-2}}$ for the lower-altitude SST45-1.6-60. However, including methane feedbacks changes these results to $26 \times 10^{-3}\,\mathrm{mW\,m^{-2}}$ and $-20 \times 10^{-3}\,\mathrm{mW\,m^{-2}}$ respectively. Ozone depletion from SST35-2.2-60 is also calculated to be 38 times greater, per seat-km, than for the lower-altitude aircraft, and 22 times greater per unit of fuel burned.

Finally, we find that fuel sulfur content may play a dominant role in determining the effects of supersonic aviation on atmospheric composition and radiative forcing. In addition to providing over half of the ozone depletion resulting from SST45-1.6-60, inorganic aerosols (almost exclusively sulfur) provide the largest negative component of radiative forcing from supersonic aviation.

Future investigations may consider the use of higher-resolution meteorological data, which may be able to provide more insights into the relationship between stratospheric dynamics and the long-term chemical impacts of supersonic aviation. Additional research is also needed to better constrain the role of sulfur on the impacts of supersonic aircraft with intermediate Mach numbers ($\simeq$1.5), and the sensitivity of these results to the representation of aerosol microphysics and heterogeneous chemistry in atmospheric models.

Extended sensitivity analysis We use adjoint-derived sensitivities to compute the nine year-mean column ozone response to any change in aviation emissions. We then apply these sensitivities to explore the variability of the atmospheric response with different notional aircraft and overflight restriction scenarios. We find a net change in nine year-mean column ozone of +0.071 and -1.5 mDU/bn seat-km for the subsonic and SST45-1.6-60 supersonic scenarios respectively. Effects from other supersonic scenarios range between -0.54 and -12.4 mDU/bn seat-km, with cruise altitude being the dominant source of variability.

As shown previously, sulfur emissions from supersonic aviation contribute between 25% and 75% of the total ozone column response. We find that there is an area of increased sensitivity to sulfur emissions between 15 and 25 km altitude, in which emissions of either sulfur dioxide or sulfate aerosol result in greater ozone depletion than results from NO_x emissions. Accordingly, we find that—for a nine-year outlook with the emissions indices given here—the 13–15 km altitude band is approximately column ozone-neutral. A higher NO_x emissions index or lower fuel sulfur content would drive this ozone-neutral altitude upward.

Although cruise altitude is the dominant factor in determining the change in column ozone and aerosol optical depth resulting from supersonic aviation, we find changes in these quantities in response to the implementation of different flight restrictions. Banning supersonic flight over land results in a 12% increase in total aerosol optical depth per seat-km flown, relative to a scenario with no flight restrictions. This increase is due to the increase in fuel burn associated with the indirect routing.

We also quantify the effect of contrail ice surface area on total column ozone. We find a mean value of -0.64 and -16 mDU per ((mm^2/cm^3)/year) in the 8–12 km and 12–16 km altitude bands respectively, with greatest sensitivity occurring during hemispheric winter and outside the tropics. This finding must be considered alongside the expectation of fewer, but longer-lived, contrails from supersonic aircraft as discussed earlier.

Finally, we find that incorporation of plume-scale processing reduces the estimated, nine-year impacts of aviation emissions on global mean column ozone by ~5%. This is true for both subsonic aviation and most of the notional supersonic aircraft designs considered. The only exceptions are the higher-altitude SST35-1.8-60 and SST35-2.2-60, for which the inclusion of plume-scale processes increases the magnitude of the ozone response by 0.6% and 2.5%, respectively.

The results shown here cover only a few of the adjoint objective functions which could be of interest. The adjoint model could be further extended to compute sensitivities of radiative forcing or surface particulate matter concentrations to emissions. The former would provide a more direct measure of supersonic aircraft climate impacts, while the latter would provide a means of assessing air quality impacts due to supersonic aviation. The adjoint sensitivities computed using this model can also form the basis for tools that enable the rapid evaluation of multiple policy or technology scenarios, and can be used to propagate uncertainties in the emissions to uncertainties in their impacts. The adjoint approach could also be directly incorporated into models of supersonic aircraft routing, so that routes with minimal environmental impact can be identified while accounting for routing inefficiencies.

References

Abrantes, P. A. L. and M. R. Wardman (2011). “Meta-analysis of UK values of travel time: an update”. In: *Transportation Research Part A: Policy and Practice* 45.1, pp. 1–17. DOI: `10.1016/j.tra.2010.08.003`.

Aerion (2020). *Aerion Supersonic*. Available at `https://www.aerionsupersonic.com/as2/` (2020/05/15).

Agarwal, A., R. L. Speth, T. M. Fritz, S. D. Jacob, T. Rindlisbacher, R. Iovinelli, B. Owen, R. C. Miake-Lye, J. S. Sabnis, and S. R. H. Barrett (2019). “SCOPE11 method for estimating aircraft black carbon mass and particle number Emissions”. In: *Environmental Science & Technology* 53, pp. 1364–1373. DOI: `10.1021/acs.est.8b04060`.

Airbus (2019). *Global market forecast 2019-2038*. URL: `http://gmf.airbus.com/?_ga=2.80230110.899656949.1592605395-879329580.1592605395`.

Alegre, J. and L. Pou (2006). *An analysis of the microeconomic determinants of travel frequency*. Tech. rep. 18. DEA Working Papers. Universitat de les Illes Balears, Departament d’Economía Aplicada. URL: `https://ideas.repec.org/p/ubi/deawps/18.html`.

Allroggen, F., M. D. Wittman, and R. Malina (2015). “How air transport connects the world – A new metric of air connectivity and its evolution between 1990 and 2012”. In: *Transportation Research Part E: Logistics and Transportation Review* 80, pp. 184–201. DOI: `10.1016/j.tre.2015.06.001`.

Appleman, H. (1953). “The formation of exhaust condensation trails by jet aircraft”. In: *Bulletin of the American Meteorological Society* 34, pp. 14–20. DOI: `10.1175/1520-0477-34.1.14`.

Ashok, A. and S. R. Barrett (2016). “Adjoint-based computation of US nationwide ozone exposure isopleths”. In: *Atmospheric Environment* 133, pp. 68–80.

Axhausen, K. W., S. Hess, A. König, G. Abay, J. J. Bates, and M. Bierlaire (2008). “Income and distance elasticities of values of travel time savings: New Swiss results”. In: *Transport Policy* 15.3, pp. 173–185. DOI: `10.1016/j.tranpol.2008.02.001`.

Baughcum, S. L., I. C. Plumb, and P. F. Vohralik (2003). “Stratospheric ozone sensitivity to aircraft cruise altitudes and NO_x emissions”. In: *Air Pollution Research Report 83*. Friedrichshafen, Germany: European Commission, pp. 145–150.

Beard, K. V. and H. T. Ochs III (1995). “Collisions between small precipitation drops. Part II: formulas for coalescence, temporary coalescence, and satellites”. In: *Journal of the Atmospheric Sciences* 52.22, pp. 3977–3996.

Berton, J. J., D. L. Huff, K. Geiselhart, and J. Seidel (2020). “Supersonic Technology Concept Aeroplanes for Environmental Studies”. In: *AIAA Scitech 2020 Forum*. DOI: `10.2514/6.2020-0263`.

Bock, L. and U. Burkhardt (2016). “Reassessing properties and radiative forcing of contrail cirrus using a climate model”. In: *Journal of Geophysical Research: Atmospheres* 121, 2016JD025112. DOI: `10.1002/2016JD025112`.

Bock, L. and U. Burkhardt (2019). “Contrail cirrus radiative forcing for future air traffic”. In: *Atmospheric Chemistry and Physics Discussions*, pp. 1–22. DOI: `10.5194/acp-2018-1294`.

Boeing (2016). *Current market outlook 2016 – 2035.* URL: `https://www.boeing.com/resources/boeingdotcom/commercial/about-our-market/assets/downloads/cmo_print_2016_final_updated.pdf`.

Boeing (2019). *Commercial market outlook 2019-2038.* Library Catalog: www.boeing.com. URL: `https://www.boeing.com/commercial/market/commercial-market-outlook/`.

Bolton, D. (1980). "The computation of equivalent potential temperature". In: *Monthly Weather Review* 108, pp. 1046–1053. DOI: `10.1175/1520-0493(1980)108<1046:TCOEPT>2.0.CO;2`.

Boom (2020). *Boom Supersonic.* Available at `https://boomsupersonic.com/` (2020/05/15).

Börjesson, M., M. Fosgerau, and S. Algers (2012). "On the income elasticity of the value of travel time". In: *Transportation Research Part A: Policy and Practice* 46.2, pp. 368–377. DOI: `10.1016/j.tra.2011.10.007`.

Brasseur, G. P., R. A. Cox, D. Hauglustaine, I. Isaksen, J. Lelieveld, D. H. Lister, R. Sausen, U. Schumann, A. Wahner, and P. Wiesen (1998). "European scientific assessment of the atmospheric effects of aircraft emissions". In: *Atmospheric Environment* 32.13, pp. 2329–2418.

Bureau of Transport Statistics (2017). *BTS, 2017. Air Carrier Financial Reports (Form 41 Financial Data).* URL: `http://www.transtats.bts.gov/tables.asp?DB_ID=135` (visited on 08/02/2017).

Burgos, E. R. F., A. Trani, N. Hinze, T. Marien, K. Geiselhart, S. Dollyhigh, and J. Seidel (2020). "Global demand model to estimate supersonic commercial services". In: *AIAA Aviation 2020 Forum.* DOI: `10.2514/6.2020-3260`.

Burkhardt, U. and B. Kärcher (2009). "Process-based simulation of contrail cirrus in a global climate model". In: *Journal of Geophysical Research: Atmospheres* 114, p. D16201. DOI: `10.1029/2008JD011491`.

Caiazzo, F., A. Agarwal, R. L. Speth, and S. R. H. Barrett (2017). "Impact of biofuels on contrail warming". In: *Environmental Research Letters* 12, p. 114013. DOI: `10.1088/1748-9326/aa893b`.

Cariolle, D., D. Caro, R. Paoli, D. A. Hauglustaine, B. Cuenot, A. Cozic, and R. Paugam (2009). "Parameterization of plume chemistry into large-scale atmospheric models: application to aircraft NO_x emissions". In: *Journal of Geophysical Research: Atmospheres* 114.D19.

Center for International Earth Science Information Network (CIESIN), Columbia University (2018). *Gridded Population of the World, Version 4 (GPWv4): Population Count, Revision 11.* (Visited on 01/15/2020).

Chabrillat, S., C. Vigouroux, Y. Christophe, A. Engel, Q. Errera, D. Minganti, B. M. Monge-Sanz, A. Segers, and E. Mahieu (2018). "Comparison of mean age of air in five reanalyses using the BASCOE transport model". In: *Atmospheric Chemistry and Physics* 18.19, pp. 14715–14735.

Chen, C.-C., A. Gettelman, C. Craig, P. Minnis, and D. P. Duda (2012). "Global contrail coverage simulated by CAM5 with the inventory of 2006 global aircraft emissions". In: *Journal of Advances in Modeling Earth Systems* 4. DOI: `10.1029/2011MS000105`.

Chen, J.-P., I.-C. Tsai, and Y.-C. Lin (2013). “A statistical–numerical aerosol parameterization scheme”. In: *Atmospheric Chemistry and Physics* 13.20, pp. 10483–10504. DOI: `10.5194/acp-13-10483-2013`.

Cunnold, D. M., F. N. Alyea, and R. G. Prinn (1977). “Relative effects on atmospheric ozone of latitude and altitude of supersonic flight”. In: *AIAA Journal* 15.3, pp. 337–345. DOI: `10.2514/3.7327`.

Cziczo, D. J., P. J. DeMott, S. D. Brooks, A. J. Prenni, D. S. Thomson, D. Baumgardner, J. C. Wilson, S. M. Kreidenweis, and D. M. Murphy (2004). “Observations of organic species and atmospheric ice formation”. In: *Geophysical Research Letters* 31.12.

Damian, V., A. Sandu, M. Damian, F. Potra, and G. R. Carmichael (2002). “The kinetic preprocessor KPP-a software environment for solving chemical kinetics”. In: *Computers & Chemical Engineering* 26.11, pp. 1567–1579.

Damodaran, A. (2020). *Cost of capital by industry sector*. URL: `http://people.stern.nyu.edu/adamodar/New_Home_Page/datacurrent.html#discrate`.

Dijkstra, E. W. (1959). “A note on two problems in connexion with graphs”. In: *Numerische Mathematik* 1.1, pp. 269–271.

Dirksen, R. J., M. Sommer, F. J. Immler, D. F. Hurst, R. Kivi, and H. Vömel (2014). “Reference quality upper-air measurements: GRUAN Data Processing for the Vaisala RS92 Radiosonde”. In: *Atmospheric Measurement Techniques* 7, pp. 4463–4490. DOI: `10.5194/amt-7-4463-2014`.

DuBois, D. and G. C. Paynter (2006). “Fuel Flow Method 2 for estimating aircraft emissions”. In: *SAE Transactions* 115, pp. 1–14.

Durre, I., R. S. Vose, and D. B. Wuertz (2006). “Overview of the Integrated Global Radiosonde Archive”. In: *Journal of Climate* 19, pp. 53–68. DOI: `10.1175/JCLI3594.1`.

Durre, I. and X. Yin (2008). “Enhanced radiosonde data for studies of vertical structure”. In: *Bulletin of the American Meteorological Society* 89, pp. 1257–1262.

Dutta, M., K. O. Patten, and D. J. Wuebbles (2005). *Parametric analyses of potential effects on upper tropospheric/lower stratospheric ozone chemistry by a future fleet of high speed civil transport (HSCT) type aircraft*. Tech. rep. CR—2005-213646. NASA.

Eastham, S. D. and S. R. Barrett (2016). “Aviation-attributable ozone as a driver for changes in mortality related to air quality and skin cancer”. In: *Atmospheric Environment* 144, pp. 17–23.

Eastham, S. D., D. K. Weisenstein, and S. R. Barrett (2014). “Development and evaluation of the unified tropospheric–stratospheric chemistry extension (UCX) for the global chemistry-transport model GEOS-Chem”. In: *Atmospheric Environment* 89, pp. 52–63.

Ebert, E. E. and J. A. Curry (1992). “A parameterization of ice cloud optical properties for climate models”. In: *Journal of Geophysical Research: Atmospheres* 97.D4, pp. 3831–3836.

Energy Information Administration (2020). *Annual Energy Outlook 2020 with projections to 2050*. URL: `https://www.eia.gov/outlooks/aeo/pdf/AEO2020%20Full%20Report.pdf`.

Errera, Q. and D. Fonteyn (2001). “Four-dimensional variational chemical assimilation of CRISTA stratospheric measurements”. In: *Journal of Geophysical Research: Atmospheres* 106.D11, pp. 12253–12265.

Eyers, C. J., P. Norman, J. Middel, M. Plohr, S. Michot, K. Atkinson, and R. Christou (2004). *AERO2k global aviation emissions inventories for 2002 and 2025.* Tech. rep. QINETIC/04/01113 (QinetiQ, 2004).

Eyring, V., D. S. Stevenson, A. Lauer, F. J. Dentener, T. Butler, W. J. Collins, K. Ellingsen, M. Gauss, D. A. Hauglustaine, I. S. A. Isaksen, M. G. Lawrence, A. Richter, J. M. Rodriguez, M. Sanderson, S. E. Strahan, K. Sudo, S. Szopa, T. P. C. van Noije, and O. Wild (2007). “Multi-model simulations of the impact of international shipping on atmospheric chemistry and climate in 2000 and 2030”. In: *Atmospheric Chemistry and Physics* 7.3, pp. 757–780.

FAA (2015). *Treatment of time.* Available at `https://www.faa.gov/regulations_policies/policy_guidance/benefit_cost/media/econ-value-section-1-tx-time.pdf` (2020/06/15).

Fairlie, D. T., D. J. Jacob, and R. J. Park (2007). “The impact of transpacific transport of mineral dust in the United States”. In: *Atmospheric Environment* 41.6, pp. 1251–1266. DOI: `10.1016/j.atmosenv.2006.09.048`.

Fels, S. B., J. D. Mahlman, M. D. Schwarzkopf, and R. W. Sinclair (1980). “Stratospheric sensitivity to perturbations in ozone and carbon dioxide: radiative and dynamical response”. In: *Journal of the Atmospheric Sciences* 37.10, pp. 2265–2297. DOI: `10.1175/1520-0469(1980)037<2265:SSTPIO>2.0.CO;2`.

Fouquet, R. (2012). “Trends in income and price elasticities of transport demand (1850–2010)”. In: *Energy Policy* 50, pp. 62–71. DOI: `10.1016/j.enpol.2012.03.001`.

Fritz, T. M., S. D. Eastham, R. L. Speth, and S. R. H. Barrett (2020). “The role of plume-scale processes in long-term impacts of aircraft emissions”. In: *Atmospheric Chemistry and Physics* 20, pp. 5697–5727. DOI: `10.5194/acp-20-5697-2020`.

Gallet, C. A. and H. Doucouliagos (2014). “The income elasticity of air travel: A meta-analysis”. In: *Annals of Tourism Research* 49, pp. 141–155. DOI: `10.1016/j.annals.2014.09.006`.

Gillen, D., W. Morrison, and C. Stewart (2007). “Air travel demand elasticities: concepts, issues and measurement”. In: *Advances in airline economics volume 2: The economics of airline institutions, operations and marketing.*

Gilmore, C. K., S. R. Barrett, J. Koo, and Q. Wang (2013). “Temporal and spatial variability in the aviation $\mathrm{NO_x}$-related $\mathrm{O_3}$ impact”. In: *Environmental Research Letters* 8.3, p. 034027.

Givoni, M. and F. Dobruszkes (2013). “A review of ex-post evidence for mode substitution and induced demand following the introduction of high-speed rail”. In: *Transport Reviews* 33.6, pp. 720–742. DOI: `10.1080/01441647.2013.853707`.

Goodman, J., R. F. Pueschel, E. J. Jensen, S. Verma, G. V. Ferry, S. D. Howard, S. A. Kinne, and D. Baumgardner (1998). “Shape and size of contrails ice particles”. In: *Geophysical Research Letters* 25.9, pp. 1327–1330.

Goodwin, P. B. (1996). “Empirical evidence on induced traffic”. In: *Transportation* 23.1, pp. 35–54. DOI: `10.1007/BF00166218`.

Grainger, R. G., A. Lambert, C. D. Rodgers, and F. W. Taylor (1995). "Stratospheric aerosol effective radius, surface area and volume estimated from infrared measurements". In: *Journal of Geophysical Research: Atmospheres* 100.95, pp. 16507–16518.

Grewe, V., A. Stenke, M. Ponater, R. Sausen, G. Pitari, D. Iachetti, H. Rogers, O. Dessens, J. Pyle, I. S. A. Isaksen, L. Gulstad, O. A. Søvde, C. Marizy, and E. Pascuillo (2007). "Climate impact of supersonic air traffic: an approach to optimize a potential future supersonic fleet–results from the EU-project SCENIC". In: *Atmospheric Chemistry and Physics*, pp. 5129–5145.

Grobecker, A. J., S. C. Coroniti, and R. H. Cannon (1974). *The effects of stratospheric pollution by aircraft.* Technical Report DOT-TST-75-50. Washington, DC: Department of Transportation.

Guenther, a. B., X. Jiang, C. L. Heald, T. Sakulyanontvittaya, T. Duhl, L. K. Emmons, and X. Wang (2012). "The model of emissions of gases and aerosols from nature version 2.1 (MEGAN2.1): An extended and updated framework for modeling biogenic emissions". In: *Geoscientific Model Development* 5, pp. 1471–1492. DOI: `10.5194/gmd-5-1471-2012`.

Gupta, K. K., A. Rehman, and R. M. Sarviya (2010). "Bio-fuels for the gas turbine: a review". In: *Renewable and Sustainable Energy Reviews* 14.9, pp. 2946–2955.

Hader, M. (2020). *COVID-19 – How we will need to re-think the aerospace industry.* URL: `https://www.rolandberger.com/en/Point-of-View/COVID-19-How-we-will-need-to-rethink-the-aerospace-industry.html` (visited on 04/09/2020).

Hakami, A., D. K. Henze, J. H. Seinfeld, K. Singh, A. Sandu, S. Kim, D. Byun, and Q. Li (2007). "The adjoint of CMAQ". In: *Environmental Science & Technology* 41.22, pp. 7807–7817.

Hart, P. E., N. J. Nilsson, and B. Raphael (1968). "A formal basis for the heuristic determination of minimum cost paths". In: *IEEE Transactions on Systems Science and Cybernetics* 4.2, pp. 100–107.

Heald, C. L., D. A. Ridley, J. H. Kroll, S. R. H. Barrett, K. E. Cady-Pereira, M. J. Alvarado, and C. D. Holmes (2014). "Contrasting the direct radiative effect and direct radiative forcing of aerosols". In: *Atmospheric Chemistry and Physics* 14.11, pp. 5513–5527. DOI: `10.5194/acp-14-5513-2014`.

Henze, D. K., J. H. Seinfeld, and D. T. Shindell (2009). "Inverse modeling and mapping US air quality influences of inorganic $PM_{2.5}$ precursor emissions using the adjoint of GEOS-Chem". In: *Atmospheric Chemistry and Physics* 9.16, pp. 5877–5903.

Henze, D. K., A. Hakami, and J. H. Seinfeld (2007). "Development of the adjoint of GEOS-Chem". In: *Atmospheric Chemistry and Physics* 7, pp. 2413–2433. DOI: `10.5194/acp-7-2413-2007`.

Heymsfield, A. J., R. P. Lawson, and G. W. Sachse (1998). "Growth of ice crystals in a precipitating contrail". In: *Geophysical Research Letters* 25.9, pp. 1335–1338.

Hidalgo, H. (1974). "The stratosphere perturbed by propulsion effluents". In: *11th Annual Meeting and Technical Display*, p. 335.

Hileman, J. I., R. W. Stratton, and P. E. Donohoo (2010). "Energy content and alternative jet fuel viability". In: *Journal of Propulsion and Power* 26.6, pp. 1184–1196. DOI: `10.2514/1.46232`.

Holmes, C. D., Q. Tang, and M. J. Prather (2011). "Uncertainties in climate assessment for the case of aviation NO". In: *Proceedings of the National Academy of Sciences of the United States of America* 108.27, pp. 10997–11002. DOI: `10.1073/pnas.1101458108`.

Hudman, R. C., N. E. Moore, A. K. Mebust, R. V. Martin, A. R. Russell, L. C. Valin, and R. C. Cohen (2012). "Steps towards a mechanistic model of global soil nitric oxide emissions: implementation and space based-constraints". In: *Atmospheric Chemistry and Physics* 12.16, pp. 7779–7795. DOI: `10.5194/acp-12-7779-2012`.

Huszar, P., H. Teyssèdre, M. Michou, A. Voldoire, D. J. L. Olivié, D. Saint-Martin, D. Cariolle, S. Senesi, D. S. Y. Melia, A. Alias, F. Karcher, P. Ricaud, and T. Halenka (2013). "Modeling the present and future impact of aviation on climate: an AOGCM approach with online coupled chemistry." In: *Atmospheric Chemistry and Physics* 13.19. DOI: `10.5194/acp-13-10027-2013`.

Hymel, K. M., K. A. Small, and K. V. Dender (2010). "Induced demand and rebound effects in road transport". In: *Transportation Research Part B: Methodological* 44.10, pp. 1220–1241. DOI: `10.1016/j.trb.2010.02.007`.

IATA (2015). *Economic performance of the airline industry. 2015-mid-year report.* URL: `https://www.iata.org/en/iata-repository/publications/economic-reports/airline-industry-economic-performance---2015-mid-year---report/`.

IATA (2020). *Air passenger market analysis – April 2020.* URL: `https://www.iata.org/en/iata-repository/publications/economic-reports/air-passenger-monthly-analysis---apr-20202/`.

ICAO (2013). *Annual report of the Council - 2011 (DOC9975).* URL: `https://www.icao.int/publications/Documents/9975_en.pdf`.

ICAO (2015). *The world of air transport in 2015.* URL: `https://www.icao.int/annual-report-2015/Pages/the-world-of-air-transport-in-2015.aspx` (visited on 01/15/2020).

ICAO (2018). *ICAO long-term traffic forecast 2018.* URL: `https://www.icao.int/sustainability/Documents/LTF_Charts-Results_2018edition.pdf` (visited on 06/19/2020).

ICAO (2019). *ICAO aircraft engine emissions databank — EASA.* (Accessed on 07/07/2020). URL: `https://www.easa.europa.eu/domains/environment/icao-aircraft-engine-emissions-databank`.

InterVISTAS (2007). *Estimating air travel demand elasticities.* URL: `https://www.iata.org/en/iata-repository/publications/economic-reports/estimating-air-travel-demand-elasticities---by-intervistas/`.

InterVISTAS (2020). *InterVISTAS outlook on COVID-19: scenarios for passenger traffic recovery.* URL: `http://intervistas.com/downloads/covid19_outlook-scenarios.pdf` (visited on 06/19/2020).

Irvine, E. A. and K. P. Shine (2015). "Ice supersaturation and the potential for contrail formation in a changing climate". In: *Earth System Dynamics* 6, pp. 555–568. DOI: `10.5194/esd-6-555-2015`.

Jacobson, M. Z. (2011). “Numerical solution to drop coalescence/breakup with a volume-conserving, positive-definite, and unconditionally stable scheme”. In: *Journal of the Atmospheric Sciences* 68.2, pp. 334–346.

Jacobson, M. Z. (1997). “Development and application of a new air pollution modeling system—II. aerosol module structure and design”. In: *Atmospheric Environment* 31.2, pp. 131–144.

Jacobson, M. Z. (2003). “Development of mixed-phase clouds from multiple aerosol size distributions and the effect of the clouds on aerosol removal”. In: *Journal of Geophysical Research: Atmospheres* 108.D8.

Jacobson, M. Z., R. P. Turco, E. J. Jensen, and O. B. Toon (1994). “Modeling coagulation among particles of different composition and size”. In: *Atmospheric Environment* 28.7, pp. 1327–1338.

Jaecker-Voirol, A. and P. Mirabel (1989). “Heteromolecular nucleation in the sulfuric acid-water system”. In: *Atmospheric Environment* 23.9, pp. 2053–2057.

Jaeglé, L., P. K. Quinn, T. S. Bates, B. Alexander, and J. T. Lin (2011). “Global distribution of sea salt aerosols: new constraints from in situ and remote sensing observations”. In: *Atmospheric Chemistry and Physics* 11.7, pp. 3137–3157. DOI: `10.5194/acp-11-3137-2011`.

Jain, S., K. E. Ogunsina, H. Chao, W. A. Crossley, and D. A. DeLaurentis (2020). “Predicting routes for, number of operations of, and fleet-level impacts of future commercial supersonic aircraft on routes touching the United States”. In: *AIAA Aviation 2020 Forum*. DOI: `10.2514/6.2020-2878`.

Jara-Díaz, S. R. (2007). “Allocation and valuation of travel-time savings”. In: *Handbook of Transport Modelling*. Ed. by D. A. Hensher and K. J. Button. Vol. 1, pp. 363–379. DOI: `10.1108/9780857245670-018`.

Jensen, E. J., O. B. Toon, R. F. Pueschel, J. Goodman, G. W. Sachse, B. E. Anderson, K. R. Chan, D. Baumgardner, and R. C. Miake-Lye (1998a). “Ice crystal nucleation and growth in contrails forming at low ambient temperatures”. In: *Geophysical Research Letters* 25.9, pp. 1371–1374.

Jensen, E. J., A. S. Ackerman, D. E. Stevens, O. Toon, and P. Minnis (1998b). “Spreading and growth of contrails in a sheared environment”. In: *Journal of Geophysical Research: Atmospheres* 103.D24, pp. 31557–31567.

Jiang, J. H., H. Su, C. Zhai, L. Wu, K. Minschwaner, A. M. Molod, and A. M. Tompkins (2015). “An assessment of upper troposphere and lower stratosphere water vapor in MERRA, MERRA2, and ECMWF: reanalyses using Aura MLS observations”. In: *Journal of Geophysical Research: Atmospheres* 120, pp. 11, 468–11, 485. DOI: `10.1002/2015JD023752`.

Jung, J. G., S. N. Pandis, and P. J. Adams (2008). “Evaluation of nucleation theories in a sulfur-rich environment”. In: *Aerosol Science and Technology* 42.7, pp. 495–504.

Kärcher, B. (1998). “Physicochemistry of aircraft-generated liquid aerosols, soot, and ice particles: 1. model description”. In: *Journal of Geophysical Research: Atmospheres* 103.D 14, pp. 17111–17128.

Kärcher, B., U. Burkhardt, A. Bier, L. Bock, and I. J. Ford (2015). “The microphysical pathway to contrail formation”. In: *Journal of Geophysical Research: Atmospheres* 120.15, pp. 7893–7927.

Kärcher, B., U. Burkhardt, S. Unterstrasser, and P. Minnis (2009). "Factors controlling contrail cirrus optical depth". In: *Atmospheric Chemistry and Physics* 9.16, pp. 6229–6254.

Kärcher, B., M. M. Hirschberg, and P. Fabian (1996). "Small-scale chemical evolution of aircraft exhaust species at cruising altitudes". In: *Journal of Geophysical Research: Atmospheres* 101.D10, pp. 15169–15190.

Kärcher, B. and T. Koop (2005). "The role of organic aerosols in homogeneous ice formation". In: *Atmospheric Chemistry and Physics* 5.3.

Kärcher, B., R. P. Turco, F. Yu, M. Y. Danilin, D. K. Weisenstein, R. C. Miake-Lye, and R. Busen (2000). "A unified model for ultrafine aircraft particle emissions". In: *Journal of Geophysical Research: Atmospheres* 105.D24, pp. 29379–29386.

Kärcher, B. and F. Yu (2009). "Role of aircraft soot emissions in contrail formation". In: *Geophysical Research Letters* 36.1.

Kärcher, B. (1999). "Aviation-produced aerosols and contrails". In: *Surveys in Geophysics* 20.2, pp. 113–167.

Kärcher, B. (2018). "Formation and radiative forcing of contrail cirrus". In: *Nature Communications* 9.1, p. 1824.

Kärcher, B., R. Busen, A. Petzold, F. P. Schröder, U. Schumann, and E. J. Jensen (1998). "Physicochemistry of aircraft-generated liquid aerosols, soot, and ice particles: 2. comparison with observations and sensitivity studies". In: *Journal of Geophysical Research: Atmospheres* 103.D14, pp. 17129–17147.

Kawa, S. R., J. G. Anderson, S. L. Baughcum, R. C. Cohen, D. E. Kinnison, P. A. Newman, J. M. Rodriquez, R. S. Stolarski, D. W. Waugh, C. A. Brock, and W. H. Brune (1999). *Assessment of the effects of high-speed aircraft in the stratosphere: 1998*. Tech. rep. TP-1999-209237. NASA.

Kharina, A., T. MacDonald, and D. Rutherford (2018). "Environmental performance of emerging supersonic transport aircraft". Available at `https://theicct.org/sites/default/files/publications/Environmental_Supersonic_Aircraft_20180717.pdf` (2020/05/15). Working paper.

Khodayari, A., S. C. Olsen, D. J. Wuebbles, and D. B. Phoenix (2015). "Aviation NO_x-induced CH_4 effect: fixed mixing ratio boundary conditions versus flux boundary conditions". In: *Atmospheric Environment* 113, pp. 135–139. DOI: `10.1016/j.atmosenv.2015.04.070`.

Klein, K., S. Albers, F. Allroggen, and R. Malina (2015). "Serving vs. settling: What drives the establishment of low-cost carriers' foreign bases?" In: *Transportation Research Part A: Policy and Practice* 79, pp. 17–30. DOI: `10.1016/j.tra.2015.03.021`.

Köhler, M. O., G. Rädel, O. Dessens, K. P. Shine, H. L. Rogers, O. Wild, and J. A. Pyle (2008). "Impact of perturbations to nitrogen oxide emissions from global aviation". In: *Journal of Geophysical Research: Atmospheres* 113.D11, pp. 1–15.

Koo, J., Q. Wang, D. K. Henze, I. A. Waitz, and S. R. Barrett (2013). "Spatial sensitivities of human health risk to intercontinental and high-altitude pollution". In: *Atmospheric Environment* 71, pp. 140–147.

Kraabøl, A. G., T. K. Berntsen, J. K. Sundet, and F. Stordal (2002). "Impacts of NO_x emissions from subsonic aircraft in a global three-dimensional chemistry transport model including plume processes". In: *Journal of Geophysical Research: Atmospheres* 107.D22, ACH–22.

Kraabøl, A. G., P. Konopka, F. Stordal, and H. Schlager (2000). "Modelling chemistry in aircraft plumes 1: comparison with observations and evaluation of a layered approach". In: *Atmospheric Environment* 34.23, pp. 3939–3950.

Küchemann, D. (1978). *The aerodynamic design of aircraft: A detailed introduction to the current aerodynamic knowledge and practical guide to the solution of aircraft design problems.* Oxford: Pergamon Press.

Lee, D. S., G. Pitari, V. Grewe, K. Gierens, J. E. Penner, A. Petzold, M. J. Prather, U. Schumann, A. Bais, T. Berntsen, D. Iachetti, L. L. Lim, and R. Sausen (2010). "Transport impacts on atmosphere and climate: Aviation". In: *Atmospheric Environment.* Transport impacts on atmosphere and climate: the ATTICA assessment report 44.37, pp. 4678–4734. DOI: `10.1016/j.atmosenv.2009.06.005`. (Visited on 05/26/2015).

Lee, D. S., D. W. Fahey, P. M. Forster, P. J. Newton, R. C. Wit, L. L. Lim, B. Owen, and R. Sausen (2009). "Aviation and global climate change in the 21st century". In: *Atmospheric Environment* 43.22, pp. 3520–3537.

Liebhardt, B. (2019). "Sonic boom carpet computation as a basis for supersonic flight routing". In: *AIAA Aviation 2019 Forum.*

Livesey, N. J., W. G. Read, P. A. Wagner, L. Froideveaux, A. Lambert, G. L. Manney, L. F. Millán Valle, H. C. Pumphrey, M. L. Santee, M. J. Schwartz, S. Wang, R. A. Fuller, R. F. Jarnot, B. W. Knosp, E. Martinez, and R. R. Lay (2020). *Aura microwave limb sounder version 4.2x level 2 and 3 data quality and description document.* NASA Jet Propulsion Laboratory.

Lukachko, S. P., I. A. Waitz, R. C. Miake-Lye, R. C. Brown, and M. R. Anderson (1998). "Production of sulfate aerosol precursors in the turbine and exhaust nozzle of an aircraft engine". In: *Journal of Geophysical Research: Atmospheres* 103.D13, pp. 16159–16174.

Lytle, J. K. (2000). "Numerical propulsion system simulation: an overview". In: *CAS 2000 Workshop/The Ames Research Center, February* 15.

Mackie, P. J., S. Jara-Díaz, and A. S. Fowkes (2001). "The value of travel time savings in evaluation". In: *Transportation Research Part E: Logistics and Transportation Review.* Advances in the valuation of travel time savings 37.2, pp. 91–106. DOI: `10.1016/S1366-5545(00)00013-2`.

Mannstein, H., R. Meyer, and P. Wendling (1999). "Operational detection of contrails from NOAA-AVHRR-data". In: *International Journal of Remote Sensing* 20.8, pp. 1641–1660.

Maycock, a. C., K. P. Shine, and M. M. Joshi (2011). "The temperature response to stratospheric water vapour changes". In: *Quarterly Journal of the Royal Meteorological Society* 137.657, pp. 1070–1082. DOI: `10.1002/qj.822`.

McCormack, J. P. and D. E. Siskind (2002). "Simulations of the quasi-biennial oscillation and its effect on stratospheric H_2O, CH_4, and age of air with an interactive two-dimensional model". In: *Journal of Geophysical Research: Atmospheres* 107, pp. 1–17.

Meijer, E. W., P. F. Velthoven, A. M. Thompson, L. Pfister, H. Schlager, P. Schulte, and H. Kelder (2000). "Model calculations of the impact of NO_x from air traffic, lightning, and surface emissions, compared with measurements". In: *Journal of Geophysical Research: Atmospheres* 105.D3, pp. 3833–3850.

Menut, L. (2003). "Adjoint modeling for atmospheric pollution process sensitivity at regional scale". In: *Journal of Geophysical Research: Atmospheres* 108.D17.

Menut, L., R. Vautard, M. Beekmann, and C. Honoré (2000). "Sensitivity of photochemical pollution using the adjoint of a simplified chemistry-transport model". In: *Journal of Geophysical Research: Atmospheres* 105.D12, pp. 15379–15402.

Miloshevich, L. M., H. Vömel, D. N. Whiteman, and T. Leblanc (2009). "Accuracy assessment and correction of Vaisala RS92 Radiosonde Water Vapor Measurements". In: *Journal of Geophysical Research: Atmospheres* 114. DOI: `10.1029/2008JD011565`.

MIT (2020). *Airline Data Project*. URL: `http://web.mit.edu/airlinedata/www/default.html`.

Molenaar, D.-M., F. Bosch, J. Guggenheim, P. Jhunjhunwala, H.-H. Loh, and B. Wade (2020). *The post-COVID-19 flight plan for airlines*. Library Catalog: www.bcg.com. URL: `https://www.bcg.com/publications/2020/post-covid-airline-industry-strategy.aspx`.

Morgenstern, J., M. Buonanno, J. Yao, M. Murugappan, U. Paliath, L. Cheung, I. Malcevic, K. Ramakrishnan, N. Pastouchenko, and T. Wood (2015). *Advanced concept studies for supersonic commercial transports entering service in the 2018-2020 period phase 2*. URL: `https://ntrs.nasa.gov/search.jsp?R=20150015837` (visited on 06/16/2020).

Murray, B. J., T. W. Wilson, S. Dobbie, Z. Cui, S. M. Al-Jumur, O. Möhler, M. Schnaiter, R. Wagner, S. Benz, M. Niemand, H. Saathoff, V. Ebert, S. Wagner, and B. Kärcher (2010). "Heterogeneous nucleation of ice particles on glassy aerosols under cirrus conditions". In: *Nature Geoscience* 3.4, pp. 233–237.

Murray, L. T., D. J. Jacob, J. A. Logan, R. C. Hudman, and W. J. Koshak (2012). "Optimized regional and interannual variability of lightning in a global chemical transport model constrained by LIS/OTD satellite data". In: *Journal of Geophysical Research: Atmospheres* 117.D20, p. 3851. DOI: `10.1029/2012JD017934`.

Napari, I., M. Noppel, H. Vehkamäki, and M. Kulmala (2002). "Parametrization of ternary nucleation rates for H_2SO_4-NH_3-H_2O vapors". In: *Journal of Geophysical Research: Atmospheres* 107.D19.

NASA (2020). *X-59 QueSST*. Available at `https://www.nasa.gov/aero/nasa-experimental-supersonic-aircraft-x-59-quesst` (2020/05/15).

Njegovan, N. (2006). "Elasticities of demand for leisure air travel: A system modelling approach". In: *Journal of Air Transport Management*. Leisure traffic and tourism: new strategies for airlines, airports and the travel trade 12.1, pp. 33–39. DOI: `10.1016/j.jairtraman.2005.09.003`.

Ovarlez, J., P. van Velthoven, G. Sachse, S. Vay, H. Schlager, and H. Ovarlez (2000). "Comparison of water vapor measurements from POLINAT 2 with ECMWF analyses in high-humidity Conditions". In: *Journal of Geophysical Research: Atmospheres* 105, pp. 3737–3744. DOI: `10.1029/1999JD900954`.

Paoli, R., D. Cariolle, and R. Sausen (2011). "Review of effective emissions modeling and computation". In: *Geoscientific Model Development* 4.3, pp. 643–667. DOI: `10.5194/gmd-4-643-2011`.

Paoli, R., X. Vancassel, F. Garnier, and P. Mirabel (2008). "Large-eddy simulation of a turbulent jet and a vortex sheet interaction: particle formation and evolution in the near field of an aircraft wake". In: *Meteorologische Zeitschrift* 17.2, pp. 131–144.

Petry, H., J. Hendricks, M. Möllhoff, E. Lippert, A. Meier, A. Ebel, and R. Sausen (1998). "Chemical conversion of subsonic aircraft emissions in the dispersing plume: calculation of effective emission indices". In: *Journal of Geophysical Research: Atmospheres* 103.D5, pp. 5759–5772.

Petzold, A., A. Döpelheuer, C. A. Brock, and F. Schröder (1999). "In situ observations and model calculations of black carbon emission by aircraft at cruise altitude". In: *Journal of Geophysical Research: Atmospheres* 104.D18, pp. 22171–22181.

Picot, J., R. Paoli, O. Thouron, and D. Cariolle (2015). "Large-eddy simulation of contrail evolution in the vortex phase and its interaction with atmospheric turbulence". In: *Atmospheric Chemistry and Physics* 15.13, pp. 7369–7389.

Pierce, B. (2020). *COVID-19: Outlook for air travel in the next 5 years.* URL: `https://www.iata.org/en/iata-repository/publications/economic-reports/covid-19-outlook-for-air-travel-in-the-next-5-years/`.

Pitari, G. and E. Mancini (2001). "Climatic impact of future supersonic aircraft: role of water vapour and ozone feedback on circulation". In: *Physics and Chemistry of the Earth, Part C: Solar, Terrestrial & Planetary Science* 26.8, pp. 571–576. DOI: `10.1016/S1464-1917(01)00049-6`.

Pitari, G., D. Iachetti, E. Mancini, V. Montanaro, N. De Luca, C. Marizy, O. Dessens, H. Rogers, J. Pyle, V. Grewe, A. Stenke, and O. A. Søvde (2008). "Radiative forcing from particle emissions by future supersonic aircraft". In: *Atmospheric Chemistry and Physics.*

Prather, M., H. L. Wesoky, R. C. Miake-Lye, A. R. Douglass, R. P. Turco, D. Wuebbles, M. Ko, and A. L. Schmeltekopf (1992). *The atmospheric effects of stratospheric aircraft: a first program report.* Tech. rep. NASA-RP-1272. NASA.

Pruppacher, H. R. and J. D. Klett (1997). *Microphysics of clouds and precipitation.* Kluwer Academic Publishers.

Rädel, G. and K. P. Shine (2010). "Validating ECMWF forecasts for the occurrence of ice supersaturation using visual observations of persistent contrails and radiosonde measurements over England". In: *Quarterly Journal of the Royal Meteorological Society* 136, pp. 1723–1732. DOI: `10.1002/qj.670`.

Radich, T. (2015). *The flight paths for biojet fuel.* URL: `https://www.eia.gov/workingpapers/pdf/flightpaths_biojetffuel.pdf`.

Rexing, B., C. Barnhart, T. Kniker, A. Jarrah, and N. Krishnamurthy (2000). "Airline fleet assignment with time windows". In: *Transportation Science* 34.1, pp. 1–20.

Rojo, C., X. Vancassel, P. Mirabel, J.-L. Ponche, and F. Garnier (2015). "Impact of alternative jet fuels on aircraft-induced aerosols". In: *Fuel* 144, pp. 335–341.

Roxburgh, G. (2004). *Concorde B.* Available at `http://www.concordesst.com/concordeb.html` (2020/01/15).

Sandu, A., D. N. Daescu, G. R. Carmichael, and T. Chai (2005). "Adjoint sensitivity analysis of regional air quality models". In: *Journal of Computational Physics* 204.1, pp. 222–252.

Schmidt, E. (1941). “Die Entstehung von Eisnebel aus den Auspuffgasen von Flugmotoren”. In: *Schriften der Deutschen Akademie der Luftfahrtforschung* Heft 44.

Schmidt, H. and D. Martin (2003). “Adjoint sensitivity of episodic ozone in the Paris area to emissions on the continental scale”. In: *Journal of Geophysical Research: Atmospheres* 108.D17.

Schröder, F., B. Kärcher, C. Duroure, J. Ström, A. Petzold, J.-F. Gayet, B. Strauss, P. Wendling, and S. Borrmann (2018). “On the transition of contrails into cirrus clouds”. In: *Journal of the Atmospheric Sciences* 75.2.

Schumann, U. (2000). “Influence of propulsion efficiency on contrail formation”. In: *Aerospace Science and Technology* 4, pp. 391–401. DOI: `10.1016/S1270-9638(00)01062-2`.

Schumann, U. (2012). “A contrail cirrus prediction model”. In: *Geoscientific Model Development* 5, pp. 543–580.

Schumann, U., F. Arnold, R. Busen, J. Curtius, B. Kärcher, A. Kiendler, A. Petzold, H. Schlager, F. Schröder, and K.-H. Wohlfrom (2002). “Influence of fuel sulfur on the composition of aircraft exhaust plumes: the experiments SULFUR 1–7”. In: *Journal of Geophysical Research: Atmospheres* 107.D15.

Schumann, U., H. Schlager, F. Arnold, R. Baumann, P. Haschberger, and O. Klemm (1998). “Dilution of aircraft exhaust plumes at cruise altitudes”. In: *Atmospheric Environment* 32.18, pp. 3097–3103.

Schumann, U., H. Schlager, F. Arnold, J. Ovarlez, H. Kelder, Ø. Hov, G. Hayman, I. S. A. Isaksen, J. Staehelin, and P. D. Whitefield (2000). “Pollution from aircraft emissions in the North Atlantic flight corridor: overview on the POLINAT projects”. In: *Journal of Geophysical Research: Atmospheres* 105.D3, pp. 3605–3631.

Seidel, J. (2020). Private communication.

Shires, J. D. and G. C. de Jong (2009). “An international meta-analysis of values of travel time savings”. In: *Evaluation and Program Planning*. Evaluating the Impact of Transport Projects: Lessons for Other Disciplines 32.4, pp. 315–325. DOI: `10.1016/j.evalprogplan.2009.06.010`.

Simone, N. W., M. E. J. Stettler, and S. R. H. Barrett (2013). “Rapid estimation of global civil aviation emissions with uncertainty quantification”. In: *Transportation Research Part D: Transport and Environment* 25, pp. 33–41.

Sölch, I. and B. Kärcher (2010). “A large-eddy model for cirrus clouds with explicit aerosol and ice microphysics and Lagrangian ice particle tracking”. In: *Quarterly Journal of the Royal Meteorological Society* 136.653, pp. 2074–2093.

Solomon, S., K. H. Rosenlof, R. W. Portmann, J. S. Daniel, S. M. Davis, T. J. Sanford, and G.-K. Plattner (2010). “Contributions of stratospheric water vapor to decadal changes in the rate of global warming”. In: *Science* 327.5970, pp. 1219–1223. DOI: `10.1126/science.1182488`.

Song, C. H., G. Chen, S. R. Hanna, J. Crawford, and D. D. Davis (2003). “Dispersion and chemical evolution of ship plumes in the marine boundary layer: Investigation of $O_3/NO_y/HO_x$ chemistry”. In: *Journal of Geophysical Research: Atmospheres* 108.D4.

Sonntag, D. (1990). “Important new values of the physical constants of 1986, vapour pressure formulations based on the ITS-90, and psychrometer formulae”. In: *Zeitschrift für Meteorologie* 40.5, pp. 340–344.

Speth, R. L., C. Rojo, R. Malina, and S. R. Barrett (2015). “Black carbon emissions reductions from combustion of alternative jet fuels”. In: *Atmospheric Environment* 105, pp. 37–42.

Stettler, M. E., A. M. Boies, A. Petzold, and S. R. Barrett (2013). “Global civil aviation black carbon emissions”. In: *Environmental Science & Technology* 47.18, pp. 10397–10404.

Tabazadeh, A., E. J. Jensen, and O. B. Toon (1997). “A model description for cirrus cloud nucleation from homogeneous freezing of sulfate aerosols”. In: *Journal of Geophysical Research: Atmospheres* 102.D20, pp. 23845–23850.

Tang, M. J., R. A. Cox, and M. Kalberer (2014). “Compilation and evaluation of gas phase diffusion coefficients of reactive trace gases in the atmosphere: volume 1. inorganic compounds”. In: *Atmospheric Chemistry and Physics* 14.17, pp. 9233–9247.

Teoh, R., M. E. J. Stettler, A. Majumdar, U. Schumann, B. Graves, and A. M. Boies (2019). “A methodology to relate black carbon particle number and mass emissions”. In: *Journal of Aerosol Science* 132, pp. 44–59. DOI: `10.1016/j.jaerosci.2019.03.006`.

The World Bank (2014). *World development indicators.* URL: `http://data.worldbank.org/data-catalog/world-development-indicators`.

Thompson, A. M., R. R. Friedl, and H. L. Wesoky (1996). *Atmospheric effects of aviation: first report of the subsonic assessment project.* Tech. rep. NASA-RP-1385. NASA.

Tie, X. X., G. Brasseur, X. Lin, P. Friedlingstein, C. Granier, and P. Rasch (1994). “The impact of high altitude aircraft on the ozone layer in the stratosphere”. In: *Journal of Atmospheric Chemistry* 18.2, pp. 103–128. DOI: `10.1007/BF00696810`.

Toon, O. B. and R. C. Miake-Lye (1998). “Subsonic aircraft: contrail and cloud effects special study (SUCCESS)”. In: *Geophysical Research Letters* 25.8, pp. 1109–1112.

Train, K. and D. McFadden (1978). “The goods/leisure tradeoff and disaggregate work trip mode choice models”. In: *Transportation Research* 12.5, pp. 349–353. DOI: `10.1016/0041-1647(78)90011-4`.

Tremmel, H. G., H. Schlager, P. Konopka, P. Schulte, F. Arnold, M. Klemm, and B. Droste-Franke (1998). “Observations and model calculations of jet aircraft exhaust products at cruise altitude and inferred initial OH emissions”. In: *Journal of Geophysical Research: Atmospheres* 103.D9, pp. 10803–10816.

Tremmel, H. G. and U. Schumann (1999). “Model simulations of fuel sulfur conversion efficiencies in an aircraft engine: Dependence on reaction rate constants and initial species mixing ratios”. In: *Aerospace Science and Technology* 3.7, pp. 417–430.

U.K. Office of National Statistics (2020). *Travelpac: travel to and from the UK.* URL: `https://www.ons.gov.uk/peoplepopulationandcommunity/leisureandtourism/datasets/travelpac`.

U.S. Department of Commerce (2013). *Survey of international air travelers. Overseas travelers to the U.S.* URL: `https://travel.trade.gov/research/programs/ifs/examples.asp`.

United Nations, Department of Economic and Social Affairs, Population Division (2013). *World population prospects: the 2012 revision, highlights and advance tables.* URL: `https://population.un.org/wpp/Publications/Files/WPP2012_Volume-I_Comprehensive-Tables.pdf`.

Unterstrasser, S. (2016). "Properties of young contrails–a parameterisation based on large-eddy simulations". In: *Atmospheric Chemistry and Physics* 16.4, pp. 2059–2082.

Unterstrasser, S. and K. Gierens (2010). "Numerical simulations of contrail-to-cirrus transition–part 1: an extensive parametric study". In: *Atmospheric Chemistry and Physics* 10.4, pp. 2017–2036.

Unterstrasser, S., K. Gierens, I. Sölch, and M. Wirth (2016). "Numerical simulations of homogeneously nucleated natural cirrus and contrail-cirrus. Part 2: interaction on local scale". In: *Meteorologische Zeitschrift*, pp. 1–19.

Unterstrasser, S., K. Gierens, and P. Spichtinger (2008). "The evolution of contrail microphysics in the vortex phase". In: *Meteorologische Zeitschrift* 17.2, pp. 145–156.

UNU-WIDER (2014). *World Income Inequality Database (WIID3.0B).* URL: `https://www.wider.unu.edu/database/previous-versions-wiid` (visited on 08/08/2016).

US Department of Transportation (2014). *2014 revised value of travel time guidance.* URL: `https://www.transportation.gov/resources/2014-revised-value-of-travel-time-guidance`.

USDA Economic Research Service (2016). *USDA ERS - International macroeconomic data set.* URL: `https://www.ers.usda.gov/data-products/international-macroeconomic-data-set/international-macroeconomic-data-set/`.

Vehkamäki, H., M. Kulmala, I. Napari, K. E. Lehtinen, C. Timmreck, M. Noppel, and A. Laaksonen (2002). "An improved parameterization for sulfuric acid–water nucleation rates for tropospheric and stratospheric conditions". In: *Journal of Geophysical Research: Atmospheres* 107.D22.

Vinken, G. C., K. F. Boersma, D. J. Jacob, and E. W. Meijer (2011). "Accounting for non-linear chemistry of ship plumes in the GEOS-Chem global chemistry transport model". In: *Atmospheric Chemistry and Physics* 11.22, pp. 11707–11722.

Vohralik, P. F., L. K. Randeniya, I. C. Plumb, and S. L. Baughcum (2008). "Effect of plume processes on aircraft impact". In: *Journal of Geophysical Research: Atmospheres* 113.D5.

Vömel, H., H. Selkirk, L. Miloshevich, J. Valverde-Canossa, J. Valdés, E. Kyrö, R. Kivi, W. Stolz, G. Peng, and J. A. Diaz (2007). "Radiation dry bias of the Vaisala RS92 Humidity Sensor". In: *Journal of Atmospheric and Oceanic Technology* 24, pp. 953–963. DOI: `10.1175/JTECH2019.1`.

Wang, J., L. Zhang, A. Dai, F. Immler, M. Sommer, and H. Vömel (2013). "Radiation dry bias correction of Vaisala RS92 humidity data and its impacts on historical radiosonde data". In: *Journal of Atmospheric and Oceanic Technology* 30, pp. 197–214. DOI: `10.1175/JTECH-D-12-00113.1`.

Wegner, T., D. E. Kinnison, R. R. Garcia, and S. Solomon (2013). "Simulation of polar stratospheric clouds in the specified dynamics version of the whole atmosphere community climate model". In: *Journal of Geophysical Research: Atmospheres* 118.10, pp. 4991–5002.

Weisenstein, D. K., M. K. W. Ko, N.-D. Sze, and J. M. Rodriguez (1996). "Potential impact of SO_2 emissions from stratospheric aircraft on ozone". In: *Geophysical Research Letters* 23.2, pp. 161–164. DOI: `10.1029/95GL03781`.

Wen, J., C. J. Weit, M. Mayakonda, A. Anand, T. Zaidi, and D. Mavris (2020). "A methodology for supersonic commercial market estimation and environmental impact evaluation (part II)". In: *AIAA Scitech 2020 Forum*.

WMO (2020). *Historical WMO Publication No. 9, Volume A, Observing Stations and WMO Catalogue of Radiosondes.* URL: `https://www.wmo.int/pages/prog/www/ois/volume-a/vola-hist-home.htm`.

Wong, H.-W. and R. C. Miake-Lye (2010). "Parametric studies of contrail ice particle formation in jet regime using microphysical parcel modeling". In: *Atmospheric Chemistry and Physics* 10.7, pp. 3261–3272.

Woolley, P. K. (1972). "A cost–benefit analysis of the Concorde project". In: *Journal of Transport Economics and Policy* 6.3, pp. 225–239.

Yi, B., P. Yang, K.-N. Liou, P. Minnis, and J. E. Penner (2012). "Simulation of the global contrail radiative forcing: a sensitivity analysis". In: *Geophysical Research Letters* 39. DOI: `10.1029/2012GL054042`.

Yu, F., R. P. Turco, and B. Kärcher (1999). "The possible role of organics in the formation and evolution of ultrafine aircraft particles". In: *Journal of Geophysical Research: Atmospheres* 104.D4, pp. 4079–4087.

Zhang, X., X. Chen, and J. Wang (2019). "A number-based inventory of size-resolved black carbon particle emissions by global civil aviation". In: *Nature Communications* 10, pp. 1–11. DOI: `10.1038/s41467-019-08491-9`.